EXPERIMENTAL STUDIES OF MARANGONI CONVECTION WITH BUOYANCY IN SIMPLE AND BINARY FLUIDS

A Thesis
Presented to
The Academic Faculty

by

Yaofa Li

In Partial Fulfillment
of the Requirements for the Degree
Doctor of Philosophy in the
George W. Woodruff School of Mechanical Engineering

Georgia Institute of Technology
August 2015

EXPERIMENTAL STUDIES OF MARANGONI CONVECTION WITH BUOYANCY IN SIMPLE AND BINARY FLUIDS

Approved by:

Dr. Minami Yoda, Advisor
George W. Woodruff School of
Mechanical Engineering
Georgia Institute of Technology

Dr. Roman Grigoriev
School of Physics
Georgia Institute of Technology

Dr. Yogendra Joshi
George W. Woodruff School of
Mechanical Engineering
Georgia Institute of Technology

Dr. Michael Schatz
School of Physics
Georgia Institute of Technology

Dr. S. Mostafa Ghiaasiaan
George W. Woodruff School of
Mechanical Engineering
Georgia Institute of Technology

Date Approved: May 14th 2015

ACKNOWLEDGEMENTS

I am sincerely grateful to all those who have made this work possible. Foremost, I would like to express my sincere gratitude to my advisor Professor Minami Yoda for her constant encouragement, trust and invaluable suggestions as I have pursued these studies. I would especially like to thank Professor Roman Grigoriev for his insightful discussions and for always being there and providing great advices. I would also like to thank the remaining members of my thesis reading committee: Professor Yogendra Joshi, Professor S. Mostafa Ghiaasiaan, and Professor Michael Schatz for their effort in reviewing this work and their advices and clarifying remarks.

I would like to extend my appreciation to Professor Myeongsub Kim at University of Central Florida for helping me get started with experimental work; to Dr. Haifeng Li at Enercon, Inc. for his great advices and helpful discussions on PIV technique and image processing fundamentals; to Mr. Benjamin M. Chan, Mr. Dennis Sadowski, Dr. Brantley Mills and Dr. Jordan Rader for their help and support in the design and construction of the experimental apparatus; to Dr. Hongzhi Wang, Dr. Zhuo Li and Mr. Joohyung Lee for their help with contact angle and surface tension measurements; to Professor Yutaka Kazoe at the University of Tokyo for his suggestions on my experiments and image processing methods; to Dr. Professor Zhuomin Zhang at Georgia Institute of Technology for his kind support during my graduate study.

My laboratory colleagues and friends have also provided me with invaluable support. I would like to thank Tongran Qin for his useful discussions on theoretical and numerical studies of this project, and Necmettin Cevheri for great discussions, for sharing

his experimental equipment with me and for always taking good care of our lab space. My appreciation also goes to Andrew Yee, Baily Zhao, Dr. Vladimer Tsiklashvili and Sam Musa for their support and help.

Finally, I wish to express my sincere appreciation to my parents and two sisters for their continuous and unconditional support and love. My deepest gratitude goes to my wife, Lu Wang, for her enduring love, patience, and understanding. Without the love, none of this would have been possible.

TABLE OF CONTENTS

LIST OF TABLES

Page

LIST OF FIGURES

Page

LIST OF SYMBOLS AND ABBREVIATIONS

Abbreviations

1D	One-Dimensional
2D	Two-Dimensional
2D-2C	Two-Dimensional Two-Component
3D	Three-Dimensional
3DSI	Three-Dimensional Stationary Instability
AOM	Acousto-Optical Modulator
CCD	Charge-Coupled Device
CO2	Carbon Dioxide
Cu	Copper
CW	Continuous-Wave
DAQ	Data Acquisition System
DDI	Distilled Deionized
DFT	Discrete Fourier Transform
DI	Deionized
EMCCD	Electron Multiplying CCD
EtOH	Ethanol
FFT	Fast Fourier Transform
H_2O	Water
HD	Hard Drive
HDMS	Hexamethyldisiloxane
HTC	Heat Transfer Coefficient
HTW	Hydrothermal Wave
UF	Unsteady Flow

LDV	Laser-Doppler Velocimetry
MeOH	Methanol
NIST	National Institute of Standards and Technology
OMC	Oscillatory Multicellular Flow
PIV	Particle-Image Velocimetry
PMC	Partial Multicellular Flow
PS	Polystyrene
PTFE	Polytetrafluoroethylene
PVC	Polyvinyl Chloride
RF	Reversed Flow
SDF	Solutocapillarity-Dominated Flow
SMC	Steady Multicellular Flow
SNR	Signal-to-Noise Ratio
SUF	Steady Unicellular Flow
TC	Thermocouple
TDF	Thermocapillarity-Dominated Flow
UNIFAC	Universal Quasichemical Functional-Group Activity Coefficients

Greek Letters

α	Thermal Diffusivity
α_s	Complex Perturbation Growth Rate (Linear Stability Analysis)
β	Coefficient of Thermal Expansion
β_s	Real Part of Perturbation Growth Rate (Linear Stability Analysis)
γ	Temperature Coefficient of Surface Tension
γ_m, γ_w	Activity Coefficients
Γ_x	Streamwise Aspect Ratio

Γ_y	Transverse Aspect Ratio
θ_k, θ_{trans}	Slopes of the Interface Curve (Image Transformation)
θ	Angular Coordinate
θ_s, Θ_s	Temperatures (Linear Stability Analysis)
λ	Laser Beam Wavelength
λ_x	Spatial Wavelength of the Rolls
κ_s	Real Part of Wave Number (Linear Stability Analysis)
μ	Dynamic Viscosity
ν	Kinematic Viscosity
ρ	Density
ρ_L	Average Liquid Density
ρ_P	Particle Area Density in Artificial Images
σ	Surface Tension
σ_A	Type A Uncertainty (Random Error)
σ_B	Type B Uncertainty (Systematic Error)
τ	Exposure Time
τ_{exp}	Measured Interfacial Temperature Gradient
τ_i	Interfacial Temperature Gradient
$\overline{\tau}_i$	Average Interfacial Temperature Gradient
ϕ	Seeding Particle Volume Fraction
ϕ_P	Particle Volume Fraction of Stock Solution
ϕ_I	Intermediate Particle Volume Fraction
ϕ_m, ϕ_w	Fugacity Coefficients
χ_{10}	Position Corresponding to Transmission of 10% of Total Power

χ_{90}	Position Corresponding to Transmission of 90% of Total Power
Ψ_s, ψ_s	Stream Functions (Linear Stability Analysis)
ω_s	Imaginary Part of Perturbation Growth Rate (Linear Stability Analysis)
ω_y	Vorticity in *y* Direction

Symbols

a, b	Dimensions of the Annular Geometry
A, B, C	Constants of Antoine Equation
A_c	Cross-Section Area
Bi	Biot Number
Bo_D	Dynamic Bond Number
c_a	Mole Fraction of Air in Gas
$C_{alcohol}$	Mole Fraction of Alcohol
c_E	Ethanol Mass Fraction
C_i	Mole Fraction of Methanol at the Interface
C_M	Mole Fraction of Methanol in Liquid
d_L	Laser Beam Diameter
d	Length of the Interface (Image Transformation)
D_0	Diffusion Coefficient
f	Focal Length
f_I	Imaging Frequency
f_{sh}	Shrinkage Factor
g	Gravitational Acceleration
h	Liquid Layer Depth
$\bar{h}$	Estimated Average Liquid Layer Depth
h_{av}	Average Liquid Layer Depth

h_{fg}	Latent Heat of Vaporization
H, L, W	Test Cell Dimensions
I, I'	Image Intensities
I_o	Laser Beam Intensity at the Center
I_c	Input Current
I_L	Laser Light Intensity
J	Jacobian Matrix
k	Integer
k_a, k_l	Thermal Conductivities
K	Dimensionless Number (Physically Inverse of Dynamic Bond Number)
ℓ	Distance between the Two Thermistors
l_c	Capillary Length
m	Liquid Mass
Ma_c	Critical Marangoni Number
M	Magnification
Ma_i	Marangoni Number
Ma_L	Laboratory Marangoni Number
p	Average Pressure of Vapor Space
P	Pressure
p_m^*	Theoretical Vapor Pressure of Pure Methanol
p_v	Vapor Pressure
p_w^*	Theoretical Vapor Pressure of Pure Water
Pr	Prandtl Number
q_s	Complex Wavenumber (Linear Stability Analysis)
q_{av}	Average Power

q_c	Cooling Power at the Cooled End
q_h	Heating Power at the Heated End
Q_c	Power Pumped by the Peltier Device
R_c	Radius of the Cylinder
R	Specific Gas Constant
r	Radial Coordinate
Ra	Rayleigh Number
s, n	Coordinate Axes in Transformed Coordinate (Image Transformation)
s_s	Imaginary Part of Wave Number (Linear Stability Analysis)
t	Time
$\mathcal{T}$	Imaging Period of the Overlap Mode
$\mathcal{T}_T$	Total Imaging Acquisition Time
T	Temperature
T_o	Ambient Temperature
T_c	Temperature of the Outer Surface of the Cooled End
T_h	Temperature of the Outer Surface of the Heated End
T_i	Interfacial Temperature
δT_s	Variation of the Inner Surface Temperature of the Test Cell
$T_{sat,w}$	Saturation Temperature of Pure Water
$T_{sat,m}$	Saturation Temperature of Pure Methanol
ΔT	Applied Temperature Difference
δT	Temperature Difference across the Peltier Device
Δt	Time Interval between Images within an Image Pair
u, v, w	Velocity Components Along the x, y and z Directions
$\bar{u}$	Average Velocity along the x Direction

U	Overall Heat Transfer Coefficient
U_S	Thermocapillary Velocity Scale
U^*	Velocity Scale
V	Input Voltage
V_r, V_θ	Radial and Angular Velocities of the Potential Flow around a Cylinder
Vol	Liquid Volume
w_L	Laser Beam Radius
x, y, z	Coordinate Axes
x_k, y_k	Location of the Interface Curve
X_M	Volume Ratio of Methanol (to Total) before Mixing

SUMMARY

The flow in a layer of volatile fluid driven by a horizontal temperature gradient is a fundamental transport model for numerous evaporative passive cooling applications. When a thin film of a volatile liquid is subject to a horizontal temperature gradient, changes in the surface tension σ at the free surface lead to Marangoni stresses that drive the flow. In a thicker liquid layer, the flow is also affected by buoyancy. This thesis describes experimental studies of convection driven by a combined action of Marangoni stresses and buoyancy in simple and binary volatile liquid layers confined in a sealed rectangular cavity heated at one end and cooled at the other. Experiments with varying concentrations of noncondensables (*i.e.*, air) c_a were performed to investigate their effect on the phase change and heat and mass transport.

In the simple liquid, thermocapillary stresses drive the liquid near the free surface away from the heated end. Varying c_a is shown to strongly affect the stability of this buoyancy-thermocapillary flow for Marangoni numbers Ma = 290 – 3600 and dynamic Bond numbers Bo_D = 0.56 – 0.82: removing air suppresses transition to multicellular and unsteady flow. The results are compared with numerical simulations and linear stability analysis. In the binary liquid considered here, a methanol-water (MeOH-H_2O) mixture, solutocapillary stresses drive the flow near the free surface towards the heated end. Four distinct flow regimes are identified for this complex flow driven by thermocapillarity, solutocapillarity, and buoyancy, and are summarized in a flow regime map as a function of c_a and the liquid composition (MeOH concentration). At low c_a, solutocapillary effects are strong enough to drive the liquid near the free surface towards the heated end over the entire liquid layer, suggesting that binary-fluid coolants could significantly reduce film dryout.

CHAPTER 1

INTRODUCTION

1.1 Motivation

Marangoni convection, the flow along an interface between two fluids driven by surface tension gradient, has been the subject of numerous experimental, numerical and analytical studies in both fluid mechanics and heat transfer. In a rectangular geometry, Marangoni convection in a thin liquid layer can be driven by a horizontal temperature gradient where the liquid is confined in a sealed rectangular cavity and one end of the cavity is heated, while the opposite end is cooled. For a simple (*i.e.*, single-component) liquid, most of the evaporation and condensation occur at the liquid-vapor interface and near the heated and cooled ends, respectively, creating a flow in the vapor space above the liquid from the heated, to the cooled, ends.

If any noncondensables (*i.e.*, air) are present in this sealed system, which often occurs in practice, this flow of vapor will "sweep" the air towards the cooled end, leading to a higher air concentration near the cooled end because the air cannot condense. Since the pressure in the vapor space is constant, the resulting horizontal gradient in relative air concentration creates a(n opposing) gradient in the pressure of the vapor. For a liquid-vapor system where evaporation balances condensation, this gradient in the pressure of the vapor will create a gradient in the interfacial temperature, which is effectively the saturation temperature (Qin *et al*. 2014).

This interfacial temperature gradient leads in turn to a surface tension gradient along the interface due to changes in surface tension σ with temperature T. And this surface tension gradient leads to thermocapillary (Marangoni) stresses that, for a simple fluid, drive the liquid near the interface away from the heated end. For thicker liquid layers, where buoyancy effects are non-negligible, this nonisothermal flow will also be subject to

buoyancy due to variations in the density with temperature, and so this flow in a simple fluid is commonly known as "buoyancy-thermocapillary convection."

Despite numerous numerical and experimental studies, our fundamental understanding of convection due to a temperature gradient in the presence of phase change, especially in three-dimensional geometries, remains limited. As noted by Schatz and Neitzel in their review of experimental investigations of thermocapillary instabilities (Schatz and Neitzel, 2001), most of the studies consider one of three flow geometries, namely cylindrical liquid bridges, rectangular layers and annular geometries. These studies have for the most part focused on mapping out flow stability regimes in terms of the Marangoni number *Ma* (which describes the relative importance of thermocapillary and viscous effects) and characterizing flow transitions from two- to three-dimensional flow, from uni- to multicellular structures, and from steady to unsteady flows (*e.g.* traveling waves, oscillatory flow, or hydrothermal waves). The Marangoni number should be defined based on the interfacial temperature gradient $\tau_i \equiv \partial T_i / \partial x$, which is a measure of the magnitude of the actual thermocapillary stresses,

$$Ma_i = \frac{\gamma h^2}{\mu\alpha}\tau_i, \tag{1-1}$$

where $\gamma = -\partial\sigma / \partial T$ is the surface tension temperature coefficient, h is the (average) depth of the liquid layer, μ is the liquid dynamic viscosity, and α is the thermal diffusivity of the liquid. However, most experimental studies use instead the laboratory Marangoni number (Riley and Neitzel, 1998)

$$Ma_L = \frac{\gamma h^2}{\mu\alpha}\frac{\Delta T}{L} \tag{1-2}$$

based on the applied temperature difference ΔT, measured in some cases at the outer surface of the channel walls, because of the practical difficulties in measuring the interfacial temperature without disturbing the flow, divided by the (longitudinal)

dimension L of the liquid layer along the direction of the applied temperature difference. In general, $\Delta T / L$ is greater than τ_i (*e.g.* De Saedeleer *et al.* 1996), and so $Ma_L > Ma_i$.

Marangoni convection in thicker liquid layers is also a function of the dimensionless dynamic Bond number, which compares the relative importance of buoyancy and thermocapillary effects:

$$Bo_D = \frac{\rho_L g \beta h^2}{\gamma} \tag{1-3}$$

where ρ_L is the density, and β the thermal expansion coefficient, of the liquid. Although a number of experimental and analytical studies have presented flow regime maps in $Ma - Bo_D$ space (Riley and Neitzel, 1998, Priede and Gerbeth, 1997), there are relatively few studies of the unsteady flow regime that occurs at higher *Ma* (Garcimartin *et al*. 1997).

More importantly, although it has been known for a half-century that noncondensables suppress phase change, especially condensation, most of the studies of Marangoni convection in volatile fluids have been performed under air at ambient conditions, and have focused on evaporation, *vs.* condensation. There is therefore little known about how the relative concentration of air affects Marangoni convection.

Although many of the fluid mechanics studies on Marangoni convection were motivated by crystal growth applications (Schatz and Neitzel, 2001), the flow of a nonisothermal liquid in the presence of phase change is also a fundamental model for a variety of passive evaporative cooling devices. Evaporative, or two-phase (liquid and vapor) cooling, which takes advantage of the large latent heat of vaporization is a leading candidate for thermal management solutions in microelectronics, where local heat fluxes exceed 300 W/cm^2 (Mahajan *et al*. 2006). This type of flow is also important in a variety of engineering applications, including desalination, refrigeration and air conditioning, and next-generation nuclear power plant designs which exploit passive cooling.

Current passive two-phase cooling technologies include capillary pumped loops, and heat pipes and spreaders (Peterson, 1994, Sobhan *et al*. 2007). In these devices, the liquid-phase coolant is driven from the cold "condenser" region to the hot "evaporator" region of a sealed cavity by a pressure gradient due in most cases to capillary effects generated by a porous "wick" or an array of microchannels. The liquid evaporates in, and cools, the evaporator region, and the vapor then flows towards, then condenses in the condenser region, releasing heat. The flow in the liquid layer is therefore nonisothermal, and characterized by strong thermal gradients. Hence thermocapillary stresses play a very important, and mostly negative, role.

Since surface tension σ decreases with temperature T for most simple fluids, thermocapillary stresses tend to destabilize the thin liquid film in the evaporator region and stabilize it in the condenser region, simply because the surface tension increases moving away from the hot spot. Destabilization of the film in the evaporator region due to thermocapillary stresses pulling fluid away from the hot spots can lead to the formation of dry spots, as shown in Figure 1.1 [right], (Savino and Paterna, 2006). This reduces the area over which phase change occurs and the associated heat flux, further increasing temperature gradients. On the other hand, stabilization of the liquid film in the condenser region reduces drainage, increasing the liquid film thickness and the associated thermal resistance, This reduces the area of bare surface where condensation can occur, decreasing the condensation rate and the associated heat flux, as shown in Figure 1.1 [left]. Both the dryout of the liquid film in the evaporator and the enhancement of filmwise condensation in the condenser are known to be major bottlenecks in improving the performance of two-phase cooling technologies, especially for microscale evaporative cooling (Sobhan *et al*. 2007).

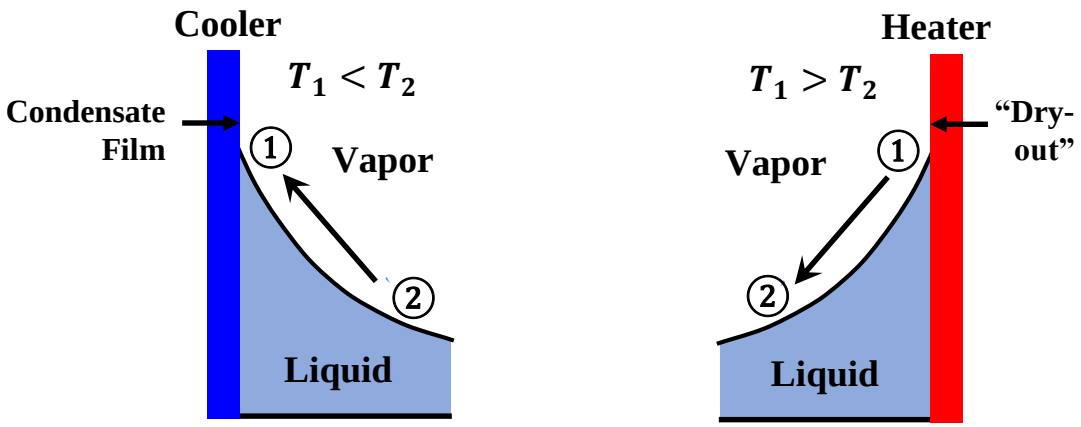

Figure 1.1 Thermocapillary flows near contact line at [right] evaporator and [left] condenser for simple liquids. The arrows at the interface show the flow directions near the evaporator and condenser, respectively.

Recently, a few studies have considered using "Marangoni condensation" to improve heat transfer in the condenser (*e.g.* Philpott and Deans, 2004, Kanatani, 2013). In Marangoni condensation, the coolant is a binary mixture. When the coolant vapors condense, the relative concentration variation of the two components in the condensate creates a gradient in the surface tension, which enhances "pseudo-dropwise" condensation (and reduces film condensation), thereby enhancing condensate drainage and reducing the thermal resistance in the condenser. These studies have, however, all focused on condensation heat transfer, and ignored evaporative cooling. The relevance of Marangoni condensation in common cooling devices, such as heat pipes is therefore unclear, since condensation and evaporation occur simultaneously in a closed cavity in a heat pipe.

As mentioned above, most of fluid mechanics literature on Marangoni convection considers the flow under air at ambient conditions, without taking into account the effect of varying levels of noncondensables. There are many heat transfer studies on how varying levels of noncondensables affect phase change (Al-Diwany and Rose, 1973, Siddique, 1992, Ghiaasiaan, 2008), starting with the classic work by Minkowycz and Sparrow (1966). Noncondensables have also been used in gas-loaded heat pipes and thermosyphons

for temperature regulation, among other applications. Nevertheless, as noted recently by Tang (2012), most heat transfer studies "provide the average heat transfer coefficient while detailed local information … is seldom presented." Indeed, it is impractical to date, to our knowledge, to experimentally measure local phase change (Kobayashi *et al*. 1991), and it has only become possible in the last decade to accurately simulate phase change.

Therefore, in brief, even in simple (*i.e.*, single-component) liquids, there are few, if any, experimental studies that consider local transport (*e.g.* local velocity fields or and phase change) in Marangoni convection under the conditions appropriate for a fundamental study relevant to evaporative cooling, namely in a layer of coolant confined in a sealed cavity in the (near-)absence of noncondensables (*i.e*., air). Moreover, very few studies have considered how varying the fraction of noncondensables affects the flowfield, which would presumably affect thermal performance.

The adverse effects of thermocapillarity in both the condenser and the evaporator in simple coolants can be reduced or even reversed by using binary-(*vs.* simple-) fluid coolants. Recently, certain water-alcohol mixtures, known as self-rewetting fluids (Tanaka, 2009), which have $d\sigma/dT > 0$ (the "inverse Marangoni effect") have been studied as promising candidate coolants for avoiding dryout. Unfortunately, these mixtures only exhibit inverse Marangoni effects over a limited range of working temperatures and compositions, which limits their applicability.

All binary fluids, whether self-rewetting or not, are however also subject to solutocapillary stresses or solutocapillarity due to variations in the surface tension of the mixture caused by variations in the relative concentrations of the two component fluids. In a binary fluid where the more volatile component has a lower σ, the higher-temperature regions of the free surface will have lower concentrations of the more volatile component, and hence higher σ. The resulting solutocapillary stresses effectively oppose the thermocapillary stresses, driving the liquid away from the cold regions towards the hot regions, thus supplying coolant to hot regions. In a methanol-water (MeOH-H_2O) mixture,

for example, the more volatile MeOH has a lower σ than H_2O. Differential evaporation reduces the relative MeOH concentration C_M (Fig. 1.2), and this mixture will therefore have a surface tension that effectively increases with T.

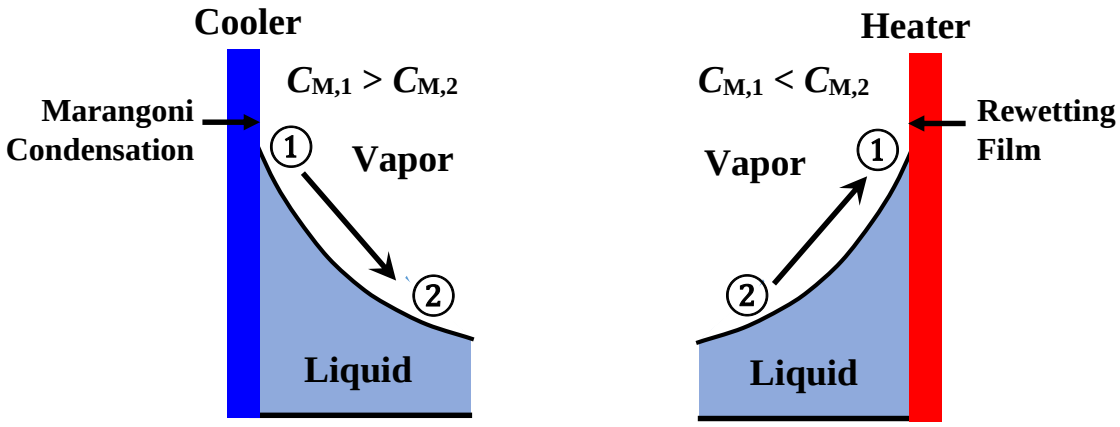

Figure 1.2 The flows near contact line region due only to solutocapillarity near the evaporator [right] and condenser [left] regions for binary liquids (*e.g.* MeOH-H_2O) where solutocapillarity opposes thermocapillarity. The arrows at the interface show the flow directions in the evaporator and condenser, respectively.

However, Marangoni convection in a binary fluid is more complex, and poorly understood, compared with that in a simple (*i.e.*, single component). First, buoyancy effects associated with changes in the density with temperature are now due both to changes in the composition of the liquid due to differential evaporation and the changes in the density of the two components with temperature. And the two effects cannot be easily separated, because it is difficult to measure the concentration field in this flow. In addition, the flow at the liquid-vapor interface is driven by both thermocapillarity (due to variation of interfacial temperature) and solutocapillarity (due to changes in the concentration). Again these two effects are difficult to decouple without knowing the concentration field, since the concentration variations are of course due to temperature variations.

Moreover, the vapor space above the binary-liquid layer is a ternary mixture of air and the vapors of the two components. As noted earlier, in the Marangoni convection of a simple fluid, the coolant vapor "sweeps" the air towards the cooled end, significantly increasing the air concentration at the cooled end. The resulting local variations in the composition of the vapor space affect the saturation temperature, and are the major source of interfacial temperature variations (Qin *et al.* 2014). Although the binary vapors could also sweep air towards the cooled end, it is unclear how the local variations in the composition of the vapor space will affect the interfacial temperature, since it is unclear what "sets" the interfacial temperature for this flow.

There are no studies, to our knowledge, of how varying levels of noncondensables affect Marangoni convection in binary liquids with non-negligible buoyancy effects. Although this is beyond the scope of this thesis, a fundamental understanding of Marangoni convection in binary coolants under varying levels of noncondensables could lead to new evaporative cooling approaches, and new robust binary-fluid coolants designed to have improved and more consistent thermal performance over a wide range of operating conditions. Indeed, given that it is difficult (and expensive) in practice to remove all noncondensables from many condenser systems, it may be more practical to develop new binary-fluid coolants where the amount of phase change is relatively unaffected by small amounts of noncondensables. Indeed, there are very few, if any, studies at all of local transport, in Marangoni convection of a binary-liquid layer where buoyancy effects are non-negligible.

1.2 Objectives

Given the lack of knowledge of how noncondensables affect Marangoni convection with phase change and of Marangoni convection in binary fluids, the specific objectives of this doctoral research are to:

1. Quantify Marangoni convection in a volatile simple fluid in a sealed rectangular geometry in terms of the velocity field and the flow regimes, especially in the unsteady flow regime, and determine how noncondensables affect the flow regimes in, and hence stability of, this flow.
2. Clarify the flow characteristics in terms of the velocity field for Marangoni convection in a binary fluid, specifically a water-methanol mixture where solutocapillarity opposes thermocapillarity.
3. Identify the range of parameters where solutocapillarity overcomes thermocapillarity and drives the liquid towards hot regions in terms of liquid phase composition and the relative concentration of noncondensables in the vapor space.

1.3 Outline

The rest of this doctoral thesis is organized as follows. Chapter 2 reviews previous studies of Marangoni convection in simple fluids, of binary-liquids coolants and Marangoni condensation, and the effects of noncondensables on Marangoni convection. Chapter 3 details the experimental setup, experimental procedures and particle-image velocimetry (PIV) processing. The experimental results for simple and binary fluids are described and discussed in Chapters 4 and 5, respectively. Finally, conclusions, contributions and recommendations for future work are presented in Chapter 6.

CHAPTER 2

LITERATURE REVIEW

Marangoni convection, an interfacial flow driven by a surface tension gradient, is named after the Italian scientist Carlo Giuseppe Matteo Marangoni, who studied the spreading of one liquid on a second immiscible liquid. He stated that liquid A spreads on another liquid, B, if the sum of the interfacial tension (*i.e.*, between the two liquids) and the surface tension (*i.e.*, in contact with air) of A, is lower than the surface tension of B (Marangoni, 1871). However, James Thomson (1855) is actually believed to have been the first to identify and study Marangoni convection, pointing out in 1855 that a flow could be created by varying the concentration in a mixture of liquids of different surface tensions. He was able to successfully, although qualitatively, explain "several very curious motions observable," including the well-known "tears of wine" phenomenon (Thomson, 1855). Bénard (1900) observed beautiful cellular convective flow patterns in a thin liquid layer above heated surfaces, which were initially attributed to buoyancy effects by Lord Rayleigh (1916). Much later, Block (1956) and Pearson (1958) showed that the convective cells could form well below Rayleigh's criterion, and concluded that Marangoni (*i.e.*, surface tension) effects must also play an important role in generating these cells. Marangoni convection has been an active area of scientific and engineering research ever since. The early history of Marangoni convection is reviewed in the book by Nepomnyashchy *et al*. (2002) and the work by Sefiane and Ward (2007), among other sources.

After more than a century of extensive study, our knowledge of Marangoni convection has encompasses numerous sub-areas, including "the study of cellular (Bénard) convection and its evolution, rippling and the generation of (nonlinear) waves and solitions, drop and bubble migration in the presence of thermal gradients, and three-dimensional surface tension gradient (Marangoni-driven) flows and related spatio-temporal problems"

(Nepomnyashchy *et al.* 2002, page xii). There are of course numerous review papers and book on the topic, including Levich (1962), Levich and Krylov (1969), Normand (1977), Davis (1987), Velarde (1982), Velarde (1988), Mutabazi *et al.* (2006), Schatz and Neitzel (2001), Sefiane and Ward (2007).

Of these reviews, the ones most relevant to the work described in this thesis are probably Davis (1987) and Schatz and Neitzel (2001), who gave theoretical and experimental reviews, respectively, of thermocapillary instabilities. These instabilities were divided into Marangoni-convection and thermocapillary-convection instabilities due to externally imposed temperature gradients mainly normal and parallel, respectively, to the interface. Given the wide range of this subject and its literature, it is impractical to give a complete and the comprehensive literature review on Marangoni convection. This Chapter will therefore focus only on the studies most relevant to this thesis.

As noted earlier, the primary objectives of this thesis are: first, to investigate Marangoni convection in simple fluids with a focus on flow stabilities and the effects of noncondensables in a rectangular geometry at $Bo_D = O(1)$, when capillarity and buoyancy are comparable, but neither dominates; second, to study the convections in regular (*i.e.*, non-self-rewetting) binary liquids, with a focus on flowfield measurement and identifying flow regimes. Hence this chapter will focus on reviewing studies on thermocapillary convection instability where the applied temperature gradient is parallel to the interface, in simple fluids in rectangular geometries, followed by studies on so-called "Marangoni condensation" and Marangoni convection in both non-self-rewetting and self-rewetting binary liquids.

2.1 Thermocapillary Convection Instability in Simple Fluids

Thermocapillary convection, as defined by Schatz and Neitzel (2001), is a flow driven by an applied horizontal temperature gradient along the liquid-vapor interface. Unlike Bénard-Marangoni convection, where a flow only exists above a certain threshold,

or critical Marangoni number, thermocapillary convection can be generated by very small temperature gradients, with no evident minimum or threshold value. At small temperature gradients, the base flow is a single circulation cell with a stable parallel return flow. As the applied temperature gradient (or effectively *Ma*) increases, flow instability sets in, as predicted by Smith and Davis (1983) and Davis (1987), and verified subsequently by experiments (*e.g.* Riley and Neitzel, 1998) and numerical simulations.

Thermocapillary convection has for the most part been studied in three geometries (Fig. 2.1), as summarized by Schatz and Neitzel (2001): *a)* the liquid bridge, heated and cooled from the bottom and top, respectively or vice versa, which is a model geometry for a float zone, in crystal-growth application; *b)* the rectangular layer or slot, heated and cooled laterally, which is the model problem considered by the hydrodynamic-stability analysis of Smith and Davis (1983) and Davis (1987); *c)* the annular geometry, heated and cooled by an inner cylinder and an outer hollow cylinder, respectively, or vice versa, which models the Czochralski crystal growth process (Schatz and Neitzel, 2001). The annular geometry has the additional advantage that it effectively eliminating the effects of side walls and can be considered an approximation of the rectangular geometry, if the annular gap width is much less than the inner cylinder diameter. This Chapter mainly reviews rectangular geometries, and the major experimental studies are summarized in Table 2-1.

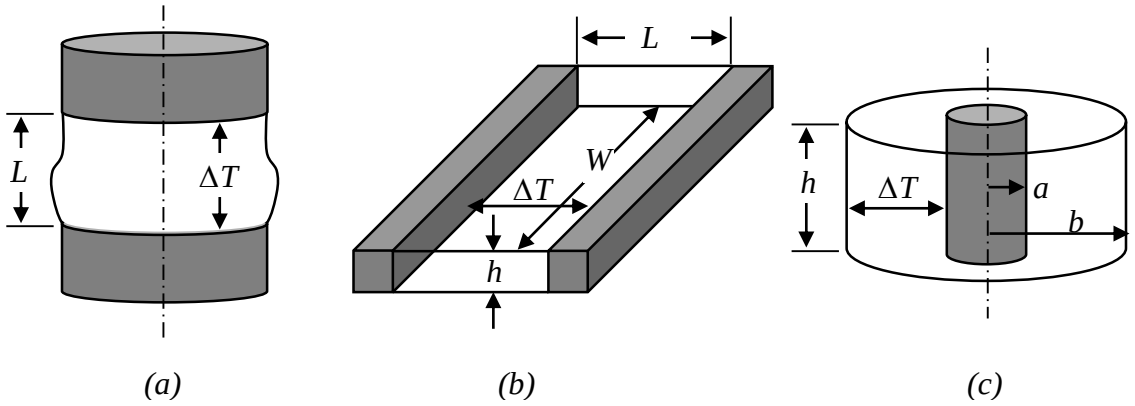

(a) *(b)* *(c)*

Figure 2.1 Three types of thermocapillary convection: *(a)* liquid bridge; *(b)* rectangular layer or slot, *(c)* annular geometry (Schatz and Neitzel, 2001).

TABLE 2-1 Summary of experimental parameters for major experimental studies of rectangular liquid layers in chronological order.

Ref.	Fluid	*Pr*	Dimensions [cm]			Γ_x	Γ_y	Maximum ΔT [℃]
			h	*L*	*W*			
Villers & Platten (1992)	Acetone	4.24	0.175 –1.43	3	1	2.1–17	0.7–5.7	9
Schwabe *et al.*(1992)	Ethanol	17	0.18, 0.26	2	4	7.7, 11.1	15.4, 22.2	38
Daviaud & Vince (1993)	0.65 cSt silicone oil	10	0.08-1	1	20	1-12.5	20-250	10
Gillon & Homsy (1996)	0.65 cSt silicone oil	8.4 (25 °C)	0.68	1	3.8	1.5	5.6	20
De Saedeleer *et al.* (1996)	Decane	15	0.25–0.47	3, 5, 7.4	1	6.4–30	2.1–4.0	9
Braunsfurth & Homsy (1997)	Acetone	4.44 (14 °C)	0.125 –1	1.1	1.0	1.1–8.5	1.0–8.2	~20
Garcimartín *et al.* (1997)	0.65 and 5 cSt silicone oil; decane	10, 30, 15	0.2–0.35 [10]	10	1	28–50	2.8–5	Not given
Riley & Neitzel (1998)	1 cSt silicone oil	13.9	0.025 -0.25	3	5	12-120	20-200	Not given
Pelacho & Burguete (1999)	0.65 cSt silicone oil	10 (25 °C)	0.125 -0.35	6	5	17-48	14-40	12
Burguete *et al.* (2001)	0.65 and 2cSt silicone oil	10, 30	0.1-1	1-3	3-25	1-30	3-250	10
Benz & Schwabe (2001)	0.65 cSt silicone oil; ethanol	N/A	0.3-0.5	2	4	4-6.7	8-13.3	12
Sakurai *et al.* (2002)	0.65 cSt silicone oil	N/A	0.05-1	1	21	1-20	21-420	~20

Most of the fluid mechanics studies of thermocapillary convection instabilities, as reviewed, for example, in Riley and Neitzel (1998) and Burguete *et al* (2001), have focused on mapping out flow regimes in terms of the Marangoni number *Ma* and characterizing transition from two- to three-dimensional flow, transition from uni- to multicellular structures, and transition to unsteady flows (*e.g.* traveling waves, oscillatory flow, or hydrothermal waves). The basic state of thermocapillary convection consists of a steady unicellular roll, where the liquid flows away from the heated end at the free surface and returns at the bottom of the liquid layer. This flow was termed steady unicellular flow (SUF) by Riley and Neitzel (1998). As *Ma* increases, the flow undergoes multiple transitions from this basic state, with the specific type of transitions depending on Bo_D. For small Bo_D (*i.e.*, $Bo_D < 0.2$), a transition to a hydrothermal wave (HTW) instability occurs (Smith and Davis, 1983); whereas for larger Bo_D (*i.e.*, $Bo_D > 0.2$), the flow transitions to steady multicellular (SMC) structures, and then unsteady flows, *i.e.*, oscillatory multicellular (OMC) flow. The following sections details these flow regimes and the transitions, including the effects of noncondensables, again mainly in rectangular geometries.

2.1.1 Return Flow Basic State

When a liquid layer bounded by a rectangular geometry with a flat bottom is subject to a sufficiently small horizontal temperature gradient, the resulting convective flow consists of a single, steady convection cell, where the liquid moves along the surface from the hot end towards the cold end, with a compensating reverse flow near the bottom. Far away from the end walls, the flow in the middle section is essentially a two-layer parallel flow, whose velocity and temperature profile can be solved analytically. This analytical solution including both thermocapillary and gravitational effects was first derived by Birikh (1966) and later re-derived by Villers and Platten (1987).

$$\frac{u(z)}{U^*} = \frac{1}{6}\left(\frac{2z}{\bar{h}} - 1\right)^3 - \frac{(1-3K)}{8}\left(\frac{2z}{\bar{h}} - 1\right)^2 - \frac{(1-K)}{4}\left(\frac{2z}{\bar{h}} - 1\right) + \frac{(1-3K)}{24} \qquad (2\text{-}1)$$

where $U^* = \rho g \beta \bar{h}^3 \tau_i / 8\mu$ and $K = 4\gamma / \rho\beta g h^2$, which is physically the inverse of dynamic Bond number.

Three years prior to Villers and Platten's work, Kirdyashkin (1984) also analytically obtained a velocity profile for this flow, which has the exactly the same shape, but with a different amplitude, given by $2[15/(3\text{-}5K)Ra]^{1/2}$ where

$$Ra = \frac{\beta g \Delta T h^3}{\alpha \nu} \qquad (2\text{-}2)$$

is the Rayleigh number, which compares the relative importance of buoyancy to viscous effects. However, this solution is incorrect, as pointed out by De Saedeleer *et al.* (1996), since a correct theory should not restrict flows to cases where $K < 3/5$ (based on the amplitude of the velocity profile). The velocity profile of the basic state flow was subsequently rederived by Riley and Neitzel (1998):

$$\frac{u(z)}{U_s} = \frac{3}{4}\left(\frac{z}{\bar{h}}\right)^2 - \frac{1}{2}\left(\frac{z}{\bar{h}}\right) + Bo_D\left[-\frac{1}{6}\left(\frac{z}{\bar{h}}\right)^3 + \frac{5}{16}\left(\frac{z}{\bar{h}}\right)^2 - \frac{1}{8}\left(\frac{z}{\bar{h}}\right)\right] \qquad (2\text{-}3)$$

where $U_s = \gamma \bar{h} \tau_i / \mu$ is the thermocapillary velocity scale and Bo_D is the dynamic Bond number.

2.1.2 Hydrothermal Waves

For $Bo_D < 0.2$, hydrothermal waves occur above a critical Ma_i, whose value depends upon Bo_D (*e.g.* $Ma_c = 328$ for $Bo_D = 0.08$) (Riley and Neitzel, 1998). The experiments in this thesis only consider values of $Bo_D > 0.2$, so hydrothermal waves are only briefly reviewed here. Smith and Davis (1983) were the first to predict and name this type of instability in an infinite fluid layer with a free surface driven by thermocapillary effects in the absence of buoyancy. At small Prandtl number (*i.e.*, $Pr \rightarrow 0$), the waves propagate along the transverse direction; at intermediate *Pr*, the waves propagate obliquely upstream,

i.e., from one corner near the cold end towards the opposite corner near the hot end, and at large Prandtl number (*i.e.*, $Pr \to \infty$), the waves propagate along a direction nearly parallel to the temperature gradient from the cold end towards the hot end. Smith (1986) explained the instability in terms of the interaction between the temperature field and the inertia- or viscosity-dominated flowfield.

Parmentier *et al.* (1993), Gershuni *et al.* (1992), and Mercier and Normand (1996) also considered the effect of buoyancy in their later analyses, and concluded that obliquely propagating hydrothermal waves would occur only when thermocapillary effects are dominant (*i.e.*, at small Bo_D). Most recently, Chan and Chen (2010) analyzed the effect of buoyancy on the stability of the thermocapillary convection in a horizontal fluid layer with adiabatic boundaries at the top and bottom, and showed that buoyancy suppresses hydrothermal waves at $Bo_D = O(1)$.

The experimental studies of Riley and Neitzel (1998) are perhaps the first to observe hydrothermal waves in a 30 mm (L) × 50 mm (W) rectangular layer of 1 cSt silicone oil (Pr = 13.9). Burguete *et al.* (2001) have also experimentally observed this transition. Schwabe *et al.* (1992) and Ezersky *et al.* (1993) also studied hydrothermal waves in a circular (*vs.* rectangular) geometry to eliminate any side wall effects, and reported observations of hydrothermal waves.

2.1.3 Steady and Oscillatory Multicellular Flow

Many of the experimental studies in rectangular geometries motivated by the search for hydrothermal waves have instead observed transitions to flow regimes different from those predicted by stability theory. As pointed out and summarized by Riley and Neitzel (1998), the transition from the steady unicellular flow (*i.e.*, the return flow basic state) to hydrothermal waves only occurs at $Bo_D \leq 0.22$, where the liquid layers are very shallow and the flow is dominated by thermocapillarity. For thicker layers where $Bo_D > 0.22$, they observe as Ma increases instead first a transition from steady unicellular flow (SUF) to a

steady multicellular flow (SMC) state, where a number of co-rotating rollers appear across the liquid layer with their axes perpendicular to the applied temperature gradient, and second a transition to oscillatory multicellular (OMC) flow where both the velocity and temperature fields become unsteady, *i.e.*, time dependent. Their results, summarized in terms of a flow regime map of *Ma vs.* Bo_D shows the transition boundaries between all four (HTW, SUF, SMC, OMC) flow regimes (Figure 2.2).

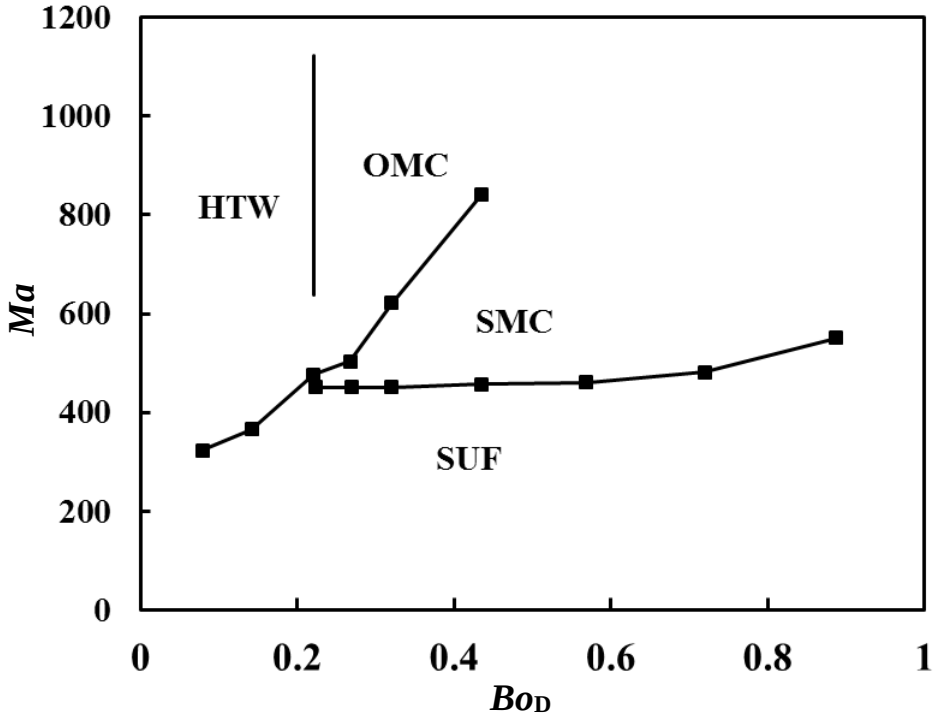

Figure 2.2 Flow regime map reproduced from the experiments of Riley and Neitzel (1998); *Ma* is calculated based on the actual temperature gradient along the free surface, and Bo_D is calculated based on the average liquid layer depth. Regimes are denoted as steady unicellular flow (SUF), hydrothermal waves (HTW), steady multi-cells (SMC), and oscillatory multi-cells (OMC).

SMC and time-dependent flows at higher *Ma* were also observed in earlier other studies. Villers and Platten (1992) used laser-Doppler velocimetry (LDV) and two-

dimensional numerical simulations to obtain velocity profiles in heated and cooled layers of acetone (Pr = 4.24) in a rectangular test cell with a conducting bottom, and reported that their flow evolved from a single convection roll to multiple convection rolls, then a time-dependent flow as Ma increased. All the cases except for one case reported in this study were performed at $Bo_D > 0.22$, so these results agree with those of Riley and Neitzel's at higher Bo_D.

Schwabe *et al.* (1992) observed transition from SUF to SMC flow at $Ma > 600$, and from SMC to OMC flow at $Ma > 3000$. Their experimental results for both conductive and adiabatic bottom walls suggest that the boundary condition at the bottom wall has little, if any, effect on the observed flow transitions. Similar transitions have been reported by De Saedeleer *et al.* (1996) in rectangular layers of varying aspect ratio, Garcimartín *et al.* (1997), and Pelacho and Burguete (1999).

Similar flow regimes have also been observed in annular geometries, which have the advantage over rectangular geometries that they have no side walls. Schwabe *et al.* (1992) performed experiments in an annular geometry (a = 20 mm and b = 77 mm), and observed transition from SUF to the SMC state, and then transition to oscillatory flow. Similar transitions were also observed in the later studies of Schwabe *et al.* (1999), Garnier and Chiffaudel (2001), Schwabe and Benz (2002) and Koehle (2007). These results strongly suggest that (the presence or absence of) side walls does not affect the existence of these flow regimes. Finally, Schwabe and Benz (2002) observed multicellular structures in an annular geometry under microgravity conditions, which suggests that buoyancy is not required for the SMC state.

Note that the transition from SUF to SMC reported in these studies is a gradual one and the definition of the onset of SMC is in many cases is not well-defined. An exception is Schwabe *et al.* (1999), who defined the transition to SMC to be the appearance of the first saddle point, *i.e.*, the second cell. In Riley and Neitzel, SMC flow appears to be defined as the flow state when cells of comparable size fill the entire length of the liquid layer and

the critical *Ma* for the transition from SUF to SMC flow is defined to be "80% of the transition value to the new [SMC flow] state". To avoid such ambiguity, this thesis defines a partial multicellular (PMC) flow regime between the SUF and SMC flow regimes defined to be the flow state where there is more than one convection cells, but the cells do not occupy the entire horizontal extent of the liquid layer.

The first transition (at large Bo_D) from SUF to SMC, is now believed, after numerous studies, to be driven by the (presence of the) end walls, which lead to an absolute flow instability (Priede and Gerbeth, 1997, Shevtsova *et al.* 2003, Pérez-García *et al.* 2004). The 2D numerical simulations by Shevtsova and Legros (2003) in decane suggest that the lateral thermal boundary layers play a major role in destabilizing the unicellular state, and the analyses by Priede and Gerbeth (1997) and Shevtsova *et al.* (2003) show that the transition from unicellular to multicellular flow is due to a local absolute instability in a liquid layer confined by end walls. Pérez-García *et al.* (2004), who performed linear stability calculations for a 0.65 cSt silicone oil, confirmed that the co-rotating rolls are due to an absolute instability, where the finite perturbation due to the boundary layer on the hot side wall is amplified and spreads throughout the layer.

Clearly, SMC flow and the transition from SUF to SMC are well studied. In contrast, there is relatively little known about the unsteady (*i.e.*, OMC or time-dependent) flow regime and the transition from SMC to this flow regime. Villers and Platten (1992) termed the time-dependent flow state at large *Ma* "oscillatory convection," and showed that the variation in the measured *x*-component of velocity was time-periodic. They could not however obtain the flow structure of the "oscillatory convection" from their experiments, because of the limitations of LDV, which only measures (usually a single component of) the velocity at a single point. They did, however, report that the critical *Ma* of the transition from SMC to OMC increases as the Rayleigh number increases, which suggests that buoyancy plays a stabilizing role in this process.

De Saedeleer *et al.* (1996) also reported transition from SMC flow to a time-periodic flow as the temperature gradient, and hence *Ma*, increased. They showed that the horizontal (x) and vertical (z) velocity components had the same period for the time-periodic flow state. Riley and Neitzel (1998) visualized the OMC regime using a combination of shadowgraphy and free-surface thermography, but noted, "it is difficult to draw definite conclusions from such shadowgraph images, however, since the shadowgraph is integrated through the spanwise extent of the domain." Their free-surface shadowgraphy results showed "strong steady multicellular structures near the hot wall and a pair of oblique waves which appear to propagate through them, beginning at the cold wall", but they were unable to observe the flow below the free surface.

A few mechanisms have been hypothesized to date for the so-called "oscillatory convection" (*i.e.*, OMC or time-dependent) flow. Garcimartín *et al.* (1997), who noted the similarity between the thermal boundary layer growth time and the time scale of the oscillation, attributed the mechanism of oscillation in this flow regime to the instability of the thermal boundary layer next to the heated wall, with the perturbations due to the oscillations of the roll next to the heated end amplified and convected towards the cooled end. Shevtsova and Legros (2003) and Shevtsova *et al.* (2003) suggested that the unsteadiness of oscillatory multicellular flow is due to interactions between large-scale thermal structures within the flow near the hot wall and the temperature-sensitive free surface, which introduces a cold finger near the hot wall, for example, leading to a perturbation on the heated end that propagates towards the cooled end.

Even in the well-studied problem of thermocapillary convection in a simple fluid within a rectangular geometry, the behavior of the time-dependent (*e.g.* OMC) flow regime at high *Ma* and Bo_D is not well-understood. In addition, the effects of phase change (*i.e.*, evaporation and condensation) at the free surface and the effects of the noncondensables above the liquid layer are also not well understood, although a number of the experimental studies have used fairly volatile liquids (*e.g.* ethanol, acetone).

2.1.4 Effects of Phase Change and Noncondensables

As mentioned above, much of the previous studies have focused on thermocapillary and buoyancy effects in layers of *nonvolatile* liquids exposed to a large, and effectively infinite, volume of air at ambient conditions, and largely neglected the effects of phase change at the interface (*i.e.*, condensation). Riley and Neitzel (1998) chose 1 cSt silicone oil in part because it had the fewest problems with evaporation compared with other silicone oils tested. Although they noticed an evaporation rate of $O(0.1\ \mu l/s)$, little was done in order to prevent the evaporation. Liquid was, however, continuously supplied from a constant-head container to keep the free surface at a constant height.

At most, studies of liquids that are quite volatile have confined or covered the liquid layer to reduce evaporation. The experiments using acetone (Villers and Platten, 1992) and Braunsfurth and Homsy, 1997) studied convection in a(n at least partially) confined cell to minimize changes in h. Braunsfurth and Homsy (1997) covered their flow cell with a "piece of glass and a silicone rubber seal," while Villers and Platten (1992) used a Teflon block "a few millimetres above the upper surface," but no details were given regarding whether the cell was sealed by this block and whether acetone mass loss was negligible. In both of these cases, evaporation is therefore at least somewhat balanced by condensation, and phase change occurs in the presence of air at ambient pressures. In the work by Burguete *et al*. (2001) and Pelacho and Burguete (1999) using 0.65 cSt and 2 cSt silicon oil, "a Plexiglas plate is inserted a few millimeters above the surface of the fluid to reduce evaporation," and the height of liquid was reported to change by less than 1% over an experimental run. Zhu and Liu (2010) instead studied convection in a $L = 4$ cm and $W = 8$ cm layer of 0.65 cSt silicone oil subject to $\Delta T \leq 14$ ℃ with an initial depth $h = 0.2$ cm where the interface was open to the surroundings.

Only two experimental studies, to our knowledge, have considered evaporation in a closed geometry. Schwabe *et al.* performed experiments in ethanol at mean temperatures of 20 °C and 30 °C (corresponding to vapor pressures of 5.7 kPa and 10.4 kPa, respectively)

under otherwise identical conditions, and found that there was no effect of temperature on the critical transition Marangoni number (taking into account the change in Prandtl number), despite the large change in vapor pressure. Schwabe and Benz (2002) used a self-replenishing system that reused the evaporated liquid, so the evaporation and condensation are balanced in their microgravity experiments.

As mentioned above (see also Chan and Chen (2010)), most of the numerical studies are 2D simulations of "one-sided" models that only consider transport in the liquid phase and ignore phase change and thermocapillarity, typically imposing instead an adiabatic boundary condition at the liquid-vapor interface (Villers and Platten, 1992 and Shevtsova *et al.* 2003). The boundary condition (effectively, evaporation or the level of noncondensables above the liquid layer) at the free surface can, however significantly affect the flow. Mercier and Normand (1996) allowed heat transfer along the vertical direction, specifically, through the upper free surface in terms of a Biot number *Bi* and found that the flow transition is strongly dependent on *Bi* (*i.e.*, heat transfer through free surface). Markos *et al.* (2006) and Ji *et al.* (2008), considered coupled effects of evaporation and thermocapillarity, but neglected buoyancy, and both found strong variations in the flow with the amount of evaporation at the free surface.

Similarly, there is little known about how varying levels of noncondensables, which are well-known to affect condensation, and would then also have a significant effect on evaporation in a closed geometry. Barthes *et al*. (2007) experimentally studied the dynamics of bubble formation in liquids with and without dissolved gases and found that the bubbles grew steadily in degassed liquids, but developed oscillations in liquids with dissolved gases. Although Barthes *et al*. did not report the relative fraction of noncondensables, they attributed the oscillations to the enhancement of thermocapillary stresses by noncondensable gases inside the bubble. Chauvet *et al.* (2012), showed that the critical *Ma* increases as the amount of noncondensable gases above the liquid layer is reduced in Marangoni-convection (*vs.* thermocapillary-convection) instability.

As mentioned previously, even small amounts of noncondensables in the vapor space significantly reduce heat transfer and condensation rates. Such noncondensables effects have been investigated in numerous heat transfer studies, reviewed by Siddique (1992), Ghiaasiaan (2008) and Zhang *et al*. (2012), among others. One of the earliest studies in this area is believed to be that by Othmer (1929), who found that the heat transfer coefficient in steam-air mixtures decreased by 50% when as little as 0.5 vol% air was added into the steam chamber. Borishanskiy *et al*. (1977, 1978) and Kageyama (1993) later observed similar effects in their experimental studies, and Borishanskiy (1977) was among the first to propose empirical correlations relating the changes in average heat transfer coefficient to the noncondensables concentration. For internal flow condensations in a confined geometry, where flow field and properties vary from location to location, Siddique *et al*. (1994) and Ghiaasiaan *et al.* (1995) have, among others, proposed different models to predict local heat transfer coefficients. Unfortunately, these heat transfer models, are not really applicable to the thermocapillary convection problem here.

In summary, a few previous studies suggest that noncondensables have significant effects on thermocapillary convection. There are, however, very few fluid mechanics studies that have considered these effects, and specifically how varying the fraction of noncondensables affects the flow. Unfortunately, most of the heat transfer studies on this topic have focused on how noncondensables affect phase change, and hence cooling or heating efficiency. Yet a fundamental model problem for evaporative cooling is the thermocapillary convection in a layer of coolant confined to a sealed cavity in the (near-) absence of noncondensables (*i.e.*, air).

2.1.5 Three-Dimensional Flow and Effects of Aspect Ratio

The transverse confinement of the flow studied here is significant (*i.e.*, $\Gamma_y = W / h$ is small), and so this flow will likely have some 3D effects. Although this thesis does not quantify the effects of aspect ratio, previous studies on this topic are briefly reviewed next.

As noted earlier, most of the numerical and theoretical analyses of buoyancy-thermocapillary convection in liquid layers have considered 2D flow in effectively infinite liquid layers where h is much less than the other dimensions of the layer. Experimental studies, however, have clearly shown that three-dimensional effects, characterized by the transverse aspect ratios $\Gamma_y = W/h$, has a major effect on the flow (Daviaud and Vince, 1993, De Saedeleer *et al.*, 1996, Gillon and Homsy, 1996, Braunsfurth and Homsy, 1997). The experimental studies that have considered 3D convection in rectangular liquid layers are mostly at low transverse aspect ratios (*i.e.*, $\Gamma_y < 10$).

The particle-image velocimetry (PIV) studies of Gillon and Homsy (1996) and Braunsfurth and Homsy (1997) reported a 2D flow at lower *Ma*, and a transition from 2D to 3D convection at higher *Ma*, although the value of the transition *Ma* was a strong function of the aspect ratios of the liquid layer. These studies observed two counter-rotating rolls, forming a cardioid structure, in agreement with the simulations by Mundrane and Zebib (1994). Benz and Schwabe (2001) and Schwabe and Benz (2002), observed three-dimensional stationary instability (3DSI), and concluded that buoyancy was required for this type of instability. Burguete *et al.* (2001) concluded that the basic flow was 2D for high transverse aspect ratio Γ_ys, and that the flow would transition to traveling waves or multicellular structures (rolls) at small or large h, respectively. However, note that Γ_y does not appear to be the sole parameter that determines whether the flow is 2D or 3D, since transition to 3D flow has also been reported at very large aspect ratios ($20 < \Gamma_y < 71$) (Daviaud and Vince 1993).

2.2 Marangoni Condensation and Binary Liquids as Coolants

A smaller number of studies of thermocapillary convection have considered binary-fluid mixtures. Moreover, a number of heat transfer studies have investigated using binary-vapor mixtures in condensation heat transfer, known as Marangoni condensation or pseudo-dropwise condensation. Marangoni condensation has the possibility of enhancing

heat transfer performance, by taking advantage of solutocapillary effects to turn regular filmwise condensation to pseudo-dropwise condensation under appropriate conditions. These studies are reviewed next.

2.2.1 Marangoni Condensation

When a binary-vapor mixture of a positive system, where the more volatile component has a lower surface tension, such as a water-ethanol mixture, condenses on a solid surface, Marangoni convection can arise due to both temperature and concentration gradients, which induces so-called Marangoni condensation. Marangoni condensation is also known as pseudo-dropwise condensation because it is qualitatively similar to the dropwise condensation of a pure vapor on a hydrophobic surface, where droplets of condensate roll off the surface under gravity and therefore has the potential to dramatically enhance heat transfer rates.

The mechanism of Marangoni condensation is explained in detail by Yang *et al.* (2008), among other studies, and shown schematically in Figure 2.3. In a water-ethanol (EtOH-H_2O) mixture, where EtOH is more volatile but has a lower surface tension, any initial perturbation in the condensate film can lead to variations in the film thickness, which in turn causes variations in the temperature along the free surface of the condensate film simply due to thermal conduction (*i.e.*, $T_{crest} > T_{valley}$). Therefore, for phase equilibrium at the interface, the less volatile component (here, H_2O) is more concentrated in the liquid film at a crest than in a valley ($c_{crest} < c_{valley}$). Since the surface tension of H_2O is much higher than that of EtOH, this concentration gradient also creates a surface tension gradient, which drives the liquid away from the valley to the crest, thinning the valley even more and forming a condensate drop at the crest.

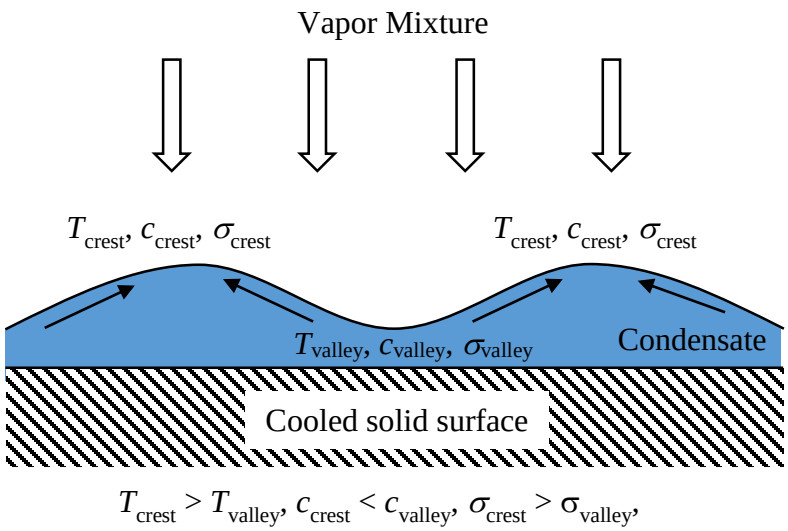

Figure 2.3 Marangoni instability mechanism in condensate film.

Marangoni condensation has been proved to significantly enhance heat transfer performance in numerous studies. Experimental studies of the condensation of ethanol-water mixtures on smooth wetting vertical surfaces have reported increases in heat transfer coefficient (HTC) by as much as a factor of eight, with the maximum increase at an EtOH mass fraction c_E = 0.5% (Utaka and Wang, 2004). Although most of the studies of Marangoni condensation have focused on EtOH-H_2O (vapor) mixtures, a few studies have also considered ammonia-water mixtures (Philpott and Deans, 2004). Experiments by various groups on condensation heat transfer of EtOH-H_2O have considered condensation on horizontal surfaces (Murase *et al.* 2007), the effects of c_E and the speed of the vapor(s) (Utaka and Wang, 2004), and the amount of noncondensables present in (Wang and Utaka, 2004) as well as the pressure of the vapor space (Yang *et al.* 2008). Overall, the experimental studies suggest that condensation heat transfer enhancement is greatest at small c_E (typically ≤1%). The studies also report that increasing the pressure (*i.e.*, amount) and the speed of the vapor(s) further enhances heat transfer; moreover, temperature gradients also enhance condensation heat transfer, which is attributed to thermocapillary effects (Wang *et al.* 2009).

This heat transfer enhancement is also very sensitive to the amount of noncondensables. For instance, it appears that at least some of the discrepancies in the reported enhancements in condensation heat transfer are due to difficulties in removing noncondensables: an air mass fraction of 10^{-4} (0.01%) can reduce heat transfer enhancement from 750% to 180%, or by more than a factor of four (Wang *et al.* 2009 and Yan *et al.* 2007). However, as noted by Murase *et al.* (2007) although "the mechanism of Marangoni or pseudo-dropwise condensation is understood in principle but no methods are available for prediction of heat transfer*"*.

In terms of modeling, the transition from filmwise to pseudo-dropwise condensation can be described using standard lubrication analysis (Hijikata *et al*. 1996 and Kanatani, 2013) but no model has been constructed to date that is capable of describing the condensation process quantitatively in the (non-stationary) pseudo-dropwise regime. In particular, the thermal resistance of the condensate layer depends on its thickness profile which can vary dramatically (the droplets are up to a few mm thick, while the thin film between the droplets can be as thin as 1 μm (Utaka and Nishikawa, 2003). Describing the dynamics of the condensate which accounts for the growth of droplets due to solutocapillary stresses, mergers between droplets due to capillarity, and the motion of droplets due to gravity and thermocapillary stresses is presently an open problem. Similarly, resistance due to diffusion of vapors in the gas phase cannot be accurately quantified using boundary-layer theory because of spatial and temporal variations in the thickness, temperature, and the composition of the condensate film. Moreover, unlike the case of filmwise condensation, heat and mass transport in both (liquid and gas) phases are important, and cannot be decoupled in the pseudo-dropwise condensation regime.

2.2.2 "Self-rewetting" Fluids

"Self-rewetting" fluids generally refer to binary mixtures (*e.g.* diluted aqueous solutions of long-chain alcohols) whose surface tension increases as temperature increases.

The solutocapillary effects due to concentration gradient and the thermocapillary effects due to temperature gradient act along the same direction in these fluids to drive fluid towards (*vs.* away from) the hot spot. This continuous inflow towards the hot spot can therefore delay film "dryout", suggesting that using such fluids as coolants could lead to an appreciable enhancement in heat transfer.

Vochten and Petre (1973) were among the first to characterize such fluids with their measurements of surface tensions of dilute aqueous solutions, *i.e.*, $C_{\text{alcohol}} = O\ (10^{-3})$, of various long-chain alcohols (number of carbons ≥ 4) in a temperature range of 10 – 90 °C and observed a minimum surface tension at a certain temperature. Abe *et al.* (2004) investigated the heat transfer performance of model wickless heat pipes using 1.5 wt% of 1-butanol aqueous solution, and reported better heat transfer performance, observing that "a considerably faster liquid return was achieved by using the self-rewetting fluid because of coupled Marangoni effects". Subsequently, Abe (2006) reported that the dryout limit of 1.5 wt% 1-butanol aqueous solution heat pipe was about 40% higher than the water heat pipe, and that the thermal resistance was reduced by 15%.

Savino *et al.* (2007) measured the surface tensions of the aqueous solutions of four alcohols (*i.e.*, water-butanol, water-pentanol, water-hexanol and water-heptanol) in a temperature range of 20 – 60 °C. For all four mixtures, the surface tension reaches a minimum at approximately 35 °C and increases with temperature for T = 35 – 60 °C. In the tests of heat pipes, their experimental results confirmed that heat pipes with long-chain alcohol solution at *suitable concentrations* perform better than heat pipes filled with pure water. Di Francescantonio, *et al*. (2008) also studied "inverse Marangoni effects" in water-n-1-heptanol and reported flow reversal at the free surface. Tanaka *et al.* (2009) and Di Paola *et al.* (2011) studied "self-rewetting" fluids in heat pipes, and both reported better performance with aqueous "self-rewetting" solutions than that with pure water.

Although "self-rewetting" fluids are promising candidate coolants for delaying dryout and thus enhance heat transfer performance, they do have a few obvious drawbacks:

self-rewetting fluids known so far are still mostly limited to the aqueous solution of a few long-chain alcohols at very low concentration (Ohta *et al.* 2007); and the "self-rewetting" fluids reported so far are only proved to work in a very limited temperature range (Vochten and Petre, 1973).

There is, however, relatively little known about the flow driven by thermocapillarity and solutocapillarity in regular (*i.e.*, not "self-rewetting") binary mixtures, such as water-methanol mixtures, as detailed next. And given that the previous studies of "self-rewetting" fluids were focused on enhancing heat transfer, these studies have considered convection only under air at ambient pressures (*e.g.* Di Francescantonio *et al.* 2008, and Cecere *et al.* 2011) or focused on global transport parameters such as total heat flux in heat pipes (*e.g.* Abe, 2006, and Savino *et al.* 2007), *vs.* local velocity or temperature fields. There are therefore still a lot of open questions regarding even what flow regimes exist in binary fluid convection, and how noncondensables affect local transport in such flows.

2.2.3 Other ("Non-Self-rewetting") Binary Fluid Studies

Although there are numerous fluid mechanics studies of convection in films (*i.e.*, thin layers with negligible buoyancy effects) of simple liquids, there are relatively few experimental studies of binary liquids. Most of the studies have either involved films of nonideal alcohol (*e.g.* methanol, EtOH, isopropanol, heptanol)-water mixtures, including so-called "self-rewetting" fluids discussed previously (Tanaka *et al.* 2009, Di Francescantonio *et al.* 2008, and Cecere *et al.* 2011) or ideal mixtures of various alkanes (*e.g.* hexane, heptane, octane, dodecane) (Fanton and Cazabat, 1998) on flat surfaces at various orientations (Vuilleumier *et al.* 1995, Hosoi and Bush, 2001, Fournier and Cazabta, 1992, Gotkis *et al.* 2006, and Azouni *et al.* 2001).

One of the best-known flow in binary films is the classic phenomenon of "tears of wine," or climbing films in H_2O-EtOH mixtures (Hosoi and Bush, 2001). To our

knowledge, Fournier and Cazabat (1992) is the first quantitative study of the "tears of wine" phenomenon in H_2O-EtOH mixtures under ambient conditions, and reported that the H_2O-EtOH mixture spontaneously wetted glass containers, *i.e.*, climbing up the side walls against gravity, and that the film grew in a diffusive fashion, with a length that was proportional to the square root of time. They also observed a "star instability" at the edge of the reservoir and a "fingering instability" at the front of the film, and showed that the climbing velocity is greater at low bulk EtOH concentrations. Although the authors found this observation "against intuition," the climbing velocity should be proportional to the derivative of the surface tension with respect to EtOH concentration, *vs.* the absolute EtOH concentration of the mixture, as pointed out by the authors.

Vuilleumier *et al.* (1995) subsequently studied the same flow on a tilted (*i.e.*, non-horizontal) flat plate, again under air under ambient conditions. They observed parallel, "forked dendrites" at the edge of the climbing film, which they attributed to a Rayleigh-like instability, and reported that the wavelength of these dendrite-like structures was determined by the slope of the plate, in agreement with the theoretical predictions by de Ryck (1999). Their measurements of EtOH concentration and velocity showed that the maximum surface tension gradient occurs at the meniscus, which led to a dip right at the edge of the meniscus.

Fanton and Cazabat (1998) studied the "tears of wine" problem using both a watch glass and a tilted petri dish in ideal binary (hexane-dodecane, heptane-dodecane, and octane-dodecane) mixtures under ambient conditions. They, like Vuilleumier *et al*. also observed dendrite-like structures, and complex interactions between these dendrites: initially, neighboring dendrites coalesce, reducing the number of dendrites, then until at later times, while the dendrites continue to merge and new dendrites are formed, the overall number of dendrites remains roughly constant.

Hosoi and Bush (2001) studied evaporative instabilities in climbing films on an inclined rigid plate using EtOH- or MeOH-H_2O mixtures again in the presence of air at

ambient conditions. Their experiments showed that there are two distinct instabilities driven by solutocapillarity in the climbing film: a convective instability characterized by flattened convection rolls aligned in the direction of flow and accompanied by free-surface deformation due to the combined influence of surface deformations and alcohol concentration gradients (*i.e.*, solutocapillarity); and an instability in the form of transverse surface waves propagating up the plate, which they suggested was similar to the hydrothermal waves observed in pure thermocapillary flow (*cf.* Section 2.1.2). The wavelength of the observed forked dendrite-like structures, in agreement with lubrication theory, again decreases as slope angle increases, and agrees with the results of Vuilleumier *et al.* (1995).

There have also been a number of studies of solutocapillarity-driven (or solutal-Marangoni) flows or instabilities due to evaporation in drops and/or horizontal layers of binary mixtures. Azouni *et al.* (2001) studied surface tension-driven flow in a thin layer of water-*n*-heptanol solution in a rectangular 1 cm × 8 cm × 0.2 cm test cell that was heated on one end and cooled on the other end. In pure water, the liquid near the free surface always flowed from hot to cold, while the flow of a water-*n*-heptanol solution was instead always from cold to hot "even in the temperature regime where the static value of surface tension decreases with temperature." They explained these different observations by noting that solutocapillary convection in binary mixtures is not simply pure thermocapillary convection with a modified dependence of the surface tension on temperature, but that evaporation and condensation of the binary mixture at the free surface must also be taken into account. The authors derived a simplified model of this flow, which neglected heat advection and phase change at the free surface; the model gave velocity fields in the near field that were in qualitative agreement with the experiments.

Serpetsi and Yiantsios (2012) used linear stability analysis and direct numerical simulations to study how solutocapillarity affected the stability of evaporating binary thin films in a liquid film under an inert gas, where the evaporation is limited by vapor

diffusion). Two types of instabilities were predicted: 1) when the surface tension increases with increasing concentration of the non-volatile solute, solutocapillarity can lead to the formation of multiple cells with small interfacial deformation, similar to the well-known hexagonal cells observed in Bénard-Marangoni convection. 2) at very small *Ma*, solutocapillarity can also lead to an instability with a long-wave oscillatory behavior. Similar studies by Doumenc *et al.* (2013) and Machrafi *et al.* (2013) in various mixtures (Polyisobutylene-toluene, Polystyrene-toluene, and H_2O-EtOH), again for a liquid layer exposed to an inert gas.

In contrast, Guéna *et al.* (2007) experimentally and theoretically studied drops of alkane mixtures evaporating in air under ambient conditions. They observed that a drop of a binary mixture often evaporates more rapidly than a simple fluid drop of the same volume of the more volatile component studied, due to surface tension gradients pointing outwards which accelerate spreading. Indeed, for mixtures containing low concentrations of the more volatile alkane, this component completely disappears before the drop finishes evaporating. At higher concentrations, both components are present, however, until drop is completely vaporized. Over an intermediate range of concentrations, a dry ring develops inside the drop due to depletion of the more volatile component at the edge, which shifts the maximum concentration gradient away from the contact line. The film thickness is then significantly reduced at the location of maximum concentration gradient by solutocapillary effects, resulting in this dry ring. There are also a number of studies on evaporation of binary drops. These other studies, however, focus mainly on global parameters, such as droplet radius and evaporation rate (Wang *et al.* 2008, Liu *et al.* 2008, Liu and Bonaccurso, 2010, Chiang and Lu, 2011), or the temperature and concentration fields within the droplet (Maqua, *et al.* 2008 and Strotos *et al.* 2011), *vs.* solutocapillary effects.

All these experimental studies of binary-liquid convection discussed focus, for the most part, on evaporation of the mixture into the surroundings, *i.e.*, an effectively infinite vapor space dominated by air or inert gases, with negligible condensation. The only study,

to our knowledge, that considered convection of a binary mixture in a sealed cavity under pure a vapor space containing only vapors of the mixture is Uguz and Narayanan (2012a, b), who investigated instability in a horizontal layer of a binary liquid below its vapor, subjected to a vertical temperature gradient in an sealed container (*i.e.*, the evaporation is balanced by condensation) in the presence and absence of gravitational effects. Note that, the vapor space in this study is different from our experiments, where there is always some amount of air (besides vapor) present in the vapor space. Although their discussions of the instability of the two-layer system in different configurations (*i.e.*, heated at the top or bottom walls) under conditions where solutocapillarity or buoyancy dominates are interesting, this flow configuration, where the temperature gradient and gravitational acceleration are along the same direction, is quite different from the problem studied here where the flow is driven by a horizontal temperature gradient.

In summary, there are hence few, if any, experimental, numerical or theoretical studies that have considered local transport parameters such as interfacial temperature and velocity fields in the convection in a relatively thick binary-liquid layer where buoyancy effects are significant. Moreover, most of the fluid mechanics studies have focused on evaporation, and neglected condensation, under a vapor space dominated by noncondensables, while most of the heat transfer studies on Marangoni condensation have focused on average (*vs.* local) HTC, and provided only qualitative visualizations of the condensate film. Yet quantifying local transport parameters is important in understanding how, and under what conditions, Marangoni condensation enhances heat transfer—and, in the long term, to optimize heat transfer enhancement due to Marangoni condensation.

CHAPTER 3

EXPERIMENTAL DESCRIPTION

This chapter details the experimental apparatus and procedures used to study Marangoni convection in simple and binary liquids. The experimental apparatus consists of a fused quartz flow cell (Section 3.1), a laser light sheet illumination system (Section 3.2.1), and an image acquisition system (Section 3.2.2). The actual experimental procedures and image processing methods are described in Sections 3.3 and 3.4, respectively.

3.1 Test Cell and Flow

This section describes the test cell and the major components required to create these nonisothermal flows driven by a temperature difference ΔT under a vapor space at a given pressure p. The methods used to prepare the working liquids for the experiments are also described here.

3.1.1 Test Cell

The flow cell used in these studies was a rectangular fused-quartz test cell, (Starna Q1938), with inner dimensions 4.85 cm (horizontal) × 1 cm (horizontal) × 1 cm (vertical) and a wall thickness of 0.125 cm. The custom design of this cell had a vacuum port on the top wall on the right and a charging port on the top wall on the left; both ports had a length (axial extent) of 1.5 cm and an ID of 0.2 cm (Fig. 3.1). All six walls of the test cell were clear (*vs.* frosted) to enable optical access through the four side walls for particle-image velocimetry (PIV) and flow visualization. The cell was heated and cooled over the two end walls using thermoelectric Peltier devices (Custom Thermoelectric 01711-5L31-03CD) powered by a dc power supply (Mastech HY3005-2) and embedded in 1.4 cm × 1.4 cm × 0.6 cm copper (Cu) blocks that were thermally coupled to the ends of the cell with thermal

grease (Arctic Alumina™ AA-1.75G). Two T-type thermocouples (TC) (Omega Engineering Inc. 5TC-TT-T-30-36) with bead diameters D = 0.6 mm (calibrated, using a TC calibrator (OMEGA CL122) and a NIST-traceable calibrated thermometer (ICL Calibration Laboratories, Inc. 210-610) to an accuracy of 0.2 ℃) were sandwiched between the Cu block and the outer surface of the test cell to monitor the temperatures T_h and T_c, which were taken to be the nominal temperatures of the outer surfaces of the heated and cooled ends, respectively. The cell was then clamped between the Cu blocks by a polyvinyl chloride (PVC) holder attached to two aluminum heat sinks, so that all four sides of the cell were exposed to air at the ambient temperature T_o. As shown in the magnified view of the heated end (Fig. 3.2 [bottom]), four additional T-type TCs (Omega Engineering Inc. 5TC-TT-T-30-36) were placed on the front and back sides of both Peltier elements, and used to monitor their surface temperatures. The temperature readings from these TCs were used in turn to estimate the power input to the heater and output by the cooler. This magnified view also depicts the coordinate system used in these studies, where x is along the temperature gradient direction, y is along the horizontal normal to x, and z is along the vertical. The origin is at the bottom and center of the inner surface of the heated end of the test cell, so the inner volume of the test cell occupies $0 \le x \le 4.85$ cm; -0.5 cm $\le y \le 0.5$ cm; and $0 \le z \le 1.0$ cm and the TCs that measure T_h and T_c are therefore nominally at (y, z) = (0, 0.5 cm).

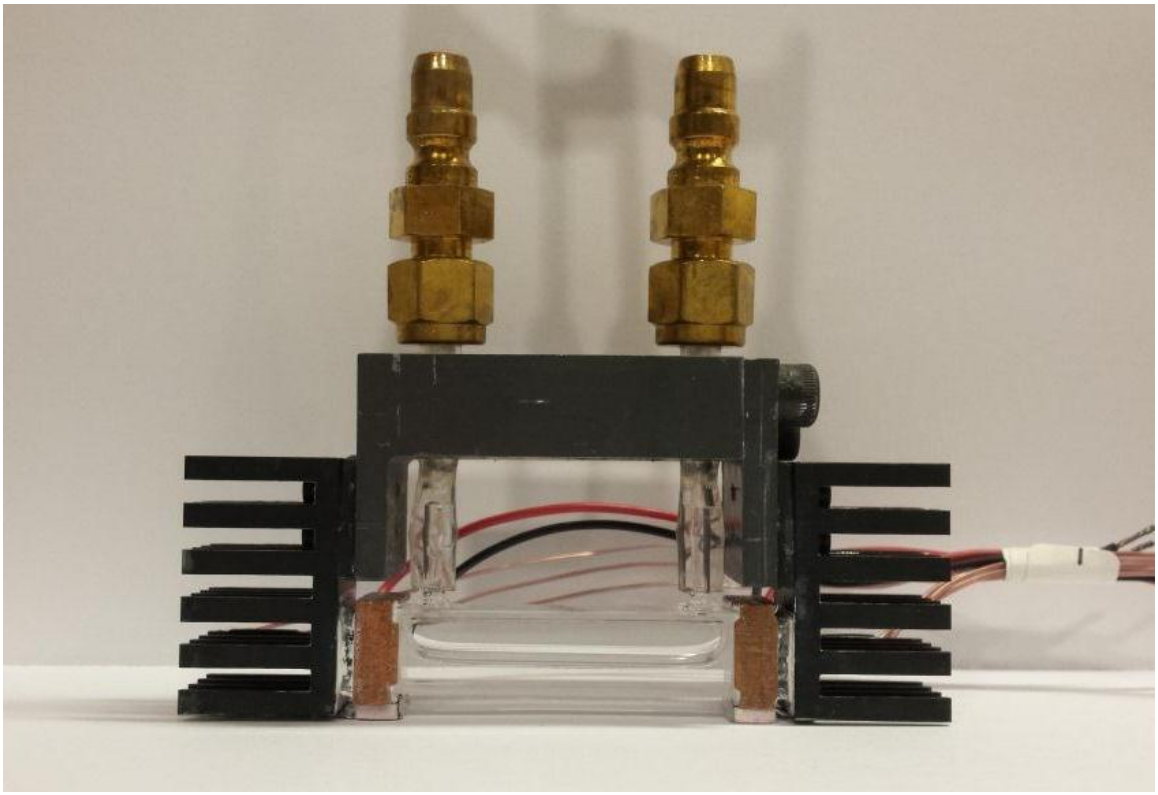

Figure 3.1 A photo of the test cell used in this study.

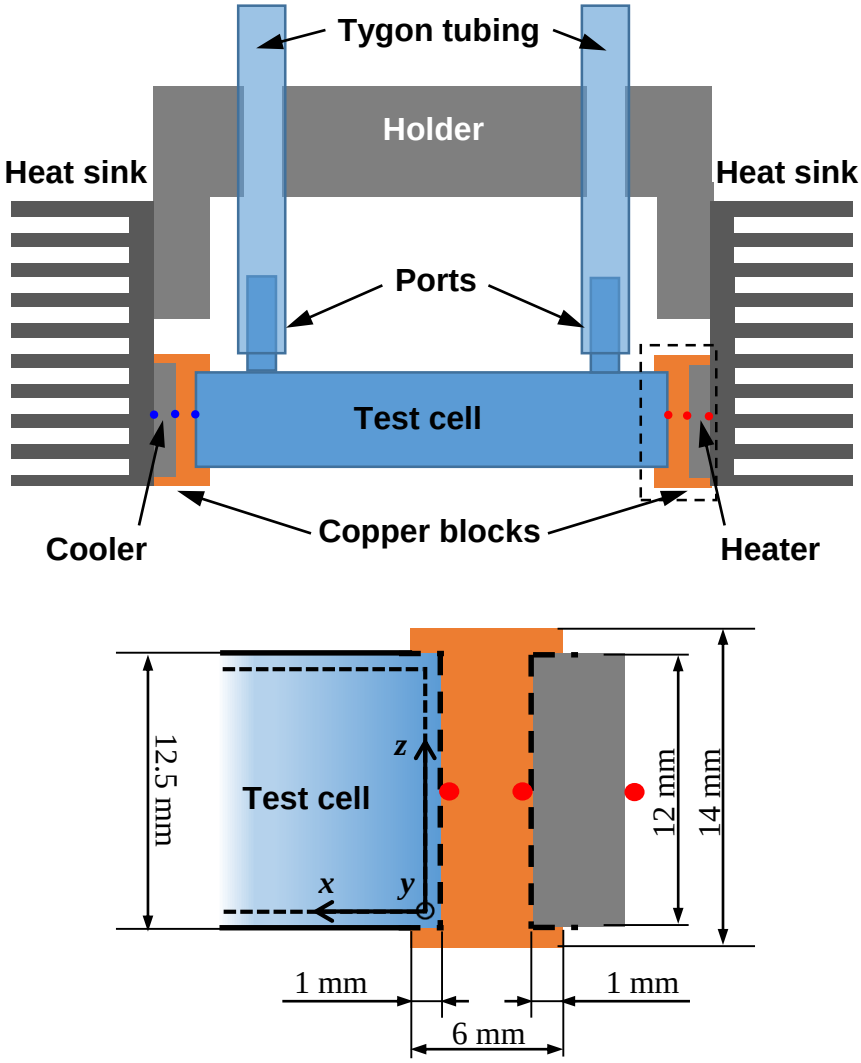

Figure 3.2 Drawing of the test cell (to scale). The heated and cooled ends are the right and left ends, respectively, in the top view. The outer dimensions of the test cell, with a wall thickness of 0.125 cm, are 5.1 cm × 1.25 cm × 1.25 cm. The closeup of the heated end depicted in the bottom view (corresponding to the region denoted by the dashed rectangle in the top view) shows the location of the three TCs (red circles) on the heated end and the coordinate system. Note that the origin of the coordinate system is at the lower right corner of the inner surface of the test cell and that there are three more TCs in similar locations with respect to the cooled end on the other side of the test cell.

The test cell was then connected to the charging and pumping lines via the charging and vacuum ports, respectively. As illustrated in Figure 3.3, the ports on top of the test cell were connected using two ~2 cm long segments of Tygon tubing to two quick connect fittings (3) (Swagelok B-QF4-S-400 and B-QF4-B-400). Two cutoff valves (2) above the two ports ensure that the test cell remains sealed during the experiments. A needle valve (1) above the cutoff valve on the charging line (on the left) was used as required to allow varying amounts of ambient air to enter the test cell to adjust the total pressure and hence the relative concentration of noncondensables (*i.e.*, air) within the test cell. A tee between the quick connect and the cutoff valve on the pumping line on the right was connected on one side to a vacuum pump (5) (Edwards E-Lab 2) which was used to evacuate the test cell, and on the other side to a digital pressure transducer (6) (Dwyer 626-23-GH-P1-E1-S4-NIST) with an accuracy of 0.26 kPa, which was used to estimate the pressure inside the test cell. The entire assembly was mounted on a multi-axis tilt platform (Newport 37 series) so that the test cell could be leveled with a sensitivity of 2 arcsec.

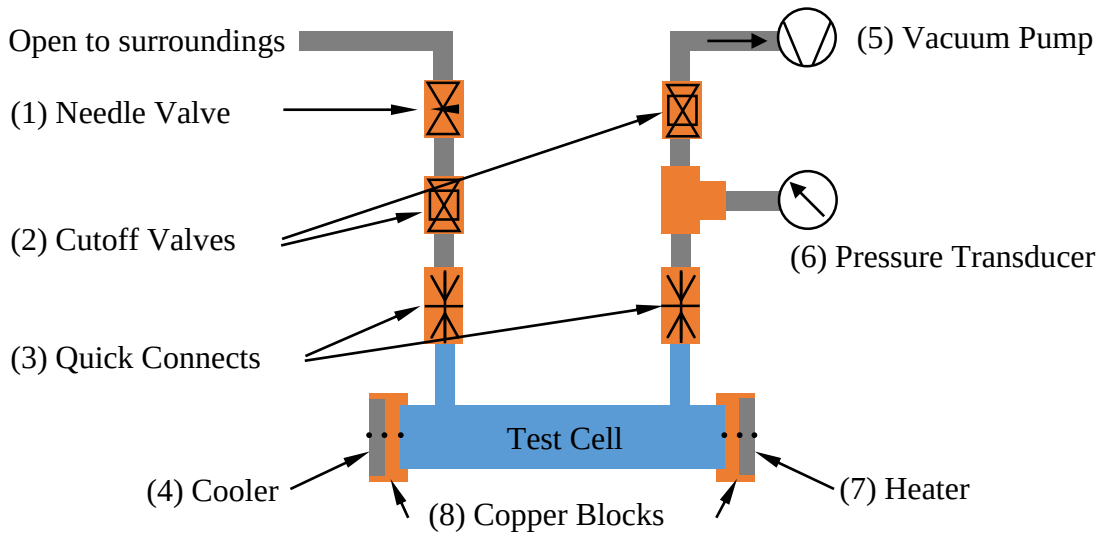

Figure 3.3 A sketch of the major components of the whole test cell assembly. The heated and cooled ends are the right and left ends, respectively, in this view.

3.1.2 Working Fluids

The liquid used in the simple-fluid experiments was the volatile silicone oil hexamethyldisiloxane (NMR grade with purity ≥ 99.5%, Sigma Aldrich 326739-100G), referred to by the acronym HMDS. The properties of this liquid are given in Table 3-1, and its Prandtl number $Pr = \mu / (\rho_L \alpha) = 9.2$. In these experiments, HMDS was seeded with fluorescent polystyrene (PS) particles (Invitrogen F8823) of diameter d = 1.1 μm and density ρ = 1.05 g/cm^3 at a nominal initial volume fraction $\phi = 4\times10^{-7}$. The particle seeding density used in these studies was determined by taking sample images and adjusting ϕ to satisfy the commonly used PIV criterion that each interrogation window (of dimensions 64×32 pixels, for example) should have 10-15 particle images (Adrian and Westerweel, 2011). To prepare the working fluid, 5 mL silicone oil was transferred into a disposable glass vial (7.4 mL, Fisherbrand™, 03-339-23C) using a disposable syringe (Air-Tite Products Co., Inc. AL5) attached to PTFE syringe tubing (Sigma Aldrich Z117323-1EA). Then 0.1 μL of a commercially available particle suspension (Invitrogen F8823, particle volume ratio ϕ_P = 2 vol%) was added to the same vial using a 10 μL micro-syringe (Hamilton Gastight 1701) with 0.1 μL graduations. The vial was then capped and sealed with ParaFilm, and the particle-laden solution was sonicated for 20 min using an ultrasonicator (Cole-Parmer 8845-4) to ensure that the tracers were well-dispersed in the fluid.

TABLE 3-1 Properties of hexamethyldisiloxane at 20 ℃. Here, p_v is the vapor pressure and h_{fg} is the latent heat of vaporization.

ρ_L [kg/m^3]	μ [kg/(m·s)]	σ [N/m]	ν [m^2/s]	α [m^2/s]	Pr	β [/K]	γ [N/(m·K)]	p_v [kPa]	h_{fg} [kJ/kg]
761	5.27×10^{-4}	0.0158	6.9×10^{-7}	7.5×10^{-8}	9.2	1.3×10^{-3}	8.9×10^{-5}	4.1	225

The working fluids (properties given in Table 3-2) used in the binary-fluid experiments were mixtures of methanol (99.9% extra dry; Acros Organics AC326950010) and double distilled deionized (DDI) water from a Thermo-Scientific Barnstead E-pure™ D4641 water purification system with an initial resistivity of ~17.8 MΩ·cm; a variety of mixtures, containing methanol (MeOH) at molar concentrations C_M = 9%–74%, were studied here.

The preparation of the working liquids for binary-fluid experiments differed from that used for the simple-fluid experiments. As will be discussed in the experimental procedures, some of the liquid evaporates and is removed from the test cell during the pumping process before the start of each experiment. Since MeOH is much more volatile than water (H_2O) (since the vapor pressure of MeOH is much greater than that of H_2O at a given temperature), more MeOH usually evaporated during this process, and so the actual MeOH concentration in the binary fluid was less than that in the original mixture. To achieve the desired final concentrations (*e.g.* C_M = 9%), the MeOH-H_2O mixture was prepared at slightly higher MeOH concentrations than the desired (*i.e.*, final). The final actual MeOH concentration was measured and calculated at the end of each experimental run to determine C_M (Appendix A).

TABLE 3-2 Properties of H_2O and MeOH at 20 ℃.

	ρ_L [g/cm^2]	μ [cP]	σ [g/s^2]	α [cm^2/s]	Pr	β [/K]	γ [g/(K·s^2)]	p_v kPa]	h_{fg} [J/kg]
H_2O	1.0	1.0	73	1.4×10^{-3}	7.1	2.1×10^{-4}	0.15	2.3	2.257×10^{6}
MeOH	0.79	0.58	25	1.0×10^{-3}	7.3	1.1×10^{-3}	0.13	13	1.097×10^{6}

To achieve C_M = 9%, a binary mixture of ~20 vol% MeOH was required. One mL methanol was therefore mixed with 4 mL water in a disposable glass vial, to obtain slightly less than 5 mL of the binary mixture (MeOH-H_2O is a nonideal mixture). Although the

volume shrinkage (*i.e.*, as great as 3.7%) due to the nonideal nature of the mixture was included in the calculation of C_M, it was considered to be negligible for particle seeding purposes.

The ~5 mL binary mixture (mixture #1) was then seeded with fluorescent polystyrene (PS) particles (Invitrogen F8823) with an average diameter of 2.0 μm (with a polydispersity of 3.5%) and density of 1.05 g/cm^3 at a nominal volume fraction of $\phi = 4\times10^{-8}$. However, given that the particle volume ratio in the stock solution was $\phi_P = 2$ vol%, only 10 nL of the commercially available particle suspension is required to seed mixture #1. Given the difficulties in accurately dispensing such a small volume, another 5 mL of the same binary mixture (mixture #2) was prepared and a two-step dilution process was used to achieve the final value of ϕ. Mixture #1 was seeded with particles at an intermediate particle volume fraction, $\phi_I = 4\times10^{-7}$, by adding 0.1 μL particle stock solution into the 5 mL binary mixture. then 0.5 mL liquid from mixture #1 was mixed with 4.5 mL liquid from mixture #2, to reach the final seeding density of $\phi \sim 4\times10^{-8}$. Both mixtures #1 and #2 were sonicated for 2 min in water using an ultrasonicator (Cole-Parmer 8845-4) to ensure that the tracers were well-dispersed in the liquid.

Similar procedures were used to prepare the MeOH-H_2O mixture at other MeOH concentrations, with different initial mixing ratios, as listed in Table 3-3. For Marangoni convection experiments where surface tension plays a major role, the working liquids should be free from contamination, and absorption of gases like CO_2 from the surroundings should be minimized. To ensure the purity of the working liquids, all the stock MeOH used in these studies was sealed in airtight bottles under ultrapure nitrogen (Airgas Inc. NI UHP 300, ultrahigh purity 5.0 grade), fresh double distilled deionized (DDI) water was used from the still for each experimental run;, and the mixtures were injected into the test cell within 10 min of preparation.

TABLE 3-3 Initial mixing volume ratios of MeOH and H_2O for all binary mixtures.

Nominal Final C_M	9%	14%	20%	28%	40%	58%	74%
Initial Volume of MeOH [mL]	1	1.5	2	2.5	3.2	4	4.4
Initial Volume of H_2O [mL]	4	3.5	3	2.5	1.8	1	0.6

3.2 Optical Setup

This section describes the major components of the optical setup, which consist of the illumination and imaging systems. The flow is illuminated by a light sheet from an argon-ion laser, which excites the fluorescence of the particle tracers suspended in the working liquid. The imaging system then collects and images the longer-wavelength fluorescence from these particles.

In all experiments presented here, a 2D "slice" of the flow was illuminated by a ~0.04 cm thick laser light sheet with a lateral extent of about 1.0-1.5 cm. This light sheet was formed by passing the wavelength λ = 514.5 nm beam of a continuous-wave (CW) argon-ion laser (Innova 90) operating in single-line mode with an output power of 2.1 W through a focal length f = –0.64 cm plano-cylindrical lens (Thorlabs LK1087L2). Two different configurations, namely the vertical view configuration and the horizontal view configuration, were used in these experiments to obtain *x*-*z* and *x*-*y* "slices" of the flow, referred to here as the vertical and horizontal views of the flow, respectively. In the vertical view configuration, as shown in Figure 3.4, a vertical laser light sheet passes through the test cell from the bottom to the top (back), so that a vertical slice of the working fluid is illuminated. In the horizontal view configuration (Fig. 3.6), a laser light sheet parallel to the "floor" of the test section passes through the test cell from the front to the back, so that a horizontal slice, or *x*-*y* plane, of the working fluid is illuminated.

Figure 3.4 shows a detailed schematic of the optical setup of the vertical view configuration; the major components of the setup are listed in Tables 3-4 and 3-6. The λ =

514.5 nm beam of a continuous-wave (CW) argon-ion laser (Innova 90) (A) with an output power of 2.1 W first passes through an (B) acousto-optic modulator (AOM) (IntraAction Corp., AOM-04), which was used to shutter the laser beam, as detailed in Section 3.2.2.2. An iris diaphragm (C) (Thorlabs ID12) was then used to spatially filter out the higher-order beams (which have more divergence) diffracted by the AOM, so that only the first-order diffracted beam reaches the test cell. This beam is focused by a spherical lens (Thorlabs LA1484) (D) of focal length f = 300 mm to reduce the diameter of the laser beam and thus the thickness of the light sheet slicing through the test section. Strictly speaking, a Gaussian beam passing through an ideal spherical lens is focused at a location slightly less than the focal length f = 300 mm of the spherical lens (Pedrotti *et al.* 1993), but the beam waist in this case occurred 340 mm (*vs.* 300 mm) away from the spherical lens, presumably due to the divergence of the laser beam itself. Moreover, as will be shown subsequently in Section 3.2.1.1, the beam diameter remained nearly constant within 8 mm of the beam waist. The overall distance from the spherical lens (D) to the working liquid in the test cell was therefore set to 340 mm, so that the light sheet would have its minimum thickness within the test cell. The beam after passing through the spherical lens was turned 90 ° from the horizontal to the vertical direction using a plane mirror (E) (Thorlabs BB1-E02) mounted right below the test cell. Finally, the beam passed through a plano-cylindrical lens (F) (Thorlabs LK1087L2), which expanded the laser beam along the x direction, to form the actual light sheet. The distance from the plano-cylindrical lens to the test cell was adjusted so that the x-dimension of the sheet was about 1.5 cm.

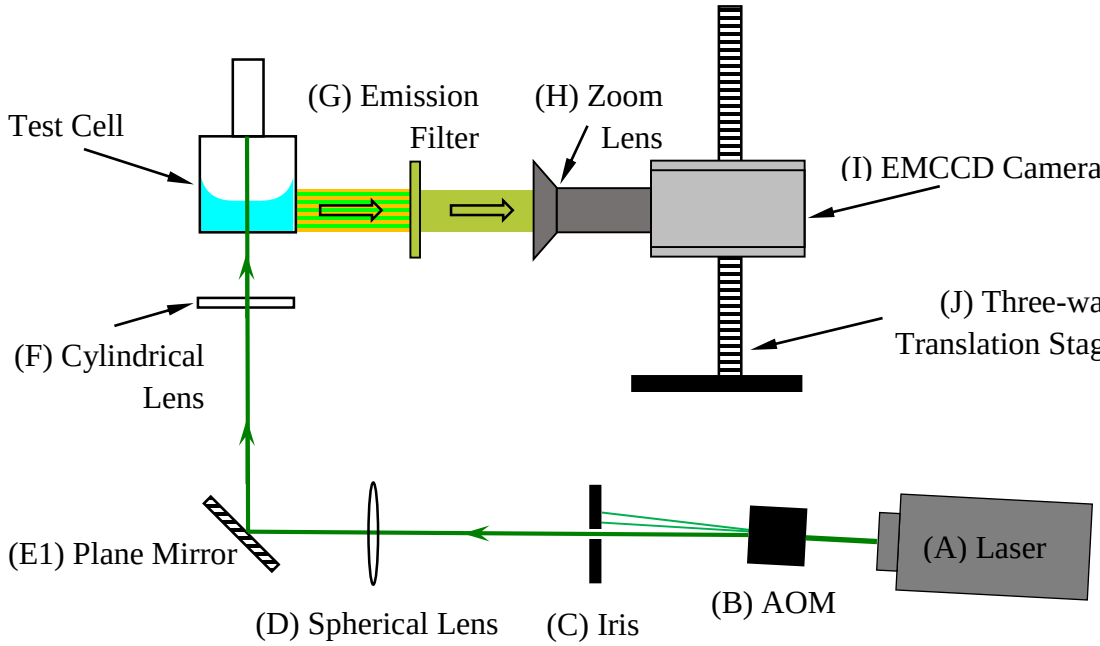

Figure 3.4 Schematic of optical setup for the vertical view configuration showing an end view of the test cell. The green lines indicate the path of the laser beam.

The fluorescence from the particles was imaged through the front side wall of the test cell through a bandpass filter (G) (BrightLine FF01-542/27-25) that only transmitted light at wavelengths λ = 529 – 556 nm and rejected the λ = 514.5 nm illumination (Fig. 3.5), imaged through a zoom lens (H) (Navitar 7000, focal length 18 – 108 mm), and recorded by an electron multiplying CCD (EMCCD) camera (I) (Photometrics Cascade 650). The absorption (dashed line) and the emission (solid red line) spectra of the fluorescent particles are shown in Figure 3.5. The dotted green line represents the laser wavelength (*i.e.*, 514.5 nm), whereas the yellow-green shaded region denotes the wavelength range of the fluorescence passing the emission filter and recorded by the EMCCD camera. The camera and the zoom lens were mounted on a three-axis translation stage (J) (Newport Corporation 462 series), which made it possible to adjust the position of the camera to visualize the entire flowfield.

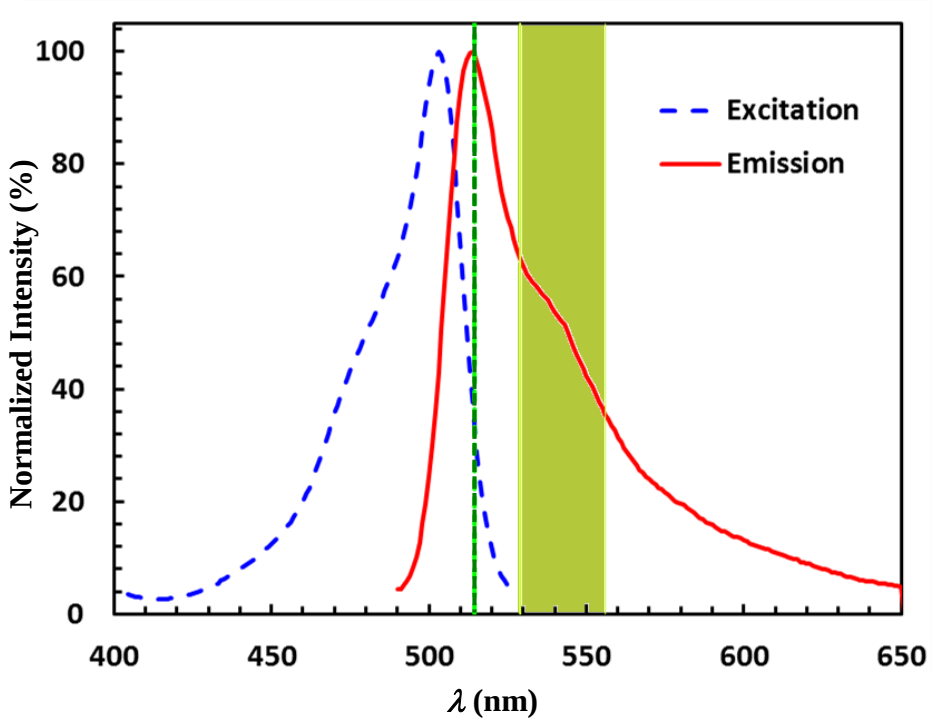

Figure 3.5 Absorption (blue dashed line) and emission (red solid line) spectra of the fluorescent particles used in the PIV studies. The dotted green line indicates the illumination wavelength of 514.5 nm, and the yellow-green shaded region represents the wavelength range imaged by the EMCCD camera.

Figure 3.6 is a schematic of the optical setup of the horizontal view configuration. The horizontal view configuration is quite similar to the vertical view configuration with the following exceptions: *a*) the horizontally propagating beam (*i.e.*, after the iris (C)) was raised to the same level as that of the test cell by four plane mirrors (E1 and E2; *b*) the laser beam, which was again expanded along the horizontal, or *x*, direction to create a light sheet parallel to the top or bottom of the test cell, passed through the test cell from the front wall to the back wall (*vs.* from the bottom to the top walls in the vertical view configuration).

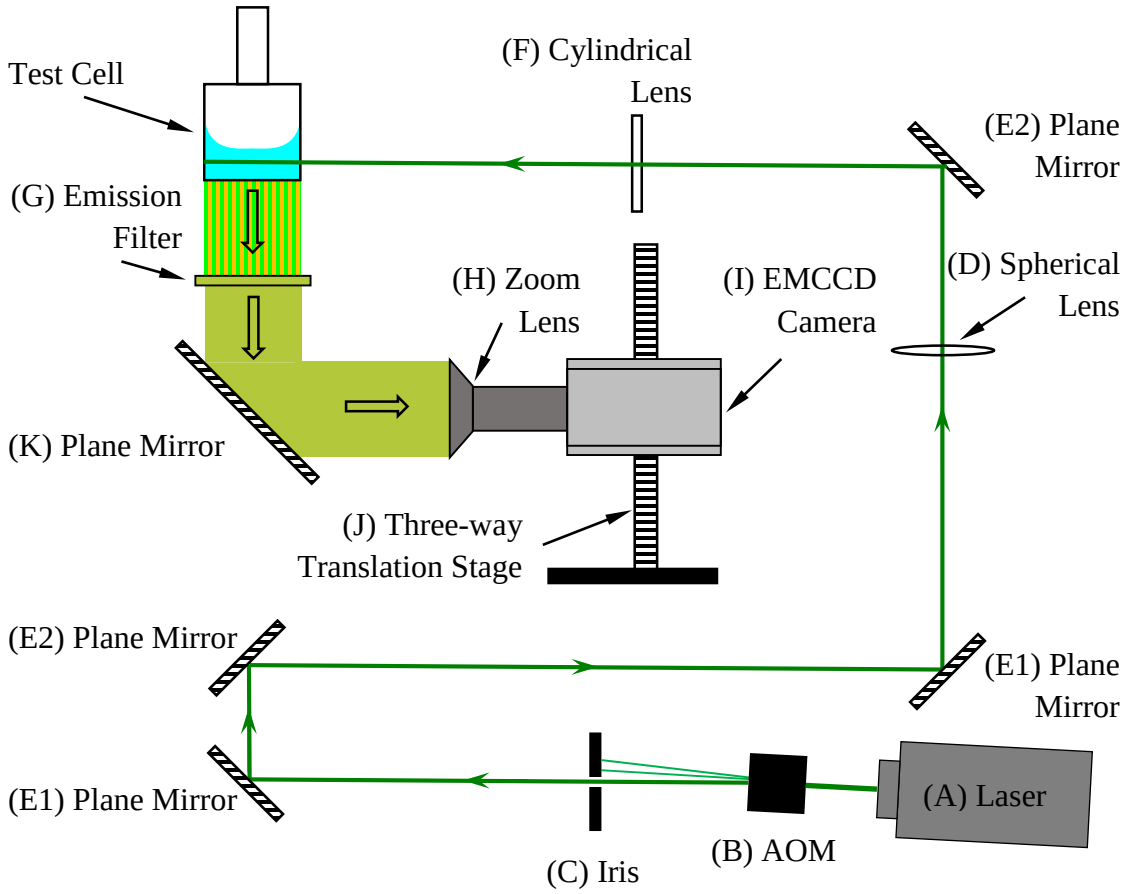

Figure 3.6 Similar to Figure 3.4, but for the horizontal view configuration.

The fluorescence from the particles was also imaged through the same bandpass filter (BrightLine FF01-542/27-25) and recorded by the same CCD (EMCCD) camera (Photometrics Cascade 650), but through the bottom window of the test cell to acquire a horizontal plane of the flow. Given the limited space underneath the test cell and the heat generated by the EMCCD camera (which could significantly affect the temperature of the test cell surroundings), the EMCCD camera and lens were not mounted beneath the test cell. A 90 °plane mirror (K) was instead used to reflect the fluorescence from the particles and the zoom lens (H) and camera (I) were mounted horizontally on the three-axis translation stage (J) to enable image acquisition over the entire test cell.

3.2.1 Illumination System

This section gives additional details of the illumination system. In this section, the major components of the illumination system are listed in Table 3-4, and the procedures used to characterize the laser light sheet are described.

Table 3-4 Components of the illumination system.

Label	Item	Manufacturer	Model #	Notes
A	Argon-Ion Laser	Inova	90	λ = 514.5 nm
B	AOM	IntraAction Corp.	AOM-04	Model ME Processor
C	Iris	Thorlabs	ID12	Ø12.0 mm max.
D	Spherical Lens	Thorlabs	LA1484	f = 300 mm
E1	Plane Mirror(s)	Thorlabs	BB1-E02	Ø1", 400-750 nm
E2	Plane Mirror(s)	Edmunds Optics	30-286	35×25mm, 400-700 nm
F	Cylindrical Lens	Thorlabs	LK1087L2	f = -6.4 mm

3.2.1.1 Measurement of Laser Light Sheet Thickness

For the PIV measurements, the laser light sheet thickness determines the depth of field. In other words, the sheet thickness determines the dimension of the plane in the flow imaged along the optical axis. Since the laser light sheet is created by expanding a round laser beam only along one direction normal to the optical axis, and the beam properties in the direction orthogonal to this direction (and the optical axis) are unaffected, the laser light sheet thickness is essentially determined by the diameter of the laser beam.

The beam emitted by this CW laser, which is dominated by the fundamental transverse or "TEM_{00}" mode, is well-approximated by a Gaussian profile (Hitz *et al.* 2012),

$$I_{\mathrm{L}}(r) = I_{\mathrm{o}} \exp\left(-\frac{2r^2}{w_{\mathrm{L}}^2}\right) \tag{3-1}$$

where $I_L(r)$ is the intensity profile, I_o is the intensity at the center of the beam, r is the radial distance from the center, and w_L is the beam radius at a certain axial location. The "edge" of the beam is defined to be the point where its intensity drops to $1/e^2$ (about 13%) of I_o, or where $r = w_L$.

The knife-edge method was used to measure the intensity profile across the laser beam (Khosrofian and Garetz, 1983). A single-edged razor blade, attached to a single-axis translation stage (Newport Corp. UMR8.25) driven by a micrometer (Newport Corp. SM25), was translated across one of the two axes of the laser beam cross section. The power of the transmitted portion of the beam was monitored by a laser power meter (Coherent Lasermate Q) as the razor blade was translated in increments of 20 μm across the bean until the entire beam was blocked by the blade.

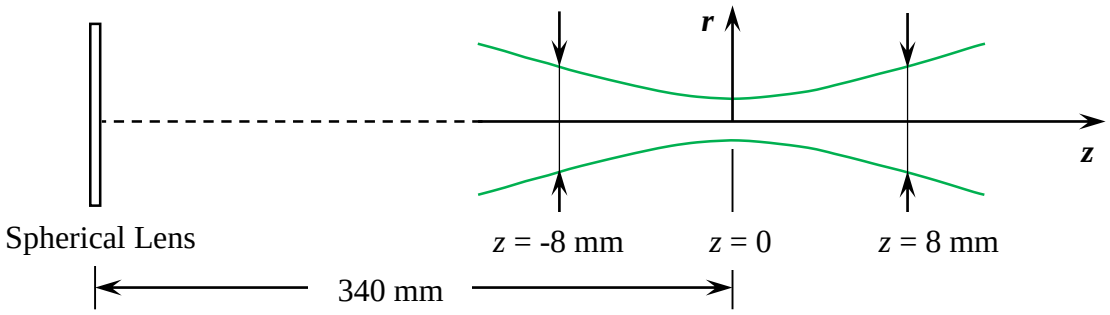

Figure 3.7 Illustration of the locations where laser beam diameters were measured; the green lines represent a propagating Gaussian beam; z is in the axial direction (in which the beam propagates) and r is in the radial direction.

Since the beam diameter varies along the axial direction, the diameter of the laser beam was measured at three different axial locations ($z = 0$, $z = –8$ mm and $z = 8$ mm as shown in Fig. 3.7). The first diameter was measured at a nominal distance of 340 mm after the spherical lens (*i.e.*, Fig. 3.7, $z = 0$), which was corresponding to the center of the test cell in an actual experiment. The beam diameters were also measured at $z = –8$ mm and z

= 8 mm (Fig. 3.7), to verify that the laser light sheet thickness remained nearly constant within the working fluid, *i.e.*, the maximum extent of the optical path in the fluid is 13 mm in the horizontal views, which is within the range of -8 mm $\leq z \leq 8$ mm. At all three locations, the beam profile was measured along the two orthogonal (*i.e.*, vertical and horizontal) directions normal to the optical axis, to estimate the thickness of the laser light sheet for both the horizontal view and vertical views.

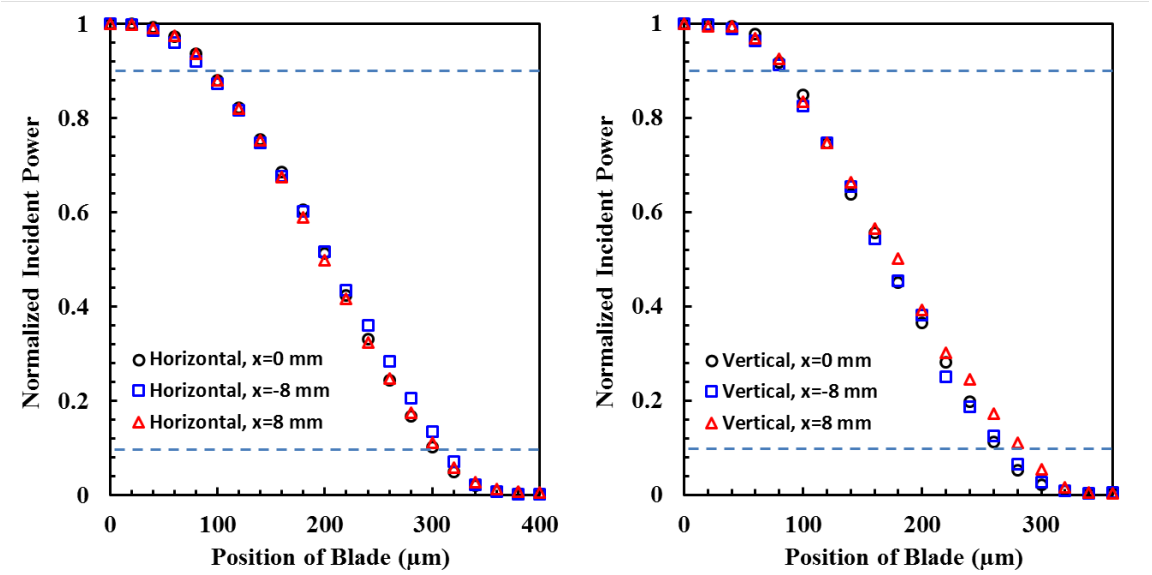

Figure 3.8 The normalized incident power as a function of the position of the blade edge at all three locations for translation along the horizontal [left] and vertical [right] directions. The dashed horizontal lines near the bottom and top of each plot represent 10% and 90% of the total beam power, respectively.

Figure 3.8 shows the normalized laser beam power as measured by the power meter as a function of the position of the edge of the razor blade. The laser beam diameters were then calculated from these experimental data points as follows (Khosrofian and Garetz, 1983),

$$d_L = 1.28(\chi_{10} - \chi_{90}) \tag{3-2}$$

where χ_{10} and χ_{90} are the blade positions across the beam corresponding to transmission of 10% and 90% of the total power (*cf.* the dashed lines in Fig. 3.8). The χ_{10} and χ_{90} locations for each beam profile were determined by interpolation after fitting a curve to all the data points using the smooting spline function in Matlab R2013b®.

The beam diameters at all three locations in both vertical and horizontal directions are summarized in Table 3-5. In all cases, the laser beam diameter was less than 0.3 mm, *vs.* a liquid layer depth and width of ~3 mm and 10 mm, respectively. Moreover, the laser beam diameter remains nearly constant for $-8 \text{ mm} \leq z \leq 8 \text{ mm}$, suggesting that the laser light sheet had a nearly constant thickness over the flow cell. Finally, the vertical extent of the beam is slightly less than the horizontal extent, suggesting that the beam has a slightly elliptical (*vs.* round cross-section, which may be due to diffraction from the the AOM.

Table 3-5 Horizontal and vertical laser beam diameters at all three locations.

Location	z = 0 mm	z = -8 mm	z = 8 mm
Horizontal Diameter (mm)	0.27	0.28	0.27
Vertical Diameter (mm)	0.23	0.24	0.25

3.2.2 Imaging System

This section provides additional details of the imaging. The major components of the imaging system are listed in Table 3-6, and the characteristics of the imaging system are discussed.

Table 3-6 Components of the imaging system.

Label	Item	Manufacturer	Model #	Notes
G	Emission Filter	BrightLine	FF01-542/27-25	Ø25 mm
H	Zoom Lens	Navitar	7000	18-108 mm, *f*/2.5
I	EMCCD Camera	Photometrics	Cascade 650	16 bit, 492×653 pixels
J	Three-Way Translation Stage	Newport Corp.	462 series	SM25Micormeter, 10 μm increment
K	Plane Mirror	Thorlabs	ME2S-P01	2"×2", 450 nm-20 mm

3.2.2.1 Magnification Calibration

Since the physical size of the EMCCD pixels is fixed, the physical dimensions of the field of view are determined by the magnification of the imaging system. Three different magnifications were used in these studies to image portions of the flow. This section details the calibrations used to accurately determine the actual magnification for all three types of experiments.

As will be discussed in Section 3.2.2.3, all the PIV measurements over the vertical *x-z* plane and those made over the horizontal *x-y* plane in the simple fluid were obtained at one magnification, $M_1 = 0.79$. The particle pathline visualizations over the vertical *x-z* plane were acquired at another magnification, $M_2 = 0.40$. Finally, the PIV measurements over the horizontal *x-y* plane in the binary liquids were obtained at magnification $M_3 = 0.36$. To accurately determine these magnification values, a borosilicate glass stage micrometer (Klarmann Rulings, Inc. KR-812) was imaged by the EMCCD through the zoom lens at each of the three magnification settings. The calibration images for all three settings are shown in Figure 3.9, with magnification decreasing from the top to the bottom. The images consist of dark (*i.e.*, low grayscale intensity) lines in a periodic pattern on a light (*i.e.*, high grayscale intensity) background. The spatial period of these lines should

then be the number of pixels between two consecutive lines, which can be accurately calculated by calculating a fast Fourier transform (FFT) of the grayscale values along the horizontal direction. The primary peaks of discrete Fourier transforms (DFT) of these grayscale value series (calculated in Matlab R2013b®) are summarized in Table 3-7. The actual magnification values are then calculated from these data based upon the physical pixel size of 7.4 μm and also summarized in Table 3-7.

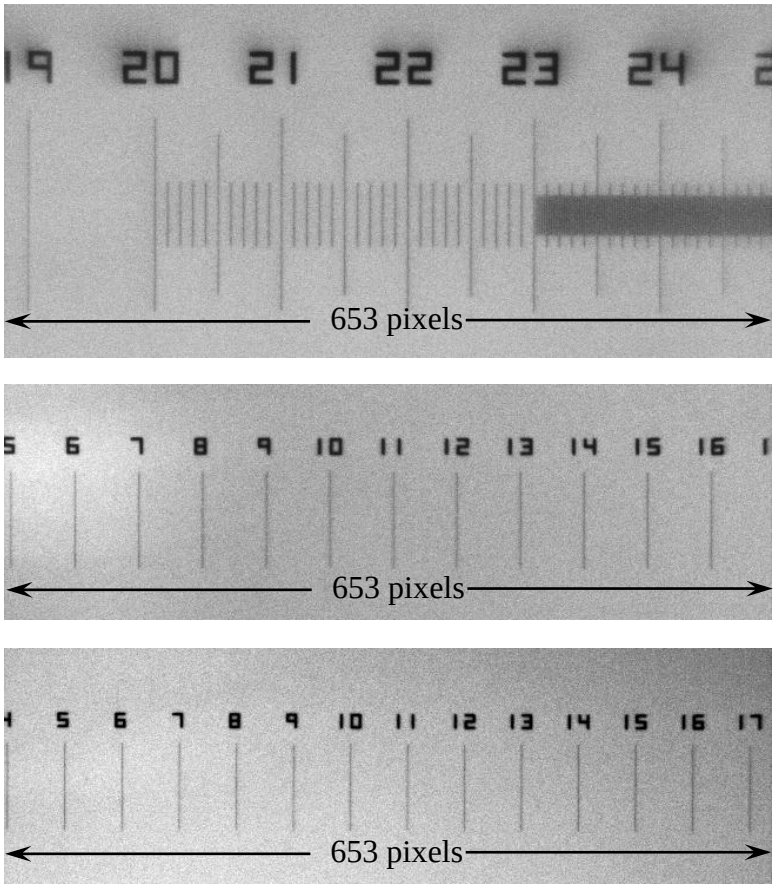

Figure 3.9 Magnification calibration images of the stage micrometer for [top] at M_1 (= 0.79) showing lines with a spacing of 0.1 mm; [middle] at M_2 (= 0.4); and [bottom] at M_3 (= 0.36), both showing lines with a spacing of 1 mm.

Table 3-7 Summary of the magnification of the three settings used in current study.

	M_1	M_2	M_3
DFT (pixel^{-1})	0.09326	0.0546	0.0488
Pixels per mm	107.2	20.51	18.31
Actual Magnification	0.79	0.40	0.36

3.2.2.2 Camera Working Mode

As will be shown in the Results chapters, the flow speeds in these experiments span nearly three orders of magnitude, ranging from $O(10\ \mu m/s)$ for the nearly stagnant flows in some of the binary-fluid cases, to almost 10 mm/s. The PIV experiments therefore used two different imaging modes, the continuous and the "overlap" modes, for different flow conditions. The continuous mode, where the camera continuously captures images at a constant frequency, was used for low- to medium-speed flows. The "overlap" mode (also known as "frame straddling"), where the camera captured pairs of images where the time interval within the pair was much less than the time interval between successive pairs, was used for medium- to high-speed flows.

In the continuous mode the camera was driven by an internal trigger. Here, the start of the exposure is driven by the main trigger, and the exposure then ends after a given (exposure) time (Fig. 3.10). The image is then read out to the hard drive (HD) of a computer, and this sequence repeats. Since the images obtained in this mode are evenly spaced in time, the time interval within an image pair Δt can be adjusted simply by adjusting the camera frequency, which was a valuable feature for low-speed flows.

Given the small volume of the working liquid (*i.e.*, $O(1\ mL)$), however, the heating of the liquid by a 2.1 W CW laser beam could be quite significant. To minimize this effect, the CW laser beam was shuttered with the AOM to ensure that the working liquids were illuminated only during the exposure time (*i.e.*, when the aperture was open). For instance, for a setting where the exposure time τ =1 ms and imaging frequency f_I = 25 Hz, the flow

was only illuminated for 1 ms out of the 40 ms imaging period, effectively reducing the heating power 40-fold (Fig. 3.10). The AOM was driven by a function generator (Wavetek 801) that was triggered by the EMCCD camera. In brief, an AOM diffracts light using a diffraction grating created in flint glass. This grating is generated by an acoustic wave that creates periodic variations in the refractive index of the glass by introducing a strain field. The diffracted beam, *i.e.*, the illumination, is then turned on and off by turning the acoustic wave on and off, respectively. Further details are given in H. Li's thesis (Li, 2008), for example. The AOM was mounted on a rotational stage (Melles Griot 07-TRS-503) with a resolution of 15 arcsec so that the angle of incidence of the beam could be adjusted to maximize the power of the diffracted beam.

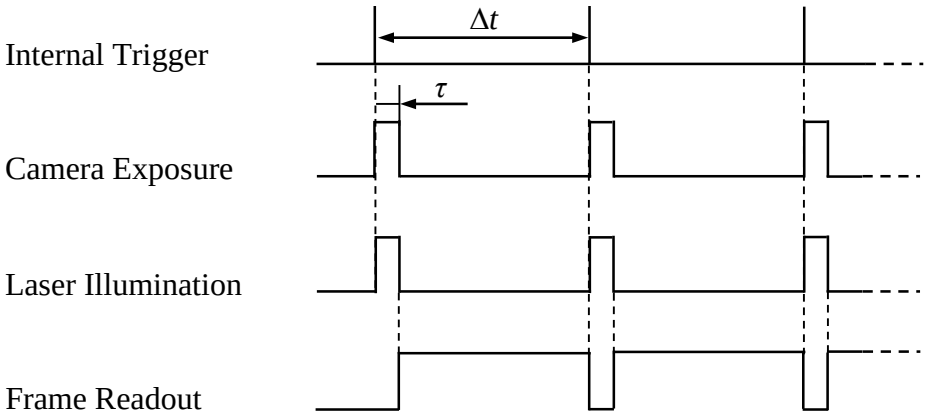

Figure 3.10 The timing diagram for the EMCCD camera working in the continuous mode.

The time interval Δt in the continuous mode can be too long, however, to resolve higher-speed flows, especially since the EMCCD camera used here has a relatively low maximum framing rate of 40 Hz, corresponding to a minimum Δt of 25 ms. The overlap mode was therefore used to significantly reduce Δt. As shown in Figure 3.11, the limitations of the EMCCD are overcome by acquiring pairs of images at times that are determined by the laser illumination (*vs.* the EMCCD) .

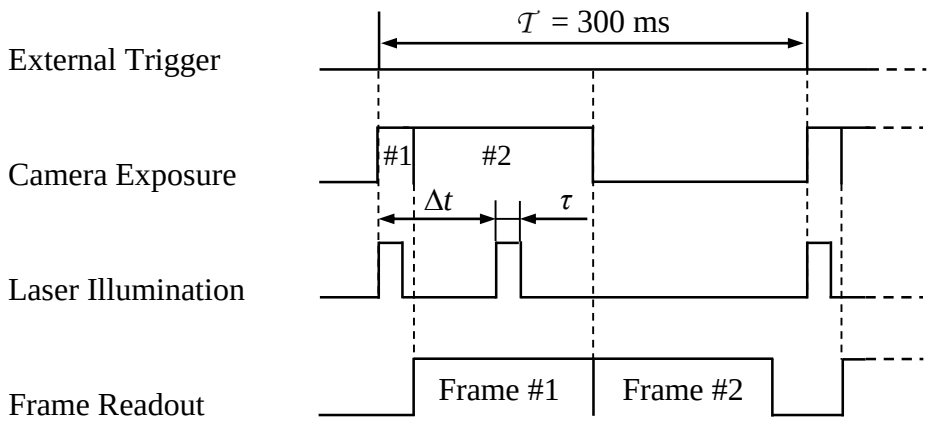

Figure 3.11 The timing diagram for the EMCCD camera working in the "overlap" mode.

In the "overlap mode," the first image in the pair is read out during the exposure time for the second image in the pair. As shown in Figure 3.11, the camera is first triggered by an external trigger at a constant frequency of 3.3 Hz (*i.e.*, period $\mathcal{T}$ = 300 ms), and the camera is then exposed for a specific amount of time (here, τ = 2 ms) to expose the first image in the pair. At the end of the first image, the first image is immediately read out. The second image is exposed simultaneously, over exactly the time interval required to read out the first image. Finally, the second image is read out, resulting in a single image pair, and this sequence then repeats. To ensure that the exposure time was consistent between the two images in the pair, the laser was shuttered by the AOM, and so both the exposure time τ and the time interval between the images within the pair Δt was effectively determined by the AOM.

To do this, the external main signal that triggers the first frame of the pair also was used to trigger the function generator (Wavetek 801), which generated two square pulses separated by Δt of the same amplitude and the same width, τ. These square pulses were used to drive the AOM, where each laser pulse had a width of τ, and the interval between the two pulses was Δt. In all overlap mode cases, 200 image pairs were obtained over each

field of view at an external triggering frequency of 3.3 Hz, giving a total imaging time for one set of image pairs of 60 s.

3.3 Experimental Procedure

This section details the experimental procedure used for both the simple and binary fluid experiments.

3.3.1 Preparation of the Test Cell

Before each experimental run, the test cell was thoroughly cleaned and using Nanostrip 2X® solution (Cyantek® KMG Nano-Strip 2X®), which is a stabilized formulation of concentrated sulfuric acid and hydrogen peroxide compounds for removing a wide variety of organic compounds. Since the entire cleaning protocol took up to ~12 h, cleaning the test cell usually started the day before the actual experiment was performed. The test cell was cleaned as follows:

a) The dirty (*i.e.*, used) test cell was rinsed multiple (at least 5) times with high-purity methanol (Fisher Scientific A412P-4, Certified ACS Reagent Grade with purity ≥ 99.8%) and fresh double distilled and deionized (DDI) water from a Thermo-Scientific Barnstead E-pure™ D4641 water purification system with an initial resistivity of ~17.8 MΩ·cm.

b) Any remaining water was blown out of the cell by compressed ultrapure nitrogen (Airgas Inc. NI UHP 300, ultrahigh purity 5.0 grade).

c) Next, the test cell was filled with ~ 5 mL Nanostrip 2X® solution using a gas tight glass syringe (Hamilton, model 1010) attached to PTFE syringe tubing (Sigma Aldrich Z117323-1EA). Since the Nanostrip 2X® solution reacts with most metals (*e.g.* steel and brass) and plastics (*e.g.* PVC and Tygon tubing), extra care was taken during the filling process to prevent Nanostrip 2X® solution from coming into contact any of the other components of the experimental setup. The glass syringe

was first filled with ~5 mL Nanostrip 2X® through the PTFE syringe tubing, and then any droplets of Nanostrip 2X® on the tip of the syringe tubing were wiped off. The syringe tubing was then carefully pushed all the way down onto the charging port (*cf.* Fig. 3.2) before any solution was pumped out of the syringe. Finally all of the Nanostrip 2X® solution was slowly injected into the fused-quartz test cell, and the syringe tubing was then carefully removed from the charging port.

d) The Nanostrip 2X® solution remained in the test cell for at least 12 h (*i.e.*, overnight) under ambient conditions.

e) The filled test cell was then sonicated for 10 min in a water bath using an ultrasonicator (Cole-Parmer 8845-4) to suspend the contaminants on the inner surfaces of the test cell in the Nanostrip solution.

f) Most of the Nanostrip solution in the test cell was then carefully removed using the same glass syringe and syringe tubing used in the filling process.

g) The (nearly) empty test cell was then rinsed by pumping ~500 mL (*i.e.*, more than 100 times of the test cell volume) fresh DDI water using the two fused quartz ports as the inlet and exit (*cf.* Fig. 3.2). The test cell was also continuously agitated during the rinsing process.

h) After blowing most of the remaining water out the test cell with compressed ultrapure Nitrogen, the test cell was attached again to the vacuum pump via the pumping line (*cf.* Fig. 3.3) and evacuated down to a pressure of ~0.4 kPa, and kept at this pressure for approximately 10 min, until all the DDI water within the test cell was removed and the inside of the test cell was completely dry.

i) The test cell was then removed from the pumping system and weighed with an analytical balance (OHAUS GT210) to get its weight when it's empty.

j) The cell was then kept in a closed plastic case to minimize any subsequent contamination.

3.3.2 Preparation of the Working Fluids

The working fluids were prepared as detailed in Section 3.1.2. In order to minimize the exposure of the working fluids to air, the working fluids were always prepared after all the other parts of the experimental setup (*i.e.*, laser and optics, test cell, *etc.*) were ready, so that the experiments were started immediately after preparing the working fluids.

3.3.3 Starting the Experiments

3.3.3.1 Simple Fluid Experiments

In all the simple fluid experiments, the test cell was charged with ~3 mL of the particle-seeded solution using a disposable syringe (Air-Tite Products Co., Inc. AL5) attached to PTFE syringe tubing (Sigma Aldrich Z117323-1EA) through the charging port. The PTFE syringe tubing was rinsed with methanol, DDI water and the working liquid, hexamethyldisiloxane (NMR grade with purity ≥ 99.5%, Sigma Aldrich 326739-100G), then blown dry with ultrapure nitrogen, before use. After charging, the test cell was connected to the charging and pumping lines (*cf.* Fig. 3.3) with the two quick connects.

Before turning on the vacuum pump, the pressure transducer and the TC data acquisition (DAQ) were turned on, the needle valve (2) was closed, and the two cutoff valves (3) were opened (*cf.* Fig. 3.3). The test cell was then evacuated through the vacuum port by the vacuum pump (Edwards E-Lab 2). After about 60 s, the cutoff valve on the charging line was closed and a hemostat was used to close the Tygon tubing immediately above on the charging port. The vacuum pump continued to evacuate the test cell for another ~60 s (so the total evacuation time was ~2 min) until the pressure inside the test cell was ~1.7 kPa, as measured by the pressure transducer. The cutoff valve on the vacuum line was then closed and the vacuum pump was turned off.

For the vapor cases, the Tygon tubing on the vacuum line was clamped with another hemostat as soon as the cutoff valve on the vacuum port was closed, to prevent any mass loss during the actual experiments. The minimum equilibrium pressure in the vapor space

p that could be achieved in these simple fluid experiments was 4.83 kPa at T_o = 20.3 °C. This pressure corresponds to a minimum c_a = 14%, or an air partial pressure of 0.69 kPa, based on a vapor pressure for HMDS of 4.14 kPa at this T_o (Yaw, 2003).

To increase the air concentration for the intermediate and air-dominated cases with C_a = 36%, 57%, and 96%, corresponding to p = 6.59 kPa, 10.1 kPa, and 101 kPa (*i.e.*, ambient conditions), respectively, the hemostat and cutoff valve on the charging line (*cf.* Fig. 3.3) were opened after evacuating the test cell and the needle valve ((1) in Fig. 3.3) was then opened a small amount, allowing ambient air to slowly enter the test cell until p reached the desired value. The needle valve was then closed. After another 5 min to ensure that the pressure in the test cell had reached its equilibrium value, the cutoff valve on the charging line was again closed and the two segments of Tygon tubing above the charging and vacuum ports were again clamped with hemostats to prevent any mass loss during the actual experiments.

During the evacuation process, about half (*i.e.*, 1.5 mL) of the coolant evaporated, leaving about 1.5 mL of liquid within the test cell. Therefore, the nominal average depth of the liquid layer, defined to be the volume of the liquid divided by the area LW, h_{av} = 0.31 cm, giving a transverse aspect ratio $\Gamma_y \equiv W / h_{av}$ = 3.2. This is about twice capillary length scale $l_c \equiv [\sigma / (\rho_L g)]^{1/2} = 0.15$ cm (where g is the gravitational acceleration) for the working fluid (*i.e.*, hexamethyldisiloxane) at 20 °C.

Then the test cell was carefully leveled by adjusting the multi-axis tilt platforms (Newport 37 series) (*cf.* Section 3.1.1) using a bubble level that was temporarily placed on top of the test cell. Once the test cell was leveled, the Peltier heater and cooler were powered by the dc power supply (Mastech HY3005-2), and a timer was started. At the same time, the laser was started so that it would have enough time to warm up to its steady-state condition. In all cases, the test cell was heated and cooled for 60–90 min, until the

temperatures of the heated and cooled ends (*i.e.*, T_h and T_c, respectively) reached their steady-state equilibrium values, defined to be temperatures that varied by less than 0.2 °C over the duration of the entire experiment, and p reached its steady-state value, defined here to be pressure that varied by less than 0.2 kPa during the experiment.

For the simple fluid studies, 21.7 °C ≤ T_h ≤ 28.6 °C and 14.9 °C ≤ T_c ≤ 20.8 °C, giving applied temperature differences $\Delta T \equiv T_h - T_c = 0.9–12.5$ °C. The average of T_h and T_c was within 0.3 °C of the ambient temperature T_o, which varied between 20.0 °C and 21.3 °C, except at larger $\Delta T \geq 11.5$ °C, where the average was within 1.9 °C of T_o. Note that the temperature difference between the inner surfaces of the end walls will of course be less than ΔT, since the thermal conductivity of quartz is ~1.3 W/(m·K), and that the laboratory Marangoni number reported here, which is based on ΔT, significantly overstates the actual Marangoni number.

It was impractical to measure the temperature distribution over the inner surfaces of the test cell in this study because there was very little direct access to the interior of the cell. However, 2D numerical simulations of buoyancy-thermocapillary convection in HMDS at $c_a = 0\%$ (*i.e.*, in the absence of noncondensables) by our collaborators (Qin *et al.* 2014, Qin *et al.* 2015) in a similar geometry show that the maximum variation in the temperature over the inner surface is about 1.2 °C for an applied temperature difference ΔT = 4 °C, as shown in Figure 3.12*a* (Qin, *et al.* 2015). Note that the largest temperature changes over the heated and cooled ends occurs over a very small region near the contact line because this is where most of phase change occurs over these surfaces. The maximum variation in the temperature over the inner surface is less, about 0.8 °C, for convection under ambient conditions ($c_a = 96\%$), because the air suppresses phase change (Fig. 3.12*b*).

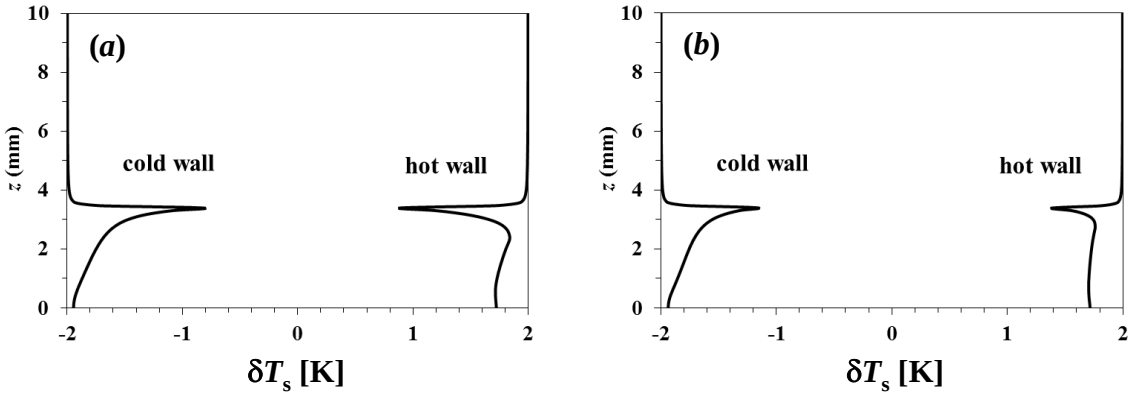

Figure 3.12 Temperature variation δT_s (compared with the average temperature of the test cell) along the inner surface of the cold/cooled and hot/heated ends from numerical simulations at $\Delta T = 4$ °C for (*a*) $c_a = 0\%$ and (*b*) $c_a = 96\%$.

3.3.3.2 Binary Fluid Experiments

In all the binary fluid experiments, the test cell was charged with ~1.8 mL (*vs.* 3 mL in the simple fluid experiments) of the particle-seeded solution using a disposable syringe (Air-Tite Products Co., Inc. AL5) attached to PTFE syringe tubing (Hamilton 90619) through the charging port. The PTFE syringe tubing used in the binary experiments was a different type from that used in simple fluid experiments; this tubing was used only with DDI water (H_2O), methanol (MeOH) and MeOH-H_2O mixtures to avoid cross contamination with HDMS. The charged test cell was then attached to the pumping system (*cf.* Fig. 3.3) again by the two quick disconnect connectors.

The evacuation procedure for the binary-fluid experiments was similar to that used for the simple fluids, so only the differences are detailed here. First, the evacuation times after closing the cutoff valve on the charging line and clamping the Tygon tubing on the charging port varied with the methanol concentration. After evacuating the test cell for 60 s, the cell was evacuated until reaching the final liquid volume of ~1.5 mL. For instance, for C_M =58% the test cell was evacuated for another 30 s (*vs.* 60 s in simple fluid cases), reaching a minimum pressure of ~ 2.8 kPa. The less volatile binary mixture (*e.g.* $C_M = 9\%$)

required a longer evacuation time before the final liquid volume of ~1.5 mL, which was the same for both the simple-fluid and binary-fluid experiments.

Second, a hemostat was not used to clamp the Tygon tubing on the vacuum line immediately after evacuating the test cell and closing the cutoff valve on the vacuum line. The test cell was instead allowed to rest for 20 min for the temperature (and the pressure) to re-equilibrate with the ambient temperature. This was re-equilibration time was necessary because the temperature of the test cell decreased significantly (*i.e.*, by as much as 10 °C) during evacuation, in part due to the large latent heats of vaporization of water and methanol (Table 3-2). After this time, the Tygon tubing on the vacuum line was clamped with another hemostat for the vapor-dominated cases. During the evacuation process, about 0.3 mL of the liquid evaporated. The minimum c_a in the vapor space that could be achieved in these binary-fluid experiments are given in Appendix C. Higher air concentrations were again achieved using the same procedure used in the simple-fluid experiments.

Next, the test cell was carefully leveled and the Peltier heater and cooler were powered up at the same time. Before starting image acquisition, the test cell was heated and cooled for 60–90 min until the temperatures of the heated and cooled ends and p reached their steady-state equilibrium values. Steady-state is defined here to be variations in the temperatures of < 0.2 ℃), and pressures of < 0.2 kPa) during the entire period of image acquisition. In these binary-fluid studies, T_h = 22.8 ℃–24.2 ℃ and T_c = 16.6 ℃–18.3 ℃, giving applied temperature differences $\Delta T \equiv T_h - T_c$ = 5.9 ℃–6.3 ℃. This value of ΔT was about half the maximum temperature difference that could be achieved with this experimental setup. The temperature difference across the cooled and heated end walls is estimated to be ~1 ℃ based on 1D conduction through fused quartz. All four sides of the cell were exposed to air at ambient temperatures T_o = 19.5 ℃–21.7

℃. The experimental conditions for all the binary experiments presented in this work are summarized in Appendix C.

3.3.4 Image Acquisition

This section describes the image acquisition procedures used to map out the entire flow. Due to the differences of flow structures observed for simple and binary fluid experiments, slightly different schemes were used accordingly.

3.3.4.1 Simple Fluid Experiments

To obtain the 2D-2C PIV measurements in the simple-fluid experiments, the entire vertical central x-z plane of the flow at $y = 0$, was imaged within a single experimental run. This vertical plane was a composite of nine overlapping (with typical overlap = 0.01 cm) 0.61 cm × 0.46 cm (653 × 492 pixels) views (Fig. 3.13*a*). Three horizontal x-y planes of the flow at $z = 0.1$ cm and $z = 0.2$ cm, each a composite of six overlapping (overlap = 0.01 cm in x, 0.06 cm in y) 0.61 cm × 0.46 cm views (Fig. 3.13*b*), were also imaged in a separate experimental run under the same conditions, where each horizontal plane was a composite of six 0.61 cm × 0.46 cm views with an overlap of 0.01 cm in x and 0.06 cm in y.

In all cases, a sequence of 200 16-bit image pairs (= 400 images) with dimensions of 653 × 492 pixels were acquired of the flow at a magnification of 0.79 as described in Section 3.2.2.2, over a total image acquisition time $\mathcal{T}_T$ using both the continuous and "overlap" modes, as tabulated in Table 3-8. A sequence of 100 images of the vertical central x-z plane at $y = 0$ were also obtained at a lower magnification of 0.40 at $\tau = 2$ ms and $\Delta t = 39$ ms. These images were averaged over $\mathcal{T}_T = 15.6$ s to obtain particle pathline visualizations of the flow, and the contrast and brightness of the average image was adjusted as required to bring out the flow features. Almost all of the entire vertical central plane of the flow was visualized in four views, each with a vertical (z) extent of 0.91 cm

(*cf.* Fig. 3.13*c*), with the exception of a small sliver at x = [2.41 cm: 2.44 cm] in the center of the test cell.

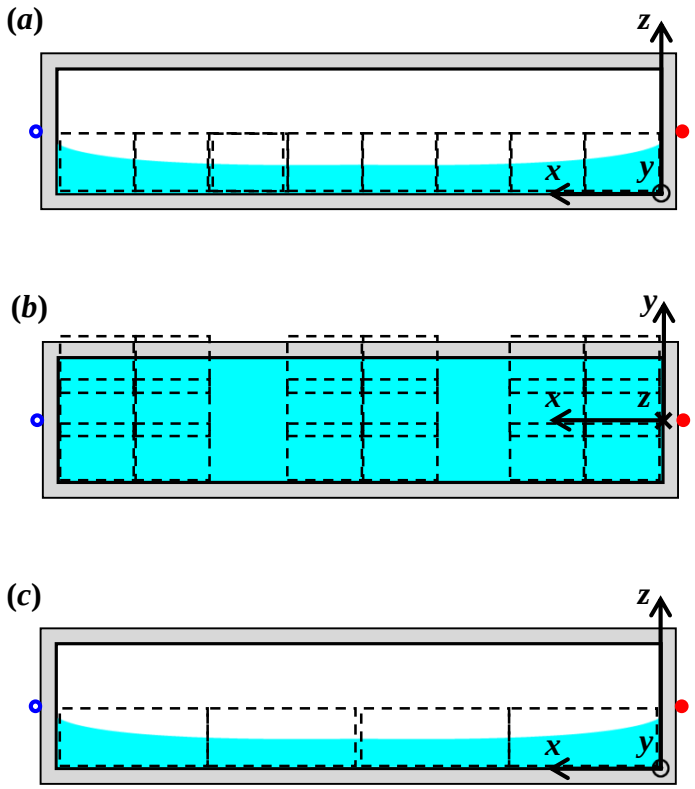

Figure 3.13 Sketch of the test cell and the liquid layer defining the coordinate system and the views used in *simple* fluid experiments for (*a*) PIV in the central vertical plane at y = 0; the (*b*) PIV in the horizontal plane at z = 0.1 cm or z = 0.2 cm and (*c*) Visualization in the central vertical plane at y = 0. Each dashed rectangle indicates a single field of view of the camera, and the filled circle on the right and the open circles on the left indicate the nominal locations of the TCs used to measure T_h and T_c, respectively.

TABLE 3-8 Summary of PIV image acquisition parameters.

ΔT [℃]	Plane	Camera Mode	τ [ms]	Δt [ms]	$\mathcal{T}_T$ [s]
		C_a = 96%			
0.9, 1.4, 1.9, 3.0, 6.5, 7.8	Vertical	Continuous	2	39	15.6
3.8	Vertical	Overlap	2	20 or 40	60
3.8	Horizontal	Continuous	2	39	15.6
11.5	Vertical	Overlap	1	5	60
		C_a = 57%			
2.8	Vertical	Continuous	2	39	15.6
3.9, 6.8, 9.8	Vertical	Overlap	2	20	60
12.5	Vertical	Overlap	2	10	60
		C_a = 36%			
3.0	Vertical	Continuous	2	39	15.6
3.9, 6.0, 7.9	Vertical	Overlap	2	20	60
11.6	Vertical	Overlap	2	10	60
		C_a = 14%			
3.9	Vertical	Overlap	2	20 or 40	60
11.6	Vertical	Overlap	2	10 or 20	60

3.3.4.2 Binary Fluid Experiment

In the binary-fluid PIV experiments, velocity fields were obtained by imaging four 0.61 cm × 0.46 cm (653 × 492 pixels) views of the central vertical *x*-*z* plane of the flow at $y = 0$ within a single experimental run at a magnification of 0.79 at a spatial resolution of 9.4 μm/pixel (Fig. 3.14*a*). Horizontal *x*-*y* planes of the flow at $z = 0.1$ cm and at $z = 0.2$ cm were also imaged in two 1.34 cm × 1.0 cm (653 × 492 pixels) views in a separate experimental run under the same conditions at a magnification of 0.36 at a spatial resolution of 20.3 μm/pixel (Fig. 3.14*b*). In all cases, a sequence of 200 16-bit image pairs (= 400 images) were acquired of the flow using the continuous mode at 25.6 Hz and $\tau = 1$ ms.

Particle pathlines of the flows were also obtained, by again averaging a sequence of 400 images (exposure time τ = 1 ms) at a magnification of 0.4 of the vertical central x-z plane at y = 0 obtained at 25.6 Hz, and adjusting the contrast and brightness of the average image as required. Nearly all of the entire vertical central plane of the flow was visualized in four views (*cf.* Fig. 3.14*c*), with the exception of x = [2.41 cm: 2.44 cm].

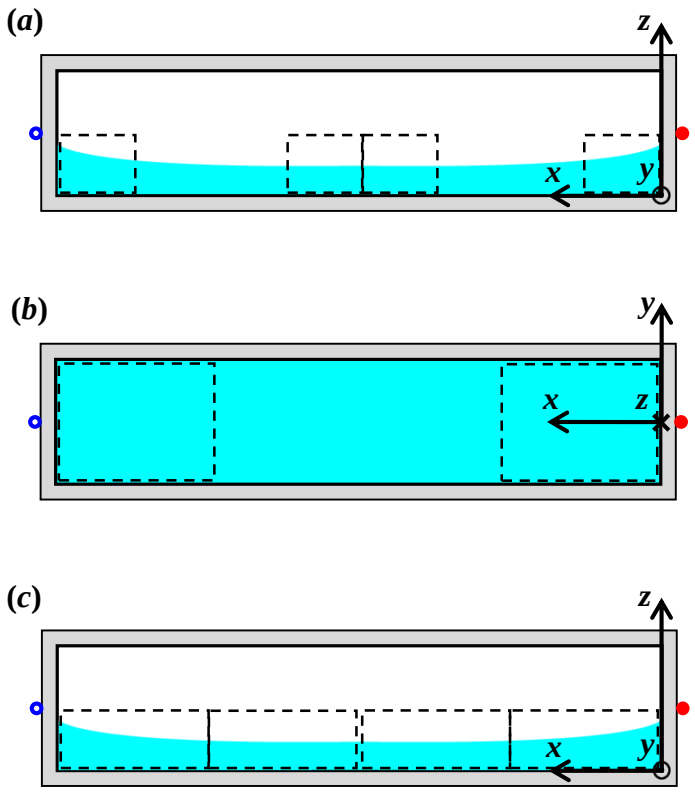

Figure 3.14 Similar to Figure 3.13, but for binary imaging.

3.3.5 After the Experiments

After image acquisition, the experiments were finished. The laser, camera, AOM and function generator were shut down, the optics were covered to protect them from dust, and the dc power supply for the Peltier heater and cooler was turned off. The final pressure inside the test cell was measured after releasing the hemostat clamp on the vacuum line (*cf.* Fig. 3.3) and waiting ~10 min at room temperature to ensure that the test cell was in thermal

equilibrium with the surroundings. The room temperature at the end of the experiment was recorded along with the final test cell pressure.

The test cell containing the working liquid was then disconnected from the vacuum and charging lines at the two quick connects. In the simple-fluid experiments, the cleaning procedure for the test cell was started so that the test cell would be ready for an experiment the following day. For the binary-fluid experiments, however, two additional steps were performed before cleaning: *a)* The test cell and the working liquid inside the cell were weighed using an analytical balance (OHAUS GT210) to determine the weight of the fluid, which was calculated by the (previously measured) weight of the empty test cell from this reading; *b)* 1 mL of the binary liquid was removed from the test cell and weighed using another analytical balance (Sartorius, M-power AZ124) to determine the density of the working liquid, which was then used to calculate the composition (*i.e.*, C_{M}) of the binary mixture (*cf.* Appendix A). The test cell was then cleaned as detailed in Section 3.3.1 for the next experiment.

3.4 Image Processing

After acquisition, the 16-bit grayscale images were first converted to 8-bit images by dividing the grayscale values by 256. The first 100 images in the sequence were averaged, and the depth (z-dimension) of the liquid layer in the central vertical x-z plane was taken to be that corresponding to the lower edge of the bright curved band, detected by the Canny edge detection method (Canny 1986) implemented in MATLAB R2010a®, representing the meniscus (*i.e.*, liquid-vapor interface) in this averaged image. Only the part of the image corresponding to the liquid (*i.e.*, from $z = 0$ to the z-position of the lower edge of this band) was processed with an in-house 2D-2C PIV code (implemented in MATLAB R2010a®) which determined the two in-plane velocity components.

The "standard" PIV processing procedures used here involved direct cross-correlation of 64 (x) × 32 (y) pixels (0.06 cm × 0.03 cm) interrogation windows in the first

image of the pair with a window of the same dimensions in the second image of the pair using window shift (Westerweel and Dabiri 1997). The window shift used was the average of the displacements obtained by correlating 64 × 32 pixel windows (with no window shift) over the first 100 image pairs. A Gaussian curve-fit to the three points nearest the correlation peak was used to interpolate the location of the peak, and hence the average displacement of the particles within the interrogation window. The interrogation windows had 50% overlap unless stated otherwise, giving a spacing of 0.03 cm along *x* and 0.015 cm along *y*.

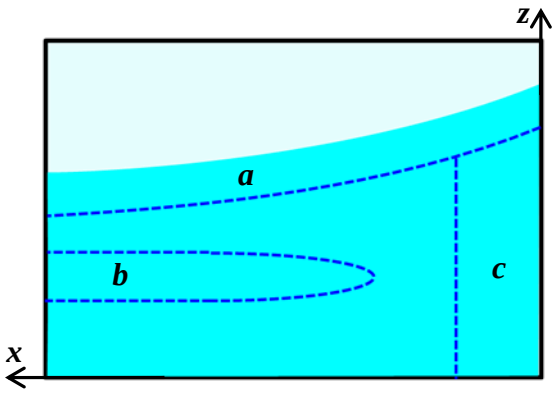

Figure 3.15 Sketch of the vertical *x*-*z* plane next to the heated end depicting the regions where "nonstandard" PIV processing methods were used, namely the (*a*) interfacial, (*b*) shear, and (*c*) near-wall regions.

This flow, with its curved menisci near the heated and cooled ends and regions of high shear, presents some PIV processing challenges. The next section summarizes the "nonstandard" PIV processing methods used in the flow regions shown in Figure 3.15. The regions near the curved menisci next to the heated and cooled ends (region *a* of Fig. 3.15) were processed using an image transformation, or window distortion, technique (Jeon and Sung, 2011), detailed in Section 3.4.1. In brief, the region within a *z*-extent of 60 pixels, or 0.056cm, of the meniscus along the interface-normal direction was "meshed" into trapezoidal elements, and mapped by bilinear interpolation to rectangular regions with a

vertical (z) dimension of 60 pixels. Rectangular 64 (x) × 16 (z) pixel (0.06 cm × 0.015 cm) windows in the first image of the pair were directly cross-correlated with a window of the same dimensions in the second image in the pair using window shift. The spacing of the PIV data were 0.03 cm and 0.0075 cm along the directions parallel and normal, respectively, to the free surface. The displacements obtained for the distorted rectangular regions were then mapped back to the actual trapezoidal regions using the Jacobian matrix of the coordinate transformation.

The convection roll(s) in the liquid layer create regions with strong velocity gradients, *i.e.*, $\partial u / \partial z$ with small velocity magnitudes near the vertical center of the layer, corresponding to $z = 0.1 - 0.2$ cm, where the flow reverses direction (region *b* in Fig. 3.15). For the steady flow cases (*i.e.*, all the flow cases except for the unsteady case at higher ΔT where the vapor space above the liquid layer was dominated by air), the time interval Δt in this region was doubled to 20 ms or 40 ms (*cf*. Table 3-8) to increase the particle displacements within the image pair, and smaller interrogation windows of 32 (x) × 16 (y) pixels (corresponding to physical dimensions of 0.03 cm × 0.015 cm) were used to reduce distortion of the particle pattern due to shear within the interrogation window. Since fewer particles are imaged in these smaller interrogation windows, cross-correlation averaging (Meinhart *et al*. 2000) over all 200 image pairs was used to effectively increase the number of particles in the window, and hence improve the signal-to-noise ratio (SNR) of the correlation peak. A Gaussian curve-fit to the three nearest neighbors of the average correlation peak was again used to determine the peak location, and hence the average displacement of the particles within the interrogation window.

Next to the vertical (heated or cooled) walls of the test cell, the flow is mainly along the vertical (*i.e.*, z) direction with strong velocity gradients along the x direction (region *c* in Fig. 3.15). A 32 pixel (0.03 cm) square interrogation window in the first image of the pair was directly cross-correlated with a window of the same dimensions in the second image of the pair using window shift.

For the (single) unsteady high ΔT case, the PIV data in the central vertical *x*-*z* plane were also used to estimate the out-of-plane vorticity component from the circulation, based on a second-order central difference method involving the eight nearest neighbor vectors. A larger overlap of 75% was used between adjacent interrogation windows to obtain a "smoother" vorticity field (Adrian and Westerweel, 2011).

In all cases, velocity vectors were obtained by dividing the particle displacements, averaged over all 200 image pairs, by Δt. Any displacements with a correlation peak-to-noise ratio (*i.e.*, the ratio of the cross-correlation peak to the highest noise peak) less than 1.2 were considered to be incorrect "outlier" vectors (Keane and Adrian 1990) and a standard median filter-based criterion was used on the remaining PIV data to identify outlier vectors (Westerweel and Scarano 2005). All outliers were replaced with vectors estimated from their nearest 8 neighbors by bilinear interpolation.

3.4.1 The Image Transformation Technique

This section details the image transformation technique applied to the interface region of the flow (region *a* of Fig. 3.15) and its validation. The method used here uses the approach developed by Jeon and Sung (2011).

3.4.1.1 Working Principle

In order to map the trapezoidal interrogation windows in the vicinity of the free surface to rectangular windows, the location of the interface, (x_k, y_k), in the original image was first determined by using the Canny edge detection method, and the slope of the interface, θ_k, at each (x_k, y_k) location was calculated by taking the derivative of a fitted polynomial to the data set of (x_k, y_k). The transformed image $I'(s,n)$ can then be interpolated from the original image $I(x, y)$ as follows:

$$I'(s,n) = I(x_{\text{trans}}, y_{\text{trans}}) \tag{3-3}$$

where

$$x_{\text{trans}} = \frac{s - d_{k-1}}{d_k - d_{k-1}} x_k + \frac{d_k - s}{d_k - d_{k-1}} x_{k-1} + n\cos\left(\theta_{\text{trans}} + \frac{\pi}{2}\right) \tag{3-4}$$

$$y_{\text{trans}} = \frac{s - d_{k-1}}{d_k - d_{k-1}} y_k + \frac{d_k - s}{d_k - d_{k-1}} y_{k-1} + n\sin\left(\theta_{\text{trans}} + \frac{\pi}{2}\right) \tag{3-5}$$

$$\theta_{\text{trans}} = \frac{s - d_{k-1}}{d_k - d_{k-1}} \theta_k + \frac{d_k - s}{d_k - d_{k-1}} \theta_{k-1} \tag{3-6}$$

Here, (x_{trans}, y_{trans}) is the coordinate location of a pixel in the original frame, (s, n) is the coordinate location of the same pixel in the new Cartesian frame, and d is the length of the interface, which is defined as:

$$\begin{cases} d_0 = 0 \\ d_k = \sum_{z=1}^{k} \sqrt{(x_z - x_{z-1})^2 + (y_z - y_{z-1})^2}, k = 1, 2, 3... \end{cases} \tag{3-7}$$

As shown in Figure 3.16, the meniscus along the interface-normal region was originally "tiled" by a series of trapezoidal interrogation windows and the interrogation windows can be mapped to rectangles using equations (3-3) to (3-7), as shown in Figure 3.17, and these rectangular interrogation windows are then be processed using standard cross-correlation PIV. Finally, the velocities obtained in the new coordinate system are transformed back to the original coordinates using the Jacobian matrix J,

$$\begin{pmatrix} dx \\ dy \end{pmatrix} = J \begin{pmatrix} ds \\ dn \end{pmatrix} \tag{3-8}$$

where ds and dy are the particle displacements along the horizontal and vertical directions, respectively, in the new Cartesian system, and dx and dy are the particle displacements along x and y direction, respectively, in the original coordinate system. The Jacobian matrix

$$J = \begin{pmatrix} \frac{x_k - x_{k-1}}{d_k - d_{k-1}} - n\frac{\theta_k - \theta_{k-1}}{d_k - d_{k-1}}\sin\left(\theta_{\text{trans}} + \frac{\pi}{2}\right) & \cos\left(\theta_{\text{trans}} + \frac{\pi}{2}\right) \\ \frac{y_k - y_{k-1}}{d_k - d_{k-1}} + n\frac{\theta_k - \theta_{k-1}}{d_k - d_{k-1}}\cos\left(\theta_{\text{trans}} + \frac{\pi}{2}\right) & \sin\left(\theta_{\text{trans}} + \frac{\pi}{2}\right) \end{pmatrix} \tag{3-9}$$

3.4.1.1 Validation Using Synthetic Images

To validate the image transformation technique, a sequence of synthetic or artificial PIV images simulating potential flow around a cylinder (Fig. 3.16) was created. Approximately 1.5×10^4 particles were randomly distributed over an image domain of 653 $\times$ 653 pixels, corresponding to a particle area density $\rho_p = 0.05$ particles/pixel^2, in each synthetic image. The average diameter of the particles were 5 pixels, a value comparable to the actual particle size in a typical PIV image in the experiments, and the intensity profile of the particles in the synthetic images was a 2D Gaussian. No background noise was added to the images, because the objective of this validation with synthetic images was to evaluate the image transformation technique, and background noise should have little, if any, effect on the coordinate transformation.

After generating the first image, the particles were displaced by a distance (in pixels) corresponding to the, displacement due to the potential flow velocity field around a cylinder, to generate the second image of the image pair. This velocity field in cylindrical polar coordinates is of course

$$V_r = U\left(1-\frac{R_c^2}{r^2}\right)\cos\theta \tag{3-10}$$

$$V_\theta = -U\left(1+\frac{R_c^2}{r^2}\right)\sin\theta \tag{3-11}$$

where U is the uniform incoming velocity of the flow, R_c is the diameter of the cylinder, r and θ are the radial and angular coordinates, respectively, and V_r and V_θ are the radial and angular velocities, respectively. Potential flow around a cylinder was chosen for this validation because the cylinder has a curved surface, although this is a solid-liquid (*vs.* gas-liquid) interface, and because the flow speed is nonzero, and maximum, at the curved interface, as would be expected for a flow driven by thermocapillarity or solutocapillarity.

Figure 3.16 shows a typical synthetic image. The dark region in the top left corner is the cylinder, and there are of course no particles in this region. Note that the center of the cylinder, which is also the origin of the coordinate system, is at the top left corner, and only a quarter of the cylinder is shown here. To transform the region near the surface of the cylinder, the location and the slope of the surface were determined first by the Canny edge detector and the interface region within 60 pixels of the interface along the interface-normal direction was then transformed using equations (3-3)–(3-6). The solid lines in Figure 3.16 denote the interrogation windows along the interface in the original images (only every second window, *vs.* every window with 50% overlap, is shown here for clarity). Figure 3.17 shows the corresponding transformed image of the same region, where the trapezoidal interrogation windows have now been mapped to rectangles.

The image in Figure 3.17 was then processed using the standard PIV methods detailed in Section 3.4 by cross-correlating interrogation windows of 32×16 pixels. The resulting displacements were then converted to the actual displacements by transforming back to the original coordinate system using equations (3-8) and (3-9). Figure 3.18 compares the velocities at the surface of the cylinder predicted by the analytical solution for potential flow around a cylinder with the velocities obtained using the synthetic images processed using this image transformation technique and standard PIV. Note that the PIV results were mapped to the surface of the cylinder by linear extrapolation from the values at the nearest interrogation window. The two sets of data are in good agreement with a root-mean-square error (RMSE) of 0.09 pixels, which is less than the typically quoted accuracy of standard PIV methods of 0.1 pixels. These validation results therefore suggest that the image transformation technique can be used to obtain PIV velocities with reasonable accuracy in the vicinity of curved surfaces, and here, menisci.

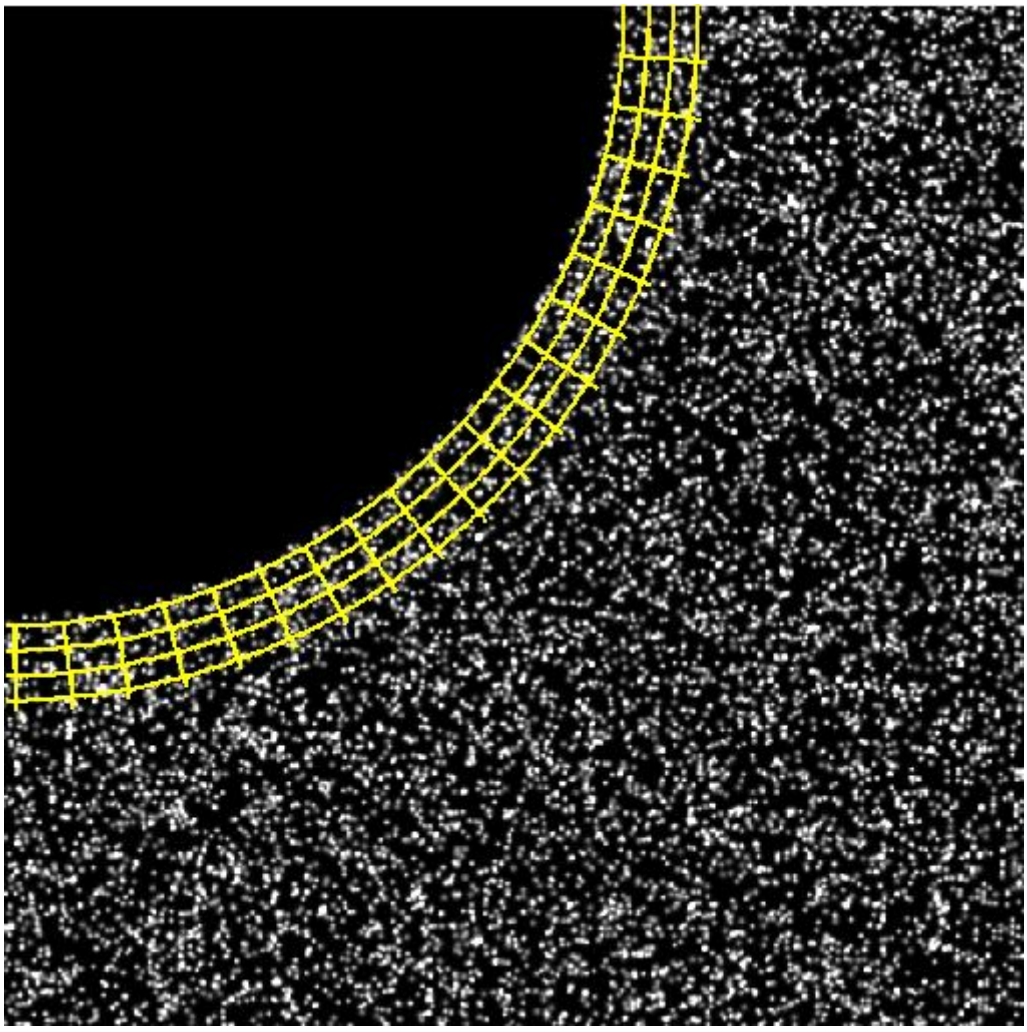

Figure 3.16 A typical synthetic particle image of potential flow around a cylinder used to validate the image transformation technique. The dark region in the top left corner is a quarter of the cylinder, and the curvilinear grid shown here represents every second interrogation window in the original coordinate system.

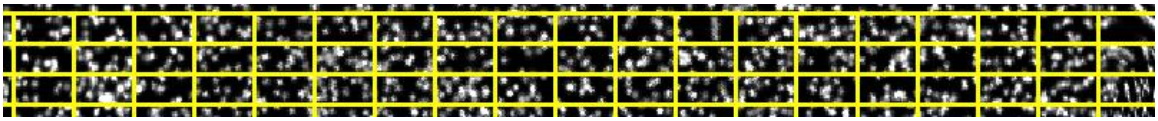

Figure 3.17 Transformed image of the interface region. The upper edge of the image corresponds to the curved surface of the cylinder in Figure 3.16, and the trapezoidal windows in Figure 3.16 have been mapped to the rectangular windows denoted here by the rectilinear grid in the new coordinate system.

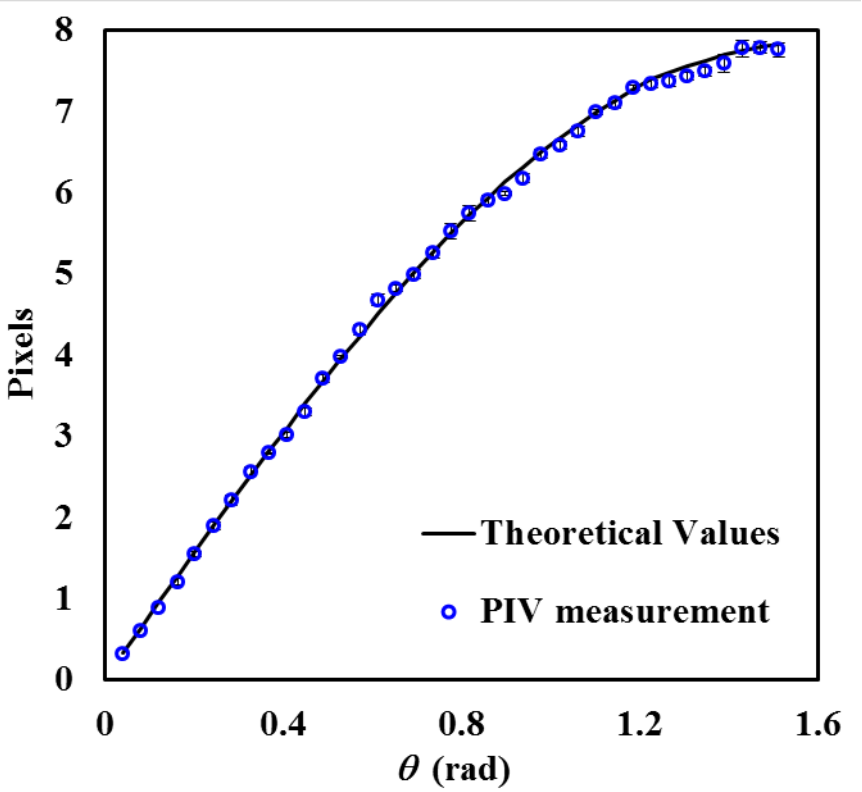

Figure 3.18 Comparison of the flow speeds at the surface of the cylinder predicted by potential-flow theory and obtained from PIV processing of the artificial images with window transformation. The theoretical predictions are the values of equations (3-10) and (3-11) at $r = R_c$, and the PIV values at the cylinder surface were obtained by linear extrapolation from the nearest PIV result. The error bars, denoting the standard deviations, are not visible because they are smaller than the symbols. The root-mean-square error of the experimental values (compared with the theoretical values) the two sets of data is 0.07 pixels.

CHAPTER 4

BUOYANCY-THERMOCAPILLARY CONVECTION IN SIMPLE FLUID

This chapter details the main results on and analysis of buoyancy-thermocapillary convection in a simple fluid (*i.e.*, HMDS) obtained using the methods and procedures described in the previous chapter. Section 4.1 presents all the experimental results for a wide variety of experimental conditions. Section 4.2 discusses at length the mechanisms that may explain these observations, while Section 4.3 summarizes the major conclusions from these results and the discussion. Much of the material in this Chapter is available in a recent paper published in *Physics of Fluids* (Li *et al.* 2014).

4.1 Experimental Results

4.1.1 Convection at c_a = 96%

For buoyancy-thermocapillary convection where the relative concentration of air in the vapor space above the liquid c_a = 96% at p = 101 kPa (*i.e.*, at ambient conditions), the major flow structure in the central vertical (x–z) plane of the flow are rolls with a counterclockwise rotation (when viewed with the heated end on the right end, and the cooled end on the left end, of the liquid layer), *i.e.*, a positive ω_y. At the lowest applied temperature difference ΔT = 0.9 °C, two rolls are observed, consisting of a "small" roll with a horizontal (x) extent comparable to the depth of the liquid layer next to the heated end and a "large" roll occupying the rest of the flow shown in Figure 4.1. Following previous studies, this state is defined to be steady unicellular flow (SUF) (Riley and Neitzel, 1998). As ΔT increases, the large roll "splits," and more small rolls with an x-extent comparable to the depth of the liquid layer form near the heated end; the formation of the first such roll is shown in Figure 4.2 at ΔT = 1.9 ℃. We call this state partial

multicellular flow (PMC). As ΔT increases further, the small rolls spread across the test cell towards the cold end, until there are a maximum of nine rolls occupying the entire test cell at ΔT = 3.0 ℃, which is defined here as the onset of steady multicellular flow (SMC) (Riley and Neitzel, 1998). The average *x*-dimension of the five rolls in the central section of the flow, taken to be the spatial wavelength of the rolls, λ_x = 0.57 cm.

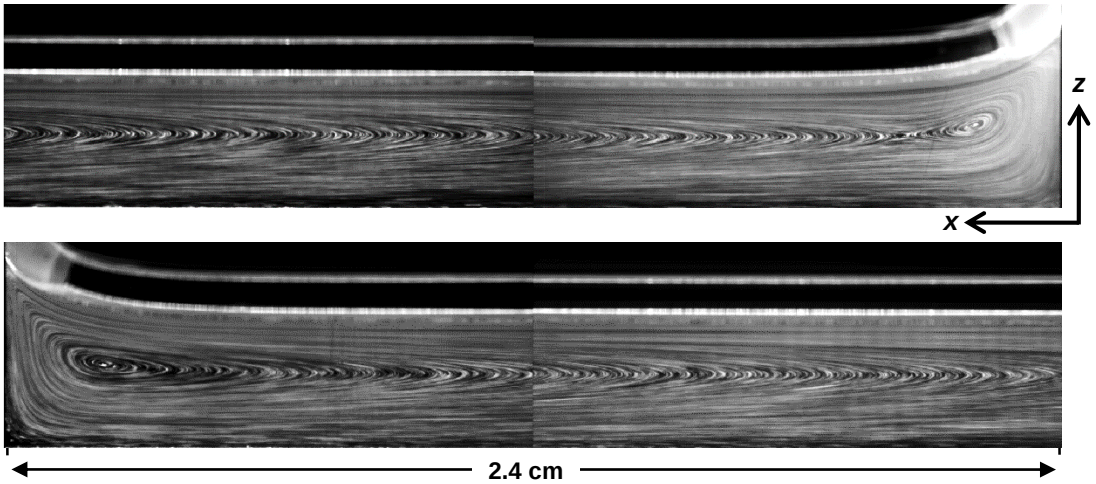

Figure 4.1 Particle pathline visualization of SUF flow in a liquid layer with an estimated average layer depth $\bar{h}$ = 0.263 cm in the central vertical (*x*-*z*) plane at an estimated interfacial Marangoni number Ma_i = 170 [ΔT = 0.9 ℃], for $0 \le x/L \le 0.49$ next to the heated end [top] and $0.51 \le x/L \le 1$ next to the cooled end [bottom], showing all but a small portion of the center of the liquid layer.

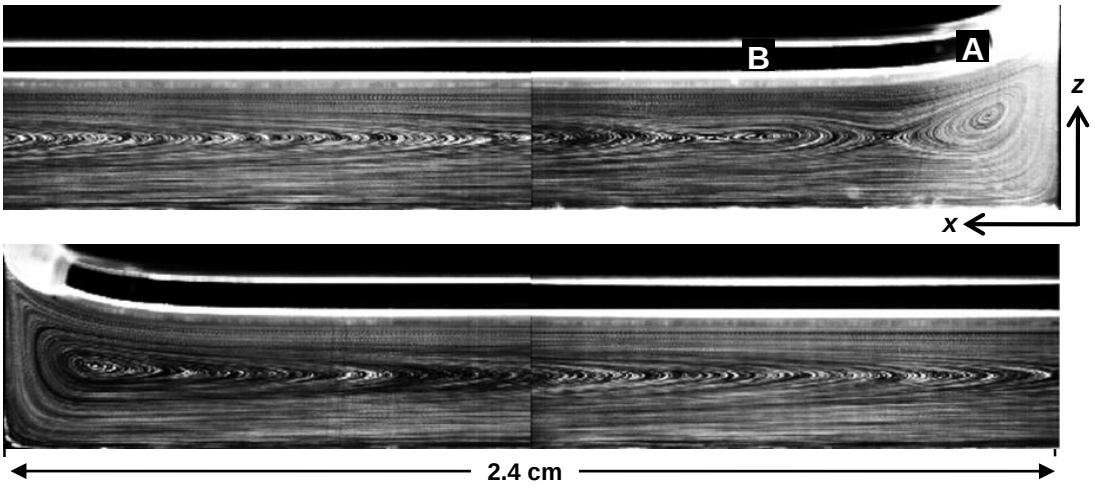

Figure 4.2 Particle pathline visualization of PMC flow in a liquid layer with an estimated average layer depth $\bar{h}$ = 0.266 cm in the central vertical (*x*-*z*) plane at an estimated interfacial Marangoni number Ma_i = 320 [ΔT = 1.9 ℃], for $0 \le x/L \le 0.49$ next to the heated end [top] and $0.51 \le x/L \le 1$ next to the cooled end [bottom], showing all but a small portion of the center of the liquid layer. Two rolls, labeled A and B, where B is much less evident than A, are visible next to the heated end [top] on the right. Note that the axes shown here and in the subsequent Figures only denote the coordinate directions.

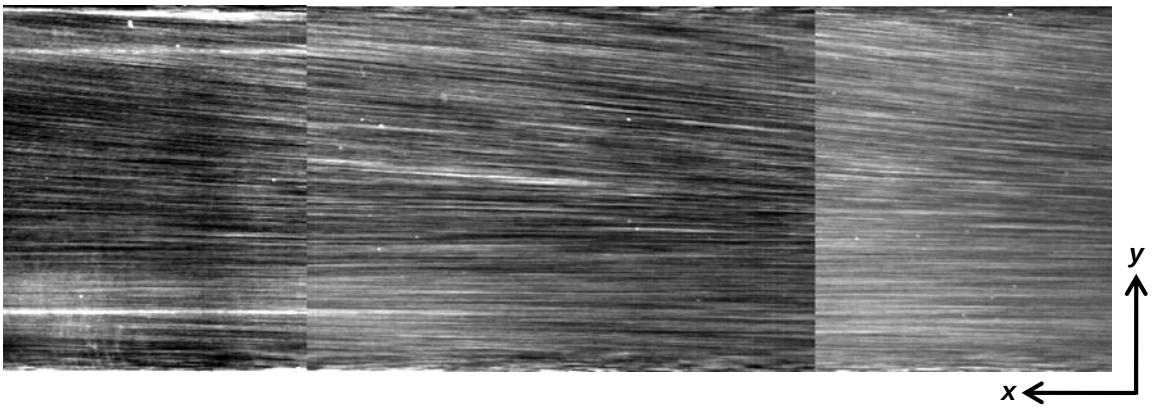

Figure 4.3 A particle pathline visualization of the flow at ΔT = 1.9 ℃ in a horizontal *x*-*y* plane for 1 cm ≤ *x* ≤ 4 cm at *z* = 0.1 cm.

The particle pathline visualization shown in Figure 4.3 of a horizontal *x*-*y* plane of the flow at ΔT = 1.9 ℃ (*cf.* Fig. 4.2) in the central portion of the cell at *z* = 0.1 cm shows that there is a slight asymmetry in the flow, with a "tilt" in the flow from the upper left corner towards the lower right corner, corresponding to a slope $dy/dx < 0$. This is likely due to a weak secondary flow driven by the temperature difference between the "front" of the test cell (*i.e.*, the bottom of the Figure), which faces the laser and the camera and the ambient conditions at the "back" of the test cell (*i.e.*, the top of the Figure). During the experiments, the temperature of the outer surface of the front wall of the test cell at *y* =

0.625 cm, which faces the laser and the camera, is 0.4 ℃ higher than that at the back wall of the test cell at $y = -0.625$ cm, based on TC measurements with an uncertainty of 0.1 ℃, and measurements of the air temperature about 5 cm away from the test cell suggest that the ambient temperature in the front of the test cell is about 0.9 ℃ higher than that behind the test cell. As shown in Figure 4.3, the liquid near the bottom of the cell therefore flows in the direction of the temperature gradient, since the temperature increases from left to right, towards the heated end (*i.e.*, along the negative *x*-direction), and from top to bottom, towards the front of the test cell (*i.e.*, along the negative *y*-direction).

Moreover, it appears that the magnitude of the slope of the pathlines decreases towards the bottom of this image. This suggests that the flow in a *y*-*z* cross-section of the test cell is a superposition of two secondary flows, namely 1) a single convection cell spanning the entire *y*-extent of the test cell (due to front wall being hotter than the cooler back wall) as shown in Figure 4.4 [top], and 2) two convection cells symmetrically arranged with respect to the *x*-axis (due to the bulk fluid being hotter than the front/back walls), as shown in Figure 4.4 [bottom]. The latter could account for the positive vertical component of the flow in the *x*-*z* midplane shown in Figure 4.2, which is ignored in the linear stability analyses of this problem.

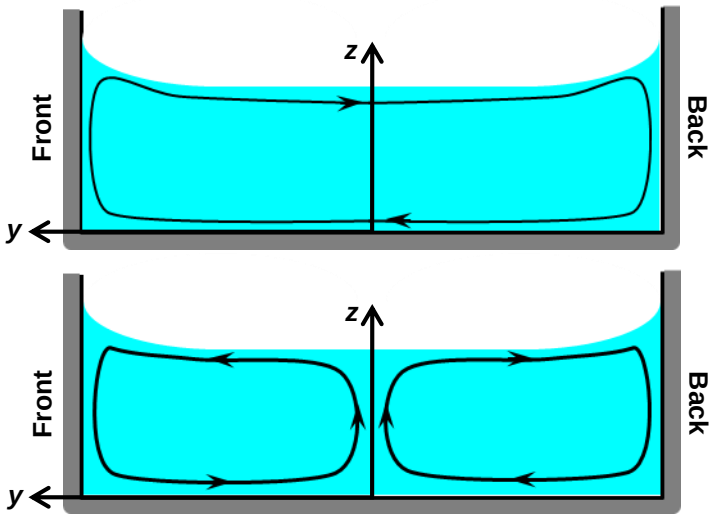

Figure 4.4 Sketches of the two secondary flows in a *y*-*z* plane, one with a single convective cell [top] and another with two convective cells [bottom]. In both views, *x* goes into the page, and the front and back side walls are as shown.

As ΔT is increased further, the number of the rolls decreases (and their wavelength increases). Figure 4.5 shows a particle pathline visualization of the entire liquid layer (except for the central portion at $0.49 \leq x/L \leq 0.51$) typical of SMC at ΔT = 3.8 ℃ (T_h = 22.2 ℃, T_c = 18.4 ℃), with a total of eight rolls spanning the entire *x*-extent of the test cell. The period, or *x*-dimension, of the rolls decreases slightly towards the heated end.

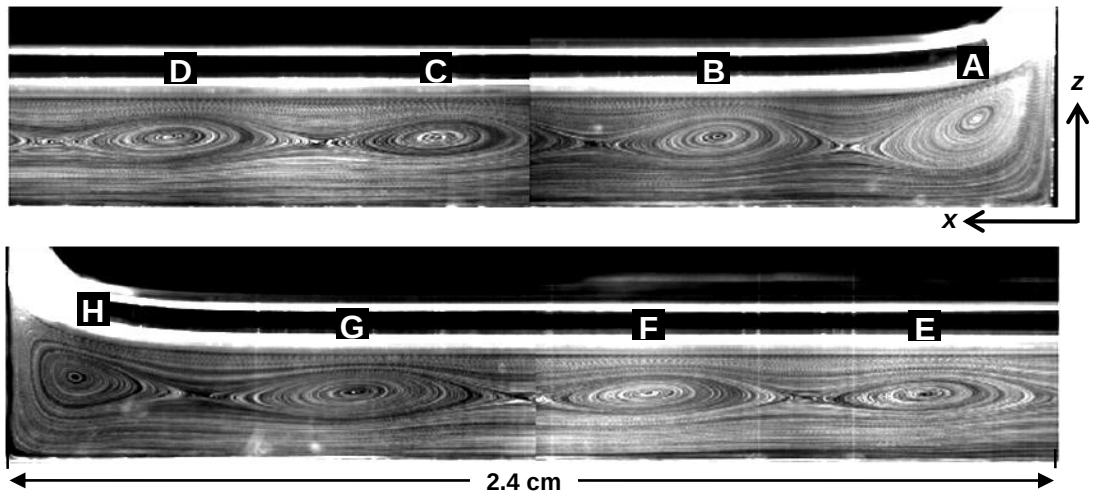

Figure 4.5 Particle pathline visualization of SMC flow in the central vertical (*x*-*z*) plane of a $\bar{h}$ = 0.260 cm liquid layer at an estimated Ma_i = 510 [ΔT = 3.8 ℃] over $0 \leq x/L \leq 0.49$ next to the heated end [top] and $0.51 \leq x/L \leq 1$ next to the cooled end [bottom]. Letters are used to label the eight rolls, with roll A immediately adjacent to the heated end [top] on the right and roll H next to the cooled end [bottom] on the left.

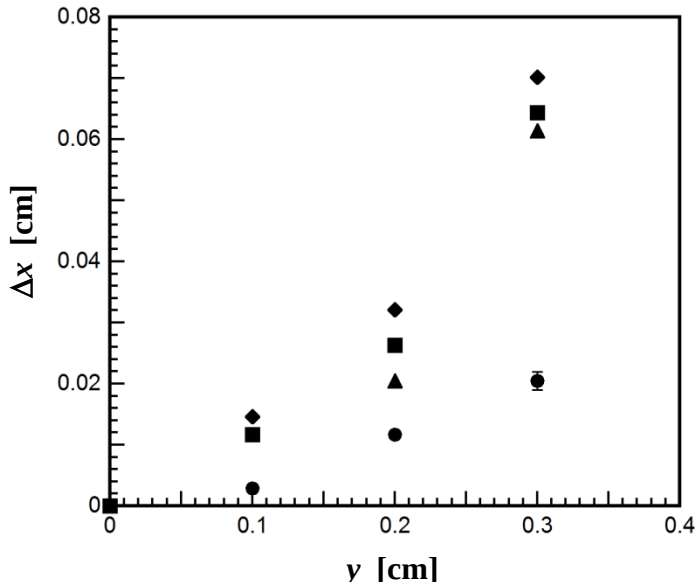

Figure 4.6 The difference between the *x*-coordinate of the center of rolls C (◆), D (■), E (▲) and F (●) (*cf.* Fig. 4.5) Δx and that of the center of the roll at $y = 0$ as a function of the *y*-coordinate at $\Delta T = 3.8$ ℃. The error bar denotes the 30 μm uncertainty in determining the *x*-position of the center of each roll.

To determine the orientation of these rolls, pathline visualizations were also obtained at $y = 0.1$, 0.2 and 0.3 cm. The location of the center of each roll (in pixels) was visually estimated from these images with an uncertainty of one pixel, or 30 μm, and used to calculate Δx, the shift along *x* of the center compared with its location at $y = 0$. Figure 4.6 shows Δx as a function of *y* for the four central rolls (C, D, E and F); the *x*-positions of the centers of these rolls at $y = 0$ are 1.40 cm, 2.04 cm, 2.68 cm and 3.36 cm, respectively. The axes of all four rolls appear to be slightly oblique with respect to the *y*-axis, with centers whose *x*-position increases slightly as *y* increases. This orientation is consistent with the slight tilt of the flow (due to the nonzero temperature gradient imposed by the front/back walls of the test cell) in the horizontal *x*-*y* plane shown in Figure 4.3. The rolls appear to become less oblique towards the cooled end, with the angle between the axis of the roll and the *y*-axis decreasing as the *x*-position of the roll increases.

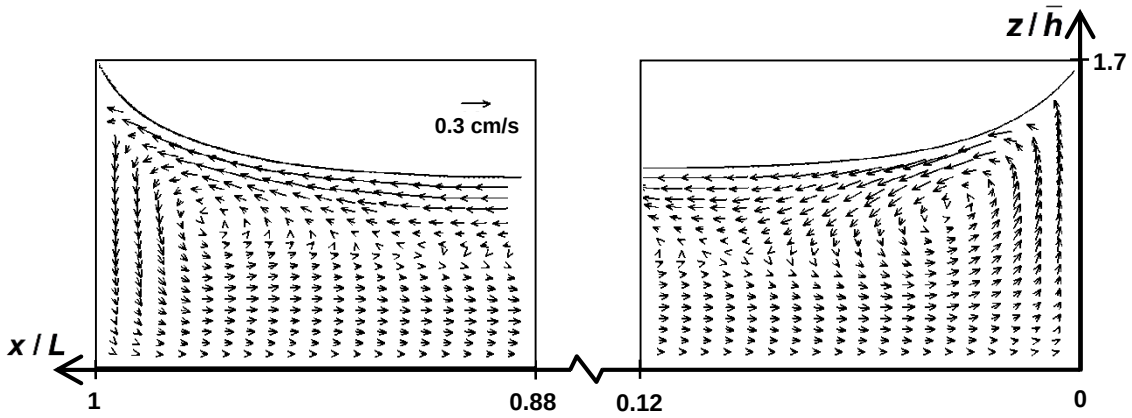

Figure 4.7 The velocity field in buoyancy-thermocapillary convection under air in the central vertical (*x*-*z*) plane of the flow at $y = 0$ next to the cooled end over $0.88 \leq x/L \leq 1$ [left], and next to the heated end over $0 \leq x/L \leq 0.12$ [right] of the test cell for SMC flow at $Ma_i = 510$ [$\Delta T = 3.8$ ℃]. The velocity scales are identical for both vector plots, and the maximum velocity magnitudes, which occur just below the free surface, are 0.41 cm/s and 0.51 cm/s near the cooled and heated ends, respectively.

Figure 4.7 shows the average liquid-phase velocity field in the central *x*–*z* plane of the flow at $y = 0$ near the heated end ($0 \leq x/L \leq 0.12$) [right], and the cooled end ($0.88 \leq x/L \leq 1$) [left] of the test cell for the same SMC flow at $\Delta T = 3.8$ ℃. As expected, the interfacial flow in the liquid is driven by thermocapillary stresses away from the heated end, *i.e.*, towards the cooled end (buoyancy effects are relatively minor for the $Bo_D < 1$ considered here). Near the bottom, the flow reverses direction, going from the cooled end towards the hot end. There are, however, stagnation points at $(x/L,\ z/\bar{h}) \approx (0.1, 0.58)$ and (0.9, 0.62) near the heated and cooled ends, respectively, which correspond to the centers of the left-/rightmost convection rolls observed in Figure 4.5. Note that only the in-plane (*i.e.*, *x* and *z*) velocity components are measured in these 2D-2C PIV data. This flow is steady, with an average standard deviation in the velocity magnitude calculated

over the 200 samples of 1.6% (based on the maximum velocity magnitude) and a maximum of 7% occurring near the contact line in the free surface region.

Figure 4.8 shows the in-plane velocity components field for the same flow in a horizontal (*x*–*y*) plane at $z/\bar{h}$ =0.77 (*z* = 0.2 cm) next to the heated ($0 \le x/L \le 0.25$) [right] and the cooled ($0.75 \le x/L \le 1$) [left] ends of the test cell. This plane is slightly below the free surface in the central portion of the test cell; the depth increases near the heated and cooled ends to a maximum of ~0.4 cm due to capillarity (*cf*. Fig. 4.5). As expected, the flow is nearly symmetric about the *x*-axis, with the flow in the center near *y* = 0 going from the heated to the cooled end, in agreement with the results shown in the vertical plane (Fig. 4.7) and from the cooled to the heated end near the side walls (*i.e.*, $y/W = \pm 0.5$). We suspect that much of the flow structure evident in this view (*i.e.*, flow reversal near the side walls) is due to the increase in the liquid depth near the walls caused by capillarity, since the contact angle is quite small.

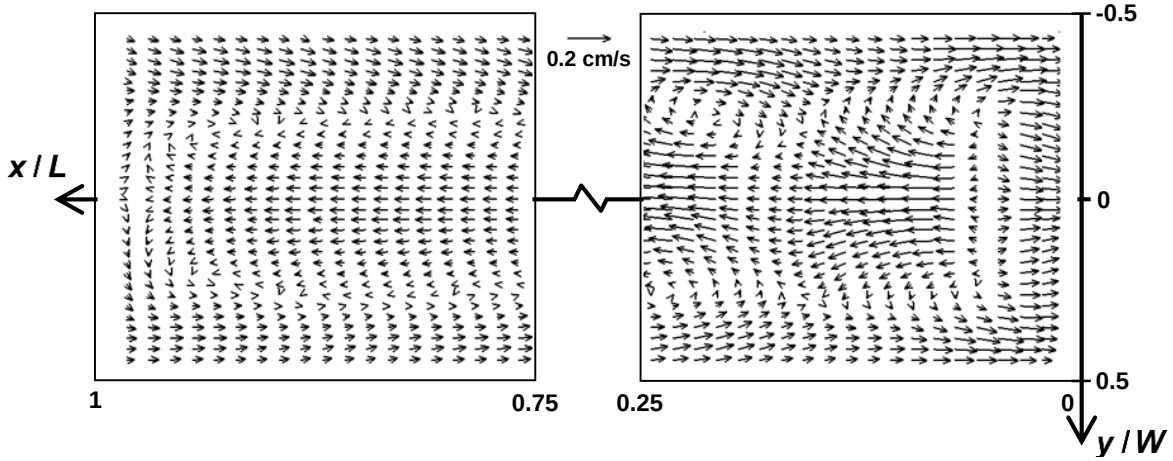

Figure 4.8 The in-plane components of the liquid-phase velocity field in SMC flow for Ma_i = 510 in a horizontal (*x*-*y*) plane at $z/\bar{h}$ = 0.77. Both vector plots have the same velocity scale, given in the center. The maximum velocity magnitudes are 0.08 cm/s and 0.19 cm/s near the cooled and heated ends, respectively.

Although the depth of the liquid layer can be estimated from visualizations of the flow, this estimate is flawed because the glare at the liquid-vapor interface and at the bottom of the test cell due to reflected light (*cf.* Figs. 4.1 and 4.2) makes it difficult to precisely determine their actual locations. We instead estimated the depth of the liquid layer, as well as the interfacial temperature gradient, by curve-fitting the analytical solution for unidirectional return flow in a laterally infinite layer originally obtained by Birikh (1966) and later rederived by Villers and Platten (1987) to the measured profile of the horizontal (x) velocity component u over the depth of the liquid layer in the central section of the flow. Following the notation of Riley and Neitzel (1998):

$$\frac{u(z)}{U_s} = \frac{3}{4}\left(\frac{z}{\bar{h}}\right)^2 - \frac{1}{2}\left(\frac{z}{\bar{h}}\right) + Bo_D\left[-\frac{1}{6}\left(\frac{z}{\bar{h}}\right)^3 + \frac{5}{16}\left(\frac{z}{\bar{h}}\right)^2 - \frac{1}{8}\left(\frac{z}{\bar{h}}\right)\right], \tag{4-1}$$

where $U_s = \gamma \bar{h} \tau_i / \mu$ is the thermocapillary velocity scale.

Our use of this analytical solution describing unicellular flow is based on the observation (supported by a number of numerical and experimental studies) that, for volatile liquid layers under ambient conditions and for sufficiently low ΔT, the interfacial temperature gradient τ_i is constant in the central portion of the flow between the thermal boundary layers that form near the temperature-controlled end walls. An extension of Birikh's analytical solution to the flow in the gas phase shows that the magnitude of the gradient is controlled by diffusion of vapor through air (Qin *et al.* 2014). At higher ΔT, when convection rolls appear, the advection of heat in the liquid layer causes modulation of the interfacial temperature about the linear profile (see, for example, Fig. 10*a* of Riley and Neitzel (1998)). Numerical simulations performed by our group (Qin *et al.* 2015) confirm that the average slope $\bar{\tau}_i$ remains well-defined well above onset of multicellular convection and can be used to describe the average temperature gradient inside the entire liquid layer. Furthermore, a number of linear stability analyses (Chan and Chen, 2010, Mercier and Normand, 1996, Priede and Gerbeth, 29) show that the flow in the liquid can

be described by a sinusoidal perturbation in x about (4-1). The velocity profile averaged along the x direction should therefore still be described by this analytical solution at ΔT even somewhat above the onset of the multicellular state.

These observations enable us to estimate both the average liquid layer thickness $\bar{h}$ and the average interfacial temperature gradient $\bar{\tau}_i$ by comparing the spatially averaged horizontal velocity profiles with the analytical solution (4-1) even for the flows studied here which are not, strictly speaking, unidirectional. For instance, for the flows shown in Figures 4.2 and 4.5 the vertical (z) velocity component w does not vanish due to the presence of convection rolls in the liquid layer. We obtained the mean velocity profile $\bar{u}(z)$ by spatially averaging the horizontal component u over $0.37 \leq x/L \leq 0.62$. The two vertical locations in the liquid layer where $\bar{u} = 0$, corresponding to the z-coordinates of the bottom of the test cell and the location in the bulk of the layer where flow reversal occurs, were determined by linear interpolation, and the roots of Eq. (4-1) were determined numerically to estimate $\bar{h}$ and the dynamic Bond number Bo_D. Finally, $\bar{\tau}_i$ was determined from the curve-fit of $\bar{u}(z)$ to Eq. (4-1) that gave the minimum rms error, and the interfacial Marangoni number Ma_i was calculated based on $\bar{\tau}_i$ and $\bar{h}$.

Figure 4.9 shows the curve-fits to the average measured nondimensional velocity profiles, and compares them to the analytical solution (solid line) given in Eq. (4-1) based on the average Bond number of 0.69 for all the cases in the SUC, PMC and SFC states. The good agreement between the spatially averaged velocity data and the analytical solution suggests this procedure can be successfully used to estimate $\bar{h}$ and $\bar{\tau}_i$. The error bars representing the maximum standard deviation in the velocity data are plotted only for the cases in the SMC state (*i.e.*, Ma_i = 430, 510, and 750), where the velocity data are averaged over multiple cells, resulting in significant spatial variations in u (*cf.* Fig. 4.5). The maximum standard deviations normalized by the velocity at the free surface for Ma_i

= 430, 510 and 750 are 8.1%, 9.4% and 18.4%, respectively, while the average standard deviations over the depth are 2.5%, 3.3% and 9.8% respectively. The maximum standard deviations for all the SUF and PMC cases are less than 3%, or smaller than the size of the symbols.

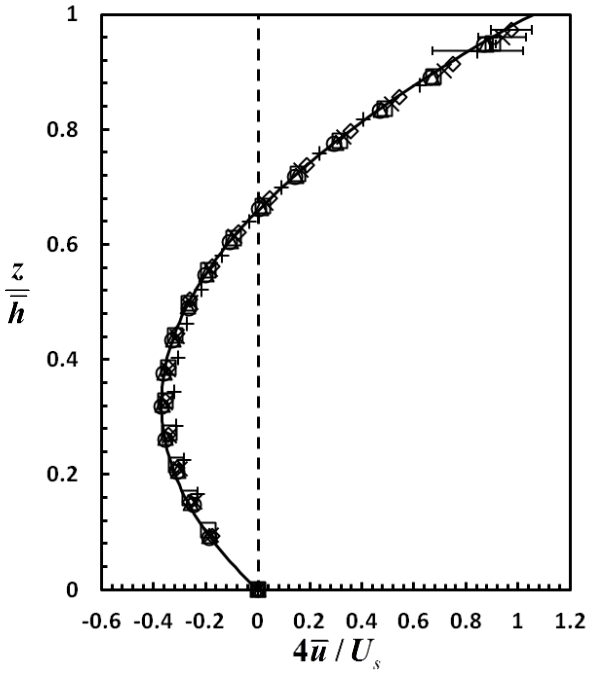

Figure 4.9 Spatially averaged profiles of the normalized *x*-velocity component $4\bar{u}/U_s$ in the liquid layer as a function of the depth normalized by the estimated average liquid layer depth $z/\bar{h}$ for the flows in the SUC, PMC and SMC states at Ma_i = 170 [ΔT = 0.9 ℃] (○), 260 [1.4 ℃] (△), 320 [1.9 ℃] (□), 430 [3.0 ℃] (◇), 510 [3.8 ℃] (×), and 750 (6.5 ℃) (+). The solid curve is the analytical solution for the velocity profile obtained by evaluating Eq. (4-1) at Bo_D = 0.69.

TABLE 4-1 Summary of experimental parameters, and the estimates of Marangoni and Bond numbers based on the curve-fit to Eq. (4-1).

ΔT [℃]	Ma_L	τ_{exp} [℃/cm]	$\bar{\tau}_i$ [℃/cm]	$\bar{h}$ [cm]	$u(\bar{h})$ [cm/s]	Ma_i	Bo_D	State
				c_a = 96%				
0.9	290		0.11	0.263	0.13	170	0.76	SUF
1.4	450		0.17	0.263	0.20	260	0.76	SUF
1.9	620		0.20	0.266	0.24	320	0.78	PMC
3.0	910		0.29	0.256	0.34	430	0.72	SMC
3.8	1190	0.38	0.33	0.260	0.39	510	0.74	SMC
6.5	1880		0.53	0.249	0.60	750	0.68	SMC
7.8	2260		0.56	0.250	0.63	780	0.69	OMC
11.5	3590	0.81	0.66	0.260	0.77	990	0.74	OMC
				c_a = 57%				
2.8	750		0.28	0.240	0.30	370	0.63	SUF
3.9	1050		0.37	0.241	0.39	480	0.64	PMC
6.8	1790		0.52	0.238	0.56	670	0.62	PMC
9.8	2600		0.64	0.239	0.69	830	0.63	SMC
12.5	2960		0.73	0.226	0.73	870	0.56	SMC
				c_a = 36%				
3	870		0.31	0.249	0.35	440	0.68	SUF
3.9	1090		0.37	0.245	0.41	500	0.66	SUF
6	1690		0.50	0.246	0.55	680	0.67	PMC
7.9	2150		0.58	0.242	0.63	770	0.65	PMC
11.6	2910		0.73	0.233	0.75	880	0.59	PMC
				c_a = 14%				
3.9	1340	0.38	0.38	0.273	0.47	630	0.82	SUF
11.6	3420	0.71	0.72	0.252	0.82	1040	0.70	PMC

Table 4-1 summarizes the flow states and parameters obtained from this curve-fitting procedure for all the experimental cases studied. For convection at c_a = 96%, these estimates suggest that the onset of PMC occurs at Ma_i = 320, and the onset of SMC occurs at Ma_i = 430, with the nondimensional wavelength of $\lambda_x / \bar{h} \approx 2.2$. The Table also gives the velocity at the interface $u(\bar{h})$ based on Eq. (4-1). Note that Ma_L is calculated based on $\bar{h}$ = 0.26 cm. For comparison, this Table also includes a limited set of estimates of the interfacial temperature gradient $\tau_{exp} = \Delta T_i / \ell$ based on the temperature difference measured by the thermistors inserted below the free surface ΔT_i and the spacing between these thermistors ℓ = 3.95 cm. These thermistor readings are, however, unlikely to provide a reliable estimate of the interfacial temperature gradient because of the difficulties in accurately positioning the thermistor beads with respect to the free surface, the deviations from linearity in the interfacial temperature profile near the walls (due to thermal boundary layers), and the large temperature gradient in the vertical direction.

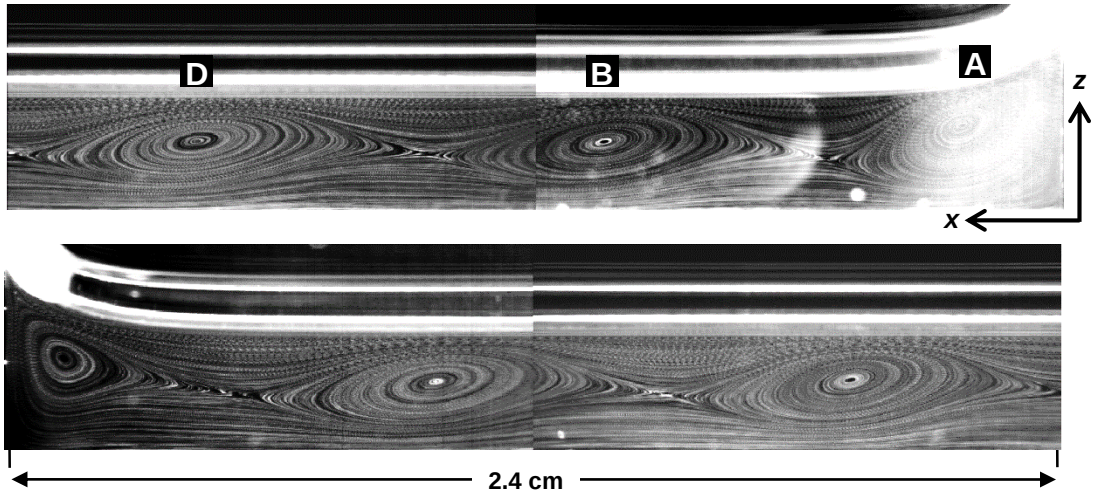

Figure 4.10 Particle pathline visualization of SMC flow in the central vertical (x-z) plane of a $\bar{h}$ = 0.249 cm liquid layer at an estimated Ma_i = 750 [ΔT = 6.5 ℃] over $0 \le x/L \le$ 0.49 next to the heated end [top] and $0.51 \le x/L \le 1$ next to the cooled end [bottom]. The

eight rolls are identified by letter, with roll A immediately adjacent to the heated end [top] on the right and roll H next to the cooled end [bottom] on the left.

As ΔT continues to increase, the flow remains steady and the number of rolls decreases, with six rolls observed at $Ma_i = 750$ ($\Delta T = 6.5$ ℃) (Fig. 4.10). For higher values of ΔT, however, the flow starts to become unsteady, as can be seen in the comparison of particle pathline visualizations shown in Figure 4.11 of a single roll over a quarter of the test cell ($0.51 \leq x/L \leq 0.75$) over $\mathcal{T}_T = 3.9$ s at $\Delta T = 6.5$ ℃ (*a*) and 7.8 ℃ (*b*). This unsteady flow was termed an oscillating multicellular flow (OMC) (Riley and Neitzel, 1998), and PIV results (not shown) give a standard deviation in the velocity magnitude of 10% (of the maximum velocity magnitude). Note that this may actually be an underestimate of the fluctuations, since these PIV data may not temporally resolve the flow in the OMC state.

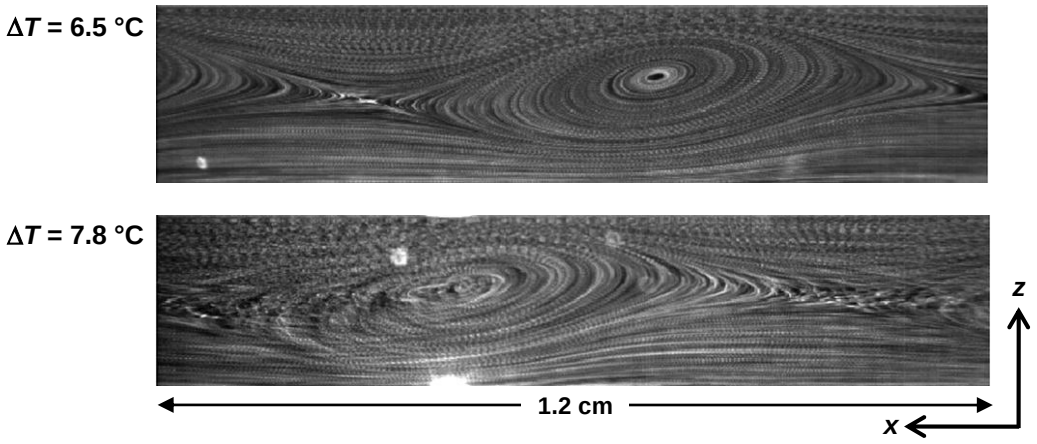

Figure 4.11 Magnified particle pathline visualizations of the flow over about a quarter of the test cell ($0.51 \leq x/L \leq 0.75$) in the central vertical (*x*-*z*) plane at $Ma_i = 750$ [$\Delta T = 6.5$ ℃] [top] and $Ma_i = 780$ ($\Delta T = 7.8$ ℃) [bottom]. Note the blurring of the pathlines at the higher Ma_i.

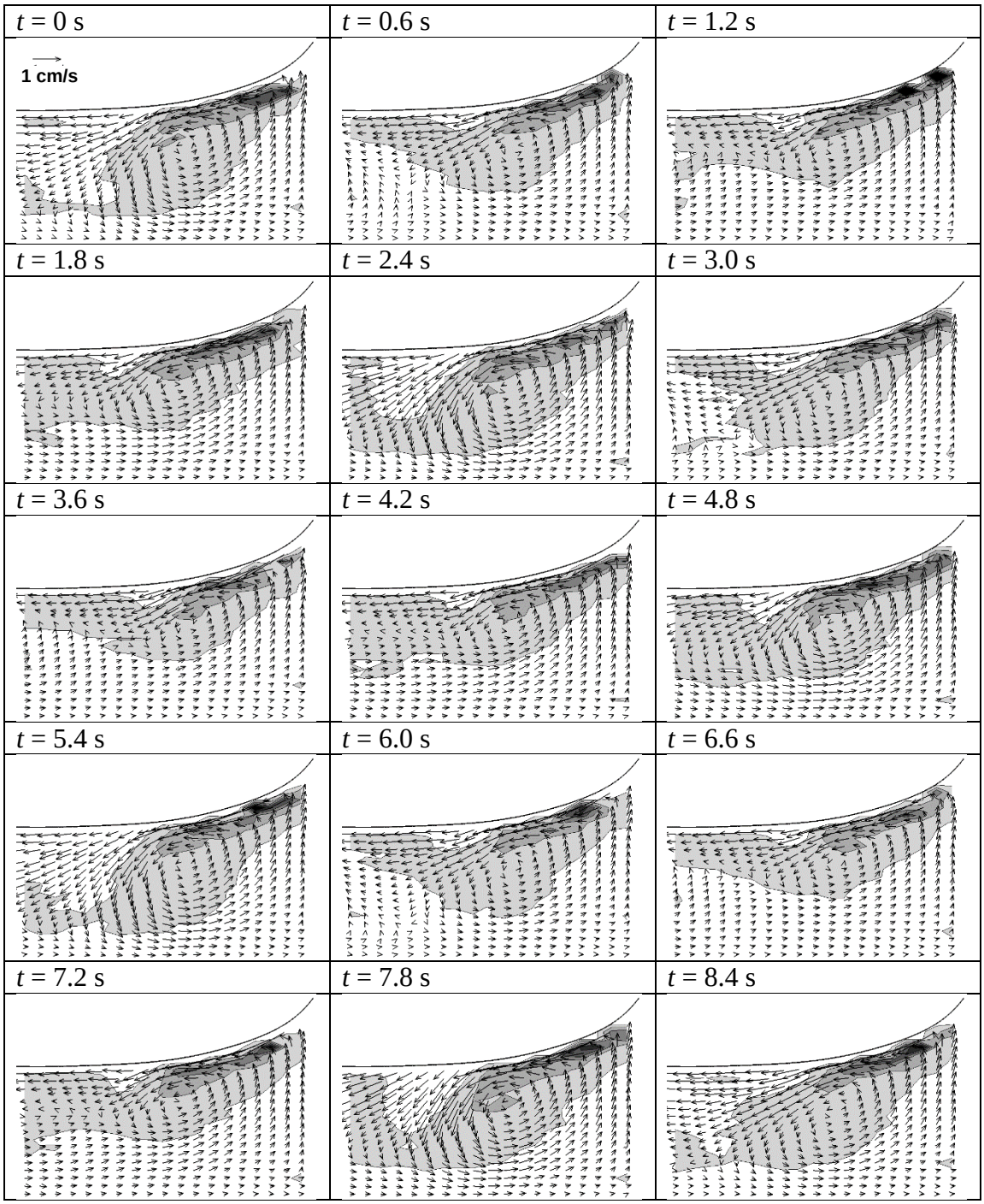

Figure 4.12 Time sequence showing the *y*-component of the vorticity every 0.6 s calculated from the PIV data next to the heated end over $0 \leq x/L \leq 0.12$ at an estimated $Ma_i = 990$ [ΔT = 11.5 ℃] and $Bo_D = 0.74$. The shading denotes the vorticity, with the light gray shade representing 3 $s^{-1} \leq \omega_y \leq 19.2$ s^{-1}, the medium gray shade representing 19.2 $s^{-1} \leq$

$\omega_y \leq 35.4$ s^{-1}, and the dark grey shade representing $\omega_y > 35.4$ s^{-1}. These vorticity contour plots overlay the PIV velocity data, which all have the same velocity scale (given in the image at $t = 0$) with a maximum speed of 2.12 cm/s at $t = 7.8$ s.

Figure 4.12 shows a sequence of "snapshots" of velocity field $\Delta T = 11.5$ ℃ ($T_h = 28.1$ ℃, $T_c = 16.6$ ℃) overlaid with the out-of-plane (y) component of the vorticity ω_y calculated from the PIV data in the vertical (x-z) central plane at $y = 0$ next to the heated end ($0 \leq x/L \leq 0.25$). Here, ω_y was determined using PIV results that were obtained as discussed previously with an overlap of 75% between adjacent interrogation windows from the circulation, calculated using filtered second-order differencing of the eight nearest neighbor velocities (Adrian and Westerweel, 2011).

In this sequence, the roll next to the heated end (*cf.* roll A in Fig. 4.5) appears to oscillate, while the next roll (*cf.* roll B in Fig. 4.5) appears to travel towards the cooled end. In these plots, the free surface is denoted by the uppermost curved line, and the in-plane velocity field, shown by the arrows, is overlaid with a contour plot of ω_y thresholded so that only values of $\omega_y > 3$ s^{-1} (*i.e.*, regions with significant counterclockwise rotation) are shown. The sequence of images starting at $t = 0$ shows the roll next to the heated end; this roll grows in both horizontal and vertical extent with the region where $\omega_y > 3$ s^{-1} reaching its maximum depth around $t = 2.4$ s, where we observe a "pocket" of high-speed, but low-vorticity fluid near the liquid-vapor interface. This pocket is much smaller by $t = 3.0$ s, and the vertical extent of the roll decreases with time until we see a structure at $t = 5.4$ s very similar to that at the beginning of this sequence, or $t = 0$. Although not shown here, this oscillation in the height of this roll, represented here by the region where $\omega_y > 3$ s^{-1}, is observed over several periods during the total PIV data acquisition time of 60 s.

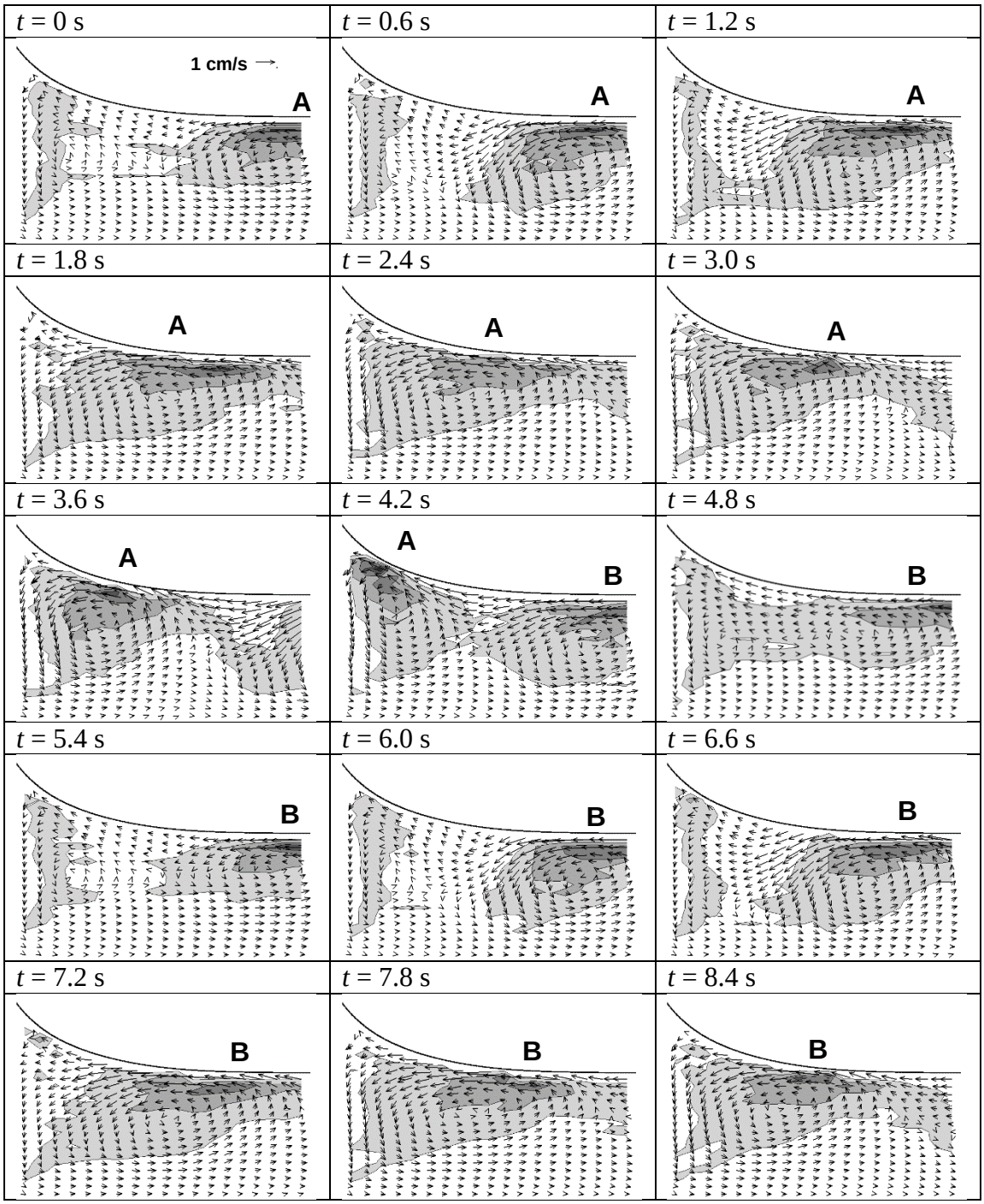

Figure 4.13 Similar to the previous Figure, but for the flow next to the cooled end over $0.88 \leq x/L \leq 1$. Each roll is labeled by a letter above its region of highest ω_y. The shading denotes the vorticity, with the light gray shade representing $3\ s^{-1} \leq \omega_y \leq 10.8\ s^{-1}$, the medium gray shade representing $10.8\ s^{-1} \leq \omega_y \leq 18.6\ s^{-1}$, and the dark grey shade

representing ω_y > 18.6 s^{-1}. The out-of-plane vorticity component overlays the PIV velocity data, which all have the same scale (given in the inset of the image at t = 0); the maximum speed is 1.13 cm/s at t = 6.0 s.

Figure 4.13 shows a similar sequence of ω_y "snapshots" in the vertical (x-z) central plane at y = 0 next to the cooled end ($0.75 \leq x/L \leq 1$) for the same flow. No oscillatory behavior is observed near the cooled end, with rolls instead traveling to the left, or towards the cooled end. Starting at t = 0, a roll (A), represented here by the region where ω_y > 3 s^{-1}, enters on the right side and travels towards the cooled end, becoming more elongated and reaching the cooled wall by t = 4.2 s, when the second roll in the pair (B) enters on the right side. Roll B then travels towards the cooled end, with the high-vorticity "core" of roll A no longer evident by t = 4.8 s, and by t = 6.6 s, the position of roll B looks much like that of roll A at t = 1.2 s. This sequence suggests that the interval between successive rolls, based on when they enter on the right side of this field of view, is about 5.4 s, in agreement with the period observed in the sequence near the heated end in the previous Figure.

Figure 4.14 plots interfacial temperature readings over 30 s from glass-sealed thermistors (Honeywell 111-103EAJ-H01, with bead dia. 0.036 cm and accuracy of 0.1 ℃) 0.028 cm below the interface near the cooled [left] and heated [right] ends at $x/L \approx$ 0.11 and 0.92, respectively, from another realization of the flow under the same conditions. Unfortunately, difficulties in reproducibly locating the thermistors, which were inserted through the two test cell ports on flexible wires >7 cm in length before evacuating the test cell (and hence before knowing the location of the free surface), made it impractical to do more than monitor temperatures near the interface with this approach.

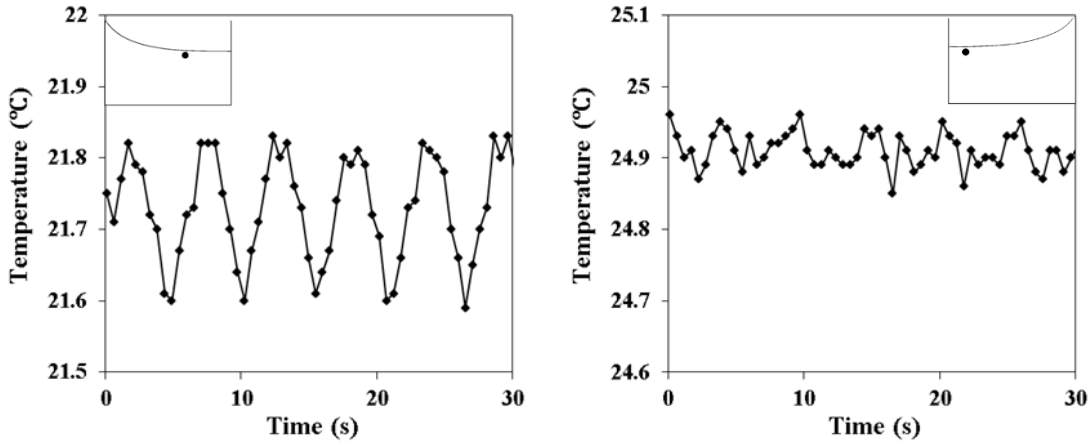

Figure 4.14 The variation in temperature over time near the cooled [left] and heated [right] ends for the flow shown in Figures 4.12 and 4.13 at $Ma_i = 990$ [$\Delta T = 11.5$ ℃]. The actual temperature readings are given by the symbols, and the lines connecting the data points are provided as a visual guide. Note that the extent of the vertical axis (0.5 ℃) is the same for both plots. The insets in the upper outer corners of each plot show the position of the thermistors as black dots with respect to the cooled and heated ends and the liquid-vapor interface.

Near the cooled end ($x / L = 0.92$, *cf.* inset), the interfacial temperature has marked oscillations with a peak-to-peak amplitude of about 0.3 ℃. An FFT of these temperature data gives a strong peak at a frequency of 0.177 Hz, corresponding to an oscillation period of 5.6 s, in agreement with the observations near the cooled end in Figure 4.13. The temperature near the heated end ($x / L = 0.11$, *cf.* inset) also appears to have weak fluctuations, but their amplitude is comparable to the measurement accuracy, and the fluctuations appear to be less periodic than those observed near the cooled end, although an FFT of these data also has a distinct peak at a frequency of 0.177 Hz, in agreement with the observations from Figure 4.12.

The strongly time-oscillatory behavior observed in the temperature here at a single point near the free surface in Figure 4.14 [left] is qualitatively similar to that observed in

the single-point LDV measurements by the work of De Saedeleer (1996) and Villers and Platten (1992) and qualitatively similar oscillatory behavior is also observed in the velocities measured using PIV (admittedly obtained at much lower sampling frequencies and at significantly coarser spatial resolution than the LDV measurements) at the same location, as shown in Figure 4.15.

Surprisingly, the curve-fitting procedure used to estimate $\bar{h}$ and $\bar{\tau}_i$ for the steady flow states appears to work reasonably well for the spatially and temporally averaged velocity data in the OMC state as well, as shown in Figure 4.16. Estimates of $\bar{h}$, $\bar{\tau}_i$, Ma_i and Bo_D are therefore also given in Table 4-1 (for c_a= 96%). Based on these estimates of the interfacial Marangoni number, the onset of time-dependent flow appears to occur at a critical Ma_i between 750 and 780, and $\bar{h}$ = 0.260 cm. These estimates also give Ma_i = 990 and Bo_D = 0.74 for the flow shown in Figures 4.12–4.15.

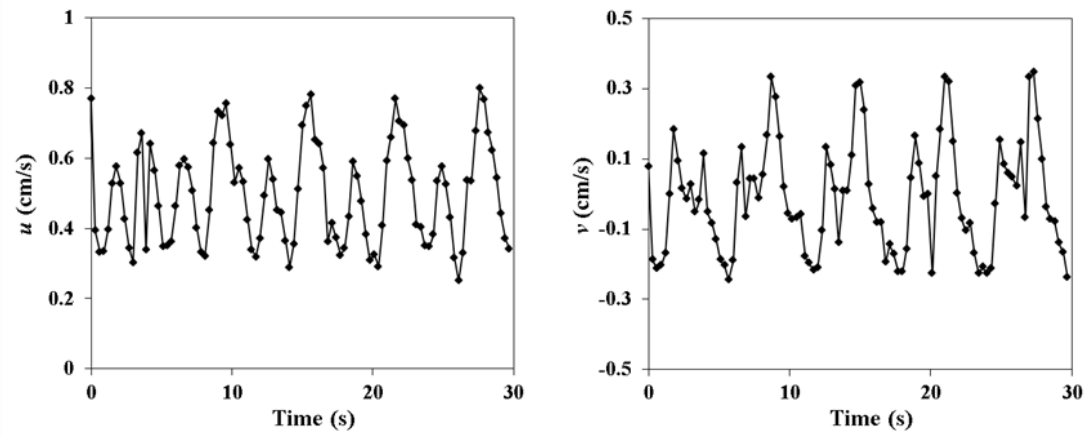

Figure 4.15 Graphs showing *u* [left] and *v* [right], the velocity components along *x* and *y*, respectively, as a function of time for the same flow at Ma_i = 990 [ΔT = 11.5 ℃] just below the liquid-vapor interface at x/L = 0.92, corresponding to the location of the temperature data given in Figure 4.14 [left]. Again, the actual velocities are given by the symbols, and the lines are a visual guide.

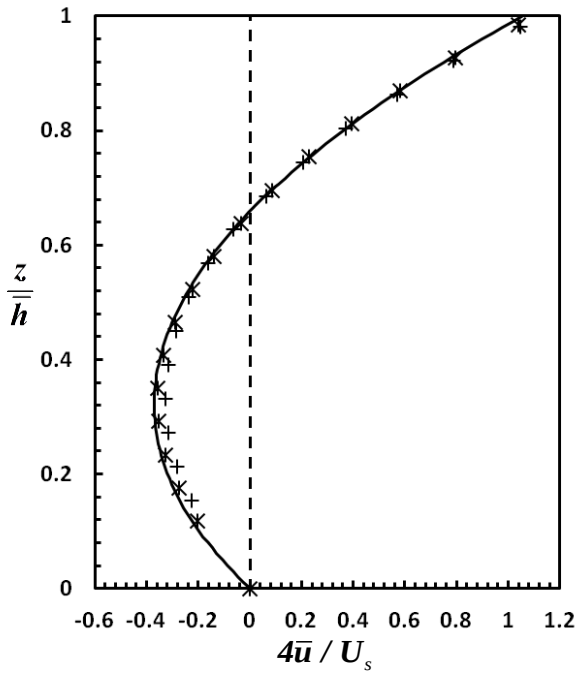

Figure 4.16 Similar to Figure 4.9, but for the OMC cases at Ma_i = 780 [ΔT = 7.8 ℃] (+) and 990 [11.5 ℃] (∗).

4.1.2 Convection at c_a = 57% and 36%

Buoyancy-thermocapillary convection was also studied under a vapor space containing 57% and 36% air under otherwise similar conditions. Flow visualizations (not shown here) for these "intermediate" air concentrations over a similar range of ΔT (Table 4-1) show that reducing c_a (and the pressure) in the vapor space affects the stability of the flow, and increases the critical Marangoni numbers for the onset of different flow states. At c_a = 57%, the flow transitions from the SUF to PMC to SMC states as ΔT increases; the OMC state is not observed at even the highest ΔT value of 12.5 ℃ (Ma_i = 870). At c_a = 36%, the flow only transitions from the SUF to PMC states, and neither SMC nor OMC flow is observed for $\Delta T \leq$ 11.6 ℃ (Ma_i = 880).

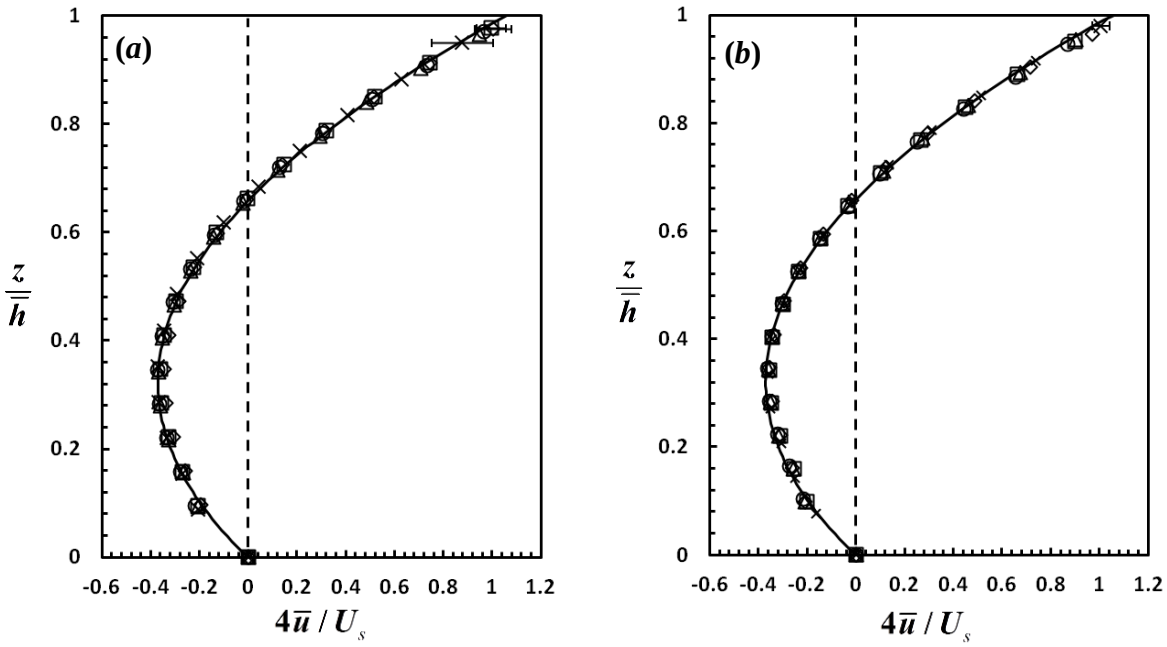

Figure 4.17 Similar to Figure 4.9, but for the c_a = 57% case (*a*) at Ma_i = 370 [ΔT = 2.8 ℃] (○), 480 [3.9 ℃] (△), 670 [6.8 ℃] (□), 830 [9.8 ℃] (◇) and 870 [12.5 ℃] (×); and c_a = 36% (*b*) at Ma_i = 440 [ΔT = 3.0 ℃] (○), 500 [3.9 ℃] (△), 680 [6.0 ℃] (□), 770 [7.9 ℃] (◇) and 880 [11.6 ℃] (×).

Figures 4.17*a* and 4.17*b* compare $\overline{u}(z)$ (*i.e.*, the velocity component spatially averaged over $0.37 \leq x/L \leq 0.62$) with that given by Eq. (4-1) at the average Bo_D = 0.69 for c_a = 57% and 36%, respectively. The experimentally measured profiles and the analytical solution are also in good agreement at these lower c_a, and estimates of $\overline{h}$, $\overline{\tau}_i$, Ma_i and Bo_D are also given in Table 4-1. The error bars again represent the maximum standard deviations in the spatially averaged velocity, which occurs near the free surface. For c_a = 57%, the maximum standard deviations normalized by the velocity at the free surface at Ma_i = 670, 830 and 870 are 5.9%, 7.6% and 12.2%, respectively (Fig. 4.14*a*), with average standard deviations of 2.9%, 4.2% and 8.1%, respectively. For c_a = 36%, the

maximum and average standard deviations at Ma_i = 880 are 3.4% and 1.9%, respectively. For all other cases, the maximum standard deviations are again smaller than the symbols.

4.1.3 Convection at c_a = 14%

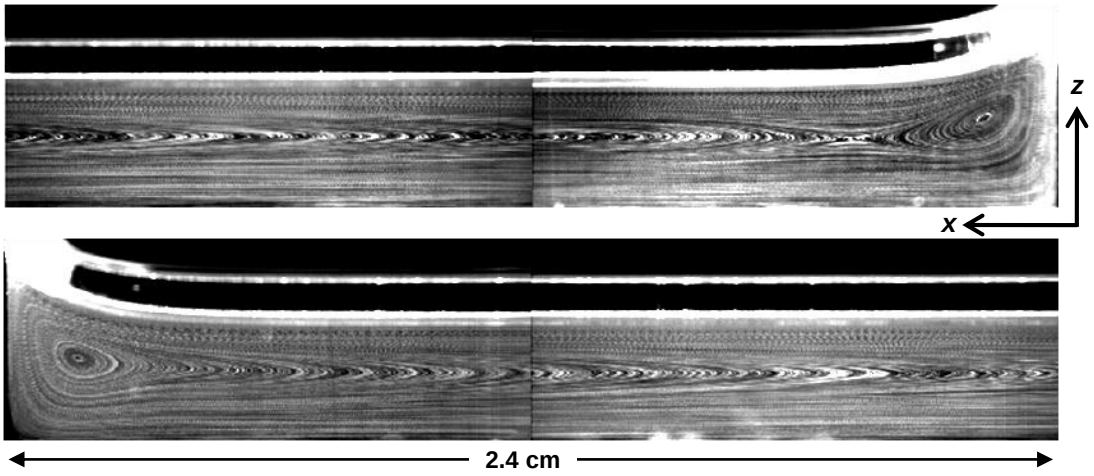

Figure 4.18 Particle pathline visualization of the flow in the central vertical (x-z) plane of a liquid layer with an estimated average depth $\bar{h}$ = 0.263 cm at an estimated Ma_i = 630 [ΔT = 3.9 ℃] and Bo_D = 0.82 for $0 \le x/L \le 0.49$ next to the heated end [top] and $0.51 \le x/L \le 1$ next to the cooled end [bottom].

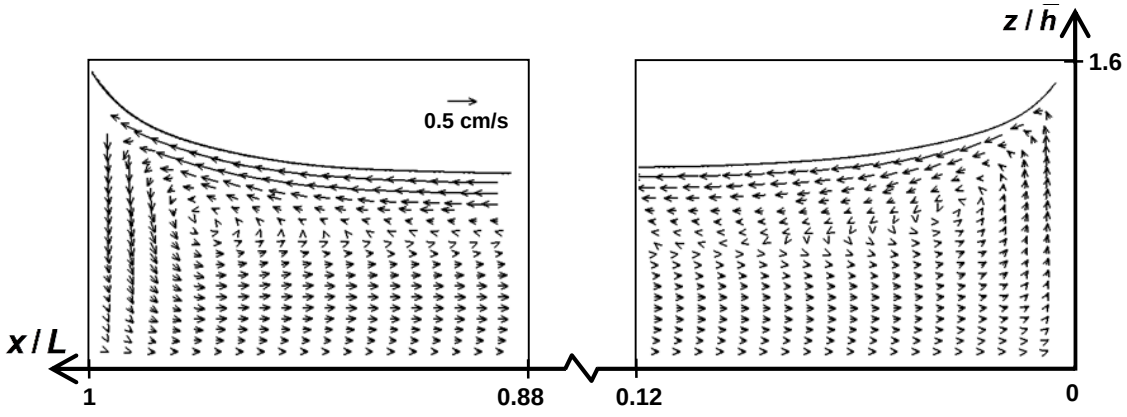

Figure 4.19 The velocity field for the same flow in the central vertical (x-z) plane next to the cooled end over $0.88 \le x/L \le 1$ [left], and next to the heated end over $0 \le x/L \le 0.12$

[left]. The maximum velocity magnitudes, which occur just below the free surface, are 0.61 cm/s and 0.43 cm/s near the cooled and heated ends, respectively.

The lowest noncondensables fraction that could be achieved in these experiments was about 14 mol%. Figure 4.18 shows a particle pathline visualization of buoyancy-thermocapillary convection at c_a = 14% over the entire liquid layer (except for $0.49 \leq x/L \leq 0.51$) at ΔT = 3.9 ℃. The flow, with a small roll next to the heated end and a large roll occupying the rest of the liquid layer is typical of SUF. Figure 4.19 shows the average liquid-phase velocity field in the central vertical (x–z) plane of the flow at y = 0 near the heated end ($0 \leq x/L \leq 0.12$) [right], and near the cooled end ($0.88 \leq x/L \leq 1$) [left] of the test cell for this case. At the maximum temperature difference studied, ΔT = 11.6 ℃, the flow is still in the PMC state, with the large roll having only "split" off a single roll, B (Figure 4.20), suggesting that the flow is just past the SUF/PMC threshold.

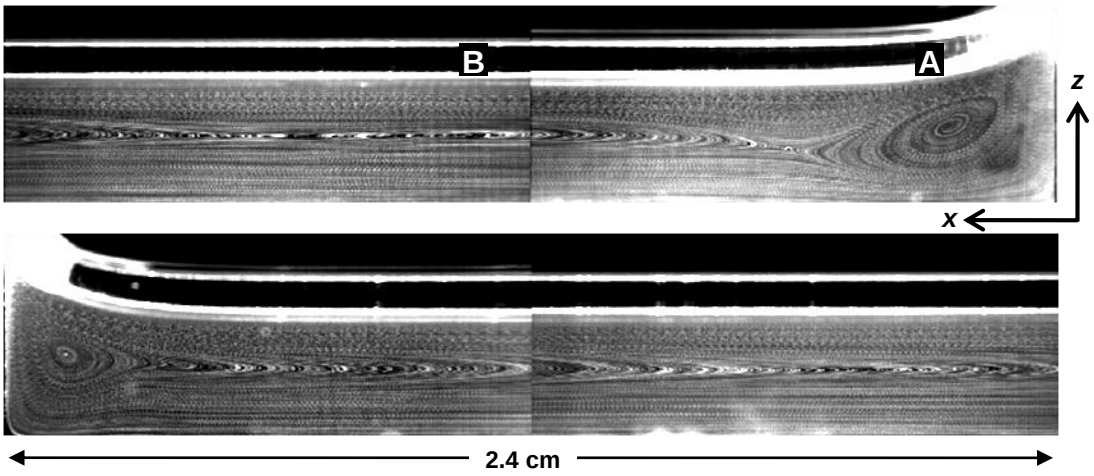

Figure 4.20 Particle pathline visualization of the flow in the central vertical (x-z) plane for c_a = 14% at an estimated Ma_i = 1040 [ΔT = 11.6 ℃] and Bo_D = 0.70, over $0 \leq x/L \leq 0.49$ next to the heated end [top] and $0.51 \leq x/L \leq 1$ next to the cooled end [bottom].

Figure 4.21 compares $\bar{u}(z)$ with the analytical solution at Bo_D = 0.69. The average velocity profiles and the analytical solution are in good agreement, as was the case at higher

c_a. Estimates for flow parameters obtained using the procedure described earlier are therefore also included in Table 4-1 for c_a = 14%. No error bars are shown on this plot because the maximum and average standard deviations in the velocity data are smaller than the symbols in all cases.

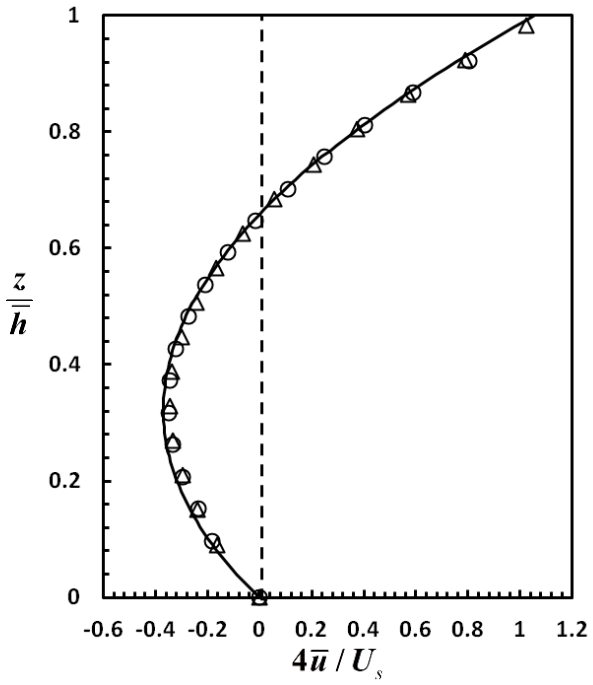

Figure 4.21 Nondimensional velocity profiles in the liquid layer $4\bar{u}/U_s$ as a function of $z/\bar{h}$ measured using PIV for c_a = 14% compared with the analytical solution for Bo_D = 0.69 at Ma_i = 630 [ΔT = 3.9 ℃] (○) and 1040 [ΔT = 11.6 ℃] (△).

4.2 Discussion

4.2.1 Convection at c_a = 96%

Our results for convection under a vapor space dominated by air at p = 101 kPa are in qualitative agreement with previous experimental studies of buoyancy-thermocapillary convection at ambient conditions and $\Gamma_y < 6$ where transverse confinement is significant (summarized by Burguete *et al.* (2001)). To our knowledge, the only experimental studies of convection in nonisothermal liquid layers where thermocapillarity, buoyancy, and

transverse confinement are significant are by De saedeleer *et al.* 1996, Braunsfurth and Homsy, 1997, Villers and Platten, 1992 and Garcimartín *et al.* 1997). The earliest study was that by Villers and Platten (1992), who measured velocity profiles in h = 0.175–1.425 cm deep acetone (Pr = 4.2) layers of dimensions L = 3 cm and W = 1 cm and compared their results with numerical simulations. They reported that the flow transitioned from a unicellular steady state to a multicellular steady state to a time-dependent flow as the Marangoni number increased. The results presented here clearly follow the same sequence, with the transition from the SUF to PMC states occurring at a critical $Ma_{\mathrm{i}} \approx 320$ for Bo_{D} = 0.78, transition from PMC to SMC states occurring at $Ma_{\mathrm{i}} \approx 430$ for $Bo_{\mathrm{D}} = 0.72$, and the transition from the SMC to OMC states occurring at a Ma_{i} between 750 and 780 for $Bo_{\mathrm{D}} = 0.69$. Villers and Platten (1992) termed the time-dependent flow state at high Marangoni numbers "oscillatory convection," and showed that the variation in the measured x-component of velocity was time-periodic. Their numerical simulations showed that a new vortex is created near the hot wall and then travels about half way to the cold wall, in the direction opposite to that of the hydrothermal waves, after which it dissipates and the process repeats. The authors reported that they "never observe travelling waves with the appearance of rolls near one wall and the corresponding disappearance near the opposite wall." Their numerical results are consistent with our observations only near the hot wall. Near the cold wall, however, we find that the waves are travelling towards the cold wall. This difference is likely due to the larger streamwise aspect ratio of the present studies, $\Gamma_x = 20$, *vs.* the $\Gamma_x = 9$ considered by Villers and Platten (1992). The numerical simulations of a two-sided model performed by our collaborators for $\Gamma_x = 19.8$ produce OMC states that are very similar to the experimental observations near both end walls (Qin *et al.* 2014)

In a subsequent study, De Saedeleer *et al.* (1996) also measured velocity profiles in h = 0.25–0.47 cm deep layers of decane (Pr = 15) with L = 7.4 cm and W = 1 cm, and also

reported transition from a steady unicellular flow to steady multicells (which they attributed to confinement) to time-periodic flow as the temperature gradient, and hence Marangoni number, increased. They showed that the horizontal (x) and vertical (z) velocity components had the same period for the time-periodic flow state, but did not further study this flow state because of the limitations of LDV, which "is not very well suited to perform measurements of a rapidly changing velocity pattern" because it measures (usually a single component of) the velocity at a single point.

Garcimart ń *et al.* (1997) visualized the temperature field using interferometry and the flow using shadowgraphy in L = 7 cm, W = 1 cm and h = 0.2–0.35 cm deep layers of decane and 0.65 and 2.0 cSt ($Pr \approx 10$ and 30, respectively) silicone oils. By imaging the entire flow, they showed that the time-dependence was associated with oscillation of the roll nearest the heated end combined with the adjacent roll traveling towards the cooled end, and noted that similar waves traveling towards the cooled end were also observed in the experiments of Ezersky *et al.* (1993) with 5.0 cSt silicone oil, albeit in a cylindrical geometry. They suggested that these "waves propagating from the hot side to the cold side" were due to an instability of the thermal boundary layer *along the hot wall*, with the perturbations due to the oscillations of the roll next to the heated end amplified and convected towards the cooled end.

Our PIV results further quantify the phenomena reported by Garcimartín *et al.* (1997) in terms of the velocity field. The observed period can be compared with the recirculation times for roll A, *i.e.*, the roll immediately adjacent to the heated end, which can be computed by integrating the inverse of the speed along the streamlines of the time-averaged flow reconstructed from the PIV data. We find that the period matches the recirculation time for the streamlines that lie at the periphery of the roll (Fig. 4.22). These streamlines are much closer to the free surface, with a minimum distance of about 0.02 cm, than they are to the hot wall, with a minimum distance of about 0.1 cm. This suggests that the instability is likely driven by the jet of rapidly moving hot fluid at the free surface,

rather than the vertical thermal boundary layer forming at the hot wall, as was suggested by Garcimartín *et al.* A more likely mechanism for this instability is due to the momentum transfer between the free surface and the interior of the convection roll. We conjecture that an increase of the temperature gradient $\overline{\tau}_i$ at the free surface near the hot wall leads to an increase in the thermocapillary stresses which accelerate the hot interfacial jet, whose momentum is gradually transferred to the convection roll. The enhanced advection of heat flattens the temperature gradient at the free surface, reducing the thermocapillary stresses, slowing the interfacial hot jet and, subsequently, the recirculation in the convection roll. This eventually leads to an increase of the temperature gradient and a new cycle. Since the extrema in the velocity of the liquid at the free surface and inside the convection roll are out of phase, the cycle can repeat indefinitely, if the time required for the thermal disturbances to travel around the convection roll is the same as the period of the momentum transfer.

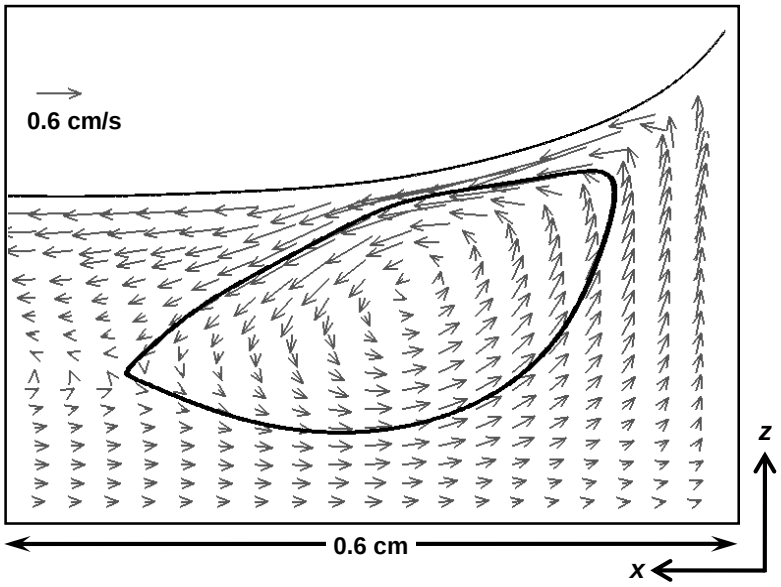

Figure 4.22 A streamline calculated from the time-averaged velocity vectors (also shown) of Figure 4.12 for convection at c_a = 96% and an estimated Ma_i = 990 [ΔT = 11.5 ℃] over $0 \leq x/L \leq 0.12$ corresponding to the periphery of the counterclockwise roll immediately

next to the heated end. The curved line indicates the free surface. The recirculation time for the streamline is estimated to be 5.2 s.

While our experimental results are in qualitative agreement with other experimental and numerical studies of buoyancy-thermocapillary convection in the limit of $Bo_D = O(1)$ (*i.e.*, when buoyancy is non-negligible), there are definite quantitative differences. Unfortunately, none of the previous experimental studies have clearly defined the threshold between the SUF and SMC states; as the results presented here show, the transition from unicellular to steady multicellular flow is gradual and involves an intermediate state (PMC), which exists over a reasonably broad range of Ma_i and features between three and eight convection cells that do not fill the entire liquid layer. Transition to SMC eventually takes place at a critical Marangoni number $Ma_i = 430$ (at $Bo_D = 0.72$) when nine convection cells do fill the entire layer.

This is lower than the critical $Ma_i = 482$ found by Riley and Neitzel (1998) at $Bo_D = 0.72$. The discrepancy is most likely due to the difference in the Prandtl number of the liquids ($Pr = 9.2$ for HMDS, compared with $Pr = 13.9$ for the higher-viscosity silicone oil used by Riley and Neitzel). As the linear stability analysis of Priede and Gerbeth (1997) showed, Ma_i increases with Pr (for Pr above ~1). Another difference between the two experiments is the (transverse) aspect ratio Γ_y, which was much larger for Riley and Neitzel than that studied here, although the flow structure was essentially two-dimensional in both studies, so it seems unlikely that transverse confinement would significantly affect either the structure of the flow or its stability.

Unfortunately, there are also remarkably few theoretical studies that can be used for quantitative comparison. While the numerical simulations (Villers and Platten, 1992, Shevtsova *et al.* 2003, Ben Hadid and Roux, 1992) suggest, in agreement with experiments, that the unicellular flow transitions to a steady multicellular flow at $Bo_D = O(1)$, their

predictions are based on one-sided 2D models which ignore transport in the gas phase as well as phase change and use different values of Bo_D and *Pr*. The numerical study (also 2D) by our collaborators finds that the transition from SUF to PMC for Bo_D = 0.70 and *Pr* = 9.2 occurs at Ma_i between 302 and 394, and that from PMC to SMC occurs at Ma_i between 541 and 602 (Qin *et al.* 2014).

Numerical simulations also suggest that the critical Ma_i is likely to be quite insensitive to the curvature of the free surface near the end walls. The numerical results for a wide range of contact angles show the curvature of the free surface near the end walls has a very small effect not only on the heat transfer, but also on the flow regime (Qin *et al.* 2014). On the other hand, the curvature near the side walls (*e.g.* 3D effects) could play a significant role. Our observations based on sessile drop visualizations suggest that the contact angle of HMDS on fused silica is very small, less than 10°. As a result, the thickness of the liquid layer near the side walls is estimated to be greater by about 40% compared to the average thickness $\bar{h}$, which would effectively double the values of Bo_D and Ma_i.

The theoretical studies which used linear stability analysis for an unbounded liquid layer (Chen and Chan, 2010, Parmentier *et al.* 1993) predict transition to an oscillatory instability at all values of Bo_D, with convection rolls traveling from the cold to the hot wall for smaller Bo_D and in the opposite direction for larger Bo_D. Mercier and Normand (1998) showed that transition to the SMC state is possible in the presence of a strong vertical heat flux (*i.e.*, non-zero Biot number *Bi*), which is not the case for our experimental setup. The only (to our knowledge) linear stability study that predicts a transition towards a stationary multicellular state for adiabatic boundary conditions is due to Priede and Gerbeth (1997) who argued that the end walls play a very important role. Indeed, in a bounded system (finite Γ_x), disturbances that would be amplified as a result of an

oscillatory instability are swept to one of the end walls before they can grow sufficiently to be observed. Their calculations predict the onset of steady multicellular flow to occur at $Ma_i = 540$ for $Bo_D = 0.75$ and $Pr = 13.9$, which is slightly higher than the value found by Riley and Neitzel (1998).

Transition from the SMC to the OMC states in our system occurs at the laboratory Marangoni number $Ma_L \approx 2100$ which is also lower than the value $Ma_L < 3800$ found by Villers and Platten (1992) at $Bo_D = 0.7$ in acetone (no estimate of Ma_i is possible since τ_i was not measured in these studies). This discrepancy is likely also be due to differences in Prandtl number (the silicone oil used here has *Pr* that is more than twice that of acetone, with $Pr = 4.2$).

4.2.2 Effect of Noncondensables

The present study is, to our knowledge, the first to investigate how changing the relative concentration of noncondensables in the vapor space affects buoyancy-thermocapillary convection. Figure 4.23 summarizes the flow state observations at c_a = 14% (*filled black*), 36% (*open black*), 57% (*filled gray*), and 96% (*open gray symbols*) on a $Ma_i - c_a$ flow regime map. Noncondensables have a very pronounced effect on the stability of the different flow states. As c_a is decreased, all of the transition thresholds increase monotonically. In fact, some of the states disappear completely at lower values of c_a. In particular, unsteady (OMC) flow is only observed at c_a = 96% here, and SMC flow is only observed at c_a = 57% and 96%.

These experimental observations are consistent with the results of parallel numerical studies (Qin *et al.* 2014, Qin *et al.* 2015 and Qin and Grigoriev, 2014), which also show that lowering c_a increases the critical Marangoni number for all the transitions. The predicted interfacial flow velocity for the base flow (SUF) is also in reasonable agreement with experimental observations. In the experiments, we find that the flow speeds

near the interface and the estimates of τ_i remain essentially independent of c_a over the range from 14% to 96%, which suggests that the thermocapillary stresses remain essentially constant (at a fixed ΔT) until c_a decreases to even lower values. For example, at ΔT = 3.8–3.9 ℃ (when the flow is steady in all cases), the velocity at the interface $u(\bar{h})$ varies from 0.39 cm/s to 0.47 m/s, and τ_i varies from 0.33 to 0.38 ℃/cm (Table 4-1). Similarly, the numerical simulations predict that τ_i decreases only slightly (by about 18%) as c_a is reduced from 96% to 16% for ΔT = 10 ℃ (Qin *et al.* 2014). As shown in Ref. (Qin *et al.* 2015), the interfacial temperature is essentially equal to the saturation temperature, which is a function of the local concentrations of air and vapor. As long as c_a is not too small (at least ~8%, according to Qin *et al.* (2014), the gradient in the relative concentration of the two components (and hence partial pressure and saturation temperature) persists, and τ_i remains essentially independent of c_a, in agreement with these experimental results.

The observation that the critical Ma_i for transition to the PMC and SMC states increases as c_a decreases is also consistent with the related experimental study by Barthes *et al*. (2007), who explored the dynamics of bubbles forming in liquids with and without dissolved gases and found that the bubbles grew steadily in degassed liquids, but developed oscillations in liquids with dissolved gases. Although the study did not report the relative fraction of noncondensables, the oscillations were attributed to the enhancement of thermocapillary stresses by noncondensable gases inside the bubble; these stresses, of course, effectively disappear in the absence of noncondensables.

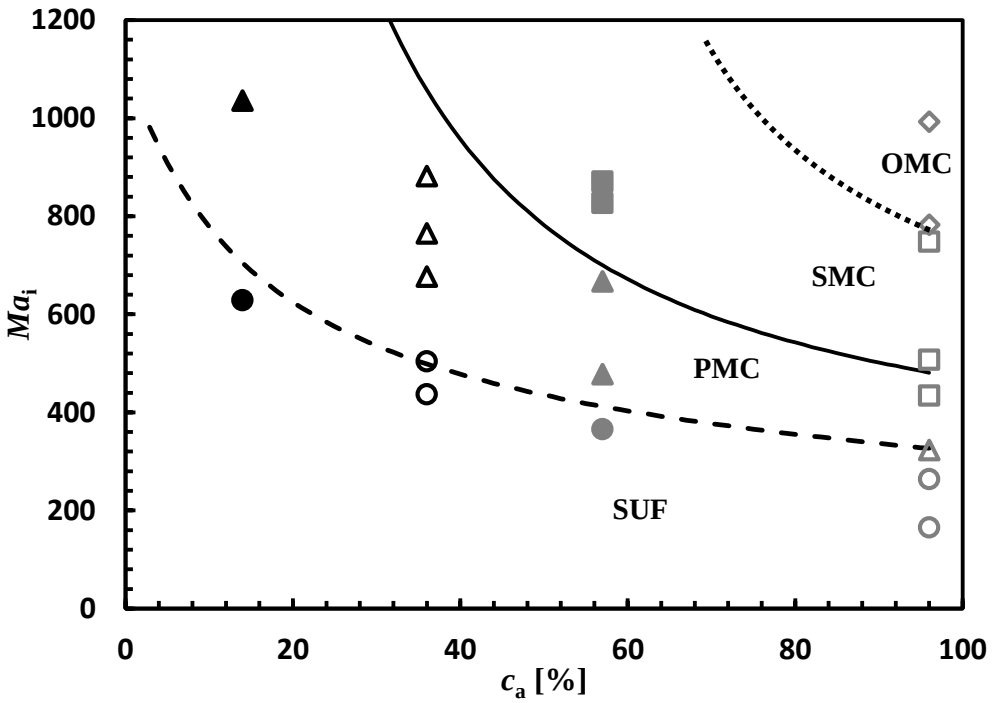

Figure 4.23 Flow regime map showing Ma_i as a function of c_a for buoyancy-thermocapillary convection at c_a = 14% (*filled black*); 36% (*open black)*; 57% (*filled grey*); and 96% (*open grey*). The type of symbol denotes the actual flow state: SUF (*circles*); PMC (*triangles*); SMC (*squares*); and OMC (*diamonds*). The thresholds predicted by linear stability are shown as a dashed line (PMC) and solid line (SMC). The dotted line is a sketch of the boundary between SMC and OMC states based on experimental data.

In order to gain a better understanding of how the presence of noncondensables affects the flow stability, linear stability calculations similar to those by Priede and Gerbeth (1997) and Mercier and Normand (2002) were performed by our collaborator Dr. Grigoriev at $Bo_D = 0.72$ and $Pr = 9.2$ using the expression for a wavenumber-dependent Biot number derived by Chauvet *et al.* (2012). The dependence of *Bi* on the composition of the gas phase can be obtained in explicit form using Clausius-Clapeyron equation:

$$Bi = q_s \bar{h} \left[\frac{c_a k_a + (1-c_a) k_v}{k_l} + \frac{1-c_a}{c_a} \left(\frac{h_{fg}}{R_v T_0} \right)^2 \frac{D_0 p_0}{k_l T_0} \right], \tag{4-2}$$

where k_a, k_v and k_l are thermal conductivities, D_0 is binary diffusion coefficient, R is specific gas constant, p is the total pressure, h_{fg} is latent heat of vaporization, and the subscripts indicate air (*a*), liquid (*l*), vapor (*v*), and reference, *i.e.*, ambient, conditions (0). The analysis is based on solving a boundary-value problem involving two coupled partial differential equations for perturbations, relative to the base solution (4-1), of the temperature $\theta_s(x,z,t) = \Theta_s(z)\exp\{\alpha_s t - i q_s x\}$ and stream function $\psi_s(x,z,t) = \Psi_s(z)\exp\{\alpha_s t - i q_s x\}$ in the liquid layer. The boundary-value problem defines both the vertical profiles $\Theta_s(z)$ and $\Psi_s(z)$ of the perturbations and the growth rate $\alpha_s = \beta_s + i\omega_s$ as a function of the (complex) wavenumber $q_s = \kappa_s + i s_s$ and all of the nondimensional parameters. The asymptotic amplitude of the perturbations is determined by the strength of convection cell A that exists for all ΔT near the hot wall and the value of *s* defines the spatial attenuation of the perturbation (or the number of convection cells). The threshold values of Ma_i and the wavenumber $\kappa_s = 2\pi/\lambda_x$ are found by requiring the perturbation to be critical (*i.e.*, $\beta_s = 0$) and stationary (*i.e.*, $\omega_s = 0$). The solutions of the boundary value problem were found using Matlab 2013a® (specifically, the function bvp5c) and validated by reproducing the data of Priede and Gerbeth (1997) for the Pr = 13.9 silicone oil (with $Bi = 0$ and $s_s = 0$).

As shown in Figure 4.23, linear stability gives reasonable predictions for the critical Ma_i for transitions from SUF to PMC (which corresponds to $s_s = (\bar{h})^{-1}$) and from PMC to SMC (which corresponds to $s_s = (\Gamma_x \bar{h})^{-1}$) in the entire range of c_a considered here. It should be noted, however, that the analysis of Chauvet *et al.* (2012) on which the expression (4-2) is based accounts for the diffusion of heat and vapor in the gas phase, but ignores advection, so perfect agreement is not expected. For instance, at atmospheric

conditions, the critical wavenumber $\lambda_x / \bar{h} = 1.86$ predicted by linear stability analysis for the threshold of SMC is lower, while the critical Ma_i = 481 is higher than the values found experimentally (respectively, 2.2 and 430).

The linear stability calculations showed that the critical Ma_i is very weakly dependent on Bo_D over the limited range of (estimated) values studied here ($0.56 \leq Bo_D \leq 0.82$). Indeed, at $Bo_D = O(1)$ and c_a exceeding ~4%, thermocapillary stresses are significantly stronger than buoyancy (Qin *et al.* 2015). Furthermore, buoyancy should play a stabilizing role (the temperature at the top of the liquid layer is higher than at the bottom) and so cannot be responsible for the transitions. Hence thermocapillary stresses are expected to determine both the structure of the base flow and its stability. Thermocapillary stresses depend on the interfacial temperature profile, which is a function of the composition of the gas phase, therefore noncondensables should play an important role in the transition between different flow regimes. Since the average temperature gradient τ_i is only weakly dependent on c_a, the effect of noncondensables on the flow stability is described mainly by the variation of the Biot number. The first term in (4-2) describes the change in the thermal conductivity of the gas phase with c_a. This term, however, is only significant when the gas phase is dominated by noncondensables. At lower c_a the second term in (4-2), which describes the effect of latent heat released or absorbed at the interface due to phase change, is dominant. Hence the increase in Ma_i at lower concentrations of noncondensables is due primarily to the enhancement of phase change and a resulting decrease in the variation in the interfacial temperature gradients about average.

4.3 Conclusions

Buoyancy-thermocapillary convection in a layer of a volatile silicone oil subjected to a horizontal temperature gradient was investigated experimentally under a vapor space containing 14% to 96% air at pressures ranging from 4.8 kPa to 101 kPa, respectively. The

spatially averaged velocity data were curve-fit to an analytical solution for steady uniform flow to estimate the average layer depth and interfacial temperature gradient. Based on these estimates the interfacial Marangoni number was determined for a range of flow regimes. The results for ambient conditions (*i.e.*, 96% air) are in qualitative agreement with other experimental and numerical studies. An analysis of the velocity field of the oscillatory state suggests that its time scales are consistent with a convective instability of the thermal boundary layer which forms at the free surface next to the heated end of the test cell.

The average concentration c_a of noncondensables appears to have little effect on the base flow, at least over the range of c_a considered here. c_a does, however, have a major effect on flow stability, and the critical Marangoni numbers for transition between the various flow states (SUF, PMC, SMC, OMC) increase as c_a decreases, in surprisingly good agreement with the predictions of linear stability analysis. For example, unsteady flow is only observed in convection under ambient conditions, and the steady multicellular state is only observed for convection at the two higher air concentrations.

Related numerical and analytical studies show that description of the flow in the liquid layer and its stability at reduced concentrations of air requires detailed description of bulk mass transport in the vapor (space), which is a *binary* mixture (*i.e.*, air and vapor), and cannot be understood by simply using the momentum, heat and mass balance at the liquid-vapor interface. This is especially true in situations where air has been almost completely evacuated (as is the case in many evaporative cooling applications). Linear stability analysis shows that both the latent heat associated with phase change and the heat transfer in the vapor space affect the flow stability. In particular, reducing the concentration of noncondensables enhances phase change, thereby suppressing transitions to more complex convective patterns.

CHAPTER 5

BUOYANCY-MARANGONI CONVECTION IN VOLATILE BINARY FLUIDS

This chapter details the results of buoyancy-Marangoni convection in volatile binary fluids (*i.e.*, MeOH-H_2O mixtures). Here, we use the term "buoyancy-Marangoni" (*vs.* buoyancy-thermocapillary) to refer to convection that is driven by buoyancy, thermocapillarity *and* solutocapillarity. Section 5.1 defines and describes four flow regimes observed in the binary fluid experiments, and presents an overall flow regime map in the c_a–C_M space (*i.e.*, air concentration in the vapor space *vs.* MeOH concentration in the liquid phase). Section 5.2 then gives detailed flow field visualizations and PIV measurements in each flow regime, and the driving mechanisms and velocity scaling are also discussed. Section 5.3 evaluates the heat transfer performance of selected cases and discusses the effects of noncondensables on heat transfer. Finally, the chapter is summarized in Section 5.4.

5.1 Flow Regimes and Flow Regime Map

Although the flow regimes of thermocapillary convection in a simple fluid are quite well characterized as discussed in Chapter 4, far less is known about the flow regimes, specifically the convection patterns in the liquid-phase flow for buoyancy-Marangoni convection in binary liquid films. This section therefore first defines and describes four flow regimes observed in our binary fluid experiments and presents an overall flow regime map in the c_a–C_M space that summarizes the experimental results for our study of a methanol-water mixture.

5.1.1 Flow Regime Map

Convection in simple fluid layers (Chapter 4), is driven by thermocapillarity and buoyancy, which drive the flow away from the heated end and towards the cooled end in all cases, despite differences in local flow structures (*e.g.* number of rolls in SMC and time-dependent flow in OMC). The flows in binary-liquid layers are, however, much more complex because these flows are also driven by solutocapillarity, which opposes thermocapillarity in the binary fluid studied here. As discussed earlier, solutocapillarity is due to changes in σ due to concentration gradients, and such gradients should be greatest at the liquid-vapor interface, *i.e.* the region where phase change occurs. Since MeOH is more volatile and has a lower σ than water, the surface tension of this binary fluid will effectively decrease as temperature decreases because more MeOH than water will evaporate (from the interface) at a given temperature.

In order to characterize convection in this binary fluid, the flow regimes were mapped out on a c_a *vs.* C_M plot. In these experiments, C_M = 9 – 74 mol%, and c_a = 1 – 96 mol%, and the applied temperature difference $\Delta T \approx 6.0$ ℃ and the average liquid layer depth $h_{av} \approx 0.3$ cm were kept constant.

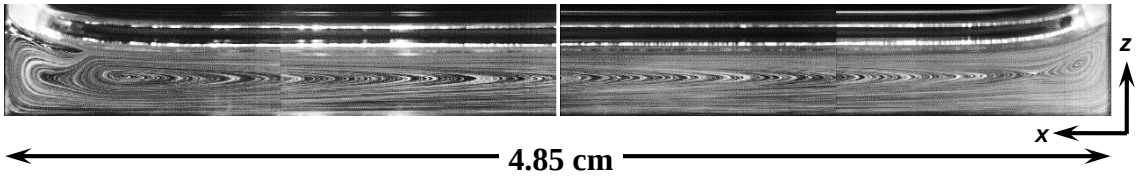

Figure 5.1 Flow visualizations of a typical thermocapillarity-dominated flow (TDF) in the central vertical plane for C_M = 58.6% and c_a = 90.4% at p = 101 kPa and ΔT = 6.0 °C.

For buoyancy-Marangoni convection in binary liquids under a vapor space dominated by noncondensables (where the at pressure is at or slightly below atmospheric), the major flow structure of the liquid phase in the central vertical (x–z) plane is a large

eddy, or single cell with a counterclockwise rotation, *i.e.*, a positive ω_y, that occupies almost the entire horizontal extent of the liquid layer (Fig. 5.1). The direction of the flow near the free surface is therefore away from the heated end, which is consistent with thermocapillarity, and so this flow regime is termed thermocapillarity-dominated flow (TDF). Although the flow patterns in TDF are very similar to the SUF regime in buoyancy-thermocapillary convection of simple fluids (*cf.* Fig. 4.1 in Chapter 4), this TDF does not go drive the fluid near the free surface away from the heated end near the cooled wall. Instead, there is a small region next to the cooled wall where the liquid flows away from the cooled wall, suggesting that flow in this small region may be driven by solutocapillarity. Figure 5.1 shows particle pathline visualizations of a typical TDF over a total time of 15.6 s in the central vertical x–z plane at $y = 0$ with the heated end on the right and the cooled end on the left for $C_M = 58.6\%$ and $c_a = 90.4\%$ at $p = 101$ kPa.

As c_a decreases and more air is removed from the vapor space, phase change, and hence solutocapillarity due to differential evaporation, which causes variations in the MeOH concentration along the interface, are enhanced. At intermediate noncondensables levels (*e.g.* $c_a \approx 50\%$), the flow is unsteady or time-dependent, with the strongest fluctuations near the free surface, due presumably to the competition between thermocapillarity, solutocapillarity and buoyancy. We call this flow regime unsteady flow (UF). Figure 5.2 shows particle pathline visualizations, again averaged over 15.6 s, in the central vertical plane of a typical unsteady flow for $C_M = 58.6\%$ and $c_a = 52\%$ at $p = 19.7$ kPa. The unsteadiness of the flow is more evident in the magnified view (of the region inside the dashed rectangle on the right side of Fig. 5.2) shown in Figure 5.3. Note the crossing of the particle pathlines as the flow cells change their positions over this 15.6 s interval.

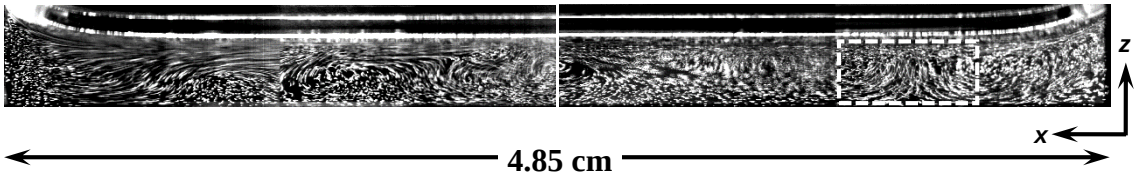

Figure 5.2 Flow visualizations of a typical unsteady flow (UF) in the central vertical plane for C_M = 58.6% and c_a = 52% at p = 19.7 kPa and ΔT = 6.1°C

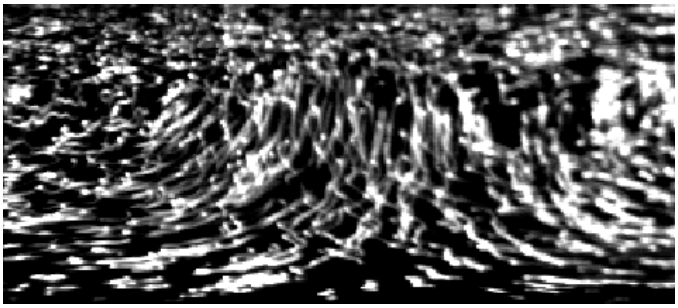

Figure 5.3 A closeup of the region inside the dashed rectangle shown in Figure 5.2.

As even more air is removed from the vapor space, and c_a decreases to a point where the vapor space is dominated by MeOH and H_2O vapor, solutocapillarity starts to become the dominant driving force for the flow near the free surface. The major flow structure in the central vertical (x–z) plane under these conditions is a cell with clockwise rotation, *i.e.*, negative ω_y, where the liquid near the free surface flows towards the heated end over the entire horizontal extent of the liquid layer, with a return flow near the bottom of the liquid layer (Fig. 5.4). This flow state is defined to be solutocapillarity-dominated flow (SDF).

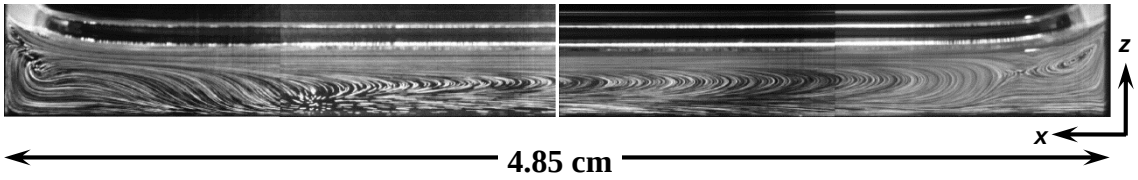

Figure 5.4 Flow visualizations of a typical solutocapillarity-dominated flow (SDF) in the central vertical plane for C_M = 58.6% and c_a = 3.3% at p = 9.7 kPa and ΔT = 6.1 °C

If c_a remains small (*i.e.*, the vapor space is dominated by vapor), and C_M is reduced, the flow reverses with liquid flowing away from the heated end over a small region next to the heated end when C_M falls below a critical, or threshold, value (~10% for $c_a \approx 2\%$), which depends on c_a. We call this flow regime reversed flow (RF). Figure 5.5 shows an example of RF for $C_M = 8.9\%$ and $c_a = 1.5\%$ at $p = 4.4$ kPa. The arrow denotes the location of the stagnation point near the free surface where the flow reverses.

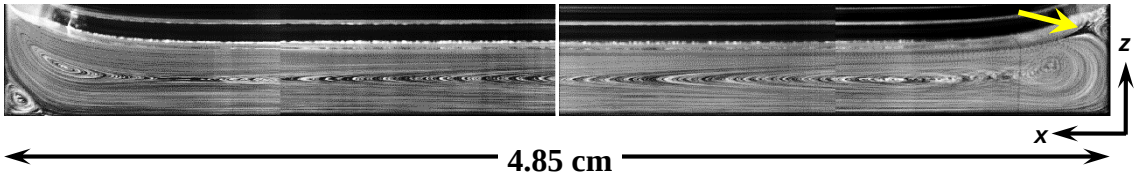

Figure 5.5 Flow visualizations of a typical reversed flow (RF) in the central vertical plane for $C_M = 8.9\%$ and $c_a = 1.5\%$ at $p = 4.4$ kPa and $\Delta T = 6.1$ °C.

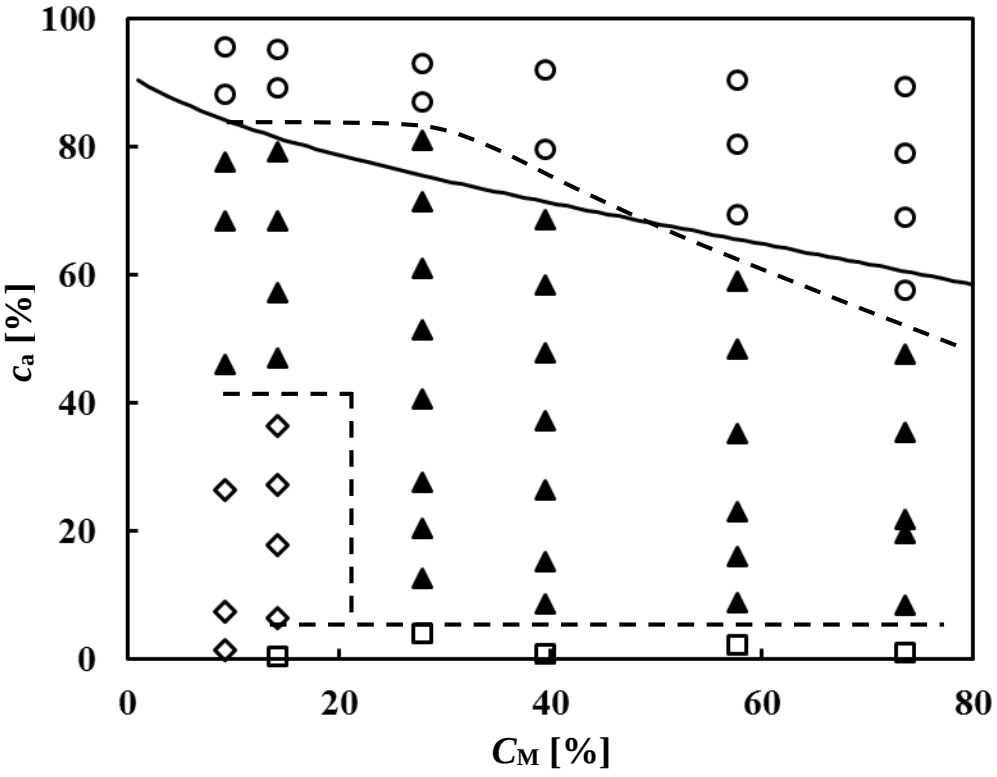

Figure 5.6 Flow regime map in the c_a - C_M space, including all four flow regimes: TDF (○), UF (▲), SDF (□) and RF (◇), and ΔT and h_{av} are fixed at ~6.0 ℃ and ~0.3 cm,

respectively for all the cases; the dashed lines indicate the tentative boundaries between flow regimes and the solid line indicates an isobar at p = 27 kPa.

Figure 5.6 shows the resulting flow regime map in the $c_a - C_M$ space. The flow is classified into one of four flow regimes, thermocapillarity-dominated flow (TDF), unsteady flow (UF), solutocapillarity-dominated flow (SDF) and reversed flow (RF), denoted by circles (○), triangles (▲), squares (□) and diamonds (◇), respectively. The dashed lines roughly indicate the boundaries between these four flow regimes. Note that the experimental conditions of all the data points are summarized in Table C-3 in Appendix C.

5.1.2 Discussion of the Flow Regime Map

The flow regime map that summarizes the results of 11 experiments shows that TDF, (circles) only occurs for large c_a space, when phase change is suppressed. The critical c_a where the flow transitions from TDF to UF decreases monotonically as C_M, and hence the fraction of the more volatile component, increases. This transition boundary is close to the isobar corresponding to a constant total pressure p = 27 kPa in the vapor space (Fig. 5.6 solid line), suggesting that the amount of phase change is controlled by the total amount of gases—noncondensables and vapor—in the vapor space *vs.* c_a. Note that the value of 27 kPa was chosen as the best "match" to the transition boundary observed in these experiments, which are admittedly at a single value of ΔT and h_{avg}.

On the other hand, SDF (squares) only occurs when the noncondensables concentration c_a is very low (*i.e.*, <6%). This is expected, since solutocapillary requires significant phase change, which occurs only in the near-absence of noncondensables.

Unsteady flow (triangles) occurs at intermediate noncondensables levels, suggesting that thermocapillarity and solutocapillarity are of comparable importance in this flow regime, and that the unsteadiness is due to the competition between thermocapillarity

and solutocapillarity. Although beyond the scope of this thesis, the stability characteristics of this flow regime warrant further investigation.

Finally, RF (diamonds) occurs when both c_a and C_M are small (*i.e.*, the bottom left corner of the flow regime map). Solutocapillarity is still dominant over most of the liquid layer in this flow regime, for the most part the flow, but thermocapillarity (in conjunction with buoyancy) is stronger than solutocapillarity near the contact line region of the heated end.

5.2 PIV Measurements of Velocity Fields

Based on the flow regime map shown in Figure 5.6, detailed flow field visualizations and PIV measurements for representative thermocapillarity-dominated, solutocapillarity-dominated and unsteady flow cases are presented and discussed in this section. The maximum velocities measured experimentally are also compared with the velocity scales from a lubrication-type analysis for solutocapillarity-dominated flow.

5.2.1 Thermocapillarity-Dominated Flow

This section details the results of buoyancy-Marangoni convection in binary liquids when the vapor space is dominated by noncondensables (circles in Fig. 5.6). Since phase change (*i.e.*, evaporation and condensation) is suppressed in this case, there is little (differential) evaporation of methanol. There is therefore little variation in MeOH concentration at the free surface, and the flow in the liquid phase is driven mainly by thermocapillary (*vs.* solutocapillary) stresses due to the temperature gradients along the free surface, which drive the flow away from the heated end and towards the cooled end. Figure 5.7*a* shows particle pathlines visualizations of convection in the $C_M = 58.6\%$ binary liquid under a vapor space at relative air concentrations $c_a = 90.4\%$, corresponding to an average pressure $p = 101$ kPa. The pathlines are shown over a total time of 15.6 s in the central vertical x–z plane of the flow at $y = 0$ with the heated end on the right and the cooled end on the left. The velocity fields, u and w, namely the x- and z-components, in the liquid

layer measured by 2D-2C PIV are shown in Figure 5.7*b* in this central vertical plane next to the cooled end over 4.25 cm ≤ x ≤ 4.85 cm ([left]) and next to the heated end over 0 ≤ x ≤ 0.6 cm ([right]). The velocity vectors are colored with their magnitudes (*cf.* color scale); the out-of-plane (y) component of the velocity should be zero by symmetry in this central plane. The physical dimension of the velocity vector plots shown in Figure 5.7*b* are ~0.6 (x) × 0.44 cm (z), corresponding to the dashed rectangles in Figure 5.7*a*.

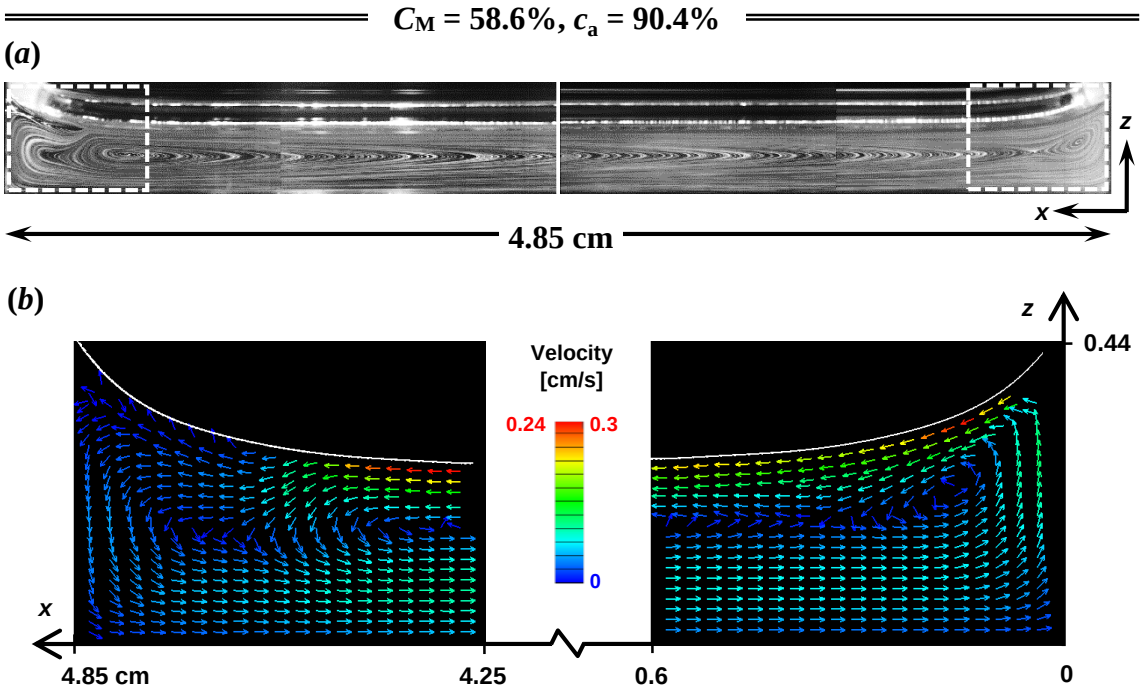

Figure 5.7 Flow visualizations (*a*) and velocity fields (*b*) in the central vertical plane for C_M = 58.6% and c_a = 90.4% at p = 101 kPa, for convection driven by an applied temperature difference (measured on the outer surface of the test cell) ΔT = 6.0 ℃.

In this typical example of TDF, the liquid near the interface flows away from the heated end (*i.e.*, to the left), consistent with thermocapillarity, over most of the liquid layer (*i.e.*, 0 ≤ x ≤ ~4.46 cm). The flow next to the cooled wall, however, flows instead away from the cooled end (*i.e.*, to the right), consistent with solutocapillarity, over a small portion of the free surface (*i.e.*, ~4.46 cm ≤ x ≤ 4.85 cm). Although this flow reversal near the

cooled wall is not obvious in Figure 5.7*b* [left], due to the limitation in the accuracy and spatial resolution of the PIV data, a closeup of the pathline visualization in Figure 5.8 clearly shows the stagnation point near the free surface at $x \approx 4.85$ cm, and the change in flow direction near the cooled wall The maximum flow speed near the heated end (Fig. 5.7*b* [right]) of ~0.29 cm/s is comparable to that near the cooled end of ~0.24 cm/s (Fig. 5.7*b* [left]); both of these maxima occur near the interface. However, the flow to the right in the region near the cooled end is much weaker than that near the free surface when the flow is to the left, with speeds an order of magnitude less of O (10^{-2} cm/s).

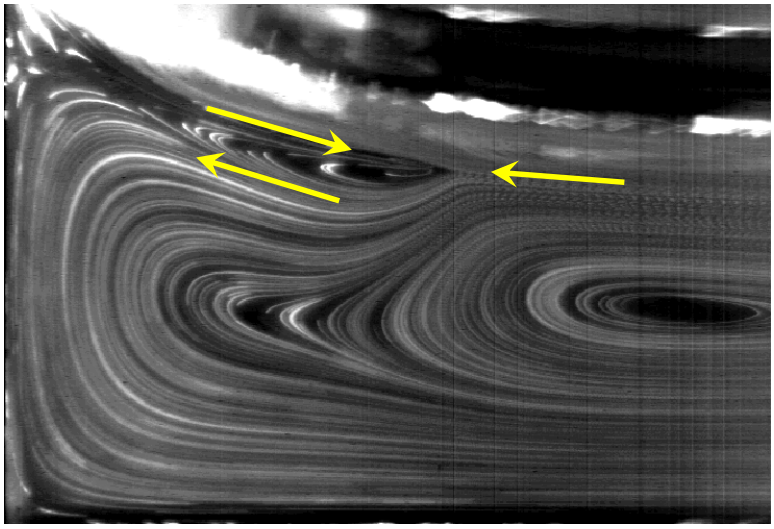

Figure 5.8 A closeup of the region inside the dashed rectangle shown in Figure 5.7*a* [left].

Assuming that buoyancy effects on the flow at the interface are negligible, the flow in this region should be driven by solutocapillarity and thermocapillarity. We conjecture that the flow is much slower near the cooled end because the MeOH-rich condensate accumulates there, and even in this case where the high concentration of noncondensables suppresses phase change, there is enough condensate to create a significant gradient in MeOH concentration at the free surface. This could enhance solutocapillarity in this small region to an extent where solutocapillarity overcomes thermocapillarity. This conjecture is consistent with the observation of a thin layer of "clear" (*i.e.*, particle-free) fluid next to

the cooled end in the pathline visualization (Fig. 5.8), which is likely condensate convected by the flow towards the heated end.

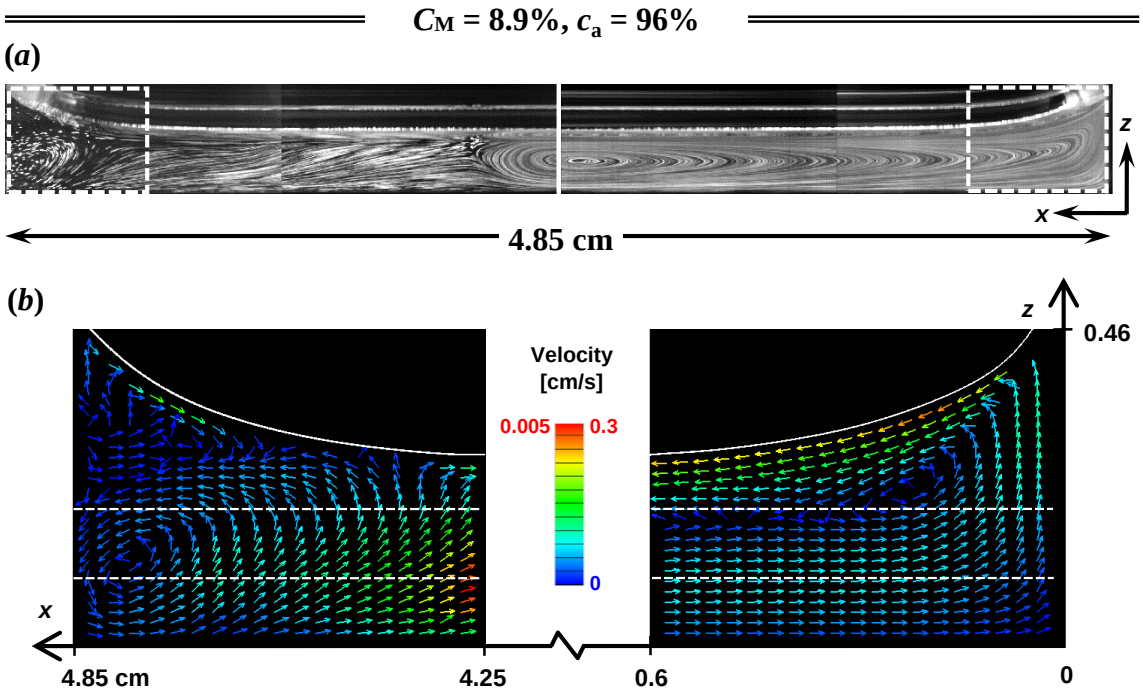

Figure 5.9 Similar to Fig. 5.7 but for C_M = 8.9% and c_a = 96% at p =101 kPa and ΔT = 6.3 ℃. The dashed lines in these figure indicate where the horizontal views were obtained shown in the following Figures 5.10 and 5.11.

Figure 5.9, like Figure 5.7, shows another example of TDF, for a C_M = 8.9% (*vs.* 58.6%) binary liquid and c_a = 96% at an average pressure p = 101 kPa. Again, the liquid near the interface flows towards the cooled end (*i.e.*, to the left), consistent with thermocapillary, over most of the liquid layer. The reversed flow (*i.e.*, to the right) region near the cooled end, is, however, much larger (*i.e.*, ~2.7 cm ≤ x ≤ 4.85 cm) than at C_M = 58.6%, and the stagnation point near the free surface is now at $x \approx$ 2.7 cm. The maximum flow speeds at the free surface near the heated end (Fig. 5.9*b* [right]) for this case of ~0.26 cm/s are almost two orders of magnitude greater than those near the cooled end of ~0.005 cm/s (Fig. 5.9*b* [left]).

Moreover, although the maximum flow speeds near the heated end are observed near the free surface, they are instead observed in the bulk of the liquid at $z \approx 0.1$ cm near the cooled end. Following the conjecture for the $C_M = 58.6\%$ and $c_a = 90.4\%$ case, these results suggest that thermocapillarity overcomes solutocapillarity over much of this flow, but over a much larger region near the free surface at the cooled end. The larger region of reverse flow implies, however, that solutocapillarity is stronger at $C_M = 8.9\%$ and $c_a = 96\%$ than at $C_M = 58.6\%$ and $c_a = 90.4\%$ Solutocapillarity should of course increase as C_M decreases, because $\partial\sigma / \partial C_M$ increases as C_M decreases, based on the $\sigma(C_M)$ data reported by Vázquez *et al.* (1995). The visualizations at $C_M = 8.9\%$ (Fig. 5.9*a*) also suggests that there is a thin layer of "clear" fluid slightly below the interface over the entire liquid layer, which we again suspect is condensate.

Figure 5.10 shows the in-plane velocity components for the same flow (*i.e.*, $C_M = 8.9\%$ and $c_a = 96$ mol% at $p = 101$ kPa) in a horizontal (x–y) plane at $z = 0.2$ cm (*i.e.*, corresponding to the upper horizontal dashed line in Fig. 5.9*b*) next to the cooled ($3.65 \text{ cm} \leq x \leq 4.85$ cm) (*a*) and heated ($0 \leq x \leq 1.2$ cm) (*b*) ends of the test cell. Only u and v, namely the x- and y-components of the velocity, respectively, are shown here. Note that these views, which extend much farther into the test cell (compared with the views of the vertical central plane in the previous Figures), show a horizontal plane slightly below the liquid-vapor interface in the central portion of the test cell and significantly below the interface near the heated and cooled ends. The depth of the liquid layer is ~0.46 cm at the ends of the test cell due to the curvature of the interface (*cf.* Fig. 5.9) The flow is essentially symmetric about the x-axis, with a fairly strong flow in the center (*i.e.*, at $|y| < 0.3$ cm) in Figure 5.10*b* away from the heated end (except for a very thin layer immediately next to the end), in agreement with the results shown in the views of the vertical central plane of the same flow case (Fig. 5.9*b*). The maximum flow speed of ~0.1 cm/s in this view occurs at an x-location where this plane is just below the interface. The liquid on the sides (*i.e.*,

$|y| > 0.3$ cm) flows instead towards the heated end. A similar pattern is evident in the flow near the cooled end shown in Figure 5.10*a*, with a flow speed of ~0.01 cm/s near the center ($|y| < 0.2$ cm) away from the cooled end, which agrees with the results shown in Figure 5.9*a*, and flow towards the cooled end on the sides.

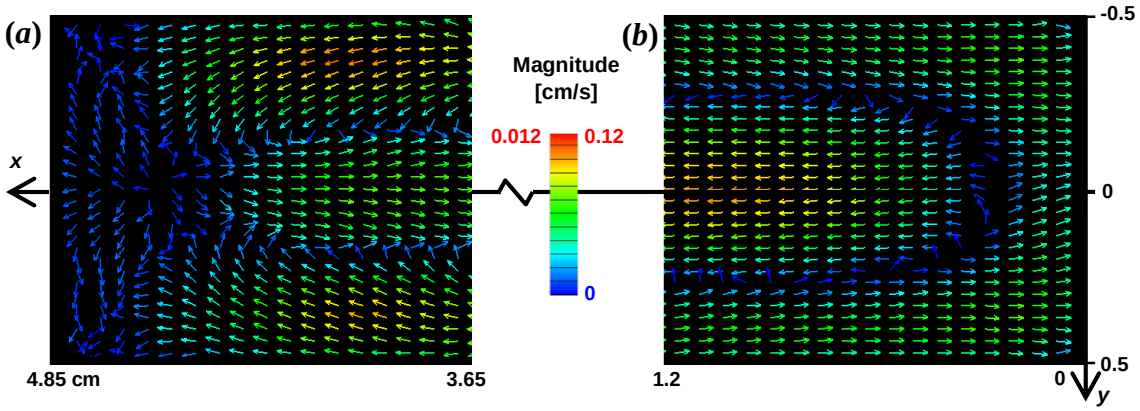

Figure 5.10 The average in-plane velocity components in the liquid layer for the flow visualized in Figure 5.9 (C_M = 8.9% and c_a = 96%, p = 101 kPa, and ΔT = 6.3 ℃) in a horizontal (x-y) plane of the flow at z = 0.2 cm next to the cooled (*a*) and heated (*b*) ends of the test cell. The vectors are colored by their magnitudes $\sqrt{u^2+v^2}$.

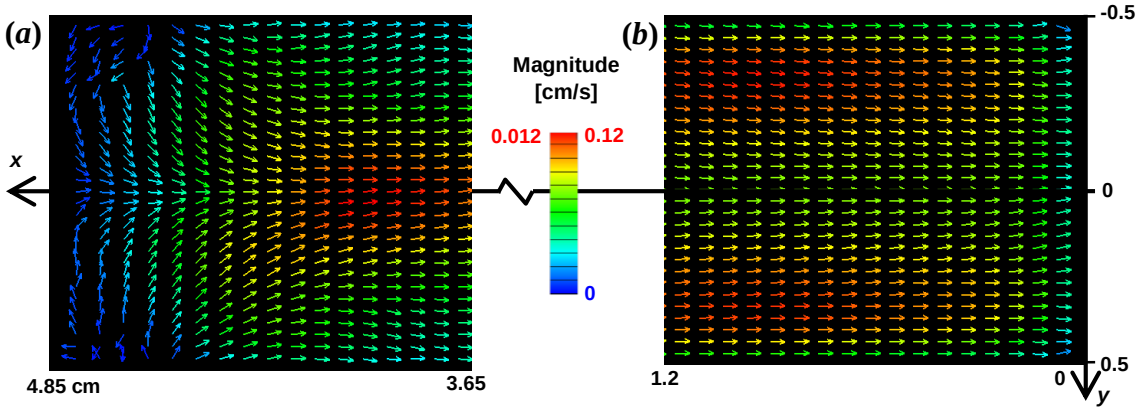

Figure 5.11 Similar to Fig. 5.10 but in a horizontal (x-y) plane of the same flow at z = 0.1 cm next to the cooled (*a*) and heated (*b*) ends of the test cell.

Figure 5.11 is similar to Figure 5.10, but in a horizontal (*x*-*y*) plane of the same flow deeper within the liquid at $z = 0.1$ cm (lower horizontal dashed line in Fig. 5.9*b*). The flow is again reasonably symmetric about the *x*-axis, with a flow going towards the heated end, in agreement with the results shown in the views of the vertical central plane of the same flow case (Fig. 5.9*b*). Since this plane is relatively far from the free surface, it should be less affected by interfacial curvature, and the flow is essentially unidirectional (*i.e.*, from right to left) within the entire plane. The flow is much weaker near the cooled end, and the maximum flow speeds of ~0.1 cm/s near the heated end and ~0.01 cm/s near the cooled end are comparable to those shown in Figure 5.10.

In summary, thermocapillarity is enhanced for buoyancy-Marangoni convection under air at ambient conditions (c_a = 90–96%), and enhanced to such an extent that thermocapillarity appears to dominate the interfacial flow over much of the liquid layer. These observations are in agreement with the numerical simulations by our collaborators (Qin *et al.* 2012). A region of reversed flow at the free surface near the cooled end is observed, and the horizontal extent of this region increases as C_M decreases, presumably because solutocapillarity, quantified by $\partial\sigma/\partial C_M$, increases as C_M decreases. We observe a thin layer of "clear" fluid slightly below the interface near the cooled end, which may be condensate that forms at the cooled end and is then convected by the flow towards the heated end.

5.2.2 Solutocapillarity-Dominated and Reversed Flow

This section details SDF and RF, the flow regime for convection at relatively low c_a (*cf.* squares and diamonds in Fig. 5.6). As noted earlier, phase change should be significant at low c_a, and hence solutocapillary stresses due to differential evaporation overcome thermocapillary stresses, driving the flow near the free surface towards the heated end. Figures 5.12 shows results for the SDF at C_M = 58.6% and c_a = 3.3% at p = 9.7 kPa.

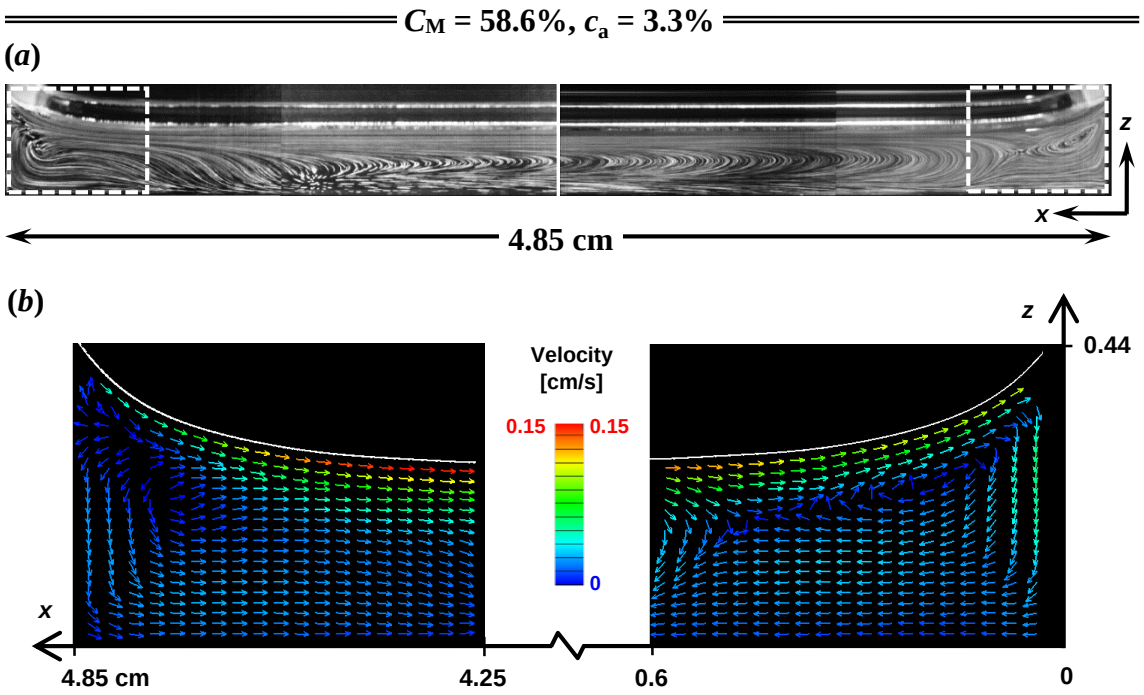

Figure 5.12 Similar to Fig. 5.7 but for SDF at C_M = 58.6% and c_a = 3.3% at p = 9.7 kPa and ΔT = 6.1 ℃

Comparing these results with those for Figure 5.7 at the same C_M but a much higher c_a, the liquid near the interface now flows towards (*vs.* away from) the heated end over the entire the liquid layer, consistent with solutocapillarity. The velocity fields near the cooled and heated ends (Fig. 5.12*b* [left] and [right]) show that the maximum flow speeds of 0.15 cm/s and 0.13 cm/s, respectively, occur just below the interface, again consistent with solutocapillarity. Indeed, the liquid flows down (*i.e.*, sinks) next to the heated wall (*i.e.*, Fig. 5.12*b* [right]), in the opposite direction for what would be expected for a buoyancy-driven flow (*i.e.*, natural convection). However, near the cooled end, the flow in the top left corner "splits," with the liquid near the free surface flowing away from the cooled end, while that next to the cooled wall flows down (*i.e.*, sinks), consistent with buoyancy.

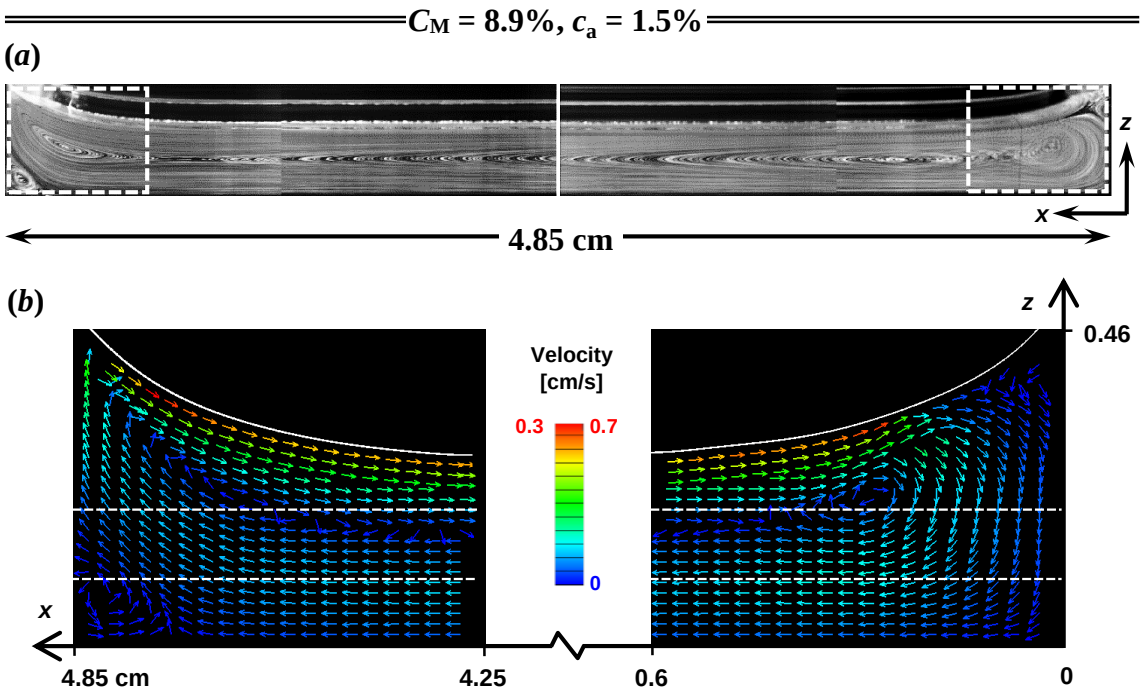

Figure 5.13 Similar to Fig. 5.7 but for C_M = 8.9% and c_a = 1.5% at p = 4.4 kPa and ΔT = 6.1 ℃. The dashed lines in these figure again indicate where the horizontal views were obtained shown in the following Figures 5.14 and 5.15.

Figure 5.13 shows results instead for C_M = 8.9% and c_a = 1.5% at an average pressure p = 4.4 kPa. The liquid near the interface again flows towards the heated end (*i.e.*, to the right) over the entire liquid layer, and the maximum flow speeds near the heated end and cooled end, occurring just below the interface in both regions, are 0.66 cm/s and 0.31 cm/s, respectively. The flow is therefore much faster than that at C_M = 58.6% and c_a = 3.3%. This increase in flow speeds is presumably due to the increase in solutocapillarity as C_M decreases. Solutocapillarity is strong enough for this case that the liquid flows down next to the heated wall and up next to the cooled wall (Fig. 5.13*b* [right] and [left]), in directions opposite to a buoyancy-driven flow. A counterclockwise cell is evident in the bottom left corner near the cooled end.

There is also a very small clear region of liquid near the heated end (Fig. 5.13*a*) with a very weak flow going away from the heated end (Fig. 5.13*b* [right]) in the upper corner of the meniscus. This region, with its flow direction opposite to the rest of the flow at the interface, may indicate the presence of a severely MeOH depleted region. Because most of the phase change occurs at the interface, there should be a water-rich layer at the free surface, which flows downwards and along the free surface due presumably to both buoyancy and thermocapillarity, resulting in a flow away from the heated end.

This clear region may still be condensate, even though it is near the heated end. We are unaware of any other way to generate a region of liquid completely free of tracer particles in this flow. Although it may seem surprising and counterintuitive for condensation to occur near the heated end, condensation near the heated end in the same geometry, albeit in a simple fluid, has been reported and explained by our collaborators in numerical simulations (Qin *et al*. 2014) when advection is stronger than heat transport in the liquid phase (*vs.* diffusion in the vapor space). The maximum speeds (and presumably strongest advection) in this flow occur just a few millimeters to the left of the stagnation point. Moreover, if this clear liquid is indeed condensate, it can only remain (relatively) pure (*i.e.*, unmixed) near the stagnation point, where there is little advection, as shown in Figure 5.13*b*.

Figures 5.14 and 5.15 show the in-plane velocity components for the same flow (*i.e.*, C_M = 8.9% and c_a = 1.5% at p = 4.4 kPa) in horizontal (x–y) planes at z = 0.2 cm and z = 0.1 cm (horizontal dashed lines in Fig. 5.13*b*), respectively, next to the cooled (3.65 cm ≤ x ≤ 4.85 cm) (*a*) and heated (0 ≤ x ≤ 1.2 cm) (*b*) ends of the test cell. The flow at z = 0.2 cm is again symmetric about the x-axis, with a fairly strong flow in the center (*i.e.*, at $|y|$ < 0.3 cm) going towards the heated end (except for a very thin layer immediately next to the end), in agreement with the results shown in the views of the vertical central plane of the same flow case (Fig. 5.13*b*). The maximum flow speeds near the heated and cooled

ends are ~0.22 cm/s and 0.09 cm/s, respectively. The flow at z = 0.1 cm is again unidirectional and away from the heated end toward the cooled end.

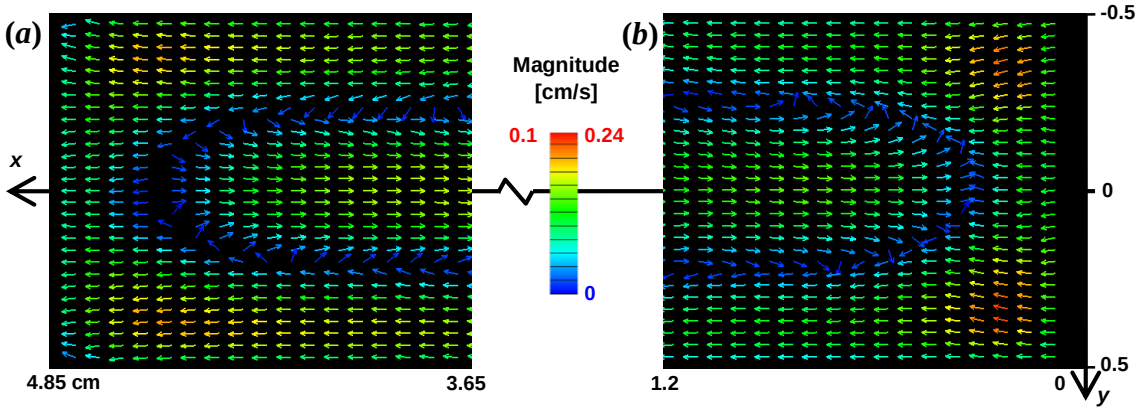

Figure 5.14 Similar to Fig. 5.10 but for C_M = 8.9% and c_a = 1.5% at p = 4.4 kPa and ΔT = 6.2 ℃, at z = 0.2 cm.

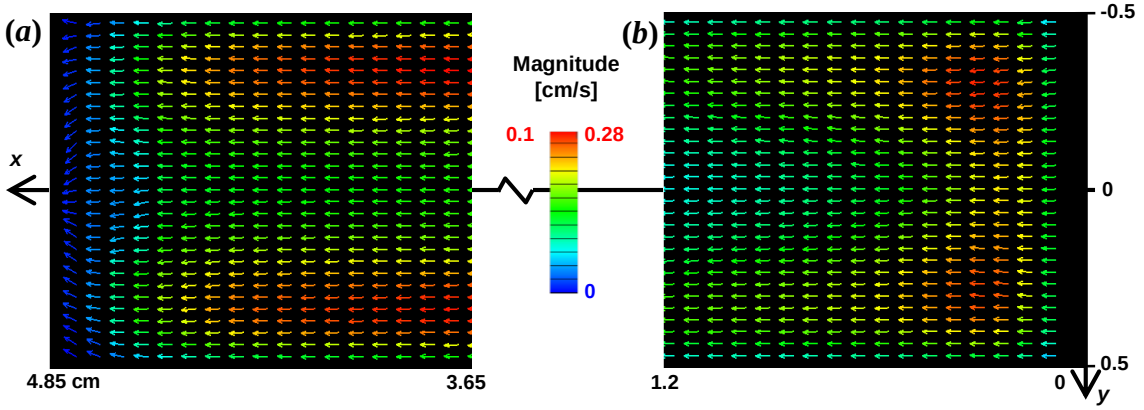

Figure 5.15 Similar to Fig. 5.14 but in a horizontal (x-y) plane of the same flow at z = 0.1 cm next to the cooled (a) and heated (b) ends of the test cell.

In summary, these results suggest that solutocapillary stresses can indeed be strong enough in this binary fluid to drive the flow at the interface all the way towards the heated end, but only when most of the noncondensables are removed from the vapor space. Since the thermal conductivity of the gas phase is relatively small, changes in c_a mainly affect

solutocapillarity by affecting the amount of phase change and hence the gradient in the liquid-phase composition at the interface (since phase change only occurs there). At high c_a, phase change is suppressed, so solutocapillary effects are weak, and thermocapillarity dominates the interfacial flow. As c_a is decreased, phase change is enhanced and at sufficiently low c_a, solutocapillarity becomes dominant, leading to a flow towards the heated end at the interface (Qin *et al.* 2012). For solutocapillarity-dominated flow (*i.e.*, with very low levels of noncondensables in the vapor space), the flow speeds at the free surface increase significantly as C_M decreases.

5.2.2.1 Scaling of Solutocapillarity-Dominated Flow

These results demonstrate that flow speeds in buoyancy-Marangoni convection of a binary liquid depend strongly on C_M, which is hardly surprising since solutocapillarity is due to the variations in MeOH concentration along the free surface. Qin *et al.* (2012) used lubrication theory to derive the velocity scale in the flow of a thin film of depth h, length L and width W (where $h << L, W$) driven by solutocapillary effects. Their derivation, reproduced here, considers a 2D flow driven solely by solutocapillarity (*i.e.*, neglecting gravity and thermocapillarity). For such a flow, the horizontal and vertical components of the momentum equation reduce to:

$$\begin{cases} \dfrac{\partial P}{\partial x} = \mu \dfrac{\partial^2 u}{\partial z^2} \\ \dfrac{\partial P}{\partial z} = 0 \end{cases} . \tag{5-1}$$

These two components can be reduced to a single equation by eliminating the pressure P to give

$$\mu \frac{\partial^3 u}{\partial z^3} = 0 . \tag{5-2}$$

The three boundary conditions required to solve equation (5-2) are:

1) no-slip boundary condition at the bottom,

$$u = 0 \text{ for } z = 0 \tag{5-3}$$

2) the conservation of mass across the liquid layer,

$$\int_0^h u\,dz = 0 \tag{5-4}$$

3) the balance in tangential stress at the free surface,

$$\mu \frac{\partial u}{\partial z} = \frac{\partial \sigma}{\partial C_{\mathrm{M}}} \nabla C_{\mathrm{i}} \tag{5-5}$$

Here, $\partial\sigma / \partial C_{\mathrm{M}}$ is the partial derivative of surface tension σ with respect to MeOH concentration C_{M}, ∇C_{i} is the concentration gradient of MeOH at the interface, and μ is the dynamic viscosity of the binary mixture. Solving equation (5-2) subject to these boundary conditions gives the velocity profile in the liquid layer

$$u_s = \frac{\partial \sigma}{\partial C_{\mathrm{M}}} \frac{\nabla C_{\mathrm{i}}}{\mu h} \left(\frac{3}{4} z^2 - \frac{h}{2} z \right). \tag{5-6}$$

And at the free surface or $z = h$, the velocity of the flow driven solely by solutocapillarity

$$u_s = \frac{h}{4} \frac{\partial \sigma}{\partial C_{\mathrm{M}}} \frac{\nabla C_{\mathrm{i}}}{\mu} \tag{5-7}$$

This equation shows that flow speeds in SDF should be proportional to $\partial\sigma / \partial C_{\mathrm{M}}$.

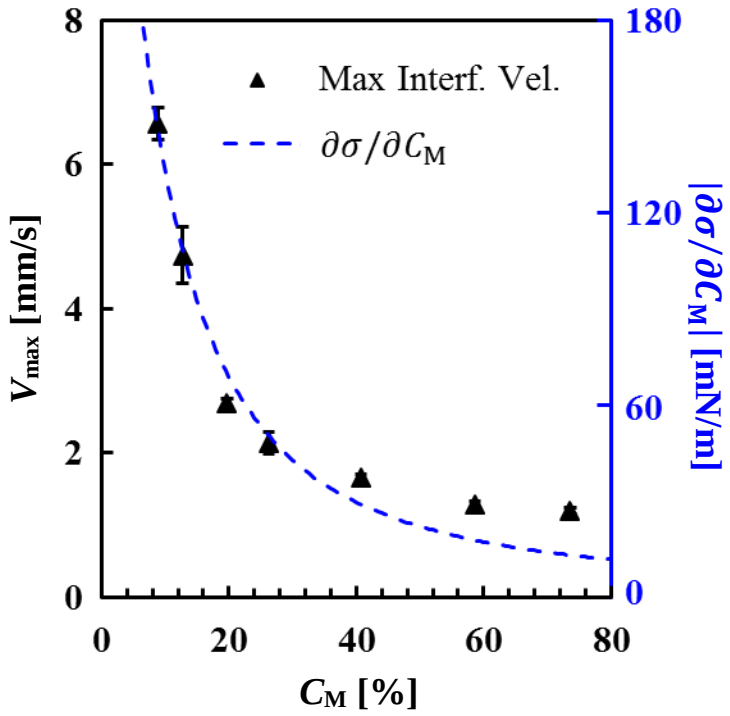

Figure 5.16 The variation of maximum interfacial velocity with the bulk MeOH concentration C_M when the vapor space is dominated by vapors. Note that this is a double *y*-axis plot: the filled triangles, plotted against the left axis, are the experimental results obtained with PIV, and the dashed line, plotted against the right axis, indicates the magnitude of $\partial\sigma/\partial C_M$ at each C_M. The error bars indicated the uncertainties of PIV measurements.

Figure 5.16 shows the maximum interfacial velocity, V_{max} measured using PIV as a function of the bulk MeOH concentration C_M (points) in buoyancy-Marangoni convection at the lowest values of c_a for that value of C_M in these experiments. The left vertical axis gives the maximum interfacial velocity, which occurs in all the cases shown here near the free surface near the heated end (*e.g.* Fig. 5.13 [right]). The right vertical axis instead gives the magnitude $\partial\sigma/\partial C_M$, calculated using second-order central differencing of the surface tension data reported by Vázquez *et al.* (1995) (dashed line). The scales of

the two vertical axes are chosen so that the dashed line best fit the experimental data points (based on their root-mean-square deviation). The results imply that the maximum interfacial velocity is roughly proportional to the gradient of surface tension, an observation that suggests that $\nabla C_i/\mu$ is roughly constant over this broad range of C_M (*i.e.*, C_M = 9 – 74 mol%) based on equation (5-7).

5.2.2.2 MeOH Concentration in the Liquid at the Interface

Although as mentioned before, the MeOH concentration in the liquid phase at the interface cannot be measured in experiments, Utaka and Wang (2004) however conjectured in their studies of Marangoni condensation in ethanol-water mixtures that the steady-state liquid-phase and vapor-phase compositions at or next to the free surface were well-approximated by the bubble point and dew point, respectively. Here, the bubble point is the lowest temperature (for a given mixture composition) where evaporation is observed as the temperature of the liquid is increased, while the dew point is the highest temperature where condensation is observed as the temperature of the vapor is decreased.

Although it is unclear if the conjecture of Utaka and Wang (2004) is valid for the Marangoni-buoyancy convection studied in this thesis, given that both evaporation and condensation are significant and the noncondensables fraction is well above 1%, we use this conjecture to estimate the liquid-phase and vapor-phase compositions near the heated end for the solutocapillary-dominated and reversed flow regimes. Figure 5.17 therefore shows the bubble-point and dew-point temperatures as a function of methanol concentration C_M at a pressure p = 9.7 kPa, corresponding to the actual measured pressure in the experiments at C_M = 58.6% and c_a = 3.3%. If the conjecture by Utaka and Wang is applicable, as the temperature increases (*i.e.*, approaching the heated wall), the MeOH concentration of the liquid at the free surface should decrease, but remain at the bubble point, suggesting that the liquid-phase MeOH concentration at the free surface will only be a function of the local interfacial temperature. This Figure, however, suggests that there

will still be some MeOH present at the interface as long as the temperature there is less than the saturation temperature for H_2O (*i.e.*, 45.3 °C at p = 9.7 kPa), and given that the maximum temperature in the entire flow must be significantly less than T_h = 23.6 °C, C_M > 0 for this case.

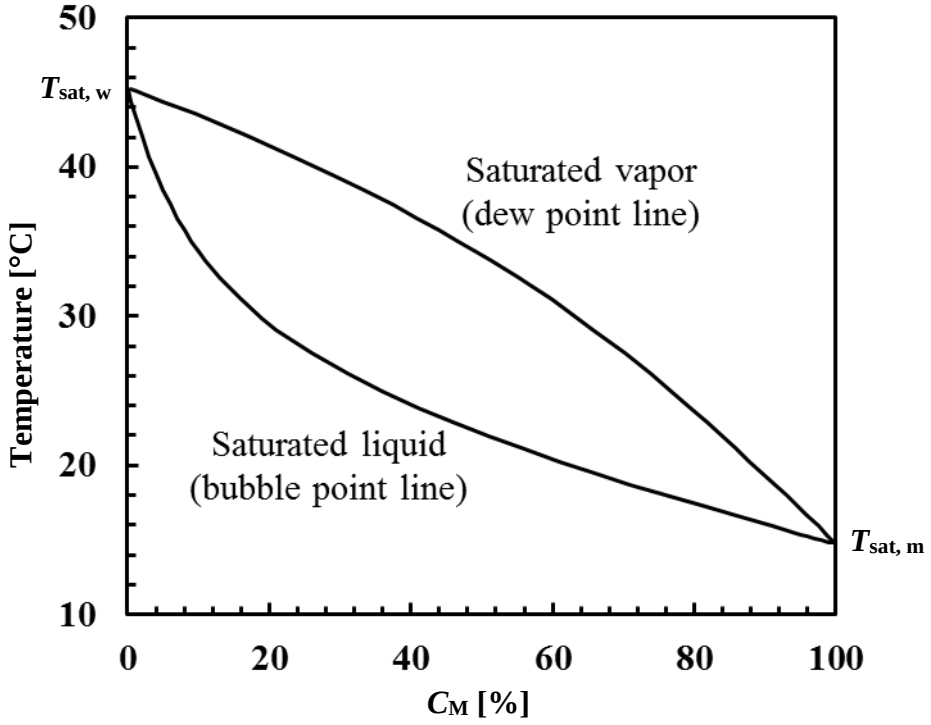

Figure 5.17 Constant-pressure phase diagram for MeOH-H_2O binary mixture for p = 9.7 kPa, corresponding to the total pressure in the vapor space for the case where C_M = 58.6% and c_a = 3.3%.

Figure 5.18 shows the corresponding bubble-point and dew-point temperatures as a function of methanol concentration C_M at a pressure p = 4.4 kPa, corresponding to the actual measured pressure in the experiments that observe RF at C_M = 8.9% and c_a = 1.5%. As expected, the dew-point and bubble-point temperatures are much lower at this lower total pressure. Based on the conjecture by Utaka and Wang (2004), the MeOH concentration at the interface is much less at a similar T_h = 23.7 °C. Since the slope of the bubble-point temperature curve is much greater at these low C_M, even a very small local

increase in interfacial temperature could easily greatly reduce the MeOH concentration, and hence solutocapillarity. Such large temperature gradients would be expected near the heated and cooled ends of the test cell because of the presence of the thermal boundary layers at these walls.

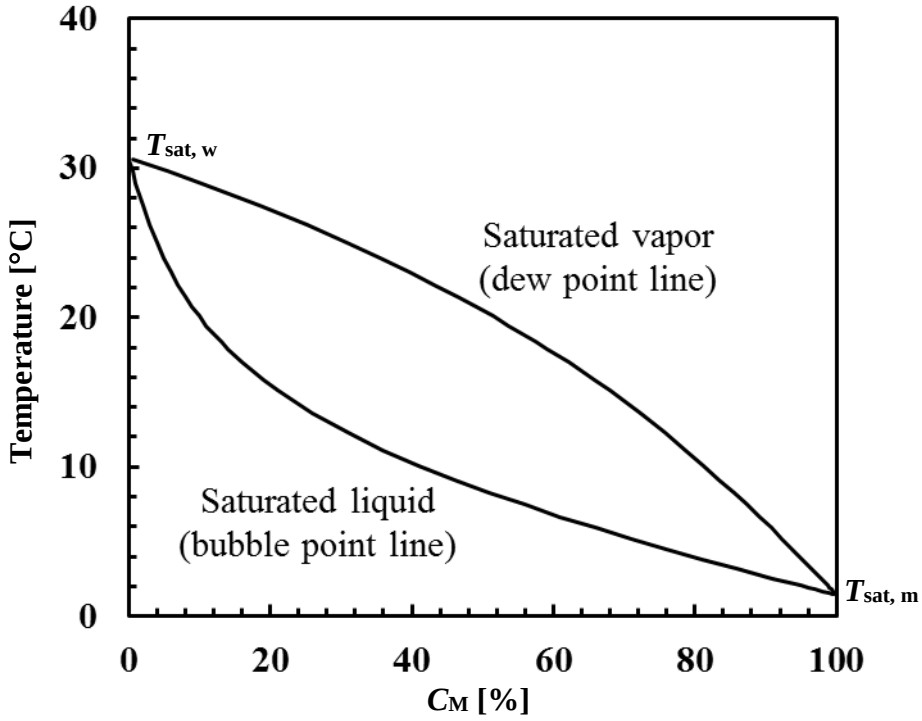

Figure 5.18 Constant-pressure phase diagram for MeOH-H_2O binary mixture for p = 4.4 kPa, corresponding to the total pressure in the vapor space for the case where C_M = 8.9% and c_a = 1.5%.

5.2.3 Unsteady Flow at Intermediate Noncondensable Levels

This section details the results of convection at intermediate c_a (*cf.* filled triangles in Fig. 5.6). As mentioned before. thermocapillarity and solutocapillarity appear to be comparable in this parameter range, which presumably leads to unsteady time-dependent flow, which we term unsteady flow (UF). These unsteady flows are difficult to characterize and appear to have fluctuations with a fairly broad frequency spectrum, based upon these initial results. The results presented here are initial flow visualizations and PIV

measurements of the flows in this parameter space, and only a few selected cases are shown. The physical mechanisms that cause the unsteadiness almost certainly involve thermo- and solutocapillarity, but cannot be fully understood without the knowledge of the temperature and concentration fields, which are not accessible in these experiments.

5.2.3.1 Time-Averaged Flow Field

Figures 5.19 shows particle pathline visualizations over a total time of 15.6 s in the central vertical (x–z) plane of the flow at $y = 0$ as well as the time-averaged velocity fields again over 15.6 s, in the liquid layer measured by 2D-2C PIV next to the cooled end (Fig. 5.19*b* [left]) and the heated end (Fig. 5.19*b* [right]), for $C_M = 58.6\%$ and $c_a = 52\%$. It clearly shows that the average flow near the interface is towards the heated end (*i.e.*, to the right), consistent with solutocapillarity, near both ends. The maximum average flow speeds near the heated end (Fig. 5.19*b* [right]) and the cooled end are 0.026 cm/s and 0.047 cm/s (Fig. 5.19*b* [left]), respectively, which are much smaller than either the TDF or SDF shown before, suggesting the two effects nearly "cancel" each other. The visualizations however over almost the entire liquid layer are quite blurred, as mentioned earlier (*cf.* Fig. 5.3), suggesting that the flow is unsteady.

Figure 5.20 shows the standard deviations in the velocity magnitudes estimated from the PIV data normalized by the maximum velocity magnitude over this entire flowfield. Clearly, the flow has the strongest fluctuations (*i.e.*, largest standard deviations) at the interface near the heated end (normalized standard deviation of ~50%), and the flow is "nearly steady," with much smaller fluctuations (~5%), near the cooled end, in agreement with the visualization shown in Figure 5.19. Note that the maximum standard deviations observed for the PIV results for what is considered to be a steady flow are typically less than 5% (*cf.* Chapter 4).

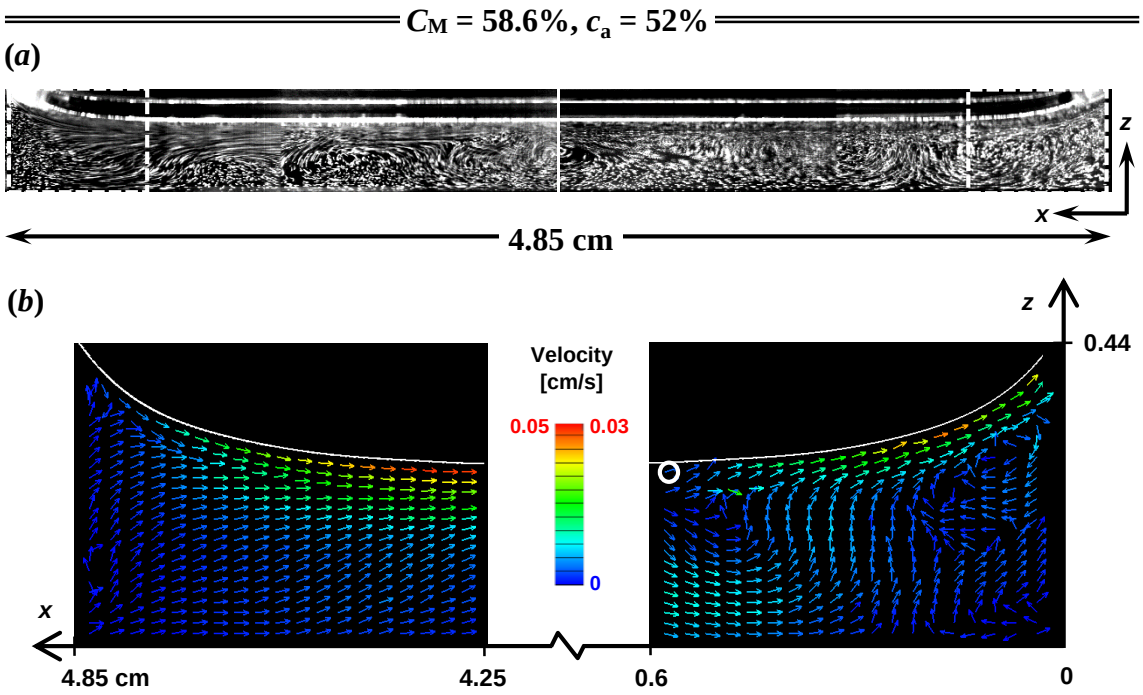

Figure 5.19 Flow visualizations averaged over 15.6s (*a*) and average velocity fields over 15.6 s (*b*) in the central vertical plane for C_M = 58.6% and c_a = 52% at p = 19.7 kPa, for convection driven by an applied temperature difference (measured on the outer surface of the test cell) ΔT = 6.1 ℃. Note the blurring and/or crossing of particle parthlines in this image. The white circle in the right vector plot indicates the location where instantaneous velocities are presented in the next section.

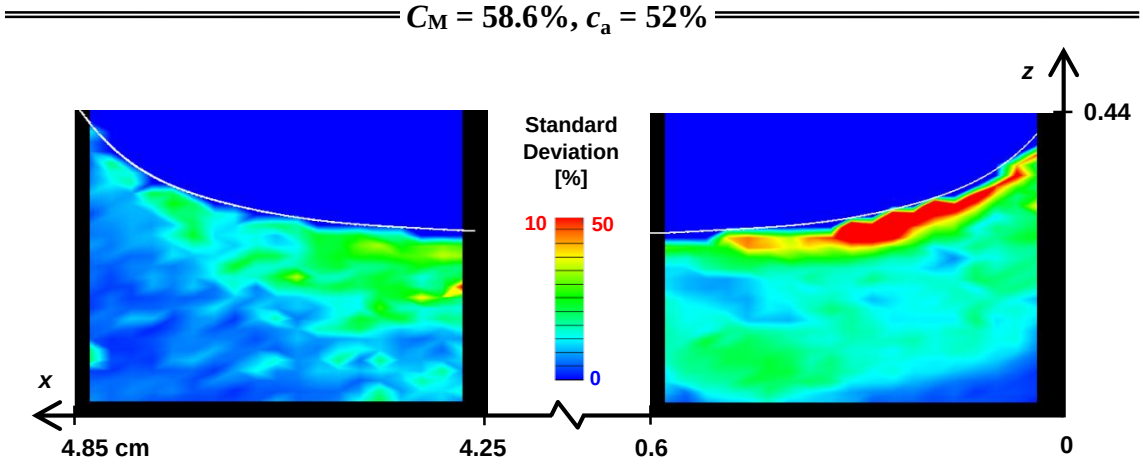

Figure 5.20 Contour plots of relative standard deviations from PIV measurements for C_M = 58.6% and c_a = 52% at p = 19.7 kPa; the standard deviations were normalized by the maximum velocity in each plot and note the different color scales for the two plots).

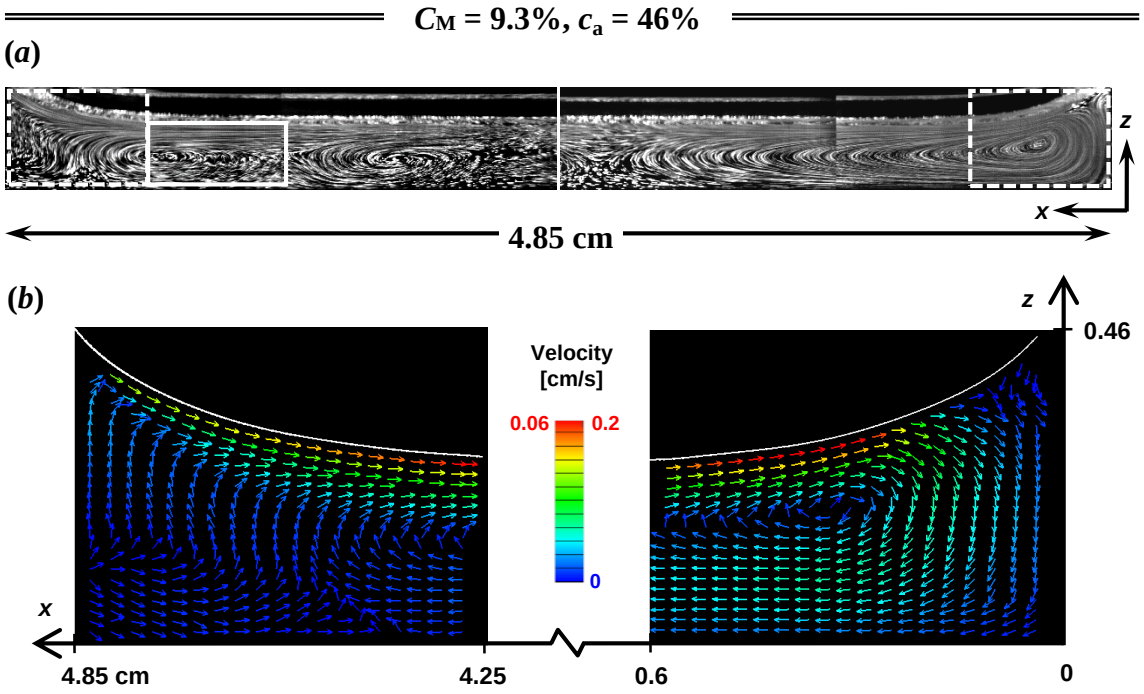

Figure 5.21 Similar to Fig. 5.19 but for C_M = 9.3% and c_a = 46% at p = 7.9 kPa and ΔT = 6.2 ℃.

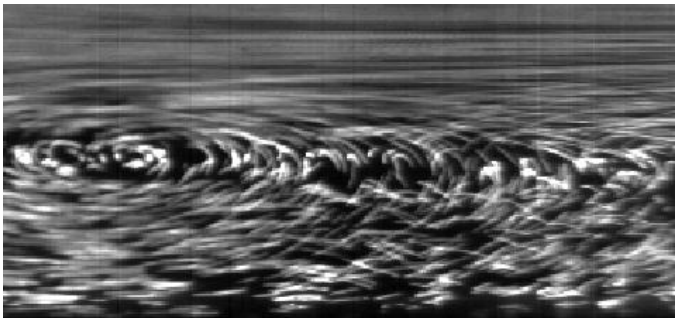

Figure 5.22 A closeup of the region inside the *solid* rectangle shown in Figure 5.21.

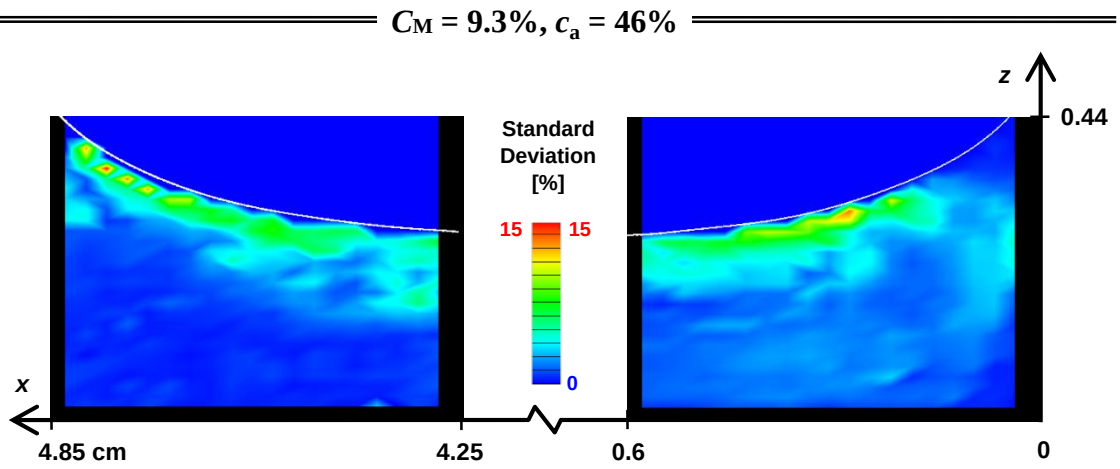

Figure 5.23 Similar to Figure 5.20 but for C_M = 9.3% and c_a = 46% at p = 7.9 kPa.

Figures 5.21 is similar to Figure 5.19 but for C_M = 9.3% and c_a = 46%. Again the particle pathlines are quite blurred (more evident in the magnified view in Fig. 5.22), especially in the middle portion, which again indicates unsteadiness in the flow. The average velocity field (Fig. 5.21*b*) suggests that the flow goes towards the heated end, with slightly larger flow speeds near the cooled end and much larger speeds near the heated end compared with the flow shown in Figure 5.19. Solutocapillarity again appears to be the major driving force in this flow. The maximum average flow speeds near the heated end (Fig. 5.21*b* [right]) and the cooled end (Fig. 5.21*b* [left]) are 0.23 cm/s and 0.06 cm/s, respectively. The maximum normalized standard deviations, which occur again near the interface, are ~15% and ~13% near the heated and cooled ends, respectively. So unlike the previous case, the fluctuations near the cooled end are comparable to those observed near the heated end.

5.2.3.2 Instantaneous Velocity Measurement

To estimate velocity fluctuations in these unsteady flows, single particle image pairs were processed to obtain (nearly) instantaneous PIV data with a temporal resolution of ~78 ms (based on a frequency of 12.8 Hz since the imaging frequency is 25.6 Hz, as

discussed in Chapter 3). Given that the frequency content of the UF is unknown, it is unclear whether these velocity data temporally resolve the flow. Nevertheless, these initial PIV results are presented and discussed next.

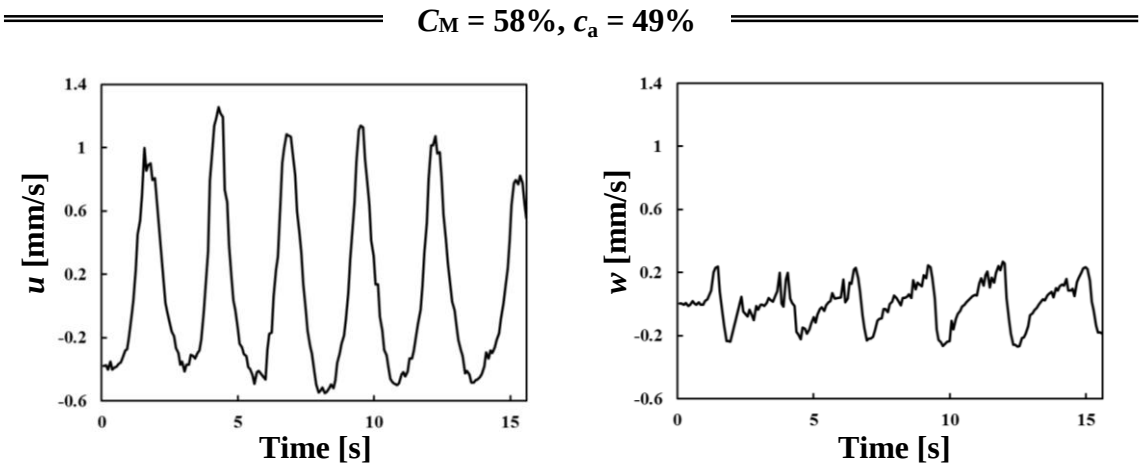

Figure 5.24 The velocity (u [left] and w [right]) variations with time at a fixed location (x, z) = (0.58, 0.25) cm, indicated by the white circle in Figure 5.19, for C_M = 58%, c_a = 49% and ΔT = 6.1 ℃ over 15.6 s.

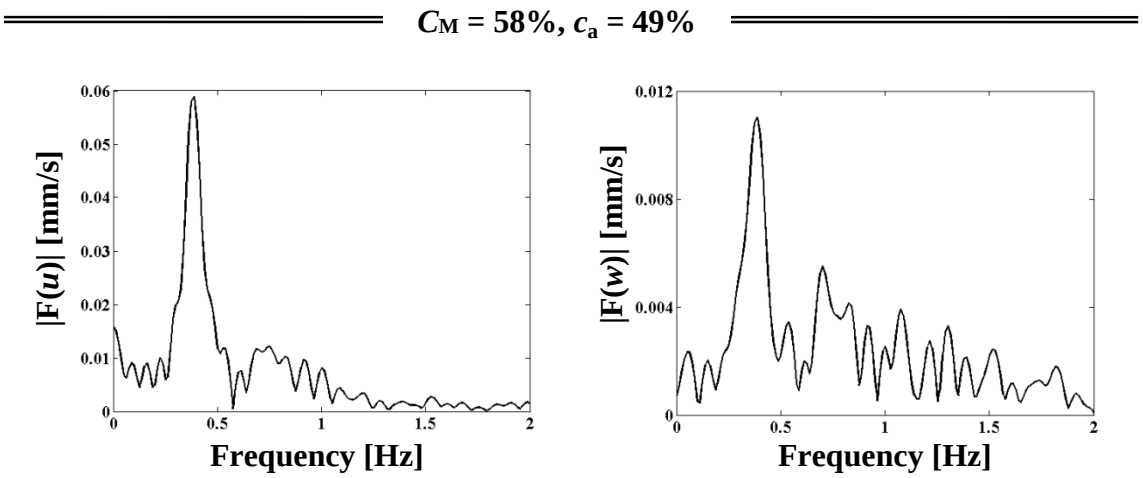

Figure 5.25 The FFT spectra of the horizontal (x) and vertical (z) velocity components (u [left] and w [right], respectively) at (x, z) = (0.58, 0.25) cm, indicated by the white circle in Figure 5.19, for C_M = 58%, c_a = 49% and ΔT = 6.1 ℃ over 15.6 s.

Figure 5.24 shows the fluctuations over time in the velocity components u [left] and w [right]) variations at a fixed location (x, z) = (0.58, 0.25) cm, which is right below the free surface and indicated by the white circle in Figure 5.19*b* [right], for C_M = 58%, c_a = 49% and ΔT = 6.1 ℃ over 15 s or the entire image sequence of 200 image pairs. The FFT spectra of these data shown in Figure 5.25 suggests that the flow in this region has a strong and frequency component at ~0.38 Hz. Note that the frequency range shown in Figure 5.25 (and Fig. 5.27) is well below the Nyquist frequency of 6.4 Hz based on the temporal resolution of the PIV measurements, suggesting that the velocity data should be able to temporally resolve these low frequencies.

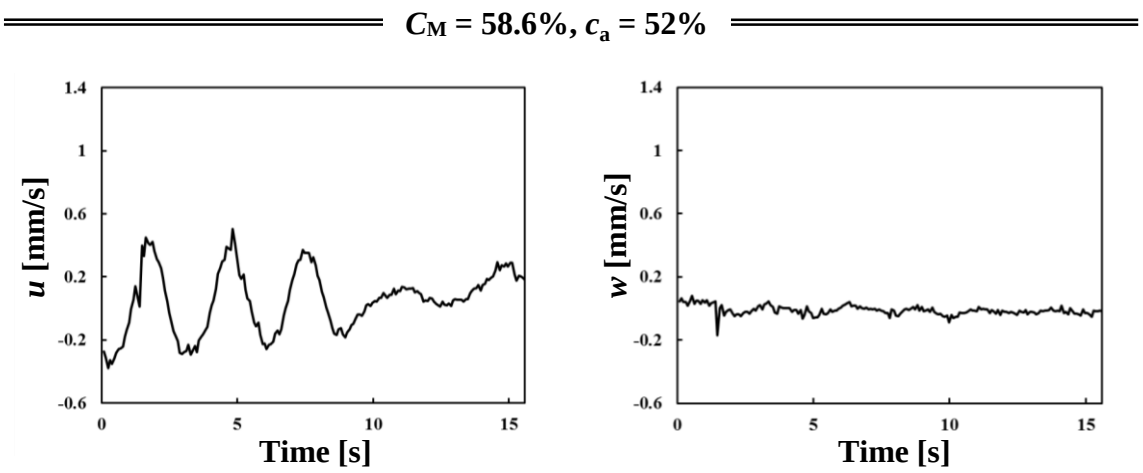

Figure 5.26 Similar to Fig. 5.24, but for a different experimental run at C_M = 58.6%, c_a = 52% and ΔT = 6.1 ℃.

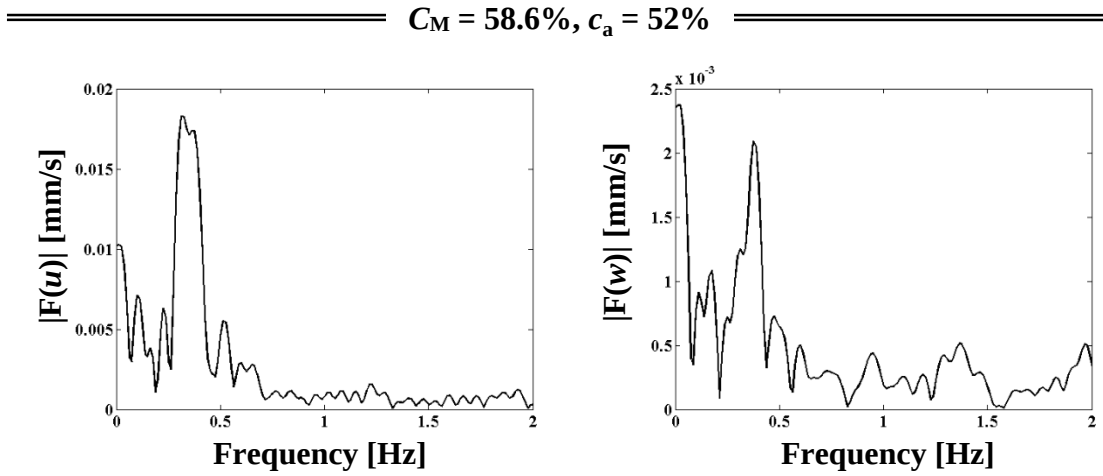

Figure 5.27 Similar to Fig. 5.25, but for a different experimental run at C_M = 58.6%, c_a = 52% and ΔT = 6.1 ℃.

Figure 5.26 shows the fluctuations in u [left] and w [right] over time at a similar physical location for a different experimental run under very similar conditions, namely C_M = 58.6%, c_a = 52% and ΔT = 6.1 ℃. Clearly, the fluctuations in the velocity components [left] are not as "periodic" as those shown in Figure 5.24. Nevertheless, the FFTs of these velocity data (Fig. 5.27) suggests that the flow has a strong frequency component at a similar frequency (as that shown in Fig. 5.25) of 0.32 Hz.

In summary the UF observed here, albeit at one value of ΔT, do not appear to be oscillatory, *i.e.*, periodic. There is some evidence of a dominant frequency between 0.3 and 0.4 Hz based on the initial results presented here, but understanding the nature of the unsteadiness of the flow at intermediate values of c_a will require further study.

5.3 Effect of c_a on Heat Transfer

Given that the motivation for studying buoyancy-Marangoni convection in binary fluids is its promise for enhancing heat transfer in evaporative cooling, a preliminary study was performed to quantify how varying the concentration of air in the vapor space affected heat transfer. Given, however, that the focus of much of this work was on flow visualization

and PIV, the flow cell used here was optimized for optical access, and therefore had quite poor performance in terms of heat transfer

Nevertheless, heat transfer in this flow has three major parts: 1) conduction through the fused-quartz walls of the flow cell; 2) conduction and advection through the liquid; and 3) conduction and advection through the vapor space. Moreover, heat exchange with the surroundings is also likely to be significant because the test cell is not insulated, and is simply exposed to ambient conditions. Calculating the contributions of each of these parts to the overall heat transfer is impractical because this would require details of the temperature and concentration fields. The contributions of all three parts are instead lumped here into the overall heat transfer coefficient U, which is commonly used to determine heat transfer in heat exchangers, by assuming 1D heat transfer,

$$q_{\mathrm{av}} = UA_{\mathrm{c}}\Delta T \tag{5-2}$$

where q_{av} is the total power going through the test cell, A_{c} is the cross-section area of test cell (*i.e.*, the surface area of the end), and ΔT is the applied temperature difference, which is measured by the thermocouples incorporated at the two ends.

The power q_{av} was obtained from the current and voltage used to drive the thermoelectric heater and cooler (details of these calculations are available in Appendix E). In order to isolate the net heat transfer due to buoyancy-Marangoni convection, the characteristics were first measured for a baseline case, where an empty (*i.e.*, evacuated) test cell was heated and cooled to a similar conditions in terms of actual temperatures as those for the actual experiments, to estimate conduction through the wall and heat exchange with the surroundings, at least at a room temperature to that in the actual experiments. Then the difference between the total power measured in the actual experiment and that for the baseline case should give a reasonable estimate of the net contribution to heat transfer due to conduction and advection in both liquid and gas phases.

Since the test cell was not insulated, the heat loss near the heated end (and heat gain near the cooled end) from the fused quartz walls (*i.e.*, the top, bottom, front and back walls)

was estimated, by modeling the thermal transport as natural convection from a flat plate in air. In this conservative estimate, the temperature was assumed to vary linearly in x, which should overestimate the heat exchange with the surroundings, since the largest temperature gradients will be across the thermal boundary layers next to the heated and cooled ends. For the applied temperature difference $\Delta T = 6$ °C studied here, the heat transfer coefficients (HTC) obtained from natural-convection correlations (Incropera *et al.* 2007) vary from 4 W/(m^{2}K) to 7.6 W/(m^{2}K), depending on whether the walls are horizontal or vertical side walls. Using these HTC values, the heat loss over the heated half of the test cell and the heat gain over the cooled half of the test cell are both ~10 mW. These conservative estimates indicate that the heat transferred to the surroundings is negligible even at the lowest powers of 0.15 W used in these experiments. This estimate also suggests that most of the heat loss (or gain) for this configuration occurs right at the heater (or cooler) and the copper blocks (instead of the side walls of the test cell), and these losses and gains are therefore estimated with reasonable accuracy in the baseline experiment.

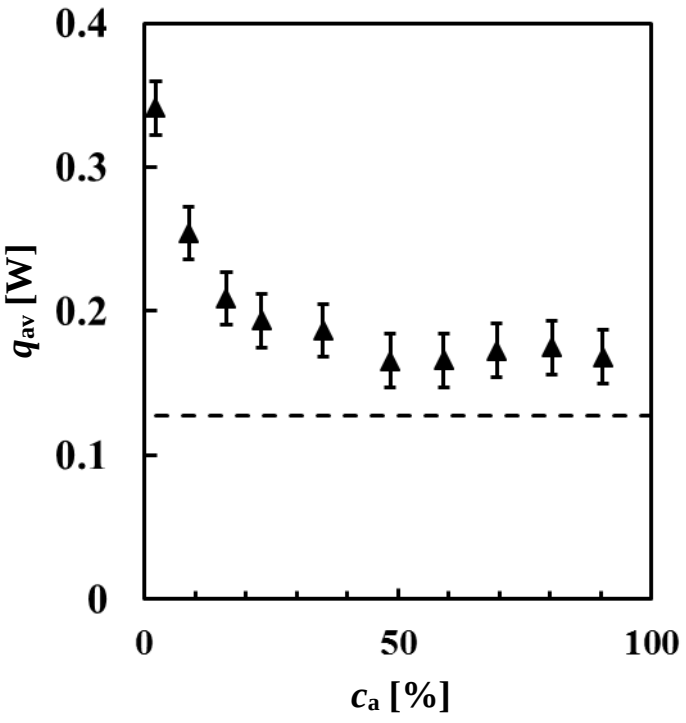

Figure 5.28 Variation of total average power with air concentration c_a in the vapor space, for C_M = 57.8% and ΔT = 6.0 – 6.2 °C; the error bars are uncertainties in measured power, and the dashed line indicates the baseline case.

Figure 5.28 plots total power, the average of the power input to the heater at the heated end and the power removed by the cooler at the cooled end, as a function of the air concentration in the vapor space c_a, for C_M = 57.8% and ΔT = 6.0 – 6.2 °C. The error bars denote the uncertainty in the measured power from an error propagation analysis (calculations are available in Appendix E). The dashed line in the figure gives the baseline case power, *i.e.*, the total power required to heat and cool an empty test cell at ΔT = 6.0 °C. The total power is almost constant for $c_a > 10\%$, presumably because where phase change is suppressed by the noncondensables and it increases significantly when $c_a < 10\%$ (*i.e.*, for c_a = 2.2% and 8.8%). Quantifying the contribution due to advection heat transfer requires measuring both the velocity and temperature fields, which is impractical. If we assume instead that the heat transfer due to advection through the liquid is comparable for these two cases based on the observation that the velocity magnitudes are comparable (Figs. 5.7 and 5.12), the total power difference between these two cases, which would then presumably be due to enhanced phase change, is 0.17W. Using an estimate of the latent heat of this mixture of 1.19×10^6 J/kg from the UNIFAC model, the rate of phase change at c_a = 2.2% is therefore approximately 0.14 mg/s, which yields $Re \approx 2$ based on the average vapor speed in the vapor space.

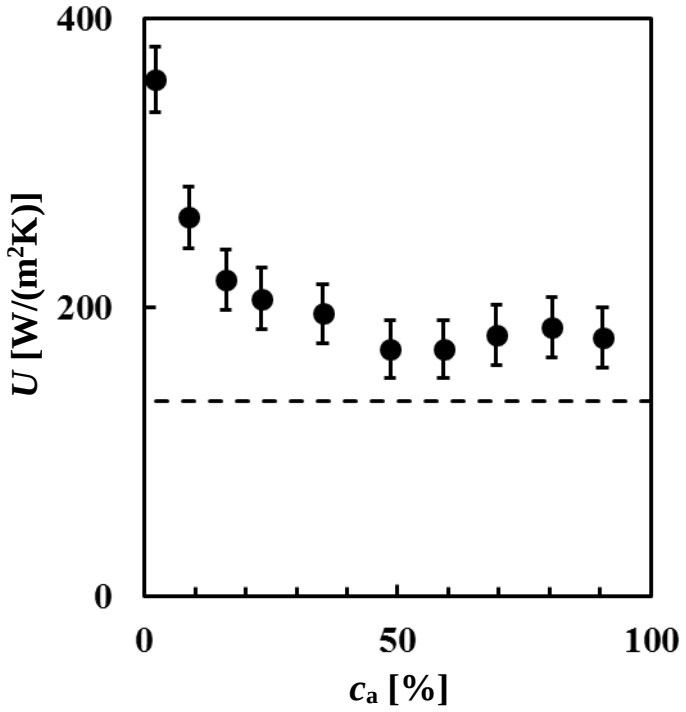

Figure 5.29 Variation of overall heat transfer coefficient with air concentration c_a in the vapor space, for C_M = 57.8% and ΔT = 6.0 – 6.2 °C; the error bars are uncertainties and the dashed line indicates the overall heat transfer coefficient based on baseline power.

Figure 5.29 shows the corresponding overall heat transfer coefficient as a function of c_a. The error bars indicate the uncertainties and the dashed line indicates the overall heat transfer coefficient for the baseline case. As expected, the maximum overall heat transfer coefficient is only a few hundred W/(m^{2}K), and therefore much lower than the values achieved by the state-of-art evaporative cooling techniques. The *local* heat transfer coefficient should however be larger, since evaporation is thought to occur for the most part over a small portion of the interface near the contact line.

The overall heat transfer coefficient for convection in pure MeOH with the vapor space dominated by its own vapor (*i.e.*, c_a = 2.1%) was experimentally determined using a similar procedure to be U = 491 W/(m^{2}K), which is much larger than any of the cases shown in Figure 29, presumably due to enhancement in advection heat transfer in the liquid

phase. So no advantage in terms of heat transfer performance was observed for convection in binary fluids (*i.e.*, reversing the direction of the interfacial flow) *in this configuration*, comparing the cases for $C_M = 57.8\%$ and $c_a = 2.2\%$ case and $C_M = 100\%$ and $c_a = 2.1\%$.

That binary-fluid coolants offer no advantage in this configuration over simple fluids, which is expected because the experiments in this thesis consider a relatively thick liquid layer, where there is always a return flow. The potential advantage of binary-fluid coolants is instead in thin film cooling applications, where the flow in a much thinner liquid layer is instead unidirectional (with no return flow near the bottom). Here, solutocapillarity in binary-fluid coolants should, by reducing the flow away from hot spots (driven by thermocapillarity), improve heat transfer performance compared with simple fluids. The results shown here have nevertheless clearly demonstrated that solutocapillarity, even in this thick liquid layer, can overcome thermocapillarity (and buoyancy) to drive liquid towards hot spots in the near-absence of noncondensables, and that solutocapillarity can overcome thermocapillarity even when there is still a small amount of air present in the vapor space above the liquid.

5.4 Summary

In summary, these results clearly demonstrate that buoyancy-Marangoni convection in a volatile confined binary-liquid layer differs significantly from that in a simple fluid. Flow visualizations and particle-image velocimetry (PIV) results suggest that the air concentration c_a in the vapor space above and the methanol concentration C_M in the liquid layer have a marked effect on this flow. Specifically, reducing the concentration of noncondensables appears to enhance phase change and hence solutocapillarity. Reducing C_M appears to also enhance solutocapillarity by increasing $\partial\sigma / \partial C_M$.

This initial investigation classified this flow into four distinct flow regimes for a H_2O-MeOH mixture driven by a temperature difference $\Delta T \approx 6$ °C. These four regimes—thermocapillarity-dominated flow (TDF), solutocapillarity-dominated flow (SDF),

reversed flow (RF) and unsteady flow (UF) —are summarized in a flow regime map in the c_a - C_M space. Thermocapillarity-dominated flow occurs under air at ambient conditions (*e.g.* c_a = 90% – 96%). Numerical simulations in binary fluids show that noncondensables increase the interfacial temperature gradient, in part by suppressing phase change, and hence enhance thermocapillarity (Qin *et al.* 2012). Solutocapillarity-dominated flow occurs under a vapor space at low c_a (*e.g.* c_a = 1.5% – 4%), and the liquid near the interface then flows towards the heated end over the entire liquid layer. The maximum interfacial speed in SDF is roughly proportional to $\partial\sigma/\partial C_M$, in agreement with a scaling analysis based on the prediction of lubrication theory. Reversed flow occurs when C_M and c_a are both relatively low. We speculate that relatively strong differential evaporation at the interface for this range of parameters leads to a severely MeOH-depleted region, where solutocapillarity is so weak that the flow is dominated by thermocapillarity and buoyancy, both driving the flow away from the heated wall. Unsteady flow occurs at intermediate c_a, where we conjecture that thermocapillarity and solutocapillarity are comparable at the interface, and the velocity fluctuations observed in this regime are due to competition between buoyancy, thermocapillarity and solutocapillarity. Unfortunately, quantitative characterization of these fluctuations is beyond the scope of this work.

Estimates of the overall heat transfer coefficient show that c_a has a significant effect on the heat transfer. The overall heat transfer coefficient is essentially constant for c_a = 10 – 90%, but then increases significantly when c_a is reduced from 10% to ~ 2%. Finally, no benefit was observed in terms of heat transfer when solutocapillarity "reversed" the direction of the interfacial flow in this specific configuration. Nevertheless, these results demonstrate that solutocapillarity can overcome thermocapillarity and reverse the flow at the interface so that liquid flows towards the heated end, suggesting that there could be significant heat transfer enhancement in convection in a thin film where buoyancy is negligible and the flow becomes *unidirectional*.

As mentioned in Chapter 1, the surface tension decreases with temperature for almost all the simple fluids used in conventional evaporative cooling device, and so thermocapillary stresses will tend to "pull" coolant away from hot spots. This thermocapillary-driven dryout was proposed as the primary mechanism responsible for the degradation in thermal performance observed for axially grooved heat pipes when noncondensables were present (Eninger and Marcus, 1978). Although the experimental conditions and geometry considered in our study differ significantly from that of actual evaporative cooling devices, such as heat pipes, where the orientation of heating and cooling surfaces differs from that of the present study, we have shown that: 1) the adverse effects of thermocapillarity can be overcome by solutocapillarity in regular binary mixtures, and 2) solutocapillarity could be an additional mechanism for pumping the coolant from the cold to the hot side, which should improve the thermal performance of these devices.

Moreover, a few studies have proposed a new type of *wickless* heat pipe, which is essentially a glass cuvette of 1 cm (H) × 1 cm (W) × 3.9 cm (L) heated and cooled at the two vertical end walls, similar to the configuration in our study, and partially filled with a layer of "self-rewetting" fluid (Savino *et al.* 2007). The heat transfer studies on these model wickless heat pipes have verified their feasibility and shown that the equivalent thermal conductivity nearly doubled when a "self-rewetting" fluid was used as the coolant, compared with pure water. Our study suggests, however, that the binary coolant in such a wickless heat pipe does not necessarily have to be "self-rewetting": a regular binary mixture may also, under appropriate conditions, have solutocapillary stresses that overcome thermocapillary stresses. If so, this work could significantly expand the range of binary-fluid coolants and the range of operating temperatures for such wickless heat pipes.

CHAPTER 6

CONCLUSIONS AND RECOMMENDATIONS

This chapter summarizes the conclusions of the thesis work on buoyancy-Marangoni convection in both simple and binary fluids. The major contributions of this work and recommendations for future research directions are also presented.

6.1 Conclusions

As stated in Chapter 1, the objectives of this doctoral thesis are to: 1) Quantify buoyancy-thermocapillary convection in a volatile simple fluid in a sealed rectangular geometry in terms of the velocity field and the flow regimes, especially in the unsteady flow regime, and determine how noncondensables affect the flow regimes in, and hence stability of, this flow. 2) Clarify the flow characteristics in terms of the velocity field for buoyancy-Marangoni convection in a binary fluid, specifically a water-methanol mixture where solutocapillarity opposes thermocapillarity, driven by a horizontal temperature gradient. 3) Identify the range of parameters where solutocapillarity overcomes thermocapillarity and drives the liquid towards hot regions in terms of liquid-phase composition and the relative concentration of noncondensables in the vapor space. The conclusions drawn from this work are detailed in the following subsections.

6.1.1 Buoyancy-Thermocapillary Convection in Simple Fluid

Buoyancy-thermocapillary convection in a layer of a volatile silicone oil subjected to a horizontal temperature gradient was investigated experimentally under a vapor space containing 14% to 96% air at pressures ranging from 4.8 kPa to 101 kPa, respectively. The spatially averaged velocity data in the center of the layer (*i.e.*, away from the end and side walls) were fitted to an analytical solution for steady uniform flow to estimate the average layer depth and interfacial temperature gradient. These estimates were used to calculate the

interfacial Marangoni number for these flows for different flow regimes. In agreement with other experimental and numerical studies, steady unicellular flow (SUF), steady multicellular (SMC) flow and oscillatory multicellular (OMC), or time-dependent, flow are observed at ambient conditions (*i.e.*, 96% air). In this thesis, we define a fourth regime, partial multicellular (PMC) flow to clarify the transition from SUF to SMC, which occurs over a range of Marangoni number. Particle pathline visualizations and particle-image velocimetry (PIV) measurements of the flow in the OMC regime show that the flow involves a single oscillating cell near the heated end, with multiple cells traveling towards the cooled end. Moreover, the time scales of OMC flow appear to be consistent with a convective instability of the thermal boundary layer formed along the free surface above the oscillating convection cell.

The average concentration of noncondensables c_a appears to have little effect on the base flow and the flow speed, at least over the range of c_a considered here. It does, however, have a major effect on the flow stability. The critical Marangoni numbers for transition between the various flow regimes (here, SUF, PMC, SMC and OMC) increase as c_a decreases, with OMC flow only observed for convection at high c_a (> 57%), and SMC flow only observed for convection at moderate to high c_a (> 36%). Moreover, the actual values observed in these experiments are in good agreement with the predictions from linear stability analysis.

6.1.2 Buoyancy-Marangoni Convection in Volatile Binary Fluids

As expected, the results from these initial binary-fluid experiments clearly demonstrate that the flow is significantly more complicated for a confined volatile binary-liquid layer. The air concentration in the vapor space above the liquid layer c_a has a significant effect on this flow, as in the case of a simple fluid. Reducing c_a enhances phase change and hence solutocapillarity. The composition of the actual binary liquid, specified here in terms of the methanol concentration C_M, also has a marked effect. Specifically,

reducing C_M also enhances solutocapillarity because $\partial\sigma/\partial C_M$ for this binary fluid increases as C_M decreases.

This initial investigation of a H_2O-MeOH mixture driven by a temperature difference $\Delta T \approx 6$ °C classified the resulting flow into four flow regimes. These regimes—solutocapillarity-dominated flow (SDF), thermocapillarity-dominated flow (TDF), reversed flow (RF) and unsteady flow (UF)—are summarized in a flow regime map of c_a *vs.* C_M. In solutocapillarity-dominated flow, which occurs at low c_a (*e.g.* $c_a < 6\%$), the liquid near the interface then flows towards the heated end over the entire liquid layer. The maximum interfacial speed in SDF is roughly proportional to $\partial\sigma/\partial C_M$, in agreement with a scaling analysis based on the lubrication theory. Thermocapillarity-dominated flow occurs at high values of c_a (*e.g.* $c_a > 90\%$). Numerical simulations in binary fluids show that increasing the noncondensables concentration increases the interfacial temperature gradient, in part by suppressing phase change, and hence thermocapillarity is enhanced for large c_a (Qin, *et al*, 2012). Reversed flow occurs at relatively low values of C_M and c_a. Since there should still be significant differential evaporation at the interface for these values of c_a, we speculate that there is a severely MeOH-depleted region near the heated end, where solutocapillarity is so weak that the flow is dominated by thermocapillarity and buoyancy, both driving the flow away from the heated wall. Finally, unsteady flow occurs at intermediate c_a, where we conjecture that thermocapillarity, and solutocapillarity are comparable at the interface, and the competition between buoyancy, thermocapillarity and solutocapillarity leads to significant velocity fluctuations.

Estimates of the overall heat transfer coefficient show that it is essentially constant for $c_a = 10 - 90\%$, but then increases significantly when c_a is reduced from 10% to ~2%. There appears to be no benefit, at least in terms of heat transfer, when solutocapillarity "reverses" the direction of the interfacial flow in this specific configuration. Nevertheless, these results demonstrate that solutocapillarity can overcome thermocapillarity and reverse

the flow at the interface so that liquid flows towards the heated end, suggesting that there could be significant heat transfer enhancement when the flow becomes *unidirectional*. In this limit (and only in this limit), solutocapillarity should suppress dryout, unlike thermocapillarity which enhances it.

6.2 Contributions

The main contributions of this work on buoyancy-Marangoni in simple and binary fluids are:

For thermocapillary-buoyancy convection in a simple fluid:

1) Experimental results that show that the concentration of noncondensables in the vapor space c_a has a major effect on flow stability, even though c_a appears to have little effect on the base flow and its speed. This suggests that transport in both the vapor and liquid phases as well as phase change must be considered in modeling such a problem, and the effects of noncondensables can only really be explained or understood by taking *vapor-phase transport* into account.
2) Characterization of the oscillatory flow: *oscillatory* multicells in literatures may not be the correct term for this flow, since our velocity field data over the central vertical plane shows the OMC flow is a combination of one oscillating cell near the heated end and multiple cells that travel towards the cooled end, at least in this flow configuration. The oscillation period of the roll near the heated end is consistent with the time scale for a convective instability of the thermal boundary layer at the free surface near the heated end.

For buoyancy-Marangoni convection in binary fluids:

3) Demonstration that solutocapillarity is strong when most, *but not necessarily all*, of the air is removed from the vapor space and solutocapillarity can overcome thermocapillarity and drive the liquid towards hot regions even in a binary fluid that is not self-rewetting, which gives the possibility of much more choices of

coolants and therefore possibly (although not shown in this work) a wider range of operating temperatures, in evaporative cooling.

4) Identification of four flow regimes (*i.e.*, TDF, SDF, RF, and UF) in buoyancy-Marangoni convection in H_2O-MeOH mixtures driven by an applied temperature difference $\Delta T \approx 6$ °C, summarized in a flow regime map of c_a *vs.* C_M. Initial observations of UF that suggest that the velocity fluctuations in this flow regime have a fairly broad spectrum, which means that the flow is aperiodic despite the presence of a strong sub-Hz frequency peak

6.3 Recommendations for Future Work

There remain a number of unresolved issues in flows driven by solutocapillarity (in mixtures), thermocapillarity, and buoyancy. This section therefore briefly summarizes recommendations for future studies.

The most interesting heat transfer aspect of this work is the ability to reduce film dryout using solutocapillary stresses. Studies of unidirectional convection in SDF in a thin film of a binary fluid (where buoyancy is negligible and there is no return flow), and quantification of the *flow field* and *heat transfer* (especially near the heated end) in such a flow, would determine whether solutocapillarity, by driving the flow towards "hot spots," provides a measurable benefit in terms of thermal performance.

Further fundamental studies of Marangoni convection in binary fluids are also desired, given the preliminary nature of these studies at a single applied temperature difference and for a single fluid (*i.e.*, a methanol-water mixture). At present, it is unknown whether there are more than four flow regimes for *different mixtures*, and how the number of flow regimes and their boundaries are affected by the liquid layer depth, or the applied temperature difference, among other factors in methanol-water *and other mixtures*.

These experiments were limited to a minimum value of c_a due to the limitations of the vacuum pump used here determined by a minimum (partial) air pressure of ~4.4 kPa.

Extending these studies in both simple and binary fluids to lower values of c_a (*i.e.*, < 1%) are recommended, especially since numerical simulations (Qin *et al*. 2015) suggest that buoyancy-thermocapillary convection in simple fluids is quite different from the flows observed here at lower c_a.

This work should also be extended to studies of the effect of c_a on the flow regimes in buoyancy-thermocapillary convection in a thin film. In such flows, hydrothermal waves (HTW) are observed at dynamic Bond numbers $Bo_D < 0.2$, and it is unclear whether and how c_a will affect the HTW regime and the transition from SUF to the HTW regime.

Finally, it is well-known that the aspect ratios of the liquid layer have a significant effect on buoyancy-thermocapillary convection in simple fluids. Given that these experiments were limited to a single geometry, studies of how the flow geometry, including liquid layer aspect ratios, affect the flow and flow regimes in flows driven by solutocapillarity, thermocapillarity and buoyancy would also provide fundamental insight into these phenomena.

APPENDIX A

CALCULATION OF METHANOL CONCENTRATION FROM THE MIXTURE DENSITY

As mentioned before, the MeOH concentration C_M for each case was calculated from measurements of the density of the binary mixture ρ at the end of each experimental run. Since H_2O has a much higher density than MeOH (*i.e.*, 0.998 *vs.* 0.791g/mL at 20 °C), the density of the mixture increases monotonically as C_M increases. So C_M can be uniquely determined from the density of the mixture.

Since H_2O-MeOH is a non-ideal mixture, however, the density is not a linear function of C_M. These non-ideal effects can be accounted for by a "shrinkage" factor f_{sh} (Carr and Riddick, 1951), which is a function of the initial volume ratio. Experimental measurements over volume ratios of MeOH to H_2O before mixing, X_M = 0-100 vol% are fitted to a 9th order polynomial to give

$$f_{sh} = p_1 X_M^9 + p_2 X_M^8 + p_3 X_M^7 + p_4 X_M^6 + p_5 X_M^5 + p_6 X_M^4 + p_7 X_M^3 + p_8 X_M^2 + p_9 X_M + p_{10} \quad \text{(A-1)}$$

where p_1 to p_{10} are the fitting coefficients, given in table A-1.

Table A-1 Fitting coefficients of the "shrinkage" factor data.

p_1	5.919295	p_6	-5.07646
p_2	-25.2348	p_7	0.794462
p_3	43.75692	p_8	-0.1159
p_4	-39.3797	p_9	-0.067
p_5	19.40315	p_{10}	1

Figure A.1 shows the "shrinkage" factor as a function of X_M. The triangles represent the experimental data by Carr and Riddick (1951) and the line represents Equation A-1. Once the "shrinkage" factor is known, the density of the mixture at a given mixing volume ratio X_M

$$\rho = \frac{\rho_M X_M + \rho_W (1 - X_M)}{f} \tag{A-2}$$

where ρ_M is the density of pure MeOH and ρ_W is the density of pure water. The corresponding mole fraction of MeOH C_M for a given mixing volume ratio of X_M is then

$$C_M = \frac{\rho_M X_M / M_M}{\rho_M X_M / M_M + \rho_W (1 - X_M) / M_W} \tag{A-3}$$

where M_M and M_W the molar masses of MeOH and H_2O, respectively. Therefore, by combing Equations (A-1), (A-2) and (A-3), one can obtain the density of MeOH-H2O mixture at a given C_M.

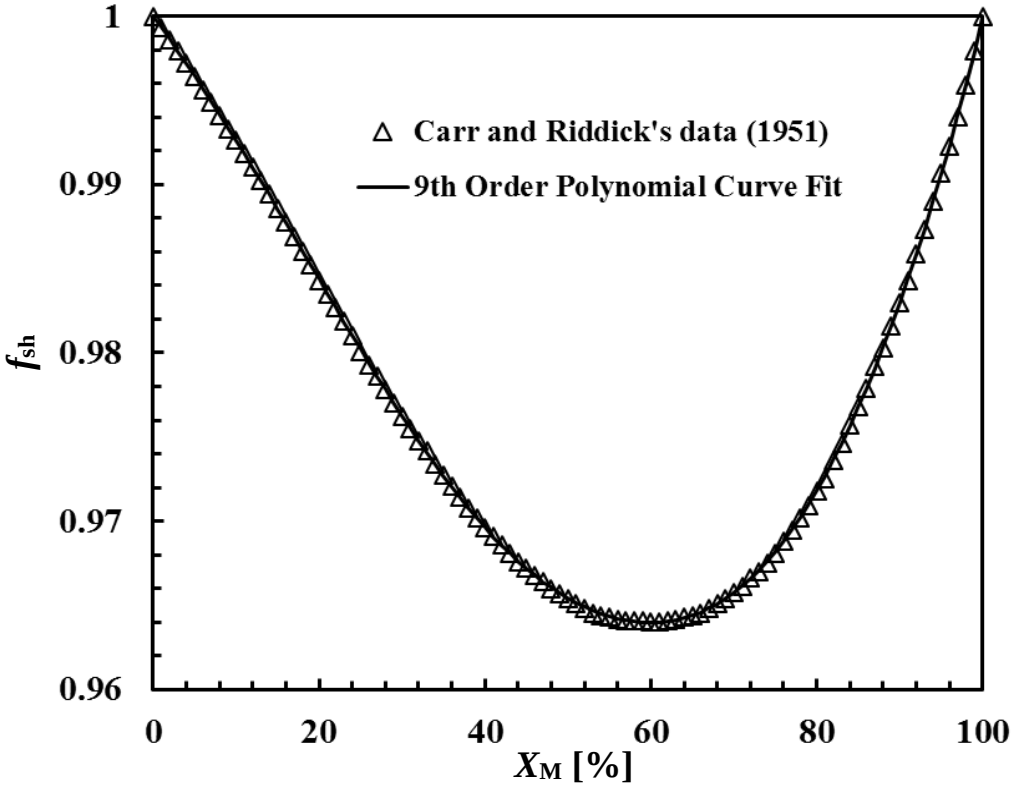

Figure A.1 The "shrinkage" factor of mixing as a function of MeOH volume ratio X_M.

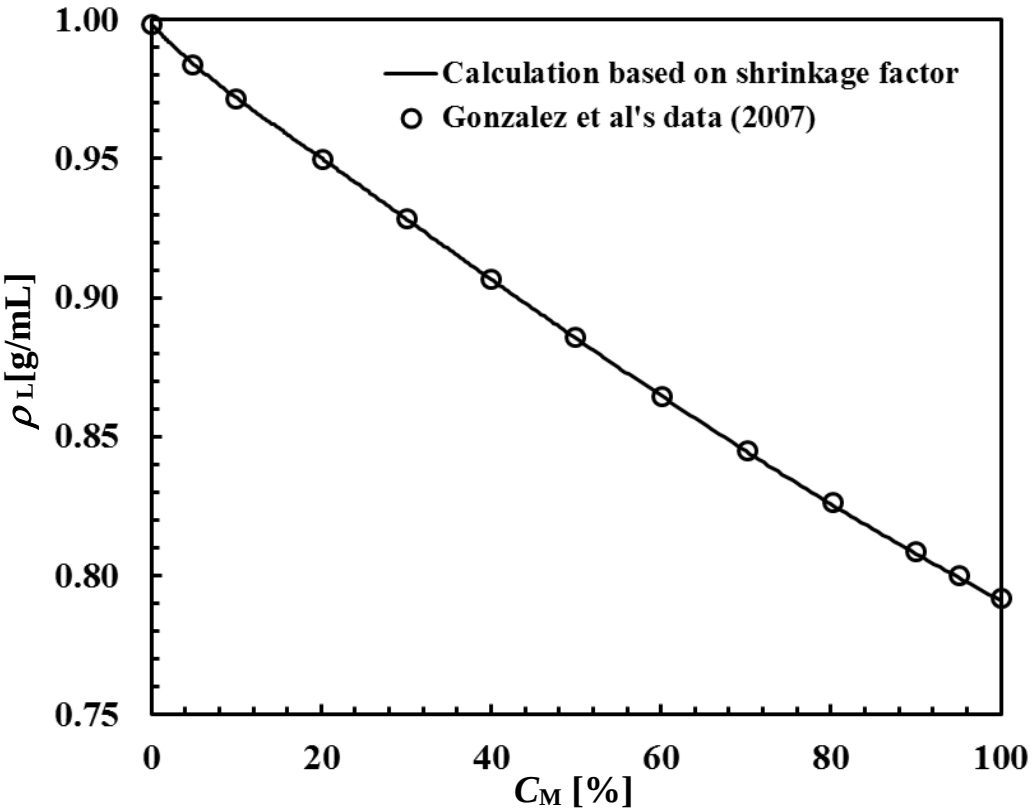

Figure A.2 Density of MeOH-H2O mixture as a function of MeOH concentration C_M.

Figure A.2 shows the density of a MeOH-H2O mixture as a function of MeOH concentration C_M. The line represents value calculated using the "shrinkage" factor, while the points represent the experimental measurements by Gonzalez *et al*. (2007). The calculated value is in excellent agreement with the experimental measurements. In order to determine C_M from the mixture density, ρ, a lookup table (Table A-2) was generated over the entire range of $0 \leq C_M \leq 1$ at increments of 0.2 mol% at 20 °C, which is the average room temperature for the binary-fluid experiments.

Table A-2 The lookup table for C_M from mixture density ρ_L .

C_M [%]	ρ_L [g/mL]	C_M [%]	ρ_L [g/mL]	C_M [%]	ρ_L [g/mL]
0.0	0.9982	8.0	0.9766	16.0	0.9588
0.2	0.9976	8.2	0.9761	16.2	0.9584
0.4	0.9969	8.4	0.9757	16.4	0.9580
0.6	0.9963	8.6	0.9752	16.6	0.9576
0.8	0.9957	8.8	0.9747	16.8	0.9571
1.0	0.9951	9.0	0.9743	17.0	0.9567
1.2	0.9945	9.2	0.9738	17.2	0.9563
1.4	0.9939	9.4	0.9733	17.4	0.9558
1.6	0.9933	9.6	0.9729	17.6	0.9554
1.8	0.9928	9.8	0.9724	17.8	0.9550
2.0	0.9922	10.0	0.9720	18.0	0.9545
2.2	0.9916	10.2	0.9715	18.2	0.9541
2.4	0.9911	10.4	0.9711	18.4	0.9537
2.6	0.9905	10.6	0.9706	18.6	0.9533
2.8	0.9899	10.8	0.9702	18.8	0.9528
3.0	0.9894	11.0	0.9697	19.0	0.9524
3.2	0.9888	11.2	0.9693	19.2	0.9520
3.4	0.9883	11.4	0.9688	19.4	0.9515
3.6	0.9877	11.6	0.9684	19.6	0.9511
3.8	0.9872	11.8	0.9679	19.8	0.9507
4.0	0.9867	12.0	0.9675	20.0	0.9502
4.2	0.9861	12.2	0.9671	20.2	0.9498
4.4	0.9856	12.4	0.9666	20.4	0.9494
4.6	0.9851	12.6	0.9662	20.6	0.9489
4.8	0.9845	12.8	0.9658	20.8	0.9485
5.0	0.9840	13.0	0.9653	21.0	0.9481
5.2	0.9835	13.2	0.9649	21.2	0.9477
5.4	0.9830	13.4	0.9644	21.4	0.9472
5.6	0.9825	13.6	0.9640	21.6	0.9468
5.8	0.9820	13.8	0.9636	21.8	0.9464
6.0	0.9815	14.0	0.9631	22.0	0.9459
6.2	0.9810	14.2	0.9627	22.2	0.9455
6.4	0.9805	14.4	0.9623	22.4	0.9450
6.6	0.9800	14.6	0.9619	22.6	0.9446
6.8	0.9795	14.8	0.9614	22.8	0.9442
7.0	0.9790	15.0	0.9610	23.0	0.9437
7.2	0.9785	15.2	0.9606	23.2	0.9433
7.4	0.9780	15.4	0.9601	23.4	0.9429
7.6	0.9776	15.6	0.9597	23.6	0.9424
7.8	0.9771	15.8	0.9593	23.8	0.9420

Table A-3 The lookup table for C_M from mixture density ρ_L (continued).

C_M [%]	ρ_L [g/mL]	C_M [%]	ρ_L [g/mL]	C_M [%]	ρ_L [g/mL]
24.0	0.9416	32.0	0.9240	40.0	0.9066
24.2	0.9411	32.2	0.9236	40.2	0.9062
24.4	0.9407	32.4	0.9231	40.4	0.9058
24.6	0.9403	32.6	0.9227	40.6	0.9053
24.8	0.9398	32.8	0.9223	40.8	0.9049
25.0	0.9394	33.0	0.9218	41.0	0.9045
25.2	0.9389	33.2	0.9214	41.2	0.9041
25.4	0.9385	33.4	0.9210	41.4	0.9036
25.6	0.9381	33.6	0.9205	41.6	0.9032
25.8	0.9376	33.8	0.9201	41.8	0.9028
26.0	0.9372	34.0	0.9196	42.0	0.9023
26.2	0.9368	34.2	0.9192	42.2	0.9019
26.4	0.9363	34.4	0.9188	42.4	0.9015
26.6	0.9359	34.6	0.9183	42.6	0.9011
26.8	0.9354	34.8	0.9179	42.8	0.9006
27.0	0.9350	35.0	0.9175	43.0	0.9002
27.2	0.9346	35.2	0.9170	43.2	0.8998
27.4	0.9341	35.4	0.9166	43.4	0.8994
27.6	0.9337	35.6	0.9162	43.6	0.8989
27.8	0.9332	35.8	0.9157	43.8	0.8985
28.0	0.9328	36.0	0.9153	44.0	0.8981
28.2	0.9324	36.2	0.9149	44.2	0.8976
28.4	0.9319	36.4	0.9144	44.4	0.8972
28.6	0.9315	36.6	0.9140	44.6	0.8968
28.8	0.9310	36.8	0.9135	44.8	0.8964
29.0	0.9306	37.0	0.9131	45.0	0.8959
29.2	0.9302	37.2	0.9127	45.2	0.8955
29.4	0.9297	37.4	0.9122	45.4	0.8951
29.6	0.9293	37.6	0.9118	45.6	0.8947
29.8	0.9288	37.8	0.9114	45.8	0.8943
30.0	0.9284	38.0	0.9109	46.0	0.8938
30.2	0.9280	38.2	0.9105	46.2	0.8934
30.4	0.9275	38.4	0.9101	46.4	0.8930
30.6	0.9271	38.6	0.9097	46.6	0.8926
30.8	0.9267	38.8	0.9092	46.8	0.8921
31.0	0.9262	39.0	0.9088	47.0	0.8917
31.2	0.9258	39.2	0.9084	47.2	0.8913
31.4	0.9253	39.4	0.9079	47.4	0.8909
31.6	0.9249	39.6	0.9075	47.6	0.8904
31.8	0.9245	39.8	0.9071	47.8	0.8900

Table A-4 The lookup table for C_M from mixture density ρ_L (continued).

C_M [%]	ρ_L [g/mL]	C_M [%]	ρ_L [g/mL]	C_M [%]	ρ_L [g/mL]
48.0	0.8896	56.0	0.8729	64.0	0.8567
48.2	0.8892	56.2	0.8725	64.2	0.8563
48.4	0.8888	56.4	0.8721	64.4	0.8559
48.6	0.8883	56.6	0.8717	64.6	0.8555
48.8	0.8879	56.8	0.8713	64.8	0.8551
49.0	0.8875	57.0	0.8709	65.0	0.8547
49.2	0.8871	57.2	0.8705	65.2	0.8543
49.4	0.8867	57.4	0.8701	65.4	0.8539
49.6	0.8862	57.6	0.8696	65.6	0.8535
49.8	0.8858	57.8	0.8692	65.8	0.8531
50.0	0.8854	58.0	0.8688	66.0	0.8527
50.2	0.8850	58.2	0.8684	66.2	0.8523
50.4	0.8846	58.4	0.8680	66.4	0.8519
50.6	0.8842	58.6	0.8676	66.6	0.8515
50.8	0.8837	58.8	0.8672	66.8	0.8511
51.0	0.8833	59.0	0.8668	67.0	0.8507
51.2	0.8829	59.2	0.8664	67.2	0.8503
51.4	0.8825	59.4	0.8660	67.4	0.8499
51.6	0.8821	59.6	0.8656	67.6	0.8495
51.8	0.8816	59.8	0.8652	67.8	0.8491
52.0	0.8812	60.0	0.8647	68.0	0.8487
52.2	0.8808	60.2	0.8643	68.2	0.8483
52.4	0.8804	60.4	0.8639	68.4	0.8479
52.6	0.8800	60.6	0.8635	68.6	0.8475
52.8	0.8796	60.8	0.8631	68.8	0.8471
53.0	0.8791	61.0	0.8627	69.0	0.8467
53.2	0.8787	61.2	0.8623	69.2	0.8463
53.4	0.8783	61.4	0.8619	69.4	0.8459
53.6	0.8779	61.6	0.8615	69.6	0.8456
53.8	0.8775	61.8	0.8611	69.8	0.8452
54.0	0.8771	62.0	0.8607	70.0	0.8448
54.2	0.8767	62.2	0.8603	70.2	0.8444
54.4	0.8762	62.4	0.8599	70.4	0.8440
54.6	0.8758	62.6	0.8595	70.6	0.8436
54.8	0.8754	62.8	0.8591	70.8	0.8432
55.0	0.8750	63.0	0.8587	71.0	0.8428
55.2	0.8746	63.2	0.8583	71.2	0.8424
55.4	0.8742	63.4	0.8579	71.4	0.8420
55.6	0.8738	63.6	0.8575	71.6	0.8417
55.8	0.8734	63.8	0.8571	71.8	0.8413

Table A-5 The lookup table for C_M from mixture density ρ_L (continued).

C_M [%]	ρ_L [g/mL]	C_M [%]	ρ_L [g/mL]	C_M [%]	ρ_L [g/mL]
72.0	0.8409	80.0	0.8258	88.0	0.8114
72.2	0.8405	80.2	0.8254	88.2	0.8110
72.4	0.8401	80.4	0.8250	88.4	0.8107
72.6	0.8397	80.6	0.8247	88.6	0.8103
72.8	0.8393	80.8	0.8243	88.8	0.8100
73.0	0.8390	81.0	0.8239	89.0	0.8096
73.2	0.8386	81.2	0.8236	89.2	0.8093
73.4	0.8382	81.4	0.8232	89.4	0.8089
73.6	0.8378	81.6	0.8228	89.6	0.8086
73.8	0.8374	81.8	0.8225	89.8	0.8083
74.0	0.8370	82.0	0.8221	90.0	0.8079
74.2	0.8367	82.2	0.8218	90.2	0.8076
74.4	0.8363	82.4	0.8214	90.4	0.8072
74.6	0.8359	82.6	0.8210	90.6	0.8069
74.8	0.8355	82.8	0.8207	90.8	0.8065
75.0	0.8351	83.0	0.8203	91.0	0.8062
75.2	0.8348	83.2	0.8199	91.2	0.8058
75.4	0.8344	83.4	0.8196	91.4	0.8055
75.6	0.8340	83.6	0.8192	91.6	0.8051
75.8	0.8336	83.8	0.8189	91.8	0.8048
76.0	0.8332	84.0	0.8185	92.0	0.8045
76.2	0.8329	84.2	0.8181	92.2	0.8041
76.4	0.8325	84.4	0.8178	92.4	0.8038
76.6	0.8321	84.6	0.8174	92.6	0.8034
76.8	0.8317	84.8	0.8171	92.8	0.8031
77.0	0.8314	85.0	0.8167	93.0	0.8027
77.2	0.8310	85.2	0.8163	93.2	0.8024
77.4	0.8306	85.4	0.8160	93.4	0.8021
77.6	0.8302	85.6	0.8156	93.6	0.8017
77.8	0.8299	85.8	0.8153	93.8	0.8014
78.0	0.8295	86.0	0.8149	94.0	0.8010
78.2	0.8291	86.2	0.8146	94.2	0.8007
78.4	0.8287	86.4	0.8142	94.4	0.8004
78.6	0.8284	86.6	0.8139	94.6	0.8000
78.8	0.8280	86.8	0.8135	94.8	0.7997
79.0	0.8276	87.0	0.8132	95.0	0.7993
79.2	0.8273	87.2	0.8128	95.2	0.7990
79.4	0.8269	87.4	0.8124	95.4	0.7987
79.6	0.8265	87.6	0.8121	95.6	0.7983
79.8	0.8261	87.8	0.8117	95.8	0.7980

Table A-6 The lookup table for C_M from mixture density ρ_L (continued).

C_M [%]	ρ_L [g/mL]	C_M [%]	ρ_L [g/mL]	C_M [%]	ρ_L [g/mL]
96.0	0.7977	97.4	0.7953	98.8	0.7930
96.2	0.7973	97.6	0.7950	99.0	0.7926
96.4	0.7970	97.8	0.7946	99.2	0.7923
96.6	0.7966	98.0	0.7943	99.4	0.7920
96.8	0.7963	98.2	0.7940	99.6	0.7916
97.0	0.7960	98.4	0.7936	99.8	0.7913
97.2	0.7956	98.6	0.7933	100.0	0.7910

EES code for calculating density of MeOH-H2O mixture

```
{specify the temperature and methanol concentration here}
T_0=20 [C]
x_m=0.08

rho_m=Density(Methanol,T=T_0,x=0)/1000
rho_w=Density(Water,T=T_0,x=0)/1000

MW_m=32
MW_w=18

m_m=MW_m*x_m
m_w=MW_w*(1-x_m)

v_m=m_m/rho_m
v_w=m_w/rho_w

x=v_m/(v_m+v_w)

v_tot=f*(v_m+v_w)
m_tot=m_m+m_w

rho_tot=m_tot/v_tot

"non-ideal mixture factor based on the paper Physical Properties of Methanol-Water System"

f = p1*x^9 + p2*x^8 + p3*x^7 + p4*x^6 + p5*x^5 + p6*x^4 + p7*x^3 + p8*x^2 + p9*x + p10
p1 =       5.919295
p2 =     -25.234821555
p3 =      43.756918
p4 =     -39.37968049
p5 =      19.4031506
p6 =     -5.076457
p7 =     0.79446169
p8 =    -0.11590484
p9 =   -0.0670037766
p10 =     1
```

APPENDIX B

CALCULATION OF THE THEORETICAL VAPOR PRESSURE OF METHANOL-WATER MIXTURE

The vapor pressure of MeOH-H2O mixture was obtained using Raoult's law extended to non-ideal mixtures,

$$p_m \cdot \phi_m = p_m^* \cdot \gamma_m \cdot C_M \quad \text{(B-1)}$$

$$p_w \cdot \phi_w = p_w^* \cdot \gamma_w \cdot (1 - C_M) \quad \text{(B-2)}$$

where p_m and p_w are the partial pressures in the vapor phase, ϕ_m and ϕ_w are the fugacity coefficients, γ_m and γ_w are the activity coefficients, and p_m^* and p_w^* are the vapor pressures at a given temperature; the subscripts "m" and "w" denote values for MeOH and H_2O, respectively. The fugacity coefficient, which is a measure of how close the actual vapor is to an ideal gas, are assumed to be 1 for both MeOH and H_2O (Dymond and Smith, 1980), since the pressures and temperatures in this work are much lower than the critical point values and the ideal gas assumption therefore works well.

The activity coefficients γ_m and γ_w, which depend on temperature and C_M, were obtained using the universal quasichemical functional-group activity coefficients (UNIFAC) method, following the procedures described in Fredenslund *et al.* (1975). Figure B.1 shows the activity coefficients of MeOH and H_2O for C_M = 0 – 100 mol% at T = 20 °C, while Figure B.2 compares the vapor pressures of the MeOH-H_2O mixture obtained using Equations B-1 and B-2 with measured values given in the literature at 25 °C and 35 °C (Gmehling and Onken, 2003). These calculations are clearly in excellent agreement with the measured values.

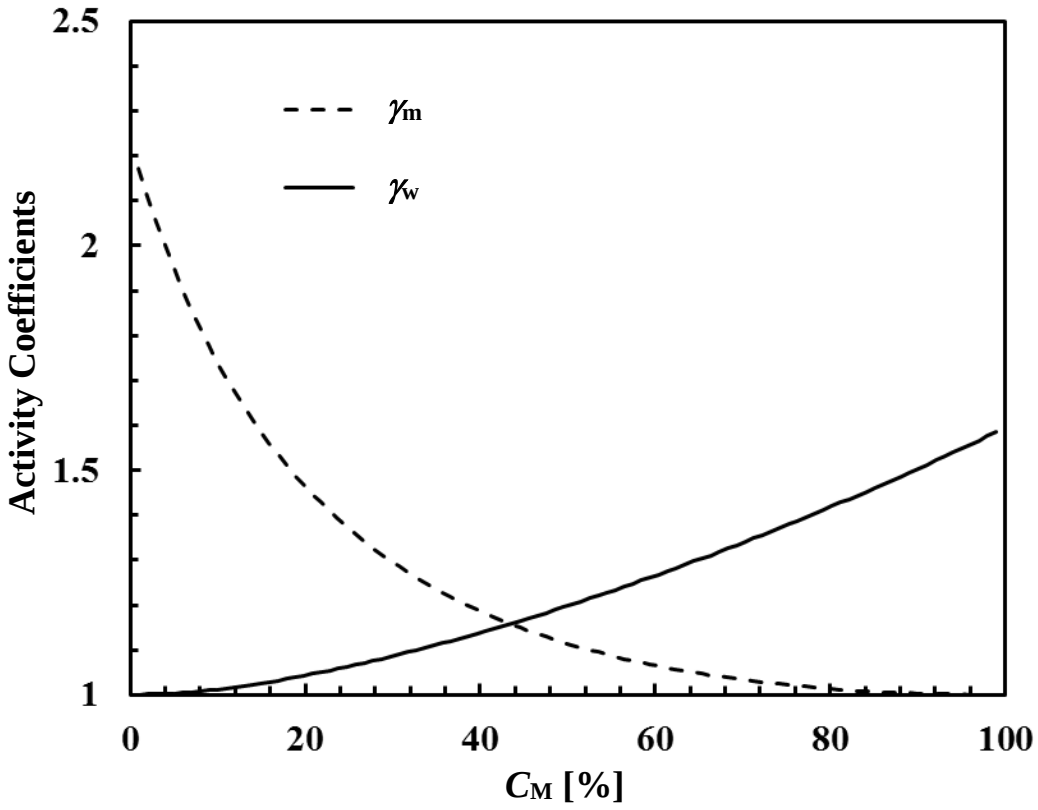

Figure B.1 Activity coefficients of MeOH and H_2O as a function of C_M at T = 20 °C.

The vapor pressure of a simple fluid (*i.e.*, MeOH or H_2O) was determined from the Antoine equation,

$$\log_{10} p_v = A - \frac{B}{C+T} \tag{B-3}$$

where A, B and C, given in table B-1, are constants specific to the fluid, and T is the reference temperature in Kelvin.

Table B-1 Constants of Antoine equation for MeOH and H_2O

	MeOH	H_2O
A	8.08097	8.07131
B	1582.27	1730.63
C	239.7	233.426

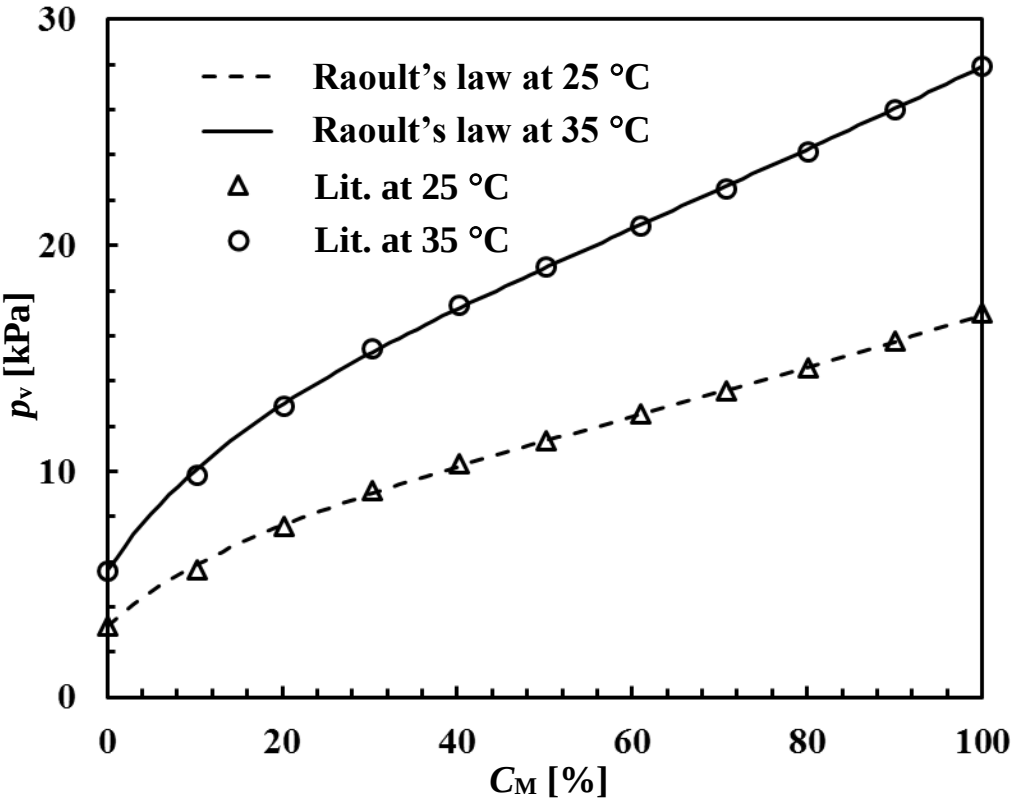

Figure B.2 Comparison of calculated vapor pressures of MeOH-H_2O mixture with literature values at T = 25 °C and 35 °C.

Table B-2 The vapor pressure of MeO-H_2O from Raoult's law (T = 19 °C).

C_M [%]	p_v [kPa]	C_M [%]	p_v [kPa]	C_M [%]	p_v [kPa]
1	2.43	34	6.80	67	9.53
2	2.66	35	6.89	68	9.61
3	2.88	36	6.98	69	9.69
4	3.09	37	7.07	70	9.77
5	3.28	38	7.15	71	9.85
6	3.47	39	7.24	72	9.93
7	3.65	40	7.33	73	10.01
8	3.81	41	7.41	74	10.10
9	3.98	42	7.49	75	10.18
10	4.13	43	7.58	76	10.26
11	4.28	44	7.66	77	10.34
12	4.42	45	7.75	78	10.42
13	4.56	46	7.83	79	10.51
14	4.70	47	7.91	80	10.59
15	4.83	48	7.99	81	10.67
16	4.95	49	8.07	82	10.75
17	5.07	50	8.16	83	10.84
18	5.19	51	8.24	84	10.92
19	5.31	52	8.32	85	11.00
20	5.42	53	8.40	86	11.09
21	5.53	54	8.48	87	11.17
22	5.64	55	8.56	88	11.26
23	5.75	56	8.64	89	11.34
24	5.85	57	8.72	90	11.43
25	5.95	58	8.80	91	11.51
26	6.05	59	8.88	92	11.60
27	6.15	60	8.96	93	11.68
28	6.25	61	9.04	94	11.77
29	6.34	62	9.12	95	11.86
30	6.44	63	9.20	96	11.94
31	6.53	64	9.29	97	12.03
32	6.62	65	9.37	98	12.12
33	6.71	66	9.45	99	12.20

Table B-3 The vapor pressure of MeO-H_2O from Roault's law (T = 20 °C).

C_M [%]	p_v [kPa]	C_M [%]	p_v [kPa]	C_M [%]	p_v [kPa]
1	2.59	34	7.20	67	10.07
2	2.83	35	7.29	68	10.15
3	3.06	36	7.39	69	10.24
4	3.28	37	7.48	70	10.32
5	3.49	38	7.57	71	10.41
6	3.68	39	7.66	72	10.49
7	3.87	40	7.75	73	10.58
8	4.05	41	7.84	74	10.67
9	4.22	42	7.93	75	10.75
10	4.38	43	8.02	76	10.84
11	4.54	44	8.10	77	10.92
12	4.69	45	8.19	78	11.01
13	4.84	46	8.28	79	11.10
14	4.98	47	8.37	80	11.18
15	5.12	48	8.45	81	11.27
16	5.25	49	8.54	82	11.36
17	5.38	50	8.62	83	11.45
18	5.50	51	8.71	84	11.53
19	5.62	52	8.80	85	11.62
20	5.74	53	8.88	86	11.71
21	5.86	54	8.97	87	11.80
22	5.97	55	9.05	88	11.89
23	6.09	56	9.14	89	11.98
24	6.20	57	9.22	90	12.07
25	6.30	58	9.30	91	12.16
26	6.41	59	9.39	92	12.25
27	6.51	60	9.47	93	12.34
28	6.61	61	9.56	94	12.43
29	6.72	62	9.64	95	12.52
30	6.81	63	9.73	96	12.61
31	6.91	64	9.81	97	12.70
32	7.01	65	9.90	98	12.79
33	7.10	66	9.98	99	12.88

Table B-4 The vapor pressure of MeO-H_2O from Roault's law (T = 21 °C).

C_M [%]	p_v [kPa]	C_M [%]	p_v [kPa]	C_M [%]	p_v [kPa]
1	2.75	34	7.62	67	10.63
2	3.01	35	7.71	68	10.72
3	3.25	36	7.81	69	10.81
4	3.48	37	7.91	70	10.90
5	3.70	38	8.01	71	10.99
6	3.90	39	8.10	72	11.08
7	4.10	40	8.20	73	11.17
8	4.29	41	8.29	74	11.26
9	4.47	42	8.38	75	11.35
10	4.64	43	8.48	76	11.44
11	4.81	44	8.57	77	11.54
12	4.97	45	8.66	78	11.63
13	5.12	46	8.75	79	11.72
14	5.27	47	8.84	80	11.81
15	5.42	48	8.93	81	11.90
16	5.56	49	9.03	82	11.99
17	5.69	50	9.12	83	12.09
18	5.83	51	9.21	84	12.18
19	5.96	52	9.30	85	12.27
20	6.08	53	9.39	86	12.36
21	6.20	54	9.47	87	12.46
22	6.32	55	9.56	88	12.55
23	6.44	56	9.65	89	12.64
24	6.56	57	9.74	90	12.74
25	6.67	58	9.83	91	12.83
26	6.78	59	9.92	92	12.93
27	6.89	60	10.01	93	13.02
28	7.00	61	10.10	94	13.12
29	7.11	62	10.19	95	13.21
30	7.21	63	10.28	96	13.31
31	7.31	64	10.37	97	13.40
32	7.42	65	10.46	98	13.50
33	7.52	66	10.55	99	13.60

EES code for calculating vapor pressure of MeOH-H2O mixture

```
{activity coefficient calculation from UNIFAC}
{subscript 1 is methanol and sbuscript 2 is water}
{----------Activity Coefficients Start----------}
T_c=20.5 "temperature in degC"
x_1=0.134 "methanol mole fraction"
x_2=1-x_1
R_5B=1.4311
Q_5B=1.432
R_6=0.92
Q_6=1.4

r_1=R_5B
r_2=R_6
q_1=Q_5B
q_2=Q_6

PHI_1=(r_1*x_1)/(r_1*x_1+r_2*x_2)
PHI_2=(r_2*x_2)/(r_1*x_1+r_2*x_2)

theta_1=(q_1*x_1)/(q_1*x_1+q_2*x_2)
theta_2=(q_2*x_2)/(q_1*x_1+q_2*x_2)

l_1=5*(r_1-q_1)-(r_1-1)
l_2=5*(r_2-q_2)-(r_2-1)

ln(gamma_1_C)=ln(PHI_1/x_1)+5*q_1*ln(theta_1/phi_1)+l_1-PHI_1/x_1*(x_1*l_1+x_2*l_2)
ln(gamma_2_C)=ln(PHI_2/x_2)+5*q_2*ln(theta_2/phi_2)+l_2-PHI_2/x_2*(x_1*l_1+x_2*l_2)

{for methanol, MCOH is 5B, there is only one function group in methanol, for water, H2O is 6}
{UNIFAC energy interaction parameters from
http://www.aim.env.uea.ac.uk/aim/info/UNIFACgroups.html}
a_5B_5B=0
a_6_6=0
a_5B_6=-181
a_6_5B=289.6
PSI_5B_5B=exp(-a_5B_5B/T)
PSI_6_5B=exp(-a_6_5B/T)
PSI_5B_6=exp(-a_5B_6/T)
PSI_6_6=exp(-a_6_6/T)

X_5B_pure=1{for pure methanol}
THETA_5B_1=1
ln(GAMMA_5B_1)=Q_5B*(1-ln(THETA_5B_1*PSI_5B_5B)-1)

X_6_pure=1{for pure water}
THETA_6_2=1
ln(GAMMA_6_2)=Q_6*(1-ln(THETA_6_2*PSI_6_6)-1)

X_5B=x_1{for methanol mole fraction of x}
X_6=1-x_1
THETA_5B=(Q_5B*X_5B)/(Q_5B*X_5B+Q_6*X_6)
THETA_6=(Q_6*X_6)/(Q_5B*X_5B+Q_6*X_6)
```

```
ln(GAMMA_5B)=Q_5B*(1-ln(THETA_5B*PSI_5B_5B+THETA_6*PSI_6_5B)-
((THETA_5B*PSI_5B_5B)/(THETA_5B*PSI_5B_5B+THETA_6*PSI_6_5B)+(THETA_6*PSI_5B
_6)/(THETA_5B*PSI_5B_6+THETA_6*PSI_6_6)))

ln(GAMMA_6)=Q_6*(1-ln(THETA_5B*PSI_5B_6+THETA_6*PSI_6_6)-
((THETA_5B*PSI_6_5B)/(THETA_5B*PSI_5B_5B+THETA_6*PSI_6_5B)+(THETA_6*PSI_6_6)/
(THETA_5B*PSI_5B_6+THETA_6*PSI_6_6)))

gamma_1_R=GAMMA_5B/GAMMA_5B_1

gamma_1=gamma_1_C*gamma_1_R

gamma_2_R=GAMMA_6/GAMMA_6_2

gamma_2=gamma_2_C*gamma_2_R

{----------Activity Coefficients END----------}
{----------Raoult's Law Start----------}
"This program is used to estimate the binary (methanol-water) vapor pressure around room
temperature"
"calculate the vapor pressure from Antoine Equation"
"http://ddbonline.ddbst.com/AntoineCalculation/AntoineCalculationCGI.exe"

T=T_c+273 [K]
A_m=8.08097 "For methanol, valid 15-100 degC"
B_m=1582.27
C_m=239.7

P_m_Hg=10^(A_m-(B_m/(C_m+T_c))) "pressure in mmHg"
P|star_m=P_m_Hg*convert(mmHg, Pa)

A_w=8.07131"For water, valid 1-100 degC"
B_w=1730.63
C_w=233.426

P_w_Hg=10^(A_w-(B_w/(C_w+T_c)))
P|star_w=P_w_Hg*convert(mmHg, Pa)

PHI_w=1"fugacity coefficient"
PHI_m=1

gamma_m=gamma_1"gamma is the activity coefficient"
gamma_w=gamma_2

"x_w and x_m are the mole fraction in liquid phase"
PHI_w*P_w=P|star_w*gamma_w*x_w
PHI_m*P_m=P|star_m*gamma_m*x_m

x_m=x_1
x_w+x_m=1

P=P_w+P_m"Total pressure"
y_m=P_m/P"fraction of methanol vapor in vapor space"
{----------Raoult's Law End----------}
```

APPENDIX C

EXPERIMENTAL CONDITIONS FOR THE BINARY FLUID EXPERIMENTS

Table C-1 Experimental conditions of PIV measurements

Figures	Date	C_M [%]	c_a [%]	m_l [g]	ρ_L [g/mL]	T_h [°C]	T_c [°C]	T_{room} [°C]
Figure 5.7	09/24/2014	58.6	90.4	N/A	0.8676	23.8	17.8	20.7
Figure 5.9	10/26/2014	8.9	95.7	N/A	0.9741	23.9	17.6	20.8
Figure 5.10	10/26/2014	8.9	95.7	N/A	0.9741	23.9	17.6	20.8
Figure 5.11	10/26/2014	8.9	95.7	N/A	0.9741	23.9	17.6	20.8
Figure 5.12	09/24/2014	58.6	3.3	N/A	0.8676	23.6	17.5	20.6
Figure 5.13	10/01/2014	8.9	1.5	1.61	0.9746	23.7	17.6	20.4
Figure 5.14	10/25/2014	8.9	1.5	N/A	0.9741	23.7	17.5	20.6
Figure 5.15	10/25/2014	8.9	1.5	N/A	0.9741	23.7	17.5	20.6
Figure 5.17	09/24/2014	58.6	52	N/A	0.8676	23.1	17.0	20.0
Figure 5.19	03/27/2015	9.3	46	1.60	0.9735	22.8	16.6	19.7

Table C-2 Experimental conditions of the data plotted in Figure 5.16.

Date	Max Vel. [mm/s]	C_M [%]	c_a [%]	m_l [g]	ρ_L [g/mL]	T_h [°C]	T_c [°C]	T_{room} [°C]
10/01/2014	6.57	8.9	1.5	1.61	0.9746	23.7	17.6	20.4
10/24/2014	4.74	12.7	0.5	1.57	0.9661	23.6	17.5	20.5
10/02/2014	2.68	19.7	1.5	1.52	0.9509	23.7	17.6	20.6
10/03/2014	2.14	26.4	2.9	1.42	0.9364	23.5	17.5	20.5
10/21/2014	1.65	40.8	1.5	1.41	0.9049	23.6	17.6	20.7
09/24/2014	1.28	58.6	3.3	N/A	0.8676	23.1	17.0	20.0
03/26/2014	1.20	73.6	1.0	1.26	0.8379	23.0	16.9	19.5

Table C-3 Experimental conditions of the data in Figure 5.6.

Date	C_M [%]	c_a [%]	m_l [g]	ρ_L [g/mL]	T_h [°C]	T_c [°C]	T_{room} [°C]
03/27/2015	9.3	7.4	1.60	0.9661	23.6	17.5	20.5
	9.3	26.5	1.60	0.9509	23.7	17.6	20.6
	9.3	46.1	1.60	0.9364	23.5	17.5	20.5
	9.3	68.5	1.60	0.9049	23.6	17.6	20.7
10/01/2014	8.9	95.7	1.61	0.9746	23.5	17.4	20.5
	8.9	1.5	1.61	0.9746	23.7	17.6	20.4
03/23/2015	9.1	88.2	1.60	0.9740	23.5	17.4	20.3
	9.1	77.6	1.60	0.9740	23.4	17.3	20.3
10/24/2014	12.7	0.5	1.57	0.9661	23.6	17.5	20.5
03/21/2015	14.2	6.4	1.54	0.9627	24.0	17.9	21.1
	14.2	17.9	1.54	0.9627	23.1	17.1	20.2
	14.2	27.3	1.54	0.9627	23.1	17.2	20.2
	14.2	36.4	1.54	0.9627	23.4	17.4	20.7
	14.2	47.0	1.54	0.9627	23.5	17.3	20.5
	14.2	57.3	1.54	0.9627	23.6	17.5	20.7
	14.2	68.4	1.54	0.9627	23.6	17.5	20.7
	14.2	79.3	1.54	0.9627	23.8	17.6	20.8
	14.2	89.2	1.54	0.9627	23.8	17.8	20.9
09/23/2014	13.4	95.2	N/A	0.9644	23.0	17.0	20.0
03/20/2015	27.9	4.1	1.44	0.9329	23.6	17.5	20.6
	27.9	12.6	1.44	0.9329	23.7	17.7	20.9
	27.9	20.4	1.44	0.9329	23.2	17.3	20.7
	27.9	27.7	1.44	0.9329	23.4	17.4	20.6
	27.9	40.7	1.44	0.9329	23.4	17.3	20.6
	27.9	51.4	1.44	0.9329	23.5	17.3	20.6
	27.9	61.1	1.44	0.9329	23.5	17.4	20.5
	27.9	71.5	1.44	0.9329	23.4	17.2	20.3
	27.9	81.0	1.44	0.9329	23.1	17.0	20.2
	27.9	87.0	1.44	0.9329	23.0	17.0	20.1
03/19/2015	39.6	0.9	1.41	0.9077	23.3	17.3	20.4
	39.6	8.6	1.41	0.9077	23.5	17.3	20.6
	39.6	15.2	1.41	0.9077	23.3	17.3	20.7
	39.6	26.5	1.41	0.9077	23.1	17.2	20.8
	39.6	37.2	1.41	0.9077	23.4	17.3	20.7

Table C-4 Experimental conditions of Figure 5.6 (continued).

Date	C_M [%]	c_a [%]	m_l [g]	ρ_L [g/mL]	T_h [°C]	T_c [°C]	T_{room} [°C]
03/19/2015	39.6	47.8	1.41	0.9077	23.7	17.7	20.9
	39.6	58.4	1.41	0.9077	23.8	17.7	20.8
	39.6	68.7	1.41	0.9077	24.0	17.9	20.9
	39.6	79.6	1.41	0.9077	24.0	18.0	21.2
	39.6	92.0	1.41	0.9077	24.2	18.3	21.6
03/18/2015	57.8	2.2	1.32	0.8694	24.1	18.0	20.8
	57.8	8.8	1.32	0.8694	23.8	17.6	21.2
	57.8	16.1	1.32	0.8694	23.9	17.9	21.0
	57.8	23.1	1.32	0.8694	24.0	18.0	21.2
	57.8	35.2	1.32	0.8694	24.1	18.0	21.2
	57.8	48.5	1.32	0.8694	24.1	17.9	21.3
	57.8	59.0	1.32	0.8694	24.1	17.9	21.5
	57.8	69.5	1.32	0.8694	24.1	18.0	21.5
	57.8	80.4	1.32	0.8694	24.2	18.2	21.7
09/24/2014	58.6	90.4	N/A	0.8676	23.8	17.8	20.7
03/26/2015	73.6	1.0	1.26	0.8379	23.0	16.9	19.5
	73.6	8.4	1.26	0.8379	23.0	16.9	19.7
	73.6	19.7	1.26	0.8379	22.8	16.7	19.5
	73.6	21.9	1.26	0.8379	23.0	17.0	19.9
	73.6	35.5	1.26	0.8379	23.1	17.0	20.1
	73.6	47.6	1.26	0.8379	23.3	17.1	20.3
	73.6	57.6	1.26	0.8379	23.6	17.6	20.4
	73.6	69.0	1.26	0.8379	23.6	17.5	20.3
	73.6	79.0	1.26	0.8379	23.4	17.3	20.1
	73.6	89.5	1.26	0.8379	23.4	17.3	20.1

APPENDIX D

PARTICLE PATHLINE VISUALIZATIONS USED TO DETERMINE THE FLOW REGIME MAP FOR BUOYANCY-MARANGONI CONVECTION IN METHANOL-WATER

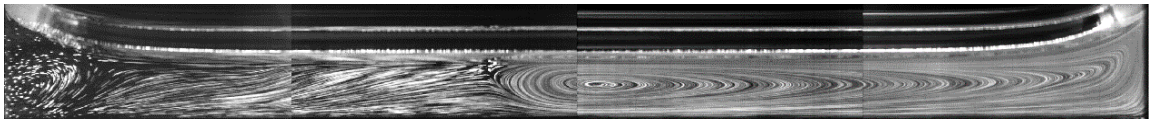

(*a*) C_M = 8.9%, c_a = 95.7%

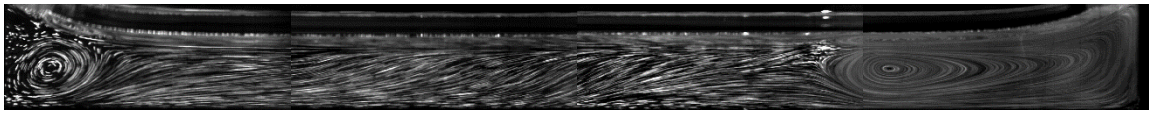

(*b*) C_M = 9.1%, c_a = 88.2%

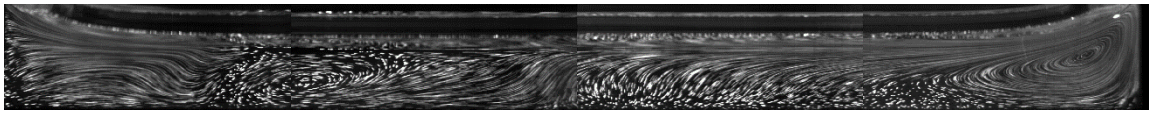

(*c*) C_M = 9.1%, c_a = 77.6%

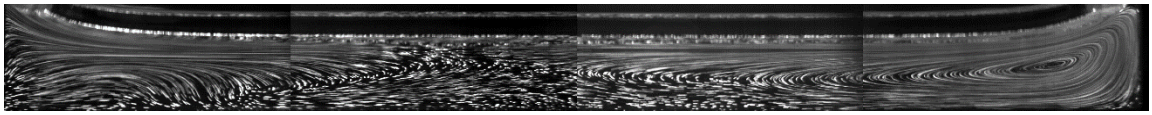

(*d*) C_M = 9.3%, c_a = 68.5%

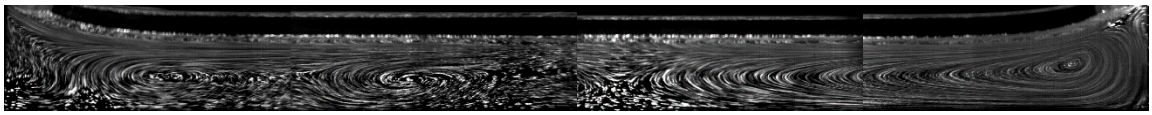

(*e*) C_M = 9.3%, c_a = 46.1%

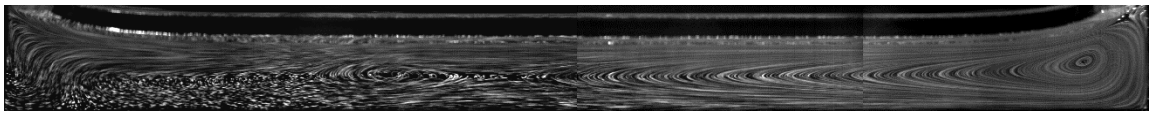

(*f*) C_M = 9.3%, c_a = 26.5%

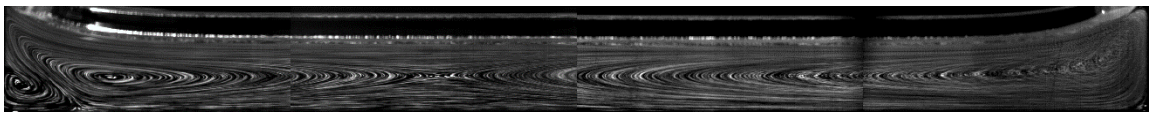

(*g*) C_M = 9.3%, c_a = 7.4%

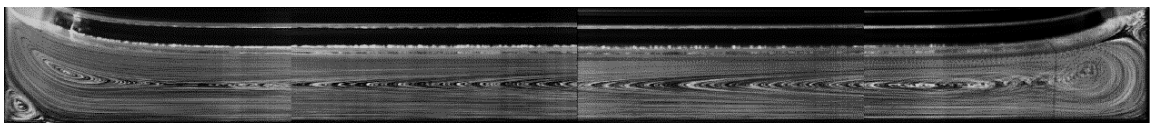

(*h*) C_M = 8.9%, c_a = 1.5%

Figure D.1 Particle pathline visualizations for the binary flow regime map at $C_M \approx 9\%$.

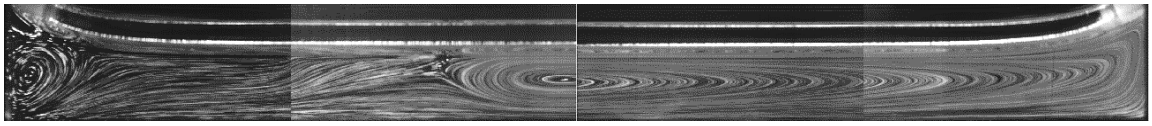

(*a*) C_M = 13.4%, c_a = 95.2%

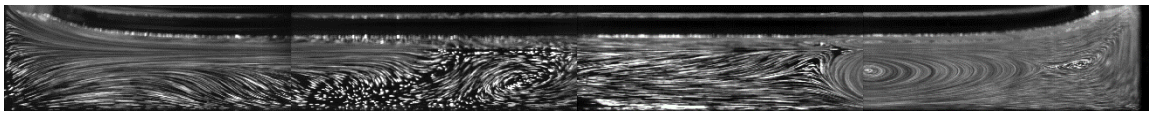

(*b*) C_M = 14.2%, c_a = 79.3%

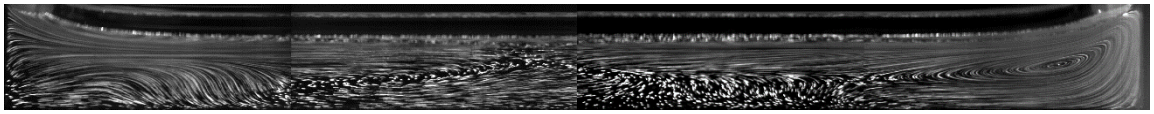

(*c*) C_M = 14.2%, c_a = 68.4%

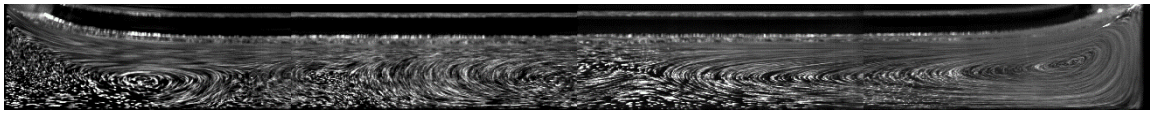

(*d*) C_M = 14.2%, c_a = 57.3%

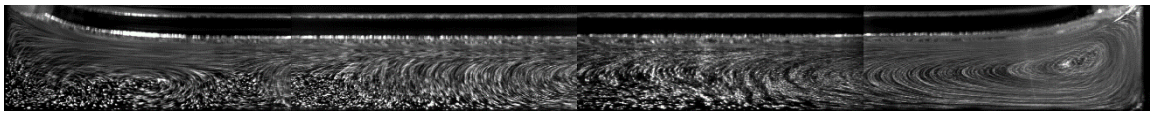

(*e*) C_M = 14.2%, c_a = 47.0%

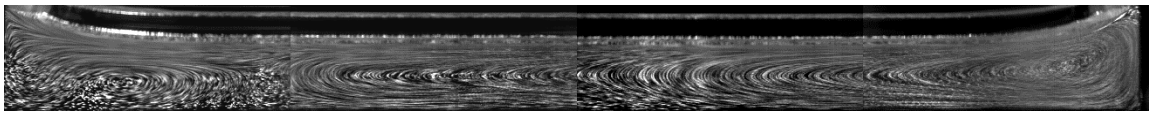

(*f*) C_M = 14.2%, c_a = 36.4%

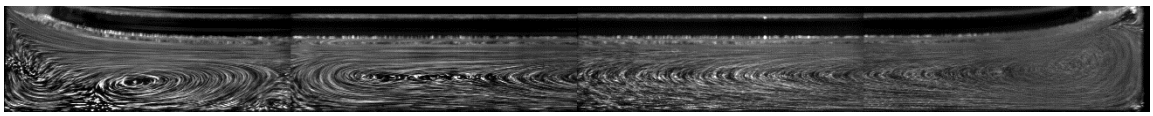

(*g*) C_M = 14.2%, c_a = 27.3%

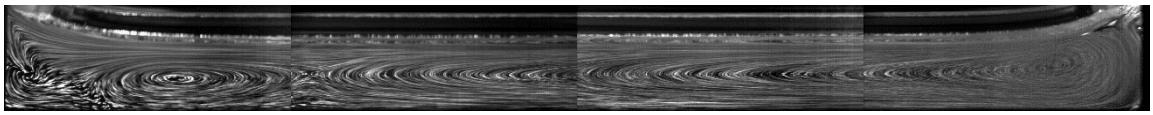

(*h*) C_M = 14.2%, c_a = 17.9%

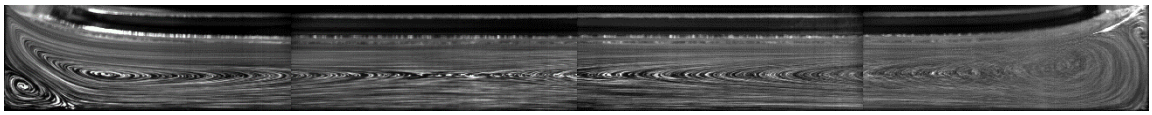

(*i*) C_M = 14.2%, c_a = 6.4%

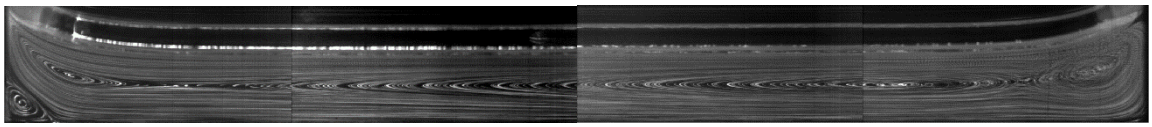

(*j*) C_M = 12.7%, c_a = 0.5%

Figure D.2 Particle pathline visualizations for the binary flow regime map at $C_M \approx 14\%$.

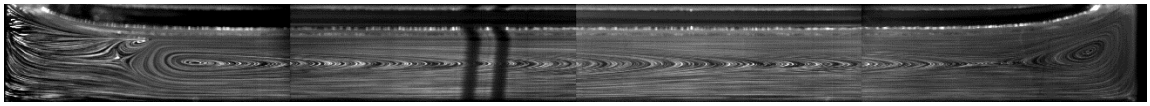

(*a*) C_M = 27.9%, c_a = 93.2%

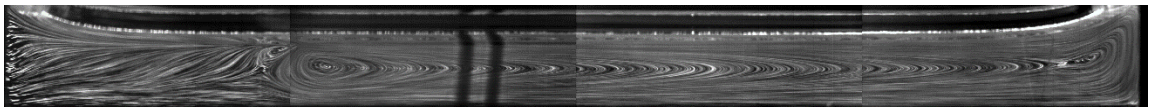

(*b*) C_M = 27.9%, c_a = 87.0%

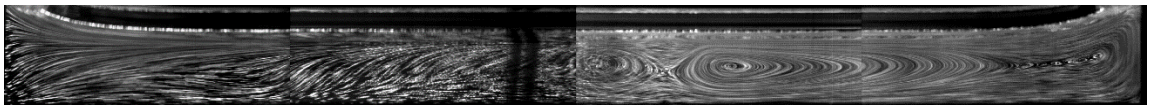

(*c*) C_M = 27.9%, c_a = 81.0%

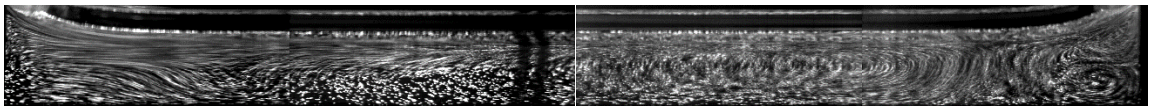

(*d*) C_M = 27.9%, c_a = 71.5%

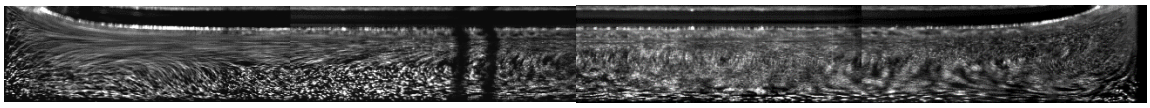

(*e*) C_M = 27.9%, c_a = 61.1%

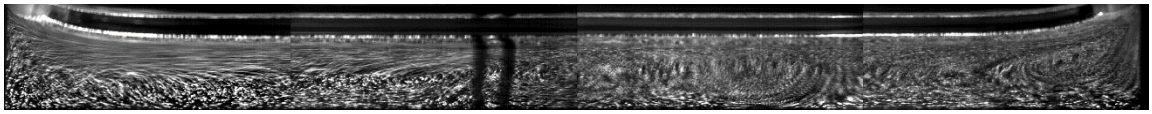

(*f*) C_M = 27.9%, c_a = 51.4%

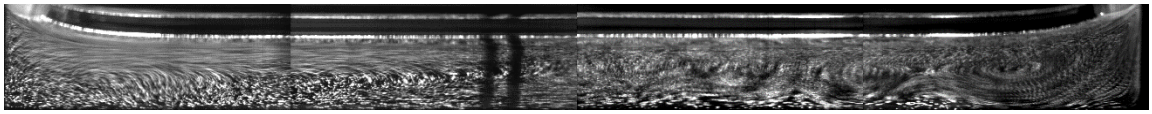

(*g*) C_M = 27.9%, c_a = 40.7%

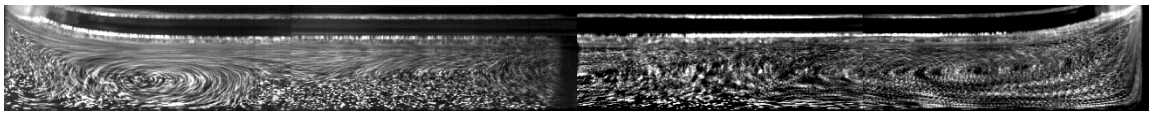

(*h*) C_M = 27.9%, c_a = 27.7%

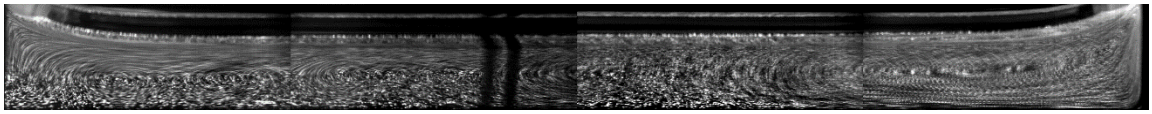

(*i*) C_M = 27.9%, c_a = 20.4%

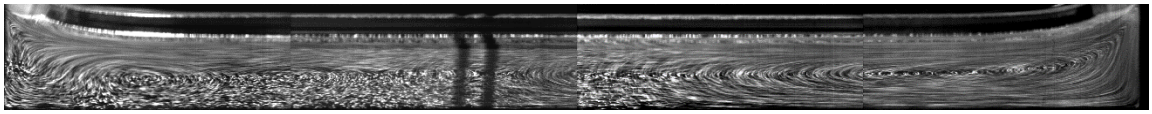

(*j*) C_M = 27.9%, c_a = 12.6%

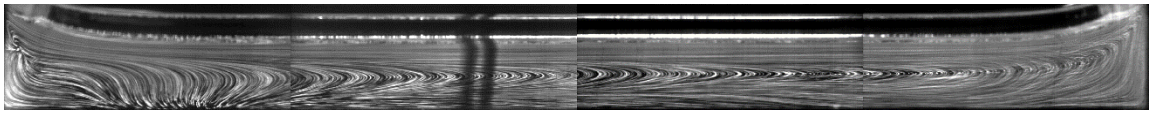

(*k*) C_M = 27.9%, c_a = 4.1%

Figure D.3 Particle pathline visualizations for the binary flow regime map at C_M = 27.9%.

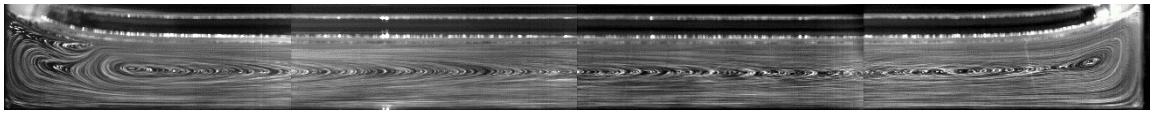

(*a*) C_M = 39.6%, c_a = 92.0%

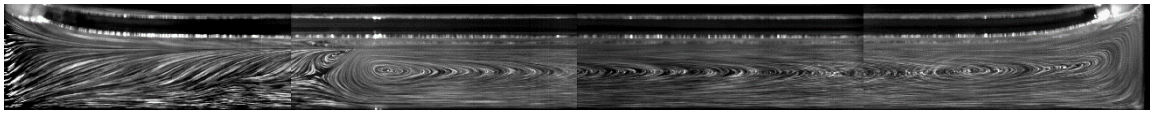

(*b*) C_M = 39.6%, c_a = 79.6%

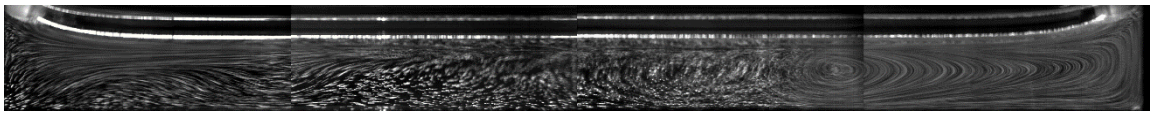

(*c*) C_M = 39.6%, c_a = 68.7%

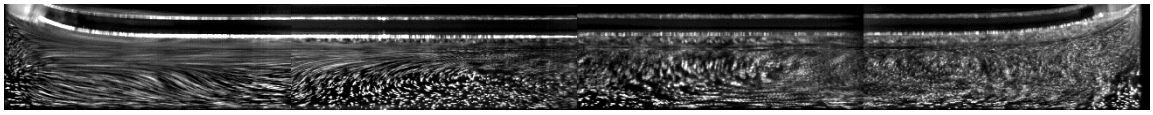

(*d*) C_M = 39.6%, c_a = 58.4%

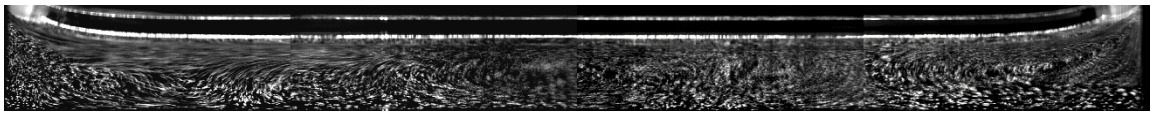

(*e*) C_M = 39.6%, c_a = 47.8%

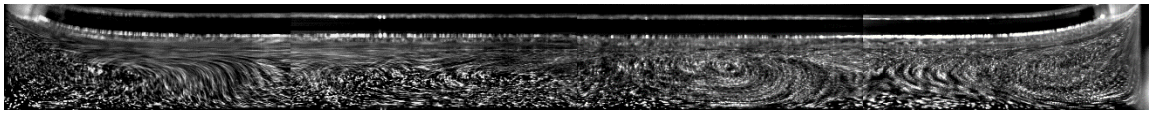

(*f*) C_M = 39.6%, c_a = 37.2%

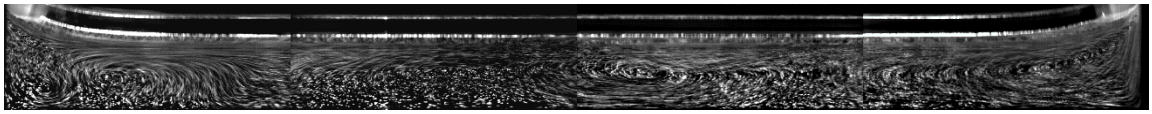

(*g*) C_M = 39.6%, c_a = 26.5%

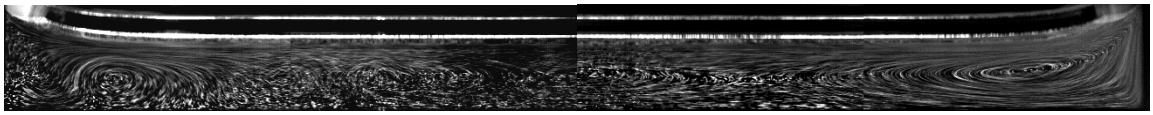

(*h*) C_M = 39.6%, c_a = 15.2%

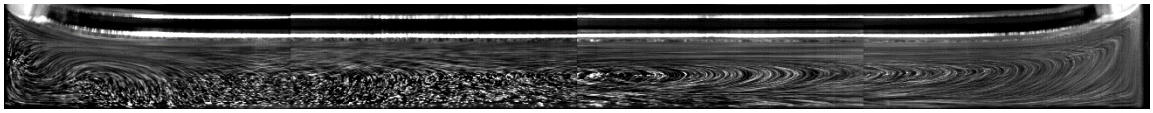

(*i*) C_M = 39.6%, c_a = 8.6%

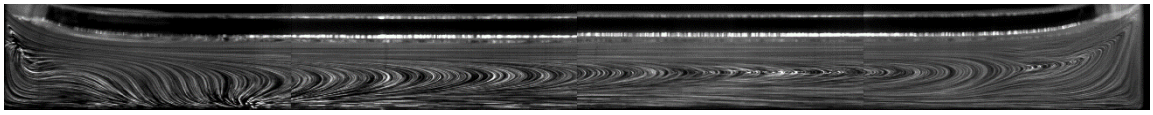

(*j*) C_M = 39.6%, c_a = 0.9%

Figure D.4 Particle pathline visualizations for the binary flow regime map at C_M = 39.6%.

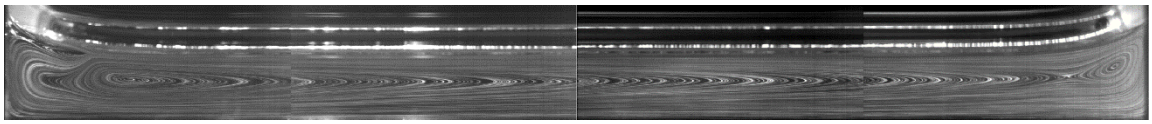

(*a*) C_M = 58.6%, c_a = 90.4%

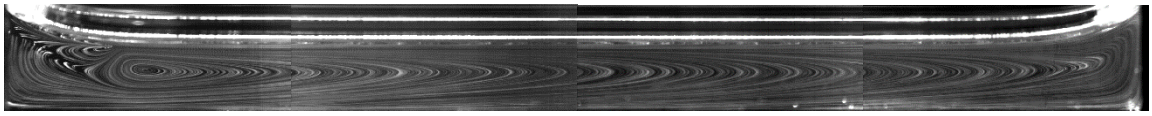

(*b*) C_M = 57.8%, c_a = 80.4%

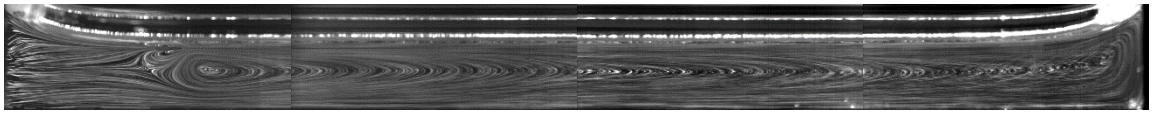

(*c*) C_M = 57.8%, c_a = 69.5%

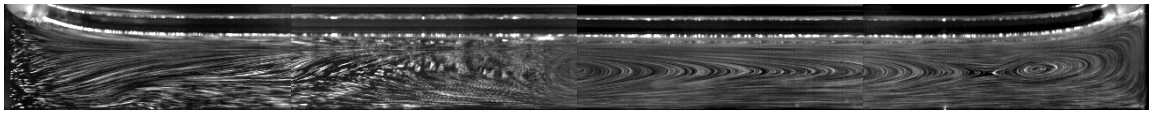

(*d*) C_M = 57.8%, c_a = 59.0%

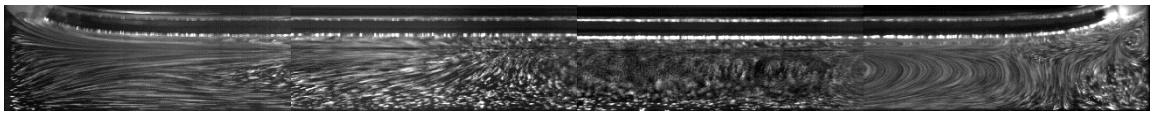

(*e*) C_M = 57.8%, c_a = 48.5%

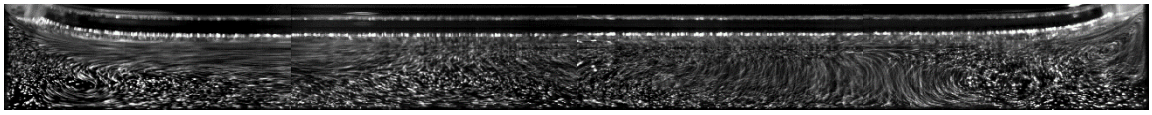

(*f*) C_M = 57.8%, c_a = 35.2%

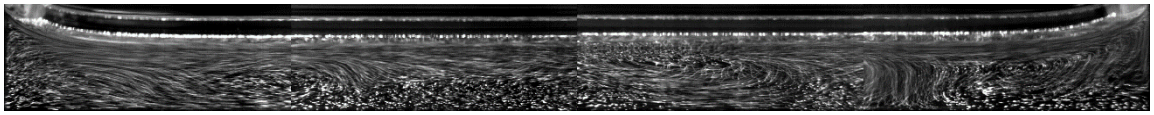

(*g*) C_M = 57.8%, c_a = 23.1%

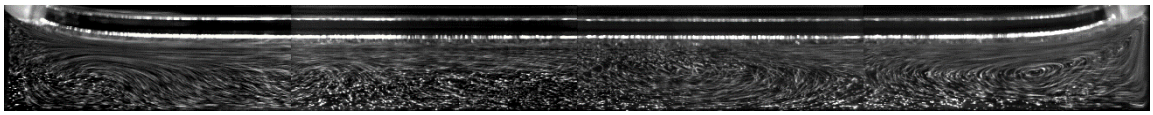

(*h*) C_M = 57.8%, c_a = 16.1%

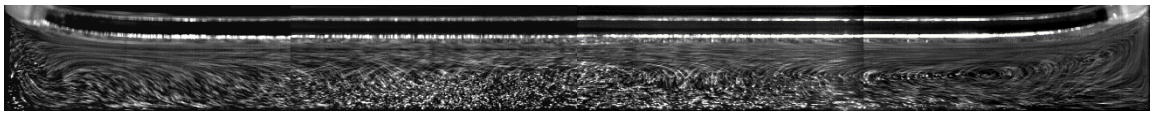

(*i*) C_M = 57.8%, c_a = 8.8%

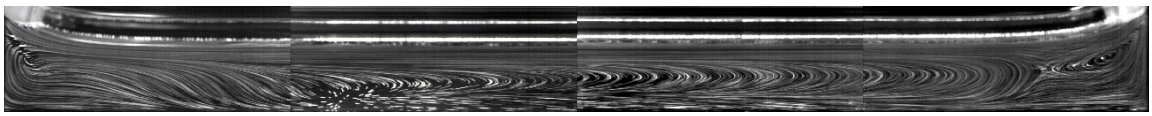

(*j*) C_M = 57.8%, c_a = 2.2%

Figure D.5 Particle pathline visualizations for the binary flow regime map at $C_M \approx 58\%$.

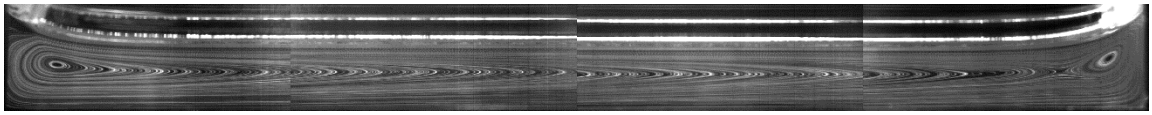

(*a*) C_M = 73.6%, c_a = 89.5%

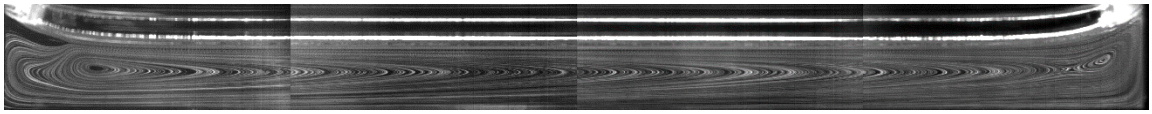

(*b*) C_M = 73.6%, c_a = 79.0%

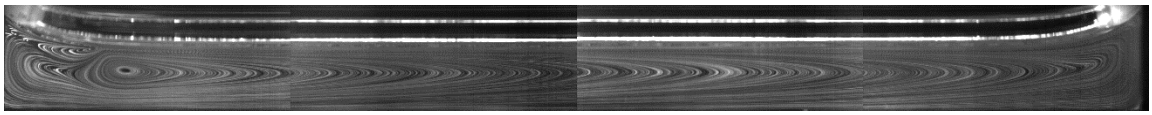

(*c*) C_M = 73.6%, c_a = 69.0%

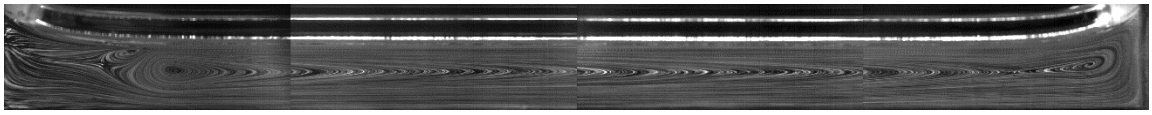

(*d*) C_M = 73.6%, c_a = 57.6%

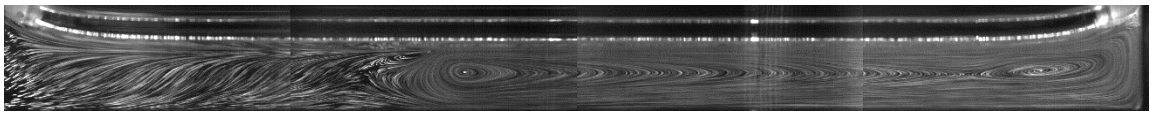

(*e*) C_M = 73.6%, c_a = 47.6%

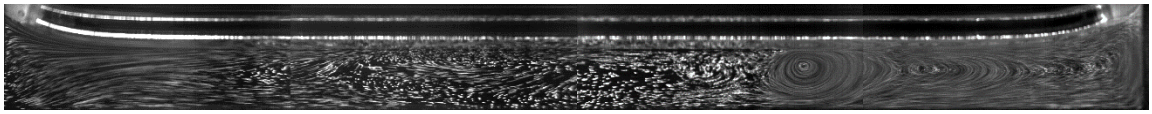

(*f*) C_M = 73.6%, c_a = 35.5%

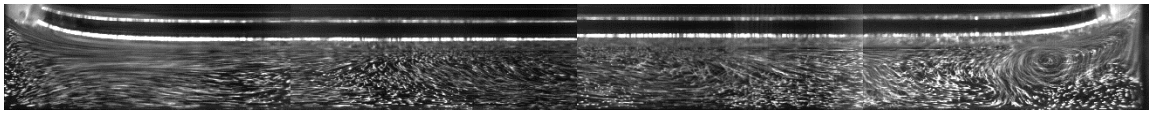

(*g*) C_M = 73.6%, c_a = 21.9%

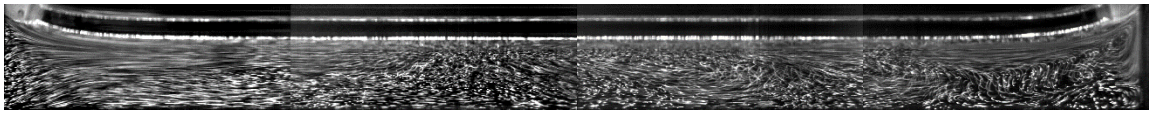

(*h*) C_M = 73.6%, c_a = 19.7%

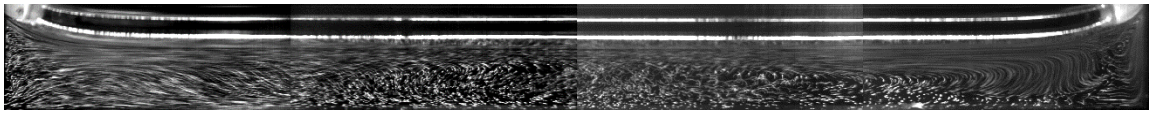

(*i*) C_M = 73.6%, c_a = 8.4%

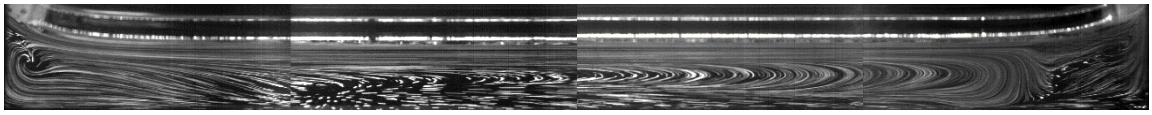

(*j*) C_M = 73.6%, c_a = 1%

Figure D.6 Particle pathline visualizations for the binary flow regime map at C_M = 73.6%.

APPENDIX E

CALCULATION OF HEATING AND COOLING POWERS

The power used to heat and cool the ends of the test cell with the Peltier devices was calculated from the applied current I and the temperature difference across the device δT based on the characteristic curves provided by the manufacturer (Figure E.1). A correlation for the power Q_c was first obtained by fitting a 4th-order polynomial in I_c and a quadratic in δT in to these characteristic curves:

$$\begin{aligned} Q_c = {} & p_{00} + p_{10}\delta T + p_{01}I_c + p_{20}\delta T^2 + p_{11}\delta T I_c + p_{02}I_c^2 + p_{21}\delta T^2 I_c \\ & + p_{12}\delta T I_c^2 + p_{03}I_c^3 + p_{22}\delta T^2 I_c^2 + p_{13}\delta T I_c^3 + p_{04}I_c^4 \end{aligned} \quad \text{(E-1)}$$

where the fitting coefficients are given in Table E-1.

Table E-1 Fitting coefficients of Equation (E-1) for the pumped power.

p_{00}	-0.00663	p_{21}	2.182e-05
p_{10}	-0.04101	p_{12}	0.001618
p_{01}	2.435	p_{03}	-0.01833
p_{20}	-2.239×10^{-5}	p_{22}	$-4.719e\times10^{-6}$
p_{11}	-0.01205	p_{13}	-7.495×10^{-5}
p_{02}	-0.352	p_{04}	0.002733

For the Peltier devices used in these experiments, Q_c is the power "pumped" from the cold to the hot sides of the Peltier to against the temperature gradient across the device. If the Peltier is used to cool the test cell, the cooling power q_c extracted from the cooled end is simply

$$q_c = Q_c, \quad \text{(E-2)}$$

which can be calculated by substituting the measured temperature difference δT and the applied current I_c into Equation (E-1). If the Peltier is used instead to heat the test cell, Joule heating must also be considered, so the heating power q_h that goes into the heated end of the test cell,

$$q_h = Q_c + VI_c \qquad \text{(E-3)}$$

The heating and cooling powers were calculated using Equations (E-2) and (E-3) for C_M = 57.8% at varying levels of noncondensables (*i.e.*, data plotted in Figure 5.22); their values q_h and q_c, and the average of these two values $q_{av} = (q_c + q_h)/2$ are shown in Table E-2.

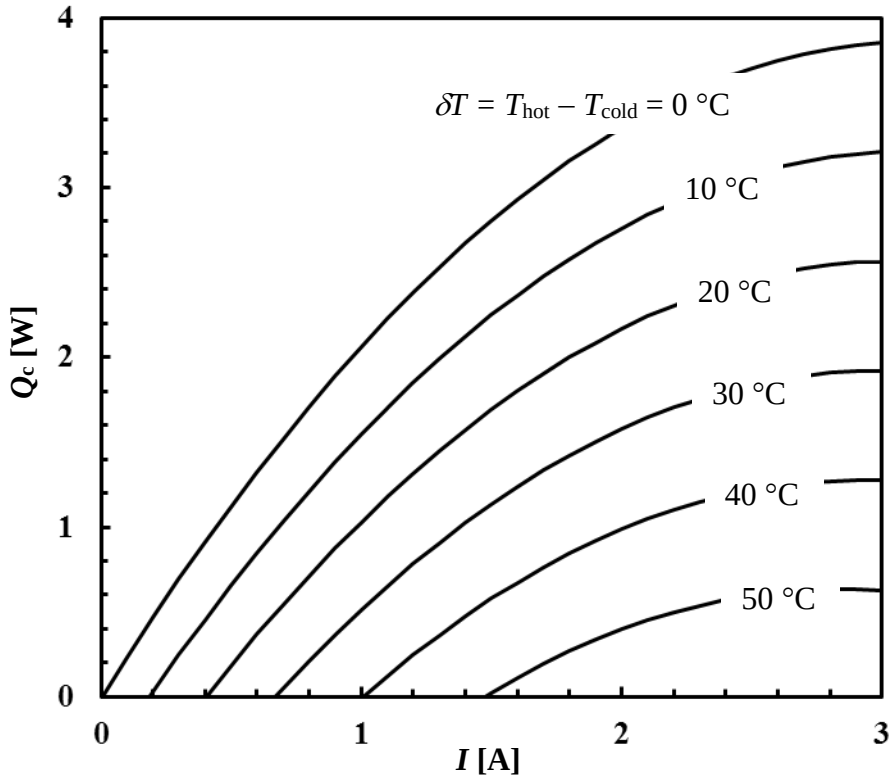

Figure E.1 Characteristics curves of the Peltier devices as a function of the driving current and the temperature difference across the Peltier.

Table E-2 Calculation of heating and cooling powers of the Peltier devices at C_M = 57.8%.

c_a	Device	I_c [A]	V [V]	T_{hot} [°C]	T_{cold} [°C]	δT [°C]	q_c or q_h [W]	q_{av} [W]
2.2%	cooler	0.30	0.307	25.5	18.0	7.5	0.357	0.341
	heater	0.21	0.193	24.1	19.4	4.7	0.325	
8.8%	cooler	0.27	0.273	24.5	17.6	6.9	0.319	0.254
	heater	0.13	0.132	23.8	20.7	3.1	0.189	
16.1%	cooler	0.22	0.213	23.9	17.9	6.0	0.250	0.209
	heater	0.12	0.123	23.9	20.9	3.0	0.168	
23.1%	cooler	0.21	0.190	23.9	18.0	5.9	0.232	0.193
	heater	0.11	0.110	24.0	21.3	2.7	0.155	
35.2%	cooler	0.20	0.178	23.6	18.0	5.6	0.223	0.187
	heater	0.11	0.111	24.1	21.3	2.8	0.151	
48.5%	cooler	0.20	0.176	23.6	17.9	5.7	0.218	0.166
	heater	0.09	0.095	24.1	21.6	2.5	0.113	
59.0%	cooler	0.20	0.114	23.6	17.9	5.7	0.218	0.166
	heater	0.09	0.096	24.1	21.6	2.5	0.113	
69.5%	cooler	0.21	0.194	23.9	18.0	5.9	0.232	0.172
	heater	0.09	0.096	24.1	21.6	2.5	0.113	
80.4%	cooler	0.21	0.181	24.1	18.2	5.9	0.232	0.175
	heater	0.09	0.096	24.2	21.8	2.4	0.117	
90.4%	cooler	0.17	0.158	21.9	16.9	5.0	0.182	0.168
	heater	0.12	0.121	22.9	19.6	3.3	0.155	

APPENDIX F

UNCERTAINTY ANALYSIS

Uncertainty propagation analyses were performed for a number of the equations used in this thesis based on the approach suggested by Moffat (1988). If a physical quantity A is a function of a n independent variables, *i.e.*, $A = f(x_1, x_2, ..., x_n)$, which have uncertainties $(\sigma_1, \sigma_2, ..., \sigma_n)$, then the resulting overall uncertainty in A, σ_A, can be calculated from the weighted root-mean squared sum of the individual uncertainties,

$$\sigma_A = \sqrt{\left(\frac{\partial f}{\partial x_1}\sigma_1\right)^2 + \left(\frac{\partial f}{\partial x_2}\sigma_2\right)^2 + ... + \left(\frac{\partial f}{\partial x_n}\sigma_n\right)^2} \tag{F-1}$$

In order to find the overall uncertainty, one usually needs to determine the uncertainty in each individual variable, as well as the partial derivative of that variable at the reference data point. However, in many cases, the function f is quite complicated, which makes it very difficult to analytically determine all of the partial derivatives required.

In these cases, a numerical (*i.e.*, finite difference) method was used instead to approximate the partial derivative at the desired data point. For an uncertainty propagation analysis at $(x_{10}, x_{20}, ..., x_{n0})$, the partial derivative with respect to x_1 can be expressed as,

$$\left.\frac{\partial f}{\partial x_1}\right|_{x_1 = x_{10}} \approx \frac{f(x_{10} + \Delta x_{10}, x_{20}, ..., x_{n0}) - f(x_{10}, x_{20}, ..., x_{n0})}{\Delta x_{10}} \tag{F-2}$$

where Δx_{10} can be a random variation, that is much less than x_{10}. Taking this even further, one can increase the reference value x_{10} by its actual uncertainty interval σ_1, and Equation (F-2) becomes,

$$\frac{\partial f}{\partial x_1}\sigma_1 \approx f(x_{10} + \sigma_1, x_{20}, ..., x_{n0}) - f(x_{10}, x_{20}, ..., x_{n0}) \tag{F-3}$$

This approach as suggested by Moffat (1988) is used for the uncertainty propagation analysis in this appendix.

F.1 Methanol Concentration C_M

As discussed above, the MeOH concentration C_M was determined from the mixture density, which was obtained by measuring the total mass, m, of a certain volume of the mixture, V. So

$$C_M = f(m, V) \tag{F-4}$$

where both m and V are possible error sources.

The total mass m was measured using an analytical balance (Sartorius, M-power AZ124), which has an uncertainty, σ_m = 0.5 mg, and the volume V was measured using a serological pipet (13-676-10B), which was calibrated to an uncertainty, σ_V =0.005 mL. By applying Equations (F-1) to (F-3), the final uncertainty of each case can be evaluated. For C_M = 8.9%, m was measured to be m_o = 0.9746 g for a volume of V_o = 1 mL,

$$C_M(m_o, V_o) = C_M(0.9746\text{ g}, 1\text{ mL}) = 8.9\% \tag{F-5}$$

$$C_M(m_o+\sigma_m, V_o) = C_M(0.9751\text{ g}, 1\text{ mL}) = 8.6\% \tag{F-6}$$

$$C_M(m_o, V_o+\sigma_V) = C_M(0.9746\text{ g}, 1.005\text{ mL}) = 11.0\% \tag{F-7}$$

From Equation (F-1), σ_{C_M} can be evaluated,

$$\sigma_{C_M} = \sqrt{(8.6\%-8.9\%)^2+(11.0\%-8.9\%)^2} = 2.1\% \tag{F-8}$$

Equations (F-5) to (F-8) are summarized in Table F-1.

Table F-1 Uncertainty propagation of C_M at C_M = 8.9%.

C_M	m (g)	V (mL)	ρ (g/mL)	C_M	σ_{C_M}
8.90%	0.9746	1	0.9746	8.9%	**2.1%**
	0.9751	1	0.9751	8.6%	
	0.9746	1.005	0.9698	11.0%	

The same method can be applied at other MeOH concentrations, as shown in Table F-2.

Table F-2 Uncertainty propagation of C_M at other MeOH concentrations.

C_M	m [g]	V [mL]	ρ [g/mL]	C_M	σ_{C_M}
12.7%	0.9661	1	0.9661	12.7%	**2.1%**
	0.9666	1	0.9666	12.4%	
	0.9661	1.005	0.9613	14.8%	
19.7%	0.9509	1	0.9509	19.7%	**2.2%**
	0.9514	1	0.9514	19.4%	
	0.9509	1.005	0.9462	21.9%	
26.4%	0.9364	1	0.9364	26.4%	**2.1%**
	0.9369	1	0.9369	26.2%	
	0.9364	1.005	0.9317	28.5%	
40.8%	0.9049	1	0.9049	40.8%	**2.1%**
	0.9054	1	0.9054	40.6%	
	0.9049	1.005	0.9004	42.9%	
58.6%	0.8676	1	0.8676	58.6%	**2.1%**
	0.8681	1	0.8681	58.4%	
	0.8676	1.005	0.8633	60.7%	
73.6%	0.8379	1	0.8379	73.6%	**2.2%**
	0.8384	1	0.8384	73.3%	
	0.8379	1.005	0.8337	75.8%	

F.2 Air Concentration of the Vapor Space c_a

The air concentration of the vapor space is determined from the measured pressure of the vapor space p_{meas}, which has an uncertainty σ_p = 260 Pa, the measured ambient temperature T_{room}, which has an uncertainty σ_T = 0.2 °C, and C_M, whose uncertainty was determined to be approximately 2% in the previous section. So

$$c_a = f\,(C_M, p_{meas}, T_{room}) \tag{F-9}$$

An uncertainty analysis was performed for two representative MeOH concentrations, $C_M \approx 9\%$ and $C_M \approx 58\%$, over a range of c_a. using an approach similar to that described in detail earlier for C_M. Table F-3 presents the results of these uncertainty analyses.

Table F-3 Uncertainty propagation of c_a when $C_M \approx 9\%$.

Cases	C_M	p_{meas} [Pa]	T_{room} [°C]	p_v [Pa]	c_a	σ_{C_M}
C_M = 8.9% c_a = 1.5%	8.9	4355	20.4	4291	1.5%	**9.6%**
	10.9	4355	20.4	4630	-6.3%	
	8.9	4615	20.4	4291	7.0%	
	8.9	4355	20.6	4341	0.3%	
C_M = 9.3% c_a = 7.4%	9.3	4557	19.8	4218	7.4%	**8.6%**
	11.3	4557	19.8	4532	0.5%	
	9.3	4817	19.8	4218	12.4%	
	9.3	4557	20	4267	6.4%	
C_M = 9.3% c_a = 26.5%	9.3	5775	19.9	4242	26.5%	**6.4%**
	11.3	5775	19.9	4558	21.1%	
	9.3	6035	19.9	4242	29.7%	
	9.3	5775	20.1	4292	25.7%	
C_M = 9.3% c_a = 46.1%	9.3	7913	20	4267	46.1%	**4.4%**
	11.3	7913	20	4585	42.1%	
	9.3	8173	20	4267	47.8%	
	9.3	7913	20.2	4317	45.4%	
C_M = 9.3% c_a = 68.5%	9.3	13638	20.1	4292	68.5%	**2.4%**
	11.3	13638	20.1	4611	66.2%	
	9.3	13898	20.1	4292	69.1%	
	9.3	13638	4343	4341	68.2%	
C_M = 8.9% c_a = 97.7%	8.9	101325	20.8	4393	95.7%	**0.3%**
	10.9	101325	20.8	4738	95.3%	
	8.9	101585	20.8	4393	95.7%	
	8.9	101325	21	4453	95.6%	

Table F-4 Uncertainty propagation of c_a when $C_M \approx 58\%$.

Cases	C_M	p_{meas} [Pa]	T_{room} [°C]	p_v [Pa]	c_a	σ_{c_a}
C_M =57.8% c_a = 2.2%	57.8	9977	20.9	9761	2.2%	**3.2%**
	59.8	9977	20.9	9938	0.4%	
	57.8	10237	20.9	9761	4.6%	
	57.8	9977	21.1	9868	1.1%	

Table F-5 Uncertainty propagation of c_a when $C_M \approx 58\%$ (continued).

Cases	C_M	p_{meas} [Pa]	T_{room} [°C]	p_v [Pa]	c_a	σ_{c_a}
C_M = 57.8% c_a = 8.8%	57.8	10845	21.2	9895	8.8%	**2.9%**
	59.8	10845	21.2	10075	7.1%	
	57.8	11105	21.2	9895	10.9%	
	57.8	10845	21.4	10004	7.8%	
C_M = 57.8% c_a = 16.1%	57.8	11898	21.3	9977	16.1%	**2.5%**
	59.8	11898	21.3	10158	14.6%	
	57.8	12158	21.3	9977	17.9%	
	57.8	11898	21.5	10087	15.2%	
C_M = 57.8% c_a = 23.1%	57.8	12967	21.3	9977	23.1%	**2.2%**
	59.8	12967	21.3	10158	21.7%	
	57.8	13227	21.3	9977	24.6%	
	57.8	12967	21.5	10087	22.2%	
C_M = 57.8% c_a = 35.2%	57.8	15388	21.3	9977	35.2%	**1.7%**
	59.8	15388	21.3	10158	34.0%	
	57.8	15648	21.3	9977	36.2%	
	57.8	15388	21.5	10087	34.4%	
C_M = 57.8% c_a = 48.5%	57.8	19595	21.5	10087	48.5%	**1.3%**
	59.8	19595	21.5	10270	47.6%	
	57.8	19855	21.5	10087	49.2%	
	57.8	19595	21.7	10198	48.0%	
C_M = 57.8% c_a = 59.0%	57.8	24763	21.6	10142	59.0%	**1.0%**
	59.8	24763	21.6	10326	58.3%	
	57.8	25023	21.6	10142	59.5%	
	57.8	24763	21.8	10254	58.6%	
C_M = 57.8% c_a =69.5%	57.8	33663	21.8	10254	69.5%	**0.7%**
	59.8	33663	21.8	10439	69.0%	
	57.8	33923	21.8	10254	69.8%	
	57.8	33663	22.0	10366	69.2%	
C_M = 57.8% c_a = 80.4%	57.8	51763	21.7	10170	80.4%	**0.4%**
	59.8	51763	21.7	10354	80.0%	
	57.8	52023	21.7	10170	80.5%	
	57.8	51763	21.9	10282	80.1%	
C_M = 58.6% c_a = 90.4%	58.6	101325	20.7	9724	90.4%	**0.2%**
	60.6	101325	20.7	9900	90.2%	
	58.6	101585	20.7	9724	90.4%	
	58.6	101325	20.9	9831	90.3%	

F.3 Heating and Cooling Powers

The uncertainties in the heating and cooling powers (and their average q_{av}) are based on the uncertainties in the applied current I of 0.01 A, the applied voltage V of 5 mV (as given by the manufacturer), and the measured temperatures T_{hot} and T_{cold} on the two sides of the Peltier σ_T = 0.2 °C. Then

$$q_{av} = (q_h + q_c)/2 = f\,(I, V, T_{hot}, T_{cold}) \tag{F-9}$$

Based on Equations (F-1) and (F-9), the uncertainty of q_{av}

$$\sigma_{q_{av}} = \frac{1}{2}\sqrt{\sigma_{q_c}^2 + \sigma_{q_h}^2} \tag{F-10}$$

where σ_{q_c} and σ_{q_h} are the uncertainties in q_h and q_c, respectively. An uncertainties analysis was performed at C_M = 57.8%; only the tabulated values are presented in Table F-6.

Table F-6 Uncertainty propagation of q_{av} for C_M = 57.8% .

c_a	Device	I [A]	V [V]	T_{hot} [°C]	T_{cold} [°C]	δT [°C]	q_c/q_h [W]	$\sigma_{q_c}/\sigma_{q_h}$ [W]	$\sigma_{q_{av}}$ [W]
2.2%	cooler	0.30	307	25.5	18.0	7.5	0.357	0.025	**0.018**
		0.31	307	25.5	18.0	7.5	0.379		
		0.30	307	25.7	18.0	7.7	0.348		
		0.30	307	25.5	18.2	7.3	0.366		
	heater	0.21	193	24.1	19.4	4.7	0.325	0.027	
		0.22	193	24.1	19.4	4.7	0.349		
		0.21	198	24.1	19.4	4.7	0.326		
		0.21	193	24.3	19.4	4.9	0.316		
		0.21	193	24.1	19.6	4.5	0.334		

Table F-7 Uncertainty propagation of q_{av} for C_M = 57.8% (continued)

8.8%	cooler	0.27	273	24.5	17.6	6.9	0.319	0.025	**0.018**
		0.28	273	24.5	17.6	6.9	0.341		
		0.27	273	24.7	17.6	7.1	0.311		
		0.27	273	24.5	17.8	6.7	0.328		
	heater	0.13	132	23.8	20.7	3.1	0.189	0.027	
		0.14	132	23.8	20.7	3.1	0.213		
		0.13	137	23.8	20.7	3.1	0.190		
		0.13	132	24.0	20.7	3.3	0.180		
		0.13	132	23.8	20.9	2.9	0.198		
16.1%	cooler	0.22	213	23.9	17.9	6.0	0.250	0.025	**0.019**
		0.23	213	23.9	17.9	6.0	0.272		
		0.22	213	24.1	17.9	6.2	0.241		
		0.22	213	23.9	18.1	5.8	0.258		
	heater	0.12	123	23.9	20.9	3.0	0.168	0.027	
		0.13	123	23.9	20.9	3.0	0.192		
		0.12	128	23.9	20.9	3.0	0.168		
		0.12	123	24.1	20.9	3.2	0.159		
		0.12	123	23.9	21.1	2.8	0.176		
23.1%	cooler	0.21	190	23.9	18.0	5.9	0.232	0.025	**0.019**
		0.22	190	23.9	18.0	5.9	0.254		
		0.21	190	24.1	18.0	6.1	0.223		
		0.21	190	23.9	18.2	5.7	0.241		
	heater	0.11	110	24.0	21.3	2.7	0.155	0.027	
		0.12	110	24.0	21.3	2.7	0.179		
		0.11	115	24.0	21.3	2.7	0.155		
		0.11	110	24.2	21.3	2.9	0.146		
		0.11	110	24.0	21.5	2.5	0.163		
35.2%	cooler	0.20	178	23.6	18.0	5.6	0.223	0.025	**0.019**
		0.21	178	23.6	18.0	5.6	0.245		
		0.20	178	23.8	18.0	5.8	0.214		
		0.20	178	23.6	18.2	5.4	0.231		
	heater	0.11	111	24.1	21.3	2.8	0.151	0.027	
		0.12	111	24.1	21.3	2.8	0.175		
		0.11	116	24.1	21.3	2.8	0.151		
		0.11	111	24.3	21.3	3.0	0.142		
		0.11	111	24.1	21.5	2.6	0.159		

Table F-8 Uncertainty propagation of q_{av} for C_M = 57.8% (continued)

48.5%	cooler	0.20	176	23.6	17.9	5.7	0.218	0.025	**0.019**
		0.21	176	23.6	17.9	5.7	0.241		
		0.20	176	23.8	17.9	5.9	0.210		
		0.20	176	23.6	18.1	5.5	0.227		
	heater	0.09	95	24.1	21.6	2.5	0.113	0.027	
		0.10	95	24.1	21.6	2.5	0.137		
		0.09	100	24.1	21.6	2.5	0.113		
		0.09	95	24.3	21.6	2.7	0.104		
		0.09	95	24.1	21.8	2.3	0.121		
59.0%	cooler	0.20	114	23.6	17.9	5.7	0.218	0.025	**0.019**
		0.21	114	23.6	17.9	5.7	0.241		
		0.20	114	23.8	17.9	5.9	0.210		
		0.20	114	23.6	18.1	5.5	0.227		
	heater	0.09	96	24.1	21.6	2.5	0.113	0.027	
		0.10	96	24.1	21.6	2.5	0.137		
		0.09	101	24.1	21.6	2.5	0.113		
		0.09	96	24.3	21.6	2.7	0.105		
		0.09	96	24.1	21.8	2.3	0.121		
69.5%	cooler	0.21	194	23.9	18.0	5.9	0.232	0.025	**0.019**
		0.22	194	23.9	18.0	5.9	0.254		
		0.21	194	24.1	18.0	6.1	0.223		
		0.21	194	23.9	18.2	5.7	0.241		
	heater	0.09	96	24.1	21.6	2.5	0.113	0.027	
		0.10	96	24.1	21.6	2.5	0.137		
		0.09	101	24.1	21.6	2.5	0.113		
		0.09	96	24.3	21.6	2.7	0.105		
		0.09	96	24.1	21.8	2.3	0.121		
80.4%	cooler	0.21	181	24.1	18.2	5.9	0.232	0.025	**0.019**
		0.22	181	24.1	18.2	5.9	0.254		
		0.21	181	24.3	18.2	6.1	0.223		
		0.21	181	24.1	18.4	5.7	0.241		
	heater	0.09	96	24.2	21.8	2.4	0.117	0.027	
		0.10	96	24.2	21.8	2.4	0.142		
		0.09	101	24.2	21.8	2.4	0.118		
		0.09	96	24.4	21.8	2.6	0.109		
		0.09	96	24.2	22.0	2.2	0.126		

Table F-9 Uncertainty propagation of q_{av} for C_M = 57.8% (continued)

c_a	Device	I [A]	V [V]	T_{hot} [°C]	T_{cold} [°C]	δT [°C]	q_c/q_h [W]	σ_{q_c} / σ_{q_h} [W]	$\sigma_{q_{av}}$ [W]
90.4%	cooler	0.17	158	21.9	16.9	5.0	0.182	0.026	**0.019**
		0.18	158	21.9	16.9	5.0	0.204		
		0.17	158	22.1	16.9	5.2	0.173		
		0.17	158	21.9	17.1	4.8	0.190		
	heater	0.12	121	22.9	19.6	3.3	0.155	0.027	
		0.13	121	22.9	19.6	3.3	0.179		
		0.12	126	22.9	19.6	3.3	0.155		
		0.12	121	23.1	19.6	3.5	0.146		
		0.12	121	22.9	19.8	3.1	0.163		

F.4 Accuracy of PIV Results

The accuracy of the PIV processing method adopted in this work was evaluated by a calibration experiment, where the displacement results obtained from this method were compared with known values. The same imaging and illumination setup and settings (*e.g.* image magnification) were used in the calibration experiment to match the actual experimental conditions as closely as possible.

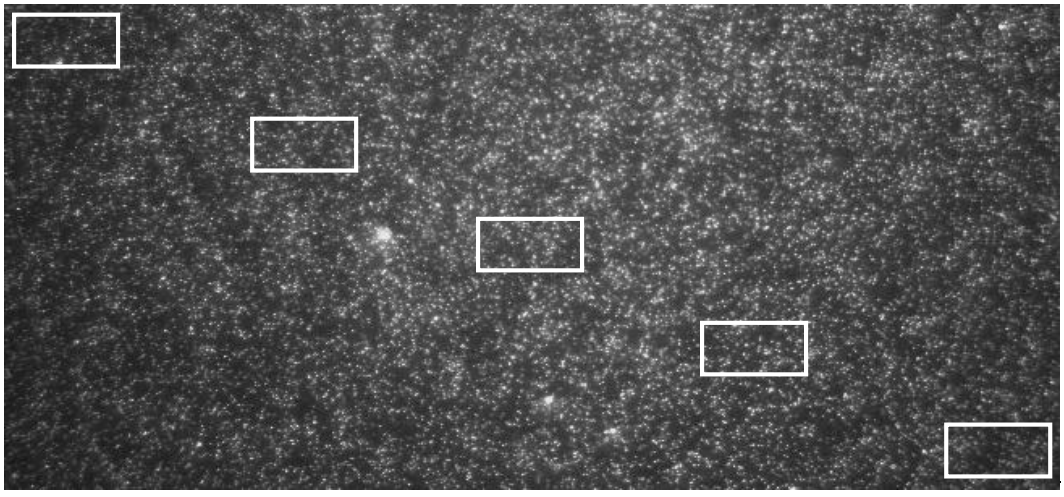

Figure F.1 A sample image of the PIV calibration experiment; the rectangles denote the locations where the measured and actual values were compared.

The first image in these calibration experiments was that of a particle-seeded fluid (nominally) at rest. The second image is then obtained of this fluid after translating the camera by a known distance measured with a micrometer. The two images are then processed using the PIV processing methods described in Chapter 3, and the resulting estimate of the displacement is compared with the known distance. The working liquid used in the calibration experiment was glycerin, a liquid with a high viscosity (= 1.41 kg/(m·s)) to minimize any random motion of the tracer particles (due to Brownian motion and natural convection, for example). The camera was mounted on a translation stage equipped with a micrometer (Newport Corp. HR13) with an accuracy of 0.5 μm.

The test cell was filled with particle-seeded glycerin and allowed to sit at rest for 20 min to ensure that it was in thermal equilibrium with the surroundings to minimize any natural convection. The camera and lens were at the same settings used in the actual experiments. After recording the first image, the second image was recorded after the camera and lens were translated by distances ranging from 5 μm to 160 μm (corresponding to 0.53–17.1 pixels at these magnifications). Finally, these two images (*i.e.*, one image pair) were processed using the in-house PIV code to estimate particle displacements.

Figure F.1 shows a sample image. The five rectangles indicate the locations where the displacements estimated using our PIV processing code were compared with the actual displacements (summarized in Table F-10). Figure F.2 compares the average particle displacements obtained using the in-house PIV code with those obtained from the micrometer. The results are in very good agreement. Table F-10 summarizes the comparisons for all five locations. The maximum root-mean-square error (RMSE) over all of these cases was 0.15 pixels, which is comparable to the typical uncertainties quoted for particle displacements obtained using PIV methods of 0.1 pixel.

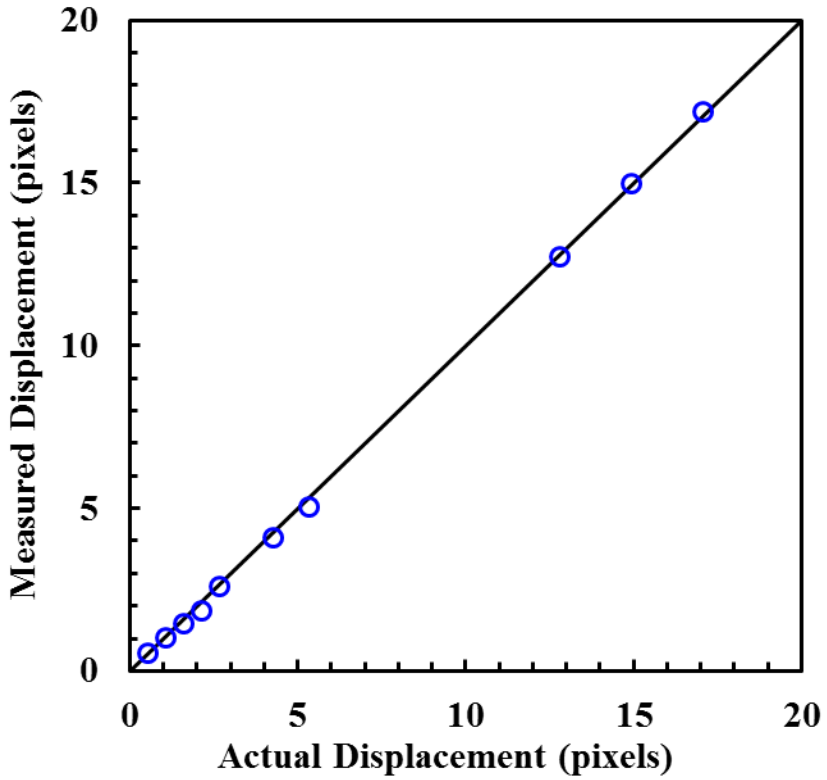

Figure F.2 Comparison of the measurements and the actual values at location 1; the solid line has a slope of 1.

Table F-10 Root-Mean-Square Error of the PIV processing at all 5 locations.

Loca -tion	Actual Displacement [pixels]										RMSE [pixels]
	0.53	1.07	1.60	2.14	2.67	4.27	5.34	12.81	14.95	17.08	
1	0.53	1.03	1.46	1.85	2.59	4.08	5.06	12.74	14.98	17.18	0.15
2	0.56	1.04	1.49	1.94	2.64	4.15	5.10	12.74	14.97	17.12	0.11
3	0.53	1.08	1.59	1.94	2.61	4.12	5.07	12.68	14.94	17.11	0.12
4	0.54	1.08	1.53	1.96	2.58	4.12	5.08	12.66	14.91	17.15	0.13
5	0.52	1.11	1.57	1.97	2.57	4.13	5.11	12.77	15.05	17.24	0.12

The uncertainty in these calibration experiments should then be a good estimate of the systematic error of the PIV measurements. The remaining random error is due to variations between independent realizations (*i.e.*, standard deviations of the measurements). Taking a typical simple-fluid case at c_a = 14% and ΔT = 11.6 °C as an

example, the sampled standard deviations at the location of the maximum flow speed (= 11.8 mm/s) *SSD* = 0.72 mm/s. The random error of this measurement is therefore

$$\sigma_{\mathrm{A}} = k_{\mathrm{c}} \frac{SSD}{\sqrt{N}} = 0.1 \text{ mm/s} \tag{F-11}$$

where N, the number of realizations is 200, and k_{c}, the coverage factor, is 2 for a 95% confidence interval. For a time interval within an image pair Δt = 10 ms, a magnification M = 0.79 and a pixel size px = 7.4 μm, the systematic error in this measurement is

$$\sigma_{\mathrm{B}} = \frac{RSME \cdot M \cdot px}{\Delta t} = \frac{0.15 \times 0.79 \times 7.4 \times 10^{-3}}{10 \times 10^{-3}} = 0.09 \text{ mm/s}. \tag{F-12}$$

Therefore the combined uncertainty is

$$\sigma_u = \sqrt{\sigma_{\mathrm{A}}^2 + \sigma_{\mathrm{B}}^2} = 0.13 \text{ mm/s} \tag{F-13}$$

which is 1.1% of the measurement.

REFERENCES

Abe, Y., A. Iwasaki and K. Tanaka (2004). "Microgravity experiments on phase change of self-rewetting fluids." Transport Phenomena in Microgravity **1027**: 269-285.

Abe, Y. (2006). "Self-rewetting fluids: beneficial aqueous solutions." Ann N Y Acad Sci **1077**: 650-667.

Adrian, R. J. and J. Westerweel (2011). Particle image velocimetry, New York, Cambridge University Press.

Aldiwany, H. K. and J. W. Rose (1973). "Free convection film condensation of steam in presence of non-condensing gases." International Journal of Heat and Mass Transfer **16**(7): 1359-1369.

Azouni, M. A., C. Normand and G. Petre (2001). "Surface-tension-driven flows in a thin layer of a water-n-heptanol solution." Journal of Colloid and Interface Science **239**(2): 509-516.

Barthes, M., C. Reynard, R. Santini and L. Tadrist (2007). "Non-condensable gas influence on the Marangoni convection during a single vapour bubble growth in a subcooled liquid." Epl **77**(1).

Bénard, H. (1900). "Les tourbillons cellulaires dans une nappe liquide. premiere partie: description generale des phenomenes." Rev. Gen. Sci. Pures Appl. (Paris) 11: 1261-1271.

Ben hadid, H. and B. Roux (1992). "Buoyancy-driven and thermocapillary-driven flows in differentially heated cavities for low-prandtl-number fluids." Journal of Fluid Mechanics **235**: 1-36.

Benz, S. and D. Schwabe (2001). "The three-dimensional stationary instability in dynamic thermocapillary shallow cavities." Experiments in Fluids **31**(4): 409-416.

Birikh, R. V. (1966). "Thermocapillary convection in a horizontal layer of liquid." Journal of Applied Mechanics and Technical Physics **3**: 69-72.

Block, M. J. (1956). "Surface tension as the cause of Bénard cells and surface deformation in a liquid film." Nature **178**(4534): 650-651.

Borishanskiy, V. M. et al., (1977) "Effect of uncondensable gas content on heat transfer in steam condensation in a vertical tube." Heat Transfer Sov. Res. **9** (2): 35-42.

Borishanskiy, V. M. et al., (1978) "Heat transfer from steam condensing inside vertical pipes and coils." Heat Transfer Sov. Res. **10** (4): 44-58.

Braunsfurth, M. G. and G. M. Homsy (1997). "Combined thermocapillary-buoyancy convection in a cavity. Part II. An experimental study." Physics of Fluids **9**(5): 1277.

Burguete, J., N. Mukolobwiez, F. Daviaud, N. Garnier and A. Chiffaudel (2001). "Buoyant-thermocapillary instabilities in extended liquid layers subjected to a horizontal temperature gradient." Physics of Fluids **13**(10): 2773.

Canny, J. (1986). "A computational approach to edge-detection." Ieee Transactions on Pattern Analysis and Machine Intelligence **8**(6): 679-698.

Carr, C. and J. A. Riddick (1951). "Physical properties of methanol-water system." Industrial and Engineering Chemistry **43**(3): 692-696.

Cecere, A., R. D. Paola, R. Savino, Y. Abe, L. Carotenuto and S. V. Vaerenbergh (2011). "Observation of Marangoni flow in ordinary and self-rewetting fluids using optical diagnostic systems." European Physical Journal-Special Topics **192**(1): 109-120.

Chan, C. L. and C. F. Chen (2010). "Effect of gravity on the stability of thermocapillary convection in a horizontal fluid layer." Journal of Fluid Mechanics **647**: 91.

Chauvet, F., S. Dehaeck and P. Colinet (2012). "Threshold of Benard-Marangoni instability in drying liquid films." Epl **99**(3).

Chiang, C. K. and Y. W. Lu (2011). "Evaporation phase change processes of water/methanol mixtures on superhydrophobic nanostructured surfaces." Journal of Micromechanics and Microengineering **21**(7).

Davis, S. H. (1983). "Rupture of thin liquid films." in Waves on Fluid Interfaces, edited by R. E. Meyer (New York Academic): 291-302.

Davis, S. H. (1987). "Thermocapillary instabilities." Annual Review of Fluid Mechanics **19**: 403-435.

Daviaud, F. and J. Vince (1993). "Traveling waves in a fluid layer subjected to a horizontal temperature gradient." Physical Review E **48**(6): 4432-4436.

de Ryck, A. (1999). "Instability of a meniscus due to surface tension gradient-driven flow." Journal of Colloid and Interface Science **209**(1): 10-15.

DeSaedeleer, C., A. Garcimartin, G. Chavepeyer, J. K. Platten and G. Lebon (1996). "The instability of a liquid layer heated from the side when the upper surface is open to air." Physics of Fluids **8**(3): 670-676.

di Francescantonio, N., R. Savino and Y. Abe (2008). "New alcohol solutions for heat pipes: Marangoni effect and heat transfer enhancement." International Journal of Heat and Mass Transfer **51**(25-26): 6199-6207.

Di Paola, R., R. Savino, D. Mirabile Gattia, R. Marazzi and M. Vittori Antisari (2011). "Self-rewetting carbon nanofluid as working fluid for space and terrestrial heat pipes." Journal of Nanoparticle Research **13**(11): 6207-6216.

Doumenc, F., E. Chenier, B. Trouette, T. Boeck, C. Delcarte, B. Guerrier and M. Rossi (2013). "Free convection in drying binary mixtures: Solutal versus thermal instabilities." International Journal of Heat and Mass Transfer **63**: 336-350.

Dymond, J. H. and E. B. Smith (1980). The virial coefficients of pure gases and mixtures: a critical compilation, New York, Oxford University Press.

Eninger, J. E. and D. B. Marcus (1978). The Marangoni effect and capacity degradation in axially grooved heat pipes. Third International Heat Pipe Conference. Palo Alto, CA, AIAA Technical Paper**:** 14–34.

Ezersky, A., A. Garcimartín, H. Mancini and C. Pérez-García (1993). "Spatiotemporal structure of hydrothermal waves in Marangoni convection." Physical Review E **48**(6): 4414-4422.

Fanton, X. and A. M. Cazabat (1998). "Spreading and instabilities induced by a solutal Marangoni effect." Langmuir **14**(9): 2554-2561.

Fournier, J. B. and A. M. Cazabat (1992). "Tears of wine." Europhysics Letters **20**(6): 517-522.

Fredenslund, A., R. L. Jones and J. M. Prausnitz (1975). "Group-contribution estimation of activity-coefficients in nonideal liquid-mixtures." Aiche Journal **21**(6): 1086-1099.

Garcimartin, A., N. Mukolobwiez and F. Daviaud (1997). "Origin of waves in surface-tension-driven convection." Physical Review E **56**(2): 1699-1705.

Garnier, N. and A. Chiffaudel (2001). "Two dimensional hydrothermal waves in an extended cylindrical vessel." European Physical Journal B **19**(1): 87-95.

Gershuni, G. Z., P. Laure, V. M. Myznikov, B. Roux, and E. M. Zhukhovitsky (1992). "On the stability of plane-parallel advective flows in long horizontal layers." Microgravity Q **2**(3): 141-151.

Ghiaasiaan, S. M. (2008). Two-phase flow boiling and condensation: in conventional and miniature systems, New York, Cambridge University Press.

Ghiaasiaan, S. M., B. K. Kamboj and S. I. Abdelkhalik (1995). "2-fluid modeling of condensation in the presence of noncondensables in 2-phase channel flows." Nuclear Science and Engineering **119**(1): 1-17.

Gillon, P. and G. M. Homsy (1996). "Combined thermocapillary-buoyancy convection in a cavity: an experimental study." Physics of Fluids **8**(11): 2953.

Gmehling, J. and U. Onken (2003). "Vapor-liquid equilibrium data collection: aqueous systems supplement 3." DECHEMA Gesellschaft für Chemische Technik und Biotechnologie e.V., Postfach 150104, D-60061 Frankfurf am Main, Germany.

Gonz âez, B., N. Calvar, E. Gomez and A. Dominguez (2007). "Density, dynamic viscosity, and derived properties of binary mixtures of methanol or ethanol with water, ethyl acetate, and methyl acetate at T=(293.15, 298.15, and 303.15) K." Journal of Chemical Thermodynamics **39**(12): 1578-1588.

Gotkis, Y., I. Ivanov, N. Murisic and L. Kondic (2006). "Dynamic structure formation at the fronts of volatile liquid drops." Physical Review Letters **97**(18).

Guéna, G., C. Poulard and A. M. Cazabat (2007). "Evaporating drops of alkane mixtures." Colloids and Surfaces a-Physicochemical and Engineering Aspects **298**(1-2): 2-11.

Hijikata, K., Y. Fukasaku and O. Nakabeppu (1996). "Theoretical and experimental studies on the pseudo-dropwise condensation of a binary vapor mixture." Journal of Heat Transfer-Transactions of the ASME **118**(1): 140-147.

Hitz, C. B., J. J. Ewing and J. Hecht (2012). Introduction to laser technology, Hoboken, New Jersey, John Wiley & Sons, Inc.

Hosoi, A. E. and J. W. M. Bush (2001). "Evaporative instabilities in climbing films." Journal of Fluid Mechanics **442**: 217-239.

Incropera, F. P., D. P. Dewitt, T. L. Bergman and A. S. Lavine (2007). Fundamentals of heat and mass transfer, sixth edition, John Wiley & Sons (Asia) Pte Ltd.

Jeon, Y. J. and H. J. Sung (2011). "PIV measurement of flow around an arbitrarily moving body." Experiments in Fluids **50**(4): 787-798.

Ji, Y., Q. S. Liu and R. Liu (2008). "Coupling of evaporation and thermocapillary convection in a liquid layer with mass and heat exchanging interface." Chinese Physics Letters **25**(2): 608-611.

Kanatani, K. (2013). "Stability of a condensing liquid film in a binary vapor mixture system." International Journal of Heat and Mass Transfer **58**(1-2): 413-419.

Kageyama, T., P. F. Peterson and V. E. Schrock (1993). "Diffusion layer modeling for condensation in vertical tubes with noncondensable gases." Nuclear Engineering and Design **141**(1-2): 289-302.

Keane, R. D. and R. J. Adrian (1990). "Optimization of particle image velocimeters .1. double pulsed systems." Measurement Science & Technology **1**(11): 1202-1215.

Khosrofian, J. M. and B. A. Garetz (1983). "Measurement of a Gaussian laser-beam diameter through the direct inversion of knife-edge data." Applied Optics **22**(21): 3406-3410.

Kirdyashkin, A. G. (1984). "Thermogravitational and thermocapillary flows in a horizontal liquid layer under the conditions of a horizontal temperature-gradient." International Journal of Heat and Mass Transfer **27**(8): 1205-1218.

Kobayashi, Y., A. Okumura and T. Matsue (1991). "Effect of gravity and noncondensable gas levels on condensation in variable conductance heat pipe." Journal of Thermophysics and Heat Transfer **5**(1): 61-68.

Kiehler, T. P. (2007). Experimental and numerical investigation of thermocapillary effects in thin liquid layers, Georgia Institute of Technology.

Levich, V. G. (1962). "Physicochemical hydrodynamics." Prentice-Hall, Englewood Cliffs, NJ.

Levich, V. G. and V. S. Krylov (1969). "Surface-tension-driven phenomena." Annual Review of Fluid Mechanics **1**: 293-316.

Li, H. (2008). An evanescent-wave based particle image velocimetry technique. Ph.D., Georgia Institute of Technology.

Li, Y., R. Grigoriev and M. Yoda (2014). "Experimental study of the effect of noncondensables on buoyancy-thermocapillary convection in a volatile low-viscosity silicone oil." Physics of Fluids **26**(12).

Liu, C. J., E. Bonaccurso and H. J. Butt (2008). "Evaporation of sessile water/ethanol drops in a controlled environment." Physical Chemistry Chemical Physics **10**(47): 7150-7157.

Liu, C. J. and E. Bonaccurso (2010). "Microcantilever sensors for monitoring the evaporation of microdrops of pure liquids and mixtures." Review of Scientific Instruments **81**(1).

Machrafi, H., A. Rednikov, P. Colinet and P. C. Dauby (2013). "Time-dependent Marangoni-Bénard instability of an evaporating binary-liquid layer including gas transients." Physics of Fluids **25**(8).

Mahajan, R., C. P. Chiu and G. Chrysler (2006). "Cooling a microprocessor chip." Proceedings of the Ieee **94**(8): 1476-1486.

Maqua, C., G. Castanet and F. Lemoine (2008). "Bicomponent droplets evaporation: Temperature measurements and modelling." Fuel **87**(13-14): 2932-2942.

Marangoni, C. G. M. (1971). "Ueber die ausbreitugn der tropfen einer flussigkeit auf der obderflache einer anderen." Ann. Phys. Chem. (Poggendorff) **143**: 337-354.

Markos, M., V. S. Ajaev and G. M. Homsy (2006). "Steady flow and evaporation of a volatile liquid in a wedge." Physics of Fluids **18**(9): 092102.

Meinhart, C. D., S. T. Wereley and J. G. Santiago (2000). "A PIV algorithm for estimating time-averaged velocity fields." Journal of Fluids Engineering-Transactions of the ASME **122**(2): 285-289.

Mercier, J. F. and C. Normand (1996). "Buoyant-thermocapillary instabilities of differentially heated liquid layers." Physics of Fluids **8**(6): 1433-1445.

Mercier, J. F. and C. Normand (2002). "Influence of the Prandtl number on the location of recirculation eddies in thermocapillary flows." International Journal of Heat and Mass Transfer **45**(4): 793-801.

Minkowycz, W. J. and E. M. Sparrow (1966). "Condensation heat transfer in the presence of noncondensables, interfacial resistance, superheating, variable properties, and diffusion." International Journal of Heat and Mass Transfer **9**: 1125-1144.

Moffat, R. J. (1988). "Describing the uncertainties in experimental results." Experimental Thermal and Fluid Science **1**(1): 3-17.

Mundrane, M. and A. Zebib (1994). "Oscillatory buoyant thermocapillary flow." Physics of Fluids **6**(10): 3294.

Murase, T., H. S. Wang and J. W. Rose (2007). "Marangoni condensation of steam–ethanol mixtures on a horizontal tube." International Journal of Heat and Mass Transfer **50**(19-20): 3774-3779.

Mutabazi, I., J. E. Wesfreid and E. Guyon (2006). Dynamics of spatio-temporal cellular structures: Henri Bénard centenary review, Springer.

Nepomnyashchy, A., M. G. Velarde and P. Colinet (2002). Interfacial phenomena and convection. Boca Raton, FL, Chapman & Hall/CRC.

Normand, C., Y. Pomeau and M. G. Velarde (1977). "Convective instability: a physicist's approach." Reviews of Modern Physics **49**(581-624).

Ohta, H., T. Sakai, S. Yamaguchi, Y. Ito, Y. Shinmoto and Y. Abe (2007). "Nucleate boiling of low-concentration alcohol aqueous solutions for the development of thermal management systems in space." Microgravity Science and Technology **19**(3-4): 141-143.

Othmer, D. F. (1929). "The condensation of steam." Industrial and Engineering Chemistry **21**: 576-583.

Parmentier, P. M., V. C. Regnier and G. Lebon (1993). "Buoyant-thermocapillary instabilities in medium-Prandtl-number fluid layers subject to a horizontal temperature-gradient." International Journal of Heat and Mass Transfer **36**(9): 2417-2427.

Pearson, J. R. A. (1958). "On convection cells induced by surface tension." Journal of Fluid Mechanics **4**(5): 489-500.

Pedrotti, F. L. and L. S. Pedrotti (1993). Introduction to optics, Prentice Hall.

Pelacho, M. A. and J. Burguete (1999). "Temperature oscillations of hydrothermal waves in thermocapillary-buoyancy convection." Physical Review E **59**(1): 835-840.

Pérez-García, C., S. Madruga, B. Echebarria, G. Lebon and J. Burguete (2004). "Hydrothermal waves and corotating rolls in laterally heated convection in simple liquids." Journal of Non-Equilibrium Thermodynamics **29**(4).

Peterson, G. P. (1994). An introduction to heat pipes: modeling, testing and applications, New York, John Wiley and Sons.

Philpott, C. and J. Deans (2004). "The enhancement of steam condensation heat transfer in a horizontal shell and tube condenser by addition of ammonia." International Journal of Heat and Mass Transfer **47**(17-18): 3683-3693.

Priede, J. and G. Gerbeth (1997). "Convective, absolute, and global instabilities of thermocapillary-buoyancy convection in extended layers." Physical Review E **56**(4): 4187-4199.

Qin, T. and R. O. Grigoriev (2012). Convection, evaporation, and condensation of simple and binary fluids in confined geometries. 3rd ASME Micro/Nanoscale Heat & Mass Transfer International Conference, Atlanta, GA.

Qin, T. and R. O. Grigoriev (2014). The effect of noncondensables on thermocapillary-buoyancy convection in volatile fluids. 11th AIAA/ASME Joint Thermophysics and Heat Transfer Conference, Atlanta, GA.

Qin, T. R., Z. Tukovic and R. O. Grigoriev (2014). "Buoyancy-thermocapillary convection of volatile fluids under atmospheric conditions." International Journal of Heat and Mass Transfer **75**: 284-301.

Qin, T. R., Z. Tukovic and R. O. Grigoriev (2015). "Buoyancy-thermocapillary convection of volatile fluids under their vapors." International Journal of Heat and Mass Transfer **80**: 38-49.

Rayleigh, L. (1916). "On convection currents in a horizontal layer of fluid, when the higher temperature is on the under side." Philosophical Magazine **32**(187-92): 529-546.

Riley, R. J. and G. P. Neitzel (1998). "Instability of thermocapillary-buoyancy convection in shallow layers. Part 1. Characterization of steady and oscillatory instabilities." Journal of Fluid Mechanics **359**: 143-164.

Sakurai, M., J. Leypoldt, H. C. Kuhlmann, H. J. Rath and A. Hirata (2002). "Pattern formation and transient thermo-capillary flow in a rectangular side-heated open cavity." Microgravity Science and Technology **13**(3): 30-35.

Savino, R. and D. Paterna (2006). "Marangoni effect and heat pipe dry-out." Physics of Fluids **18**(11): 118103.

Savino, R., N. di Francescantonio, R. Fortezza and Y. Abe (2007). "Heat pipes with binary mixtures and inverse Marangoni effects for microgravity applications." Acta Astronautica **61**(1-6): 16-26.

Siddique, M. (1992). The effects of noncondensable gases on steam condensation under forced convection conditions. Ph.D., Massachusetts Institute of Technology.

Schatz, M. F. and G. P. Neitzel (2001). "Experiments on thermocapillary instabilities." Annual Review of Fluid Mechanics **33**: 93-127.

Schwabe, D., U. Moller, J. Schneider and A. Scharmann (1992). "Instabilities of shallow dynamic thermocapillary liquid layers." Physics of Fluids a-Fluid Dynamics **4**(11): 2368-2381.

Schwabe, D., A. Cramer, J. Schneider, S. Benz and J. Metzger (1999). "Experiments on the multi-roll-structure of thermocapillary flow in side-heated thin liquid layers." Gravitational Effects in Materials and Fluid Sciences **24**(10): 1367-1373.

Schwabe, D. and S. Benz (2002). "Thermocapillary flow instabilities in an annulus under microgravity - Results of the experiment magia." Impact of the Gravity Level on Materials Processing and Fluid Dynamics **29**(4): 629-638.

Sefiane, K. and C. A. Ward (2007). "Recent advances on thermocapillary flows and interfacial conditions during the evaporation of liquids." Advances in Colloid and Interface Science **134-35**: 201-223.

Serpetsi, S. K. and S. G. Yiantsios (2012). "Stability characteristics of solutocapillary Marangoni motion in evaporating thin films." Physics of Fluids **24**(12).

Shevtsova, V., A. Nepomnyashchy and J. Legros (2003). "Thermocapillary-buoyancy convection in a shallow cavity heated from the side." Physical Review E **67**(6).

Shevtsova, V. M. and J. C. Legros (2003). "Instability in thin layer of liquid confined between rigid walls at different temperatures." Acta Astronautica **52**(7): 541-549.

Siddique, M., M. W. Golay and M. S. Kazimi (1994). "Theoretical modeling of forced-convection condensation of steam in a vertical tube in the presence of a noncondensable gas." Nuclear Technology **106**(2): 202-215.

Smith, M. K. and S. H. Davis (1983). "Instabilities of dynamic thermocapillary liquid layers .1. convective instabilities." Journal of Fluid Mechanics **132**(Jul): 119-144.

Smith, M. K. (1986). "Instability mechanisms in dynamic thermocapillary liquid layers." Physics of Fluids **29**(10): 3182-3186.

Sobhan, C. B., R. L. Rag and G. P. Peterson (2007). "A review and comparative study of the investigations on micro heat pipes." International Journal of Energy Research **31**(6-7): 664-688.

Strotos, G., M. Gavaises, A. Theodorakakos and G. Bergeles (2011). "Numerical investigation of the evaporation of two-component droplets." Fuel **90**(4): 1492-1507.

Tanaka, K., Y. Abe, M. Nakagawa, C. Piccolo and R. Savino (2009). "Low-gravity experiments of lightweight flexible heat pipe panels with self-rewetting fluids." Interdisciplinary Transport Phenomena: Fluid, Thermal, Biological, Materials, and Space Sciences **1161**: 554-561.

Tang, G.H., H. W. Zu, Z. N. Zhuang, W. Q. Tao (2012) "Film condensation heat transfer on a horizontal tube in presence of a noncondensable gas." Appl Therm Eng **36**: 414-425.

Thomson, J. (1855). "On certain curious motions observable at the surface of wine and other alcoholic liquors." Philos. Mag. **10**: 330-333.

Uguz, K. E. and R. Narayanan (2012a). "Instability in evaporative binary mixtures. I. The effect of solutal Marangoni convection." Physics of Fluids **24**(9).

Uguz, K. E. and R. Narayanan (2012b). "Instability in evaporative binary mixtures. II. The effect of Rayleigh convection." Physics of Fluids **24**(9).

Utaka, Y. and T. Nishikawa (2003). "Measurement of condensate film thickness for solutal marangoni condensation applying laser extinction method." Journal of Enhanced Heat Transfer **10**(2): 119-129.

Utaka, Y. and S. Wang (2004). "Characteristic curves and the promotion effect of ethanol addition on steam condensation heat transfer." International Journal of Heat and Mass Transfer **47**(21): 4507-4516.

Vázquez, G., E. Alvarez and J. M. Navaza (1995). "Surface-tension of alcohol plus water from 20-degrees-C to 50-Degrees-C." Journal of Chemical and Engineering Data **40**(3): 611-614.

Velarde, M. G., and J. L. Castillo (1982). "Transport and reactive phenomena leading to interfacial instability." in Convective transport and instability phenomena, edited by J. Zierep and H. Oertel (Braun-Verlag, Karlsruhe): 235-264,

Velarde, M. G. (1988). Physicochemical hydrodynamics: interfacial phenomena, New York, Plenum Press.

Villers, D. and J. K. Platten (1987). "Separation of Marangoni convection from gravitational convection in earth experiments." Physicochemical Hydrodynamics **8**(2): 173-183.

Villers, D. and J. K. Platten (1992). "Coupled buoyancy and Marangoni convection in acetone - experiments and comparison with numerical simulations." Journal of Fluid Mechanics **234**: 487-510.

Vochten, R. and G. Petre (1973). "Study of heat of reversible adsorption at air-solution interface .2. experimental determination of heat of reversible adsorption of some alcohols." Journal of Colloid and Interface Science **42**(2): 320-327.

Vuilleumier, R., V. Ego, L. Neltner and A. M. Cazabat (1995). "Tears of wine - the Stationary State." Langmuir **11**(10): 4117-4121.

Wang, S. X. and Y. Utaka (2004). "Effect of non-condensable gas mass fraction on condensation heat transfer for water-ethanol vapor mixture." Jsme International Journal Series B-Fluids and Thermal Engineering **47**(2): 162-167.

Wang, J., J. Yan, S. Hu and J. Liu (2009). "Marangoni condensation heat transfer of water–ethanol mixtures on a vertical surface with temperature gradients." International Journal of Heat and Mass Transfer **52**(9-10): 2324-2334.

Wang, Z., X. F. Peng, A. S. Mujumdar, A. Su and D. J. Lee (2008). "Evaporation of ethanol-water mixture drop on horizontal substrate." Drying Technology **26**(6): 806-810.

Westerweel, J. and F. Scarano (2005). "Universal outlier detection for PIV data." Experiments in Fluids **39**(6): 1096-1100.

Westerweel, J., D. Dabiri and M. Gharib (1997). "The effect of a discrete window offset on the accuracy of cross-correlation analysis of digital PIV recordings." Experiments in Fluids **23**(1): 20-28.

Yan, J., Y. Yang, S. Hu, K. Zhen and J. Liu (2007). "Effects of vapor pressure/velocity and concentration on condensation heat transfer for steam-ethanol vapor mixture." Heat and Mass Transfer **44**(1): 51-60.

Yang, Y., J. Yan, X. Wu and S. Hu (2008). "Effects of vapor pressure on Marangoni condensation of steam-ethanol mixtures." Journal of Thermophysics and Heat Transfer **22**(2): 247-253.

Yaw, C. L. (2003). Yaws' handbook of thermodynamic and physical properties of chemical compounds: physical, thermodynamic and transport properties for 5,000 organic chemical compounds, Norwich, NY, Knovel.

Zhang, J. X. and B. Y. Gong (2012). "A review about condensation heat transfer with non-condensable gases." Advanced Materials Research **516-517**: 239-242.

Zhu, Z. and Q. Liu (2010). "Coupling of thermocapillary convection and evaporation effect in a liquid layer when the evaporating interface is open to air." Chinese Science Bulletin **55**(3): 233-238.